A near-infrared view of the evolution, environment and multiplicity of Massive Young Stellar Objects

Robert Pomohaci

Department of Physics and Astronomy

University of Leeds

Submitted in accordance with the
requirements for the degree of

Doctor of Philosophy

21st of December 2017

The candidate confirms that the work submitted is his own, except where work which has formed part of jointly authored publications has been included. The contribution of the candidate and the other authors to this work has been explicitly indicated below. The candidate confirms that appropriate credit has been given within the thesis where reference has been made to the work of others.

The data presented in Chapter 2 were taken at the AAT by Stuart Lumsden. The initial data reduction was performed by Stuart Lumsden. All subsequent reduction - telluric correction, intrinsic line subtraction with MOLECFIT and flux calibration, as well as all the analysis presented in this thesis were done by myself.

The data presented in Chapter 3 were published in the Monthly Notices of the Royal Astronomical Society, Volume 472, Issue 3, 11 December 2017, Pages 3624-3636. The publication was titled 'Medium-resolution near-infrared spectroscopy of massive young stellar objects' and the co-authors were R. D. Oudmaijer, S. L. Lumsden, M. G. Hoare and I. Mendiguta. The data reduction, analysis and initial drafting of the manuscript was done by myself. R.D. Oudmaijer contributed by re-editing the following versions of manuscript. The other co-authors provided feedback comments for the final version of the manuscript before submission.

Acknowledgements

Firstly, my thanks to my supervisors Rene Oudmaijer and Stuart Lumsden and guidance throughout my PhD. Thanks you for your patience with the months of meetings about flat-fielding and countless paper and thesis manuscripts. You have both been better than I could have ever expected. I would also like to thank Ignacio Mendigutia, Melvin Hoare and all the other academic staff at Leeds for help with many tricky aspects over the past four years. And many thanks are in order to Amanda Clark and all the rest of the administrative support staff in the Department of Physics for all their patience and assistance.

Next, thanks to my PhD colleagues, old and new, who have all provided support and friendship throughout the years. Special thanks to Simon Purser for scientific and political correctness conversations, Marc Evans for fruitful football discussion and being an all-round instigator, Fernando Olguin Choupay for Python and Chilean culture advice and Abigail Frost for being my MYSO bro and taking over all things organising once things got a bit too busy for me.

Outside the office special thanks to my (much) better half Bethany, who has been there for me through thick and thin for the past 7 years of my life. Thank you for putting up with my constant stress and introducing me too all things English and Spanish culture. I cannot wait for our next adventure, things are always better when we are together! Thank you to Bethany's family for welcoming me into their home, I will strive to be 10% as good as Mike Smith!

Also thanks to all my friends from the Model UN debating club, especially Joe and Bansri, for introducing me to this fantastic world of debating and politics, and for dragging me away from my PhD for various conferences in places around the UK.

I would also like to thank my family. Cristi, Monica, Luiza, Carmen, Nelu, Natalia, you have taught me everything I know. I don't know what I would have done without your love, encouragement and support throughout my life in and outside of Romania, but I am certain I wouldn't be here now. Mum, thanks for teaching me to always look out for myself first. Dad thank you for teaching me that you need to be selfless sometimes as well. Luiza, thank you for showing me the creative side of things. I owe it all to all of you.

Thanks.

Abstract

This thesis presents near-infrared spectroscopy and imaging on large samples of Massive Young Stellar Objects (MYSOs) drawn from the Red MSX (RMS) survey.

Low resolution spectra of 92 MYSOs in the near-infrared (NIR) H and K spectral bands taken at the Anglo-Australian Telescope (AAT) are presented. The targets are classified under the Cooper (2013) MYSO evolutionary scheme. Based on the presence or absence of H_2, HI and FeII lines, MYSOs are placed in an evolutionary sequence ranging from Type Is, which are embedded and show strong shocks to the evolved Type IVs, which are the least embedded. Bolometric luminosity and distance are excluded as drivers of the evolutionary sequence through Kolmogoroff-Smirnoff tests. The different MYSO classes segregate in mid-IR colour space, with the youngest sources being the most embedded, and the more evolved sources bluer. The results from the spectroscopy are compared with radio data on ionised jets in MYSOs and with submilimetre data on star-forming clumps. The lowest jet detection rates are found in evolved MYSOs. The youngest sources are located in the most massive clumps.

Next, medium-resolution spectra from Gemini are presented for 36 MYSOs. This is the largest sample of MYSOs observed at this resolution in the NIR. One MYSO showed intrinsic stellar absorption lines, and was assigned a spectral type of an early A giant/supergiant with added continuum dust excess emission. This is consistent with the swollen up MYSOs found in the simulations of Hosokawa *et al.* (2010), and is the first time observational evidence for swollen up MYSOs has been found. Line luminosities and accretion rates deduced from Brγ emission are consistent with values from low-mass YSOs, supporting theories of scaled-up high mass star formation. The luminosities of various lines show strong correlations with each other, even when accounting for distance and line flux biases. This may be due to the luminosities being proportional to the stellar mass. The detection rates of P Cygni and inverse P Cygni are lower in MYSOs than in low-mass YSOs. This is consistent with a change in the accretion mechanism from magnetospheric accretion in T Taus/HAe stars to disc accretion in HBes/MYSOs. Velocity-resolved Brγ/Br12 ratios are analysed, revealing that the observed ratio features do not correlate with bolometric luminosity, NIR colour or the Cooper (2013) evolutionary sequence. The mechanism that causes the variation in profile ratio features is not clear from this data, but it may be a consequence of the variety in inclination with respect to the line of sight of the MYSOs.

Finally, a pilot adaptive optics survey in the K band has been performed on 32 MYSOs in order to search for binary companions. This is the first ever systematic study of multiplicity in MYSOs. 18 new companions are found within 3", corresponding to a raw multiplicity fraction of 31% and a companion fraction of 53%. MYSOs have larger multiplicity fractions than their lower mass or more evolved counterparts at these scales. This indicates that multiplicity increases with mass and decreases with evolutionary stage, similar to trends seen for field stars. Lower limits to companion masses and mass ratios are obtained from the K band magnitudes, correcting only for foreground extinction. Results indicate that a larger fraction than expected of the companions have high mass ratios ($q>0.5$), in disagreement with the idea that the companions are randomly captured field sources.

In summary, this thesis presents a large amount of spectra of MYSOs, forming a census of massive star formation in different environments throughout the Galaxy, probing the circumstellar region and evolution throughout the MYSO phase. Accretion rates from Brγ support high mass star formation theories based on scaling up from the low mass case. The first ever detection of a swollen up MYSO is found in this sample. The first systematic search for multiplicity in the MYSO phase is reported, and results from this investigation prove that many massive stars form as part of multiple systems.

Abbreviations

2MASS	2 Micron All-Sky Survey
3D MHD	Three-dimensional magneto-hydrodynamics
A_V	Extinction in the V band
AAT	Anglo-Australian Telescope
AMBER	Astronomical Multi-BEam combineR
AO	Adaptive Optics
Ap	Peculiar A star
APEX	Atacama Pathfinder Experiment
ATCA	Australian Telescope Compact Array
ATLASGAL	APEX Telescope Large Area Survey of the Galaxy
au	Astronomical Unit
Bp	Peculiar B star
C13	Cooper (2013)
CDF	Cumulative distribution function
CF	Companion function
CI	Colour Index
CLO13	Cooper *et al.* (2013)
CO	Carbon monoxide molecule
CONICA	Coude Near Infrared Camera
CORNISH	Co-Ordinated Radio 'N' Infrared Survey for High-mass star formation
CTT	Classical T Tauri star
DIB	Diffuse Interstellar Band
E-ELT	European Extremely Large Telescope
ES	Evolved Star
ESO	European Southern Observatory
EW	Equivalent Width
FIR	Far-infrared
FWHM	Full-Width Half-Maximum
GAIA	Graphical Astronomy and Image Analysis Tool
GLIMPSE	Galactic Legacy Infrared Midplane Extraordinaire
GMC	Giant Molecular Cloud

GNIRS	Gemini Near-Infrared Spectrograph
H_2	Molecular hydrogen
$H\alpha$	Hydrogen-alpha
Hae	Herbig Ae star
Hbe	Herbig Be star
HCHII	Hyper-compact HII region
HMC	Hot Molecular Core
IFU	Integral Field Uni
IMF	Initial Mass Function
InSb	Indium Antimonide
IPC	Inverse P Cygni-type profile
IR	Infrared
IRAS	Infrared Astronomical Satellite
IRDC	Infrared Dark Cloud
IRIS2	Infrared Interferometer Spectrometer 2
ISM	Interstellar Medium
ISOCAM	ISO Infrared Camera
JWST	James Webb Space Telescope
K-S	Kolmogoroff-Smirnoff
kpc	kiloparsec
LBLRTM	Line-By-Line Radiative Transfer Model
LMC	Large Magellanic Cloud
LSR	Local Standard of Rest
$\dot{M}$	Mass accretion rate
M_*	Stellar mass
$M_\odot$	Solar mass
MA	Magnetospheric accretion
MF	Multiplicity function
MIPS	Multiband Imaging Photometer for Spitzer
MIR	Mid-infrared
MS	Main Sequence
MSX	Midcourse Space Experiment
MYSO	Massive Young Stellar Object
NaCo	Nasmyth Adaptive Optics System
NIR	Near-infrared
ONC	Orion Nebula Cluster
PA	Position Angle
PAH	Polycyclic aromatic hydrocarbon
pc	parsec
PC	P Cygni-type profile
PN	Planetary Nebula

PSC	Point source catalogue
PSF	Point-Spread Function
PyRAF	Python IRAF
$R_\odot$	Solar radius
RJ	Rayleigh-Jeans
RMS	Red MSX survey
SED	Spectral energy distribution
SFR	Star formation rate
SINFONI	Spectrograph for Integral Field Observation in the Near Infrared
SKA	Square Kilometre Array
SMC	Small Magellanic Cloud
SNR	Signal-to-Noise Ratio
SPIRIT III	Spatial Infrared Imaging Telescope III
SR	Strehl Ratio
TIMMI2	Thermal Infrared Multimode Instrument Version 2
TT	T Tauri star
UCHII	Ultra-compact HII region
UKIDSS	UKIRT Infrared Deep Sky Survey
UT1	Unit Telescope 1
UV	Ultra-violet
VISTA	Visible and Infrared Survey Telescope for Astronomy
VLT	Very Large Telescope
VLTI	Very Large Telescope Interferometer
VVV	Vista Variable in the Via Lactea
WISE	Wide-field Infrared Survey Explorer
WTT	Weak T Tauri star
YSO	Young Stellar Object
ZAMS	Zero-age Main Sequence

Contents

List of Figures

List of Tables

Chapter 1

Introduction

1.1 Introduction

The study of stars is an important branch of astrophysics. Processes occurring throughout the life of stars drive the evolution of the galaxy they are a part of. Stars offer a unique opportunity to test extreme physics because of the conditions of high temperature, pressure and density in their interiors. The main factor affecting their evolution is the initial mass of the star, which is set by the process of star formation.

The division between low and high mass stars is 8 $M_\odot$. Stars more massive than this limit can burn hydrogen into helium through the CNO cycle while on the Main Sequence, which is more efficient than the proton–proton chain that solar–mass stars use. As such, massive stars deplete their hydrogen supplies faster than low–mass stars. High–mass stars are also able to burn elements heavier than helium through nuclear fusion. The endpoint of their evolution is a supernova, one of the most energetic explosions in the Universe, which can outshine a whole galaxy.

Massive stars have much stronger stellar winds than their low–mass counterparts. Through these winds, high–mass stars input a large amount of gas and energy into the galactic environment. This has a dramatic effect on the local surroundings, possibly triggering the formation of new stars (Sugitani *et al.* 1989).

Low–mass stars are expected to form as a result of the collapse of a molecular cloud and accretion through a circumstellar disc as per the review of Shu *et al.*

(1987). However, applying this paradigm to high–mass star formation is not straightforward. As shown by the simulations of Kahn (1974), radiation pressure halts accretion for objects more massive than 40 $M_\odot$. Given that observations have found stars of 100 $M_\odot$ and above (Crowther *et al.* 2016), there must be a way for radiation to escape without halting the accretion process.

Observing high–mass stars during their formation is also difficult. One of the reasons for this is their rarity, as predicted by the initial mass function (Salpeter 1955). As such, high–mass star–forming clouds are generally further away (distances of order kpc) than low–mass ones (distances of order hundreds of pc). Because of this, a whole star–forming complex can be spatially unresolved, resulting in biases due to source confusion. For massive stars, the timescale for contraction (known as Kelvin–Helmholtz timescale) is much shorter than the gravitational free–fall timescale. This means they are still embedded in their natal dusty cloud when they begin fusion reactions. The spectral energy distribution (SED) of massive pre–stellar objects peaks in the infrared, with most of the emission not from the star itself but from the surrounding dust cloud. There is no observed emission at wavelengths shorter than near–infrared (NIR).

There are two main theoretical approaches to explaining massive star formation: monolithic collapse of turbulent cores (McKee & Tan 2003) and competitive accretion (Bonnell & Bate 2006). Monolithic collapse suggests that high–mass stars form in a similar fashion to low mass stars, in clumps supported against collapse by turbulence, with different mechanisms being used to eliminate radiation pressure such as ionised jets and winds. Competitive accretion takes the different view that massive stars form only in the centers of clusters, where they can take advantage of the stronger gravitational potential. These theories are explained in more detail in Section 1.3

The aim of this thesis is to study precursors of high–mass stars known as massive young stellar objects (MYSOs) in order to obtain observational data that can constrain different formation theories. These objects may have started nuclear fusion in their cores, but are still embedded in their natal cloud which contains clues to their formation. Because of this, they are only observable at long wavelengths (infrared, radio). Using line tracers, the presence of winds and/or discs can be inferred.

1.2 Low mass star formation

The current understanding of low–mass star formation is summarised in the reviews of Shu *et al.* (1987) and Larson (2003).

Star formation starts in Giant Molecular Clouds (also known as GMCs, for more details see Section 1.4.1). These structures are supported against gravitational collapse by magnetic, thermal and turbulent pressure. Charged particles in GMCs are prevented from collapse by the cloud magnetic fields, but neutral molecules are not affected by this field. As such they can separate from ionised particles in a process known as ambipolar diffusion. The ionisation fraction of GMCs is low, and so ambipolar diffusion will result in a loss of magnetic and turbulent support for the cloud. The neutral atoms can start to collapse into a pre–stellar core.

Once the turbulent and magnetic support is lost, the only force opposing gravitational collapse is assumed to be thermal pressure, so the cloud is described by the virial theorem:

$$2K + U = 0 \tag{1.1}$$

The cloud is in equilibrium until any perturbations arise, which can cause it to either collapse under gravity or expand due to gas pressure. Perturbations may be caused by either a supernova explosion shock, density fluctuations when the cloud passes through the spiral arms of the Galaxy or winds from nearby OB stars (Smith & Brooks 2008).

From the virial theorem one can calculate the minimum mass for collapse, known as the Jeans mass (Jeans 1902), given by:

$$M_J = \left(\frac{5kT}{G\mu m_H}\right)^{3/2} \left(\frac{3}{4\pi\rho}\right)^{1/2}, \tag{1.2}$$

where k is Boltzmann's constant, T the temperature, μ the mean molecular weight, m_H the mass of a hydrogen atom, G the gravitational constant and ρ is the density in kg/m^{-3}. Once the collapse ensues, it proceeds in a runaway fashion under gravitational free–fall. The collapse is isothermal as long as the cloud is optically thin, and so the increase in density causes the Jeans mass to decrease. Smaller fragments start to collapse on their own, in a process which is known as fragmentation. At densities above 10^{10} cm^{--3}, the collapse becomes adiabatic. The core becomes optically thick and so line cooling is less efficient. This increases the temperature, and the Jeans mass with it as well, halting the free–fall collapse. Thermal pressure can balance gravity again and the first hydrostatic core is formed.

Once the cloud reaches 2000 K, hydrogen molecules begin to dissociate. The photon energy lost in dissociating the H_2 results in a decrease in the gas pressure. As such, gravity dominates once more and free–fall collapse can re–ensue. An accretion disc will form around the pre–stellar core due to the centrifugal force being stronger than gravity at the equator. The accretion disc helps conserve angular momentum during the collapse. The temperature keeps rising due to shocks resulting from the accreted material falling onto the core. Once the core has contracted significantly, it will be hot enough (10^6 K) to start nuclear burning of deuterium (at around 0.2 $M_\odot$ for an eventual solar–mass star).

The core becomes convective, and along with differential rotation rates this creates a stellar magnetic field. This field helps the prestellar object grow through magnetospheric accretion from the disc (for details see Section 1.2.1). The field also collimates the material ejected from the pre–stellar object into jets and bipolar outflows, which expel the angular momentum of the collapsing material (see Figure 1.1 and the review of Appenzeller & Mundt 1989). Outflows will entrain material from the surrounding medium, creating a cavity, and as a result the collimation of the jet decreases. By this stage there is little material left for accretion. With the accretion process slowing down or stopping completely the outflows decrease in intensity. Once the accretion stops, the star can begin its main sequence phase. Nuclear fusion of hydrogen into helium starts when the core temperature reaches 10^7 K.

Observationally, these different phases of low–mass pre–stellar evolution are divided into four classes according to the peak and shape of the stellar energy distribution (SED). Class 0 objects are the youngest, peaking in the submilimetre, with the emission being dominated by dust. This is a rapid accretion phase which is thought to last about 10^4 years. Class I objects emit mostly in the far–infrared. This is the main accretion phase, lasting about 10^5 years. The SED (as measured in the range 2–25 μm) can be fit by a power law with a spectral

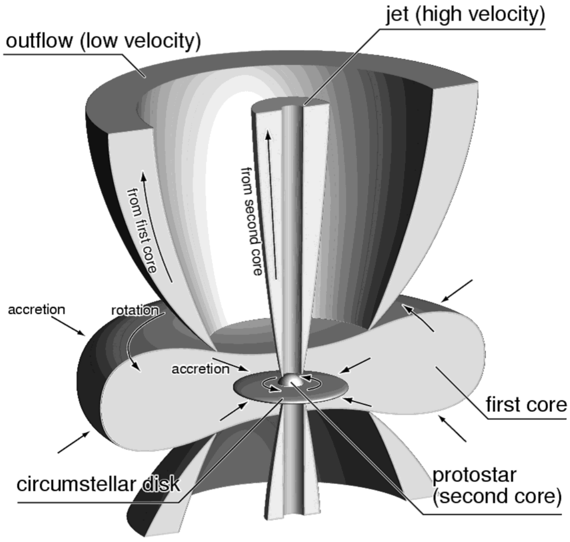

Figure 1.1: Protostellar jet and outflow diagram from Machida *et al.* (2009)

index larger than 0. In Class II objects the emission is doubly peaked, with the dominant peak in the near–IR, and a spectral index between –2 and 0. This phase lasts about 10^6 years. In the final phase, Class III, the star has reached the main sequence, but a remnant of the circumstellar dust is still being dispersed by the stellar wind, and as such the shape of the spectrum is similar to the SED of a MS star. The spectral index of the SED is lower than –2. This evolutionary sequence is displayed in Figure 1.2.

1.2.1 T Tauri stars

T Tauri stars were first identified by Joy (1945) as a new class of variable stars of low luminosity, associated with nebulosity and showing low excitation emission lines similar to the solar chromosphere. Based on their IR and UV excesses, as well as their spectral types (F–G), they were found to correspond to the solar–mass star precursors referred to as Class II YSOs. These objects are now known as Classical T Tauri stars (CTTs).

A different class of T Tauri stars was discovered by Feigelson & Kriss (1981) which are referred to as Weak T Tauri stars (WTTs). These display stronger X–ray emission than CTTs (Stelzer & Neuhäuser 2001), weaker emission lines

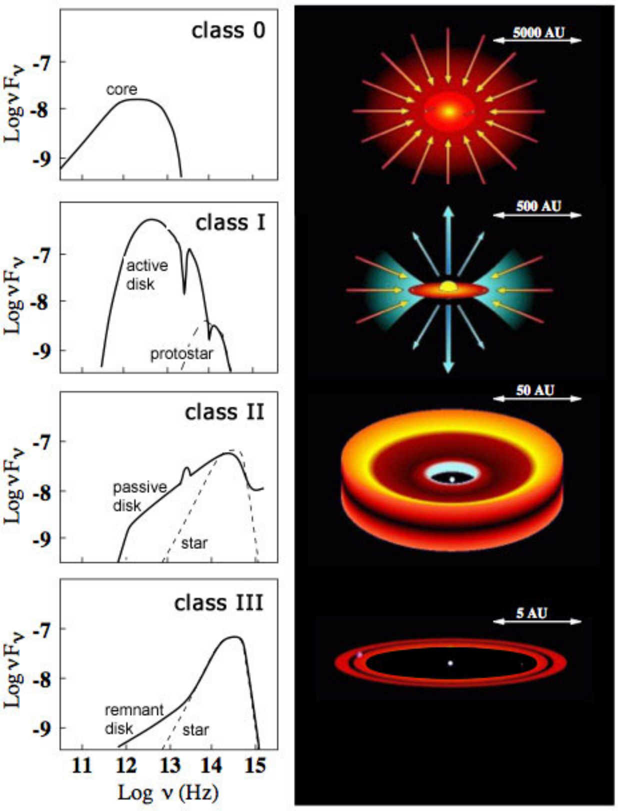

Figure 1.2: YSO classification scheme from Isella (2007)

than CTTs (EW of Hα $<$ 10 Å), no IR excess and little variability. Based on this, WTTs were identified as Classs III YSOs, at a later evolutionary stage than CTTs.

Initial theories suggested that TTs might be undergoing accretion directly from the circumstellar disc via a boundary layer (Bertout *et al.* 1988). Observations and theory (Shu *et al.* 1994, Calvet & Gullbring 1998) have established that the accretion is instead assisted by the stellar magnetic field (also known as magnetospheric accretion, or MA). The field truncates the accretion disc at a given radius from the stellar surface, depending on the field strength. Material from the inner edge of the accretion disc flows onto the star along the field lines. Once accreted material reaches the stellar surface it shocks the photosphere and produces soft X–rays. This radiation is then thermally reprocessed and can be observed as a UV excess emission. There is a wealth of observational support for this model, including strong magnetic fields (Johns-Krull 2007), measured continuum excesses and resulting accretion rates (Gullbring *et al.* 2000) and line profiles as expected from accretion columns (Muzerolle *et al.* 2001). In addition, the accretion line luminosity correlates with emission line strength (Ingleby *et al.* 2013). This relation also extends to both brown dwarfs (Natta *et al.* 2004) and intermediate mass TTs (1.5–2.5 $M_\odot$, Calvet *et al.* 2004).

1.2.2 Herbig Ae/Be stars

Intermediate mass (2–8 $M_\odot$) YSOs were first identified by Herbig (1960). These objects, which are now referred to as Herbig Ae/Be stars, have three distinguishing characteristics. Their spectral type is A or B; they show emission lines; they are located within an obscured region which they illuminate. Later surveys (The *et al.* 1994, Vieira *et al.* 2003) have used the presence of IR excess to search for Herbig Ae/Be stars.

A number of observations at different wavelengths suggest the presence of a circumstellar disc, which leads to the aforementioned IR excess. Discs have been found through direct optical imaging (Grady *et al.* 2001), submilimetre observations (Mannings & Sargent 1997) as well as polarisation measurements of light reflected from the disc (Vink *et al.* 2002). Based on the shape of the continuum, Meeus *et al.* (2001) classified the discs of Herbig Ae/Be stars into two subcategories. In Group I sources the stellar radiation causes the outer disc to become flared. Group II objects have an inner disc which shields the outer parts from the stellar radiation, and the IR excess of these sources can be fit by a power law. Group II discs show ro–vibrational CO bandhead emission only out to 1 au, whereas flared discs show this emission out to 10 au (Ilee *et al.* 2014). It has been suggested that the difference between these two types of objects may be age, with dust in flared discs eventually shielding the disc from radiation and stop the flaring. However, Maaskant *et al.* (2013) have found gaps in all Group I discs, which casts doubt on the hypothesis of evolution from Group I to II.

Dodson-Robinson & Salyk (2011) successfully modelled the gaps as being caused by protoplanets accreting disc material. This has been observed in a couple of cases, as for example in HD142527 by Close *et al.* (2014), who find Hα emission from a protoplanet within a gap accreting at a rate of $\dot{\mathrm{M}} = 6 \times 10^{-10}$ $\mathrm{M}_{\odot}$/yr.

One of the main unsolved questions about Herbig Ae/Be stars is whether the magnetospheric accretion model that explains T Tauri stars can also be applied to intermediate mass YSOs. Modelling shows it does fit observed parameters for some Herbig Ae stars (UX Ori, Muzerolle *et al.* 2004), and accretion rates are often determined from the UV excess using MA modelling (Donehew & Brittain 2011, Mendigutía *et al.* 2011). However, as Mendigutía *et al.* (2011) have shown, MA modelling of accretion rates results in unrealistic fit parameters for some high mass Herbig Be stars. In addition, it is not clear whether the magnetic fields of Herbig Ae/Be stars are strong enough to support accretion – Alecian *et al.* (2013) only detect a magnetic field in 5 out of 70 Herbig Ae/Be stars in their survey. In a recent large spectroscopic survey of Herbig Ae/Be stars, Fairlamb *et al.* (2015) found that the MA model could not be applied to the higher mass Herbig Be stars, as the observed UV excesses could not be reproduced through MA modelling in HBes. In addition, spectropolarimetric observations of Ababakr *et al.* (2017) show that HBes are consistent with discs extending to the stellar surface, as in the boundary layer model, whereas HAes show polarisation effects similar to those of TTaus.

Once they reach the Main Sequence as A and B spectral type stars, they are not expected to have strong magnetic fields, as they do not have convective envelopes that drive the dynamo effect like solar–mass stars. A small fraction (1.7% according to measurements from the solar neighbourhood by Power *et al.* 2007) of intermediate–mass stars known as Ap and Bp stars do have strong magnetic fields. They are chemically peculiar, showing an increased abundance of rare metals compared to the average MS star. The best explanations as to the presence of magnetic fields in Ap/Bp stars suggest that the field is either a remnant of the star formation process (fossil field theory) or caused by a dynamo effect in the convective cores (contemporaneous dynamo effect theory) as discussed by Braithwaite & Spruit (2017).

1.3 Theoretical picture of high-mass star formation

High–mass star formation theory and observations are summarised in the review of Zinnecker & Yorke (2007). One cannot simply apply the paradigm described above for low–mass stars to the formation of high–mass stars. This is because the intense radiation pressure of these objects means that no star over 40 $M_\odot$ can form via spherical accretion, as shown by Kahn (1974). In addition, the envelopes of massive stars are radiative rather than convective. Because of this, high–mass stars cannot sustain a magnetic field.

The main two theoretical approaches to solving the massive star formation problem are known as monolithic collapse and competitive accretion.

1.3.1 Monolithic collapse of isolated cores

This theory is seen as an adaptation of the low–mass paradigm to massive star formation, with changes made to account for the differences detailed at the start of this section. One massive core forms one massive star, and the initial mass of the clump within which the core is located is the main factor that sets the final stellar mass. The only situation where the protostar competes with others over material to accrete is in a close multiple stellar system. As a result, the pre–stellar core mass function should mirror the stellar initial mass function, which has indeed been observed by André *et al.* (2010a).

The turbulent core model of McKee & Tan (2003) sees clumps as quasi–equilibrum structures which form as a result of fragmentation. Kinetic energy from outflows and accretion shocks inside the pre–stellar cores is transferred to the wider clump they are located in to maintain the quasi–equilibrum state of these structures. Alternately, energy can flow from the GMC onto the smaller scales of the clumps to keep them in equilibrum. The cores have considerably larger densities than the clumps they are in, and the pressure is larger than the average of the diffuse ISM or the cloud they are located in. They are supersonically turbulent, and there is no need for them to become subsonically turbulent in order for star formation

to take place. The models produce timescales of massive star formation of order 10^5 yrs, with a weak dependence on stellar mass ($t \propto M_*^{1/4}$). The timescale is more sensitive to the surface density of the clump, $t \propto \Sigma_{cl}^{-3/4}$. Accretion rates are estimated to grow proportionally with time, and expected to reach 10^{-3} $M_\odot$ yr^{-1}. The rate at which material is accreted from the clump onto the core is of the same magnitude as the rate of the material being processed onto the star.
An optically thick accretion disc forms as a result of angular momentum conservation (Wolfire & Cassinelli 1987). This circumstellar disc structure creates an anisotropical distribution of the stellar radiation field, with the radiation at the poles being up to 30×stronger than in equatorial regions. As such, the optical depth is considerably larger at the equator than at the poles. This results in inefficient radiative acceleration on the dust particles in the disc. This in turn causes the accretion disc to be long–lasting, and is known as the flashlight effect, as described by Yorke & Sonnhalter (2002). 3D MHD simulations of Krumholz *et al.* (2009) find that radiative pressure escapes through optically thin bubbles and so the radiation does not halt accretion. Angular momentum is removed through outflows and jets escaping through the polar regions. Kuiper *et al.* (2011) and Kuiper & Yorke (2013) show, through full–radiative transfer modelling of massive star formation that the disc shields itself against the radiation pressure, removing the upper limit on the stellar mass. In addition to the dust opacity, the gas opacity adds to the self–shielding in order to ease the radiation pressure problem.
Recent simulations of Rosen *et al.* (2016) have included 3D radiation–hydrodynamic simulations of collapsing massive pre–stellar cores. They applied an algorithm that simulated the absorption of the direct radiation field in order to obtain an accurate solution for the radiation pressure. However, they did not include outflows, magnetic fields or photoionisation. The model was run under both initial turbulent and laminar conditions. They find that radiation bubbles develop Rayleigh–Taylor instabilities that can help deliver material to the accretion disc as modelled by Krumholz *et al.* (2009). The bubbles can overcome radiation pressure and play an important role in both turbulent and laminar cores, particularly at early stages. The existence of these bubbles results in a cooler disc which is more vulnerable to fragmentation. This produces hierarchical systems with a massive star and several low–mass companions.

Hosokawa *et al.* (2010) perform simulations of protostars with high accretion rates (10^{-3} – 10^{-4} $M_{\odot}$). They find that this results in short timescales for accretion, and so radiative cooling is inefficient at dissipating the energy generated by acccretion. The accretion becomes approximately adiabatic, and this results in a large entropy inside the star and an increase in opacity as the stellar mass grows. The temperature of the star is inversely proportional to the opacity (as per Kramer's law $\kappa \propto \rho T^{-3.5}$) and so the star cools. As $\mathrm{T}^{\alpha} \propto 1/\mathrm{R}$ (as given by the Stefan–Boltzmann law $L = 4\pi R^2 \sigma T^4$), the star will swell up to as much as 100 $R_{\odot}$. Entropy is eventually absorbed into the outer layers of the star and opacity starts to decrease. As a result of the opacity decrease, the stellar luminosity increases, and the Kelvin–Helmholtz timescale for stellar contraction will decrease. The star contracts and temperature increases until it reaches 10^7 K in the core, when hydrogen burning begins and the star reaches the ZAMS. This mechanism of swelling up provides a reason why pre–main sequence Massive Young Stellar Objects (MYSOs) have yet to ionise their surroundings and form an H II region in spite of their large stellar luminosity (as per the discussion of Hoare & Franco 2007). Due to the lower temperature of the MYSO during the swollen up phase, the peak of the stellar emission will move to a longer wavelength, and as such be unable to produce the large Lyman continuum flux required to ionise their surroundings. In conclusion, MYSOs are expected to have a structure similar to late type supergiant stars instead of MS OB stars as previously predicted.

1.3.2 Competitive accretion

A different approach is taken by competitive accretion models (Bonnell *et al.* 1998, Bonnell & Bate 2006). This theory assumes that the fragmentation in a cloud is relatively inefficient, and that there is a large reservoir of gas available for multiple cores to accrete from. Also, this gas must be able to move under the same gravitational acceleration as the cores, without being tied down by magnetic fields. Under these conditions, their simulations find that the cores closest to the cloud center will benefit from the larger gas reservoirs and deeper gravitational potential wells and so will accrete more than those in the outer parts. Also the first and largest core condensations beginning to form in a molecular cloud will be more likely to grow to become the largest stars. The material that forms an individual massive star can come from different parts of the cloud. In contrast to monolithic collapse, the initial mass of the clump will not reflect the Main Sequence mass of the star. The accretion is described by the Bondi–Hoyle law in the centre of clusters, where stellar mass dominates the gravitational potential. The initial accretion occurs at a relatively low rate, from slowly moving gas close to the cores. As they increase in mass, the area of influence of cores will expand, allowing them to accrete gas from further away, which causes a runaway accretion. In other words, in the competitive accretion model, the location of a core within a clump matters more than its initial mass in determining the final mass of the star the pre–stellar core will form. This theory also predicts the existence of discs, although they are expected to be smaller than those in the monolithic collapse models due to interactions between cores in the dense cluster environment. Krumholz *et al.* (2005) criticise this model, suggesting that the initial conditions of the simulations are of strongly gravitationally bound clouds, whereas observations find clouds to be more turbulently supported. They also suggest that the Bondi–Hoyle accretion rates are too low as a result of the high relative velocities between pre–stellar objects and the turbulent gas, and that they are less resilient to stellar radiative feedback. In their later simulations, Bonnell & Bate (2006) argue that Krumholz *et al.* (2005) have used global cloud gas parameters rather than the local properties of massive star forming cluster. They suggest that even with initial conditions of turbulent kinetic energy of a similar strength to gravitational, the results are similar, and that Larson's laws suggest similar velocities of stars and neighbouring gas. In addition, as the most massive stars form at the center of a clump in this scenario, they are likely to have little motion compared to the nearby gas. The authors argue that this scenario of star formation produces an IMF that agrees with the observed distributions and accounts for the mass segregation of young clusters, as well as for the binary properties of stars.

1.4 Observations of high-mass star forming regions

According to Zinnecker & Yorke (2007), the formation of a massive star can be split into the following stages: a) compression of GMC into starless clumps ($\geqslant 10^3 M_\odot$) and cores ($10^2 M_\odot$), b) collapse of clumps into protostellar objects through gravity, c) accretion of material onto the protostar as it approaches the Main Sequence (MS) and d) disruption of the birth cloud through feedback effects of stellar winds. These different stages can be studied observationally in the following structures.

1.4.1 Early stages – Giant Molecular Clouds, filaments and cores

The formation of a star starts in the cold molecular phase of the interstellar medium (first proposed by McKee & Ostriker 1977), in objects known as Giant Molecular Clouds (GMCs). These are structures of the order of hundreds of parsecs, containing masses of the order of $10^4 - 10^6$ $M_\odot$, and are at temperatures around 10K. GMCs have a partly fractal structure, being composed of filaments and high density clumps on small scales (Williams *et al.* 2000). Observations of large samples of GMCs by Larson (1981) show that the velocity dispersion of a cloud increases with the size as a power law:

$$\sigma(km/s) = 1.1L(pc)^{0.38}, \tag{1.3}$$

where σ is the velocity dispersion and L the size; this relationship applies for $0.1 \leq L \leq 100$ pc. The power index is similar to the Kolmogorov (1941) law which describes turbulent flows. This is an indication of the fact that these clouds are supported by turbulence against gravity.

H_2 maps of the Galaxy show that the density in the interarm region is much lower than GMC densities. This suggests that molecular cloud lifetimes must be lower than the time to travel between Galactic arms, which is 10^8 yrs at the solar position. It is believed that OB stellar feedback disrupts GMCs, causing them to have a relatively short lifetime (Blitz & Shu 1980).

100 μm infrared surveys have been used to determine whether all GMC are forming stars. Based on the ratio of infrared emission to the virialised mass within a cloud, it seems there are few quiescent GMCs in the nearest 3 kpc to the Sun. Surveys of the inner galaxy suggest that as many as 25% of GMCs may be inactive based on the lack of 100 μm emission. However, Blitz (1993) argues that many of the clouds in the inner Galaxy may appear infrared–quiet (and so not forming stars) due to source confusion. He estimates that the fraction of quiescent GMCs is probably less than 10%, and that these are only the youngest molecular clouds. Given all of this, it is likely that GMCs are a transient phase of the ISM, and that they are dissipated as a result of the process of star formation.

The Herschel Telescope Gould Belt Survey (André *et al.* 2010b) showed that massive filaments are ubiquitous in GMCs. These structures have temperatures of order ≈10K. They are long (1–80 pc, Jackson *et al.* 2010) and thin (0.1 pc wide). It is believed that they are formed as a result of the removal of kinetic energy through large scale magneto–hydrodynamic flows (André 2017). One of the best explanations for the 0.1 pc width of filaments is that this corresponds to the scale of the transition between supersonic and subsonic turbulence (André *et al.* 2014). Below this scale, subsonic turbulence cannot cause any more fragmentation of non–star forming material (Padoan *et al.* 2001).

Their radial density profiles are described by a Plummer–like function, with a power index of 2 (Arzoumanian *et al.* 2011), rather than 4 as expected for isothermal gas in hydrodynamic equilibrum. Models suggest that the density profiles are better described by polytropic equations of state, which may point to gravitational contraction occurring in the filaments (Palmeirim *et al.* 2013).

The densest filaments, with masses per unit length larger than the critical line mass of isothermal structures are believed to be undergoing gravitational fragmentation into prestellar cores. These are the cores that are thought to eventually lead to star and cluster formation.

High–mass starless cores, also referred to as infrared dark clouds (IRDCs), were first discovered by the Midcourse Space Experiment or MSX (Egan *et al.* 1998) and the Infrared Space Observatory Camera or ISOCAM (Perault *et al.* 1996). They have high densities ($>10^4$cm^{-3}) and low temperatures (<25 K), and are seen in absorption against the Galactic background in the mid–IR up to 100 μm. IRDCs present filamentary structure, which is caused by preferential collapse along the shortest dimension of a cloud. They are best observed at millimetre and submillimetre wavelengths as this is where the peak of the emission is located. Rathborne *et al.* (2006) performed an imaging survey of 38 IRDCs at 1.2 mm. They found all IRDCs to contain at least one compact core (<0.5 pc). A number of IRDCs are associated with bright mid–IR emission, which the authors interpret as indication of later evolutionary phase. The IRDC masses, sizes and densities are similar to those of later evolutionary phases of massive star formation, although they are colder. Rathborne *et al.* (2006) suggest that IRDCs are the high–mass equivalent of low–mass Bok globules. The slope of the core mass function in IRDCs is determined to be 2.1±0.4, similar to that of the stellar IMF. Also the deduced star formation rate is 2 $M_{\odot}yr^{-1}$, close to the Galactic SFR, suggesting this is the location of star formation.

The next phase is known as the hot molecular core (HMC). They are warmer (100 K) and denser (>10^7cm^{-3}) than IRDCs, are traced by methanol masers, and show a richness of submillimetre line emission and complex organic molecules that have been evaporated off dust grains (CH_3CN, $HCOOCH_3$). They are found at the centre of parsec–sized clumps, where the temperature and density peak. Cesaroni (2005) suggests that they are sites of collapse inside clumps. He suggests the largest hot molecular cores fragment to form clusters of high–mass stars. HMCs in this study are split into light (<100 $M_{\odot}$) cores, which are associated with one or a few massive stars, and heavy ones, with a higher star formation efficiency, and which are associated with the formation of a cluster of massive stars.

1.4.2 Massive Young Stellar Objects

The MYSO phase is a short–lived (10^5 years) evolutionary stage towards the end of the hot core phase. These objects may have started hydrogen fusion, but have not ionised the surrounding nebula to produce an H II region, and as such are radio–quiet. Due to dust extinction, MYSOs are invisible at wavelengths shorter than 1 μm. They are bright in mid–IR, and observed bipolar outflows indicate that accretion is still ongoing. Accretion may be halted during or at the end of this phase, which makes this an ideal point to study the physics of the accretion process and the circumstellar environment during star formation, and how this sets the final mass of the star (see the reviews of Oudmaijer & de Wit 2014 and Lumsden *et al.* 2013). This in turn is very important in order to test the theories described in section 1.3.

There is evidence of accretion discs in MYSOs, through NIR line tracers (Cooper 2013), as well as millimetre observations (Johnston *et al.* 2015, Ilee *et al.* 2016). These objects show strong winds (Bunn *et al.* 1995), outflows (Shepherd & Churchwell 1996), as well as ionised jets (Purser *et al.* 2016). However, their intense dust extinction (median A_V=42 mag as seen by Cooper *et al.* 2013), relative rarity compared to low mass sources, and large distances (of order kpc) they are usually located at has made systematic studies difficult. Often a whole star forming complex is located within only one pixel of a detector, with only the most recent instruments providing high enough spatial resolution for detailed studies of MYSOs.

The first attempts to catalogue MYSOs had been done using data from the IRAS telescope (Neugebauer *et al.* 1984). Campbell *et al.* (1989) identified 115 YSOs from IR colour selection criteria ranging in luminosity from 10–10^4 $L_\odot$.

Molinari *et al.* (1996) and Molinari *et al.* (1998) undertook NH_3 and radio follow–up observations to IRAS sources. However, they limited their observations at over 30° north of the celestial equator to sources more than 1' away from H II regions. This caused a bias against sources inside large H II regions or in wider star forming complexes.

Sridharan *et al.* (2002) and Beuther *et al.* (2002) followed up IRAS observation with FIR data, radio continuum, molecular line data and maser observations. They chose targets with similar gas densities and luminosities to UCH II regions, and with low radio flux (<25 mJy) in order to avoid confusion with UCH IIs. This caused similar biases to the Molinari *et al.* (1996) study. They found only some MYSOs to have maser emission, and not always from the same transition. This indicates that the molecules producing the maser emission are destroyed during the MYSO phase. This poses problems for catalogues of MYSOs which use masers as a detection method.

Using the GLIMPSE point source catalogue with colour selection criteria, Robitaille *et al.* (2008) identified 11000 candidate YSO sources of all masses. However, no follow–up observations were performed to distinguish YSOs from other source of similar MIR colours such as H II regions, evolved stars or planetary nebulae.

Churchwell *et al.* (2006) and Churchwell *et al.* (2007) found 600 H II regions and bubbles in GLIMPSE data. They found that 10% of these had YSOs associated with them, and 12% displayed a morphology suggestive of triggered star formation.

1.4.2.1 The RMS survey

Previous attempts to catalogue MYSOs have been hindered by low instrument resolutions, and few have done multi–wavelength follow up observations. The RMS survey aimed to address these problems by providing a full and unbiased catalogue of MYSOs in our Galaxy. It was based on data from the SPIRIT III instrument (18.3" resolution) on board the Midcourse Space Experiment (MSX). The beam size of this instrument was almost 20 times better than that its predecessor, IRAS. The MSX data was taken in 6 bands 4–21 μm as explained in Price *et al.* (2001).

The initial selection criteria described below have been presented in Lumsden *et al.* (2002), and the results in Lumsden *et al.* (2013). Data from the MSX point source catalogue (PSC) v2.3 (as described by Egan *et al.* 2003) has been used, starting with objects in the galactic plane, omitting the ±10° close to the galactic centre to avoid source confusion. The lower limit of $F_{21 \mu m}$=2.7 Jy in flux was chosen, which ensures 95% completeness for the MSX catalogue. Detections with a signal to noise ratio of at least 5 in the 21 μm band are selected.

Because of the dust extinction, it is expected that MYSOs have a rising red continuum, so the first condition imposed was that the flux increases towards the longer wavelengths ($F_8 < F_{14} < F_{21}$). Next, it was discovered that evolved stars segregate from MYSOs in colour–colour plots (F_{14}/F_8 vs F_{21}/F_{14} and F_{14}/F_{12} vs F_{21}/F_8) (see Figure 1.3). Young sources have $F_{21}/F_8 > 2$. Planetary nebulae are not embedded in a molecular cloud and this makes them bluer in near–IR, and

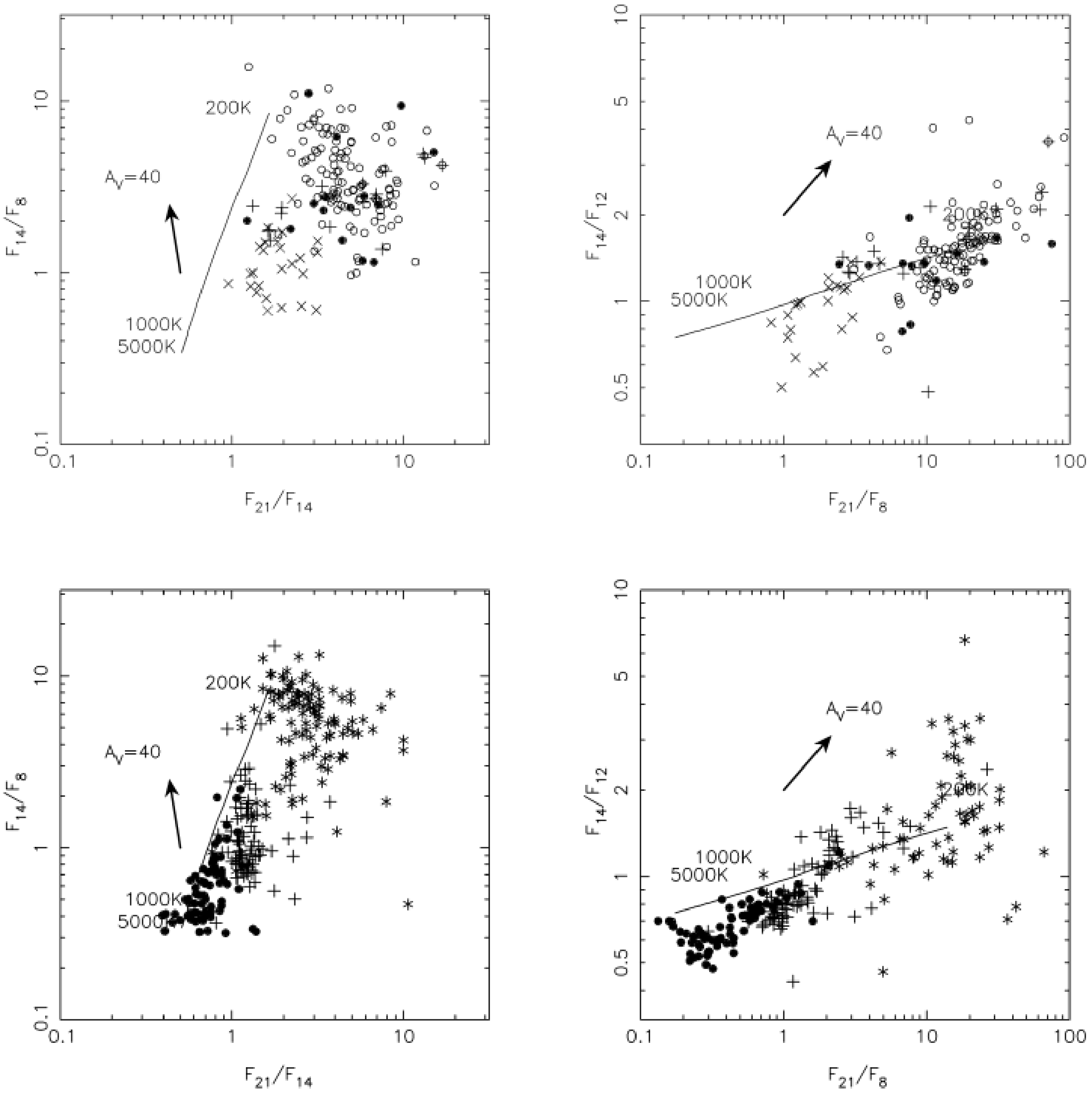

Figure 1.3: Figures 3 and 4 of Lumsden 2002 showing the infrared colour–colour plots of MSX objects. The top two plots show sources associated with star formation – Xs are Herbig Ae/Be stars, +s massive YSOs, methanol masers sources without radio emission filled dots and compact Hii regions empty dots. The bottom two plots illustrate MSX colour ratios of evolved objects – carbon stars are filled dots, OH/IR stars +s and planetary nebulae *s.

so a cut of $F_8/F_K > 5$ and $F_K/F_J > 2$ was applied for MYSOs.

A number of red objects have extended MIR emission. Object with emission larger in size than the MSX beam were rejected from the MYSO catalogue. These targets were classified as either extended H II regions ('Diffuse H II regions' in the RMS catalogue), extended background or filamentary emission around larger structures, or image artefacts caused by the presence of nearby bright sources.

Higher resolution mid–IR data was obtained from ground observations by Mottram *et al.* (2007a), the GLIMPSE Spitzer survey (described by Churchwell *et al.* 2009), as well as from the WISE satellite (Wright *et al.* 2010). These had been visually examined, as the emission was too complex for any automated routine to reliably reject the extended sources. These high–resolution MIR observations were used to resolve multiple sources in the MSX images into separate companions, which were given indices A, B, C, etc. according to their brightness. Concerns about the astrometry of the sources from the MSX PSC, especially in crowded regions was addressed by comparing with data from other catalogues (GLIMPSE, UKIDSS, VVV, 2MASS survey data and radio observations obtained as part of the RMS survey).

Radio continuum observations (see Urquhart *et al.* 2007a, Urquhart *et al.* 2009a) and data from the CORNISH survey described in Hoare *et al.* (2012) and Purcell *et al.* (2013) were used to distinguish H II regions and planetary nebulae (PN) from MYSOs. It is expected that MYSOs have a 5 GHz flux of < 10 mJy.

Some evolved stars or UCH IIs with weak radio fluxes can also appear as an MIR point sources, so near–IR imaging was used. In these images, UCH IIs appear extended, whereas MYSOs are point–like. Near–IR imaging was obtained initially from 2MASS (Skrutskie *et al.* 2006), and later completed with data from the UKIDSS (Lucas *et al.* 2008a) and VVV (Minniti *et al.* 2010) surveys. Differences in photometry between 2MASS and the latter two, especially in the K –band, were corrected with factors determined from plots of magnitudes from these surveys. It is worth noting that 2MASS data is more suitable for bright objects (K<10 mag), as UKIDSS and VVV saturate for objects brighter than this magnitude.

Millimetre ^{13}CO observations have been used by Urquhart *et al.* (2007b) and Urquhart *et al.* (2008a) to measure local standard of rest velocities (v_{LSR}) and compare these with the galactic rotation model from Brand & Blitz (1993) to obtain an estimate for kinematic distances. Far–infrared fluxes from MIPS and the IRAS Galaxy Atlas Data were obtained, with descriptions found in Mottram *et al.* (2010) and Mottram *et al.* (2011a).

Near–IR spectroscopy of the hydrogen Brγ recombination line was used by Cooper *et al.* (2013) as a final classification criterion. Point source PNs and H II regions under the radio cut–off limit mentioned above will have a stronger Brγ peak flux relative to the continuum and a narrower line profile than MYSOs.

All of this multi–wavelength information was then combined to obtain a spectral energy distribution (SED) which was fit in order to infer the luminosity of the sources by Mottram *et al.* (2011a). A final cut of luminosity was applied at $10^4 L_\odot$ in order to differentiate between low and high mass YSOs. In total, 800 YSOs were classified by the RMS survey. Using artificial star tests, as well as comparison with WISE data and other young stellar object catalogues, the completeness ratio of the RMS survey was estimated to be 90%.

MYSO positions appear to be well correlated with the Galactic arm structure, especially in the inner Galaxy. The distance from the Sun of RMS sources ranges between 0.2–16.3 kpc with an average distance of 4.5 kpc (Urquhart *et al.* 2008b). The survey was determined to be complete for young embedded sources above 2×10^4 $L_\odot$ within 18 kpc (excluding the innermost 20 degrees of Galactic longitude, which are not considered due to source confusion close to the Galactic centre.)

1.4.3 H II regions

Once the disc starts to photoevaporate, and small pockets of ionised gas form near the star, the object becomes a hypercompact H II region (HCH II), observable by broad radio hydrogen recombination lines (line width≈75 km/s). Their size is 0.03 pc or 6,000 au, which is close to the expected size scale of a single stellar system (Kurtz 2005).

When the disc is completely dissipated, the star ionises the envelope and disrupts the natal cloud, forming what is known as an ultra–compact H II region (UCH II), which has ionised a mass ≈10 times larger and has a density a factor of ∼100 lower than HCH IIs. They have hydrogen recombination line widths of order few

Table 1.1: The main properties of different classes of H II regions, taken from Kurtz (2005)

Class of region	Size (pc)	Density (cm^{-3})	Emiss. Meas. (pc cm^{-6})	Ionised Mass ($M_\odot$)
Hypercompact	<0.03	$>10^6$	$>10^{10}$	$\approx 10^{-3}$
Ultracompact	<0.1	$>10^4$	$>10^7$	$\approx 10^{-2}$
Compact	<0.5	$>5\times10^3$	$>10^7$	≈ 1
Classical	≈ 10	≈ 100	$\approx 10^2$	$\approx 10^5$
Giant	≈ 100	≈ 30	$\approx 5\times10^5$	10^3–10^6
Supergiant	>100	≈ 10	$\approx 10^5$	10^6–10^8

10s km/s (Hoare 2005). However, it is worth noting that given their size, it is likely that some UCH II may contain more than one forming star.

Finally, the birth cloud is dissipated by radiation pressure and stellar winds and the surface of the star is revealed at optical wavelengths. These final phases are the compact and classical H II region. Strong radio free–free continuum is observed. The main differences in size and properties between the classes of H II regions are summarised in table 1.1, from Kurtz (2005).

Fully formed massive stars are often found in dense OB clusters such as Orion, or OB associations which are more spread out (1–10 pc size). Some of the OB associations contain several dense OB clusters. However, these regions usually contain multiple phases of star formation. For example, the Cygnus X is a large star forming region in our Galaxy which contains the largest known OB star association, Cygnus OB2, with luminous blue variables and blue supergiants (Massey *et al.* 2001). Cygnus X also contains active star–forming regions such as S106 (Schneider *et al.* 2007)

1.5 Multiplicity studies of young stars

Duchêne & Kraus (2013) provide a comprehensive review of stellar multiplicity across mass and age, including star–forming objects.

Multiplicity is seen as an inescapable outcome of star formation, from both a theoretical and observational point of view. It is important for the study of star formation to understand the frequency of multiplicity, as well as its relation to the properties of the primary star. With the advent of all–sky surveys in the past decade, a more robust analysis of the phenomenon of multiplicity is possible. Trends observed in different stellar evolutionary stages can be fed into theoretical star formation models, inform the models on the different factors at play in star formation and help test theories.

The main measurement parameters used are multiple frequency (MF from here, defined as the percentage of multiple systems in a given stellar population) and the companion frequency (CF from here, defined as the average number of companions of primary stars in the sample). Other parameters of interest include P, the orbital period, which can be determined from spectroscopic binaries and the orbital semi–major axis, a, which can be determined from the projected separation in visual binaries. One can then parameterise the distribution of the latter two quantities as

$$f(P) = P^{\alpha} \tag{1.4}$$

A power law of α=–1 results in a log–flat distribution known as Öpik's law. In this scenario, the number of binary systems per logarithmic interval is constant. This suggests there is no preferred scale for forming binary systems. Solar–mass stars in the solar neighbourhood were found to be well fit by Öpik's law, as shown by Duquennoy & Mayor (1991). However, it is worth pointing out that dynamical interactions between the partners in binary systems can significantly change the orbiting period, so the observed distribution of binary periods may not be entirely representative of the primordial period distribution.

In terms of methodology, a survey should aim for a complete and uniform search in a volume–limited sample, as well as use varied observing methods, each appropriate to the type of system studied. Malmquist bias can be corrected by applying statistical methods to a magnitude–limited survey, although differential extinction as well as mass distribution differences can still bias a survey. A sample size of at least 100 targets is required for a precision of 5%, with hundreds of binary systems required for orbital parametrisation, as explained by Duchêne & Kraus (2013).

Several surveys of Main–Sequence stars have been undertaken, and they generally

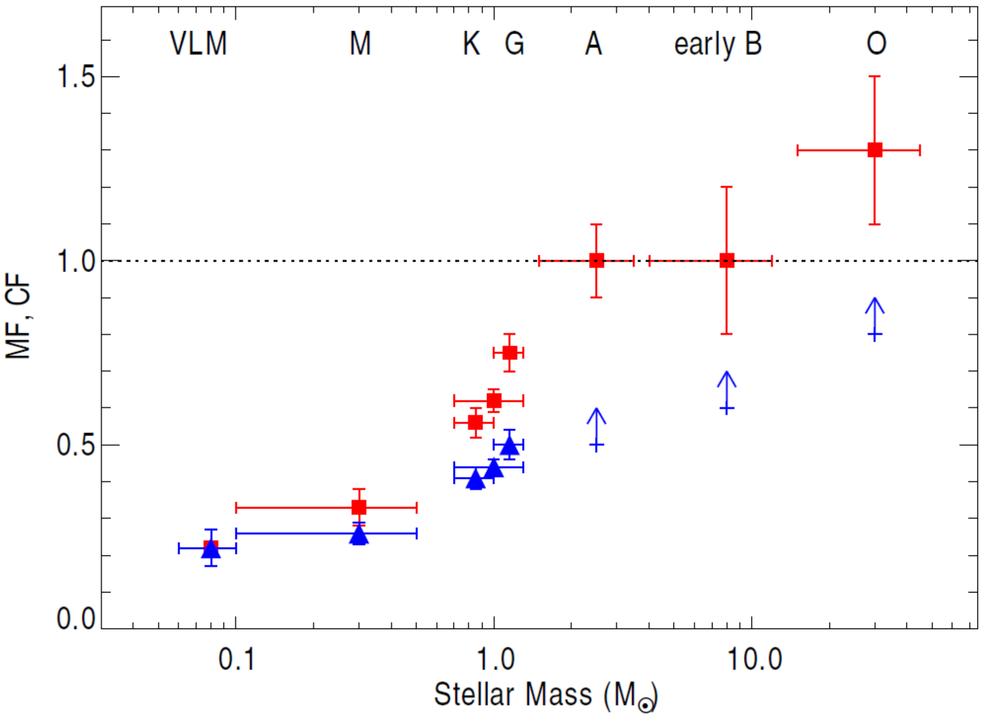

Figure 1.4: Companion fraction (red squares) and multiplicity fraction (blue triangles) as a function of stellar mass, for MS stars and field brown dwarfs, taken from Duchêne & Kraus (2013)

find that multiplicity increases with stellar mass. Whereas for solar–mass stars the fraction is less that half (46% according to Raghavan *et al.* 2010), Sana *et al.* (2012) found multiplicity frequencies of over 70% for O stars (see Figure 1.4). In addition, in 70% of the cases the binary pair was close enough for interactions to occur at some point in the evolution of the star, be it through envelope stripping, accretion and spin up, common envelope evolution or merging. This has significant consequences for stellar evolution models, as most of these are based on single stars. Cluster evolution is also shaped by stellar interactions (Parker & Reggiani 2013).

The smooth variation of parameters associated with multiplicity as a function of primary mass points to multiple systems forming in a similar manner across stellar mass. There is no indication of an upper limit on binary system separation, just a scarcity of observed systems of large separations ($\approx$1 pc). These properties seem to be set during the pre–main sequence phase, with further evolution matching the outcomes of dynamical models. The mass–ratio distributions do not agree with random pairing from the IMF. The observed eccentricities are divided into three ranges. Short orbital period systems follow circular orbits, as a result of tidal dissipation. Long period multiples follow a flat distribution in eccentricity, whilst intermediate period show a rising distribution in eccentricity. Neither of these matches what is expected from a dynamically relaxed or thermal distribution, which is what simulations of multiple systems often use. These findings highlight the need to survey young objects in order to understand the processes that shape stellar multiplicity.

However, most of the large, unbiased and complete surveys refer to fully formed stars. This raises the question of whether the high multiplicity fractions seen are primordial or a result of interactions throughout the evolution of the star.

There have been numerous theories of how massive binaries are formed (see the review of Tohline 2002). One proposed mechanism is capture, which suggests clouds collapse into single stars which then form binary pairs. In disc fragmentation the pre–stellar core is accreting material through a disc, which fragments under a gravitational instability. The disc needs to be gathering a considerable amount of material in its outer regions from the wider cloud for the companions to grow significantly (see Kratter 2010). Turbulent fragmentation (Goodwin *et al.* 2004, Offner *et al.* 2010) proposes that turbulence in a pre–stellar core can result in density inhomogeneities of mass above the local Jeans mass. These will collapse faster than the main core, and as such produce binary or multiple systems. It is worth noting that disc fragmentation is the only theory that produces binary orbits that are aligned in the same plane as the accretion disc.

Multiplicity is a result of many hydrodynamic star formation simulations as well. Krumholz *et al.* (2009) produce a binary system of 32 and 47 $M_\odot$, which corresponds to a mass ratio q$\approx$0.7. Recent work by Meyer *et al.* (2017) and Lund and Bonnell (2017, in prep.) find binaries at a large range of separations, on all scales. However, Rosen *et al.* (2016) point out that the numerical resolution in their simulations and others does not provide an adequate solution for the observed multiplicity parameters of massive stars.

Binary surveys of low–mass Class II/III YSOs in the Taurus cluster have found a very high companion frequency (65–80%, Kraus *et al.* 2011). Mass ratio distributions seem to be fairly flat. By contrast, dense clusters like the ONC show much lower companion frequencies (<10%, Köhler *et al.* 2006). Embedded Class I YSOs have lower companion frequencies than T Tauris, at 37%, but they do seem to follow Opik's law (Connelley *et al.* 2008a, Connelley *et al.* 2008b). Class 0 companion fractions are not significantly lower than Class I, although it is worth noting that there is a lot less multiplicity data for both of these very embedded source types (Looney *et al.* 2000).

The closest observations to MYSOs in mass are the spectro–astrometry studies of Baines *et al.* (2006) and Wheelwright *et al.* (2011) on Herbig Ae/Be stars. They found high multiplicity frequencies (over 70%) and high mass ratios, close to equal mass companions. This is inconsistent with random sampling from the IMF, which is a prediction of the capture theory. They also found higher mass Herbig Bes to have larger multiplicity fractions than Herbig Aes (if uncertain detections were not included), same as the trend seen for MS stars. Finally, binary orbits and disc axes were found to be coplanar at a 2.2–sigma level, based on comparisons with simulated distributions. This gives tentative support to the disc fragmentation formation scenario.

There are a few discoveries of young massive multiple systems so far such as Varricatt *et al.* (2013) and Caratti o Garatti *et al.* (2015). In a recent near–IR interferometric survey of MYSO IRAS 17216–3801, Kraus *et al.* (2017) find a binary system of 18 and 20 $M_\odot$. Both companions in this system have circumstellar discs that are not aligned along the same axis. However, there has been no targeted survey of the multiplicity of massive pre–main sequence stars. The pilot survey presented in Chapter 4 is the first such analysis for MYSOs.

1.6 Near–infrared spectroscopic studies of MYSOs

As MYSOs are embedded objects, they are only visible at NIR wavelengths and longer. Spectroscopy in the near–IR has proven to be an important method for studying the circumstellar medium of these objects, in order to obtain information about accretion discs and winds, which can then inform simulations of such objects.

Simon *et al.* (1981) observed the Brγ lines of M17IRS1 and CRL490. They found FWHM of ≈150 km/s. They argue this must be due to mass motion, as thermal broadening would require temperatures of $\sim 10^6$ K, and Stark broadening requires electron densities of $\sim 10^{15}$ cm^{-3}, neither of which are observed in MYSOs. Later work done by Lumsden *et al.* (2012) did find evidence of Stark broadening or electron scattering in the wings of HI Brackett emission lines.

Simon *et al.* (1983) have used IR spectroscopy of HI recombination lines along with radio continuum measurements at 1.3 cm to study emission of stellar envelopes associated with mass–loss in star–forming regions. They were able to separate UCH IIs from MYSOs, with the ionisation region of UCH IIs resolved in radio data, but not in MYSOs. They find the recombination rates in the envelopes larger than what is expected from the Lyman continuum flux of a Zero–Age MS star. Their observations showed that ionisation from the n=2 energy level by Balmer lines could be an important mechanism in these dense regions. They interpret the ionisation region of MYSOs as similar to a stellar envelope affected by mass loss, with a radius of tens of au. They concluded, from line ratios, that the observed mass–loss flows can be large enough for the gas to become optically thick.

Drew *et al.* (1993) attempted to model Brα/Brγ and Brα/Pfγ line ratios for the MYSO S106 IRS1. For optically thin gas, it is expected that these ratios approach a constant value, as in case B of Baker & Menzel (1938). As the optical depth increases, the longer wavelength Brα transition will become optically thick first, which decreases the Brα/Brγ and Brα/Pfγ ratios . Eventually the Brγ and Pfγ will also become optically thick, and these ratios will reach a minimum value given by $I_1/I_2=(\lambda_1/\lambda_2)^4\ S_1/S_2$, where I is the flux of a given line, λ the wavelength and S the area the line is emitted from. An accelerating stellar wind is expected to produce a parabolic shaped line ratio in velocity space, with a minimum at lower velocities. Drew *et al.* (1993) found a parabolic shape in the wings of the ratio for S106 IRS1, but also a sharp upturn towards optically thin values in the line core. They interpreted this as an accelerating wind combined with a separate slower optically thin wider nebular gas component that is decelerated by mass–loading (see Figure 1.5).

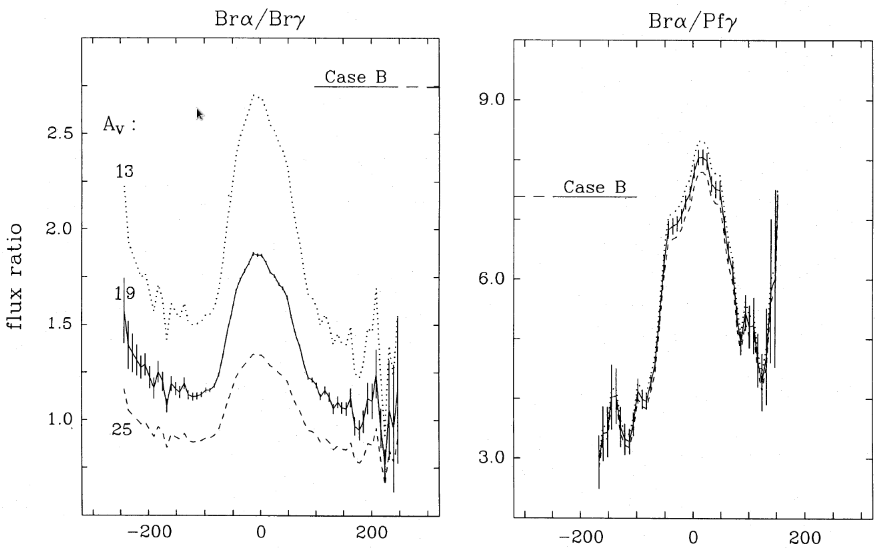

Figure 1.5: Figure 5 of Drew *et al.* (1993), showing line ratios as a function of velocity, with three different extinctions. Also overplotted are the expected Case B ratios at n_e=10^6cm^3 and $T_e \approx 10^4$K

In a subsequent paper Bunn *et al.* (1995) extended this analysis to a larger sample of 7 MYSOs. Whilst this two–component behaviour of S106 IRS1 was seen in the line ratios of some of the objects, there were a number of objects with different features. Three sources showed dish–like profiles expected for an accelerating optically thick wind, and M17 SW IRS1 showed features of a heavily extincted Herbig Be star. The authors suggest that the range of profile features seen corresponds to an evolutionary sequence. They also note that given the values of the line profile ratios, the assumption that all the gas is optically thin is inaccurate. As such, extinction determinations made on the basis of this assumption will lead to unrealistically low values of reddening.

Lumsden *et al.* (2012) also performed a similar analysis to Bunn *et al.* (1995) on the ratio of Brγ/Br12 and found a similar two–component line ratio for S106 IRS1. The Brγ/Br12 ratio is comparable to Brα/Brγ and Brα/Pfγ, as the ratio of the absorption cross–sections of Brγ to Br12 is of the same order as that for the latter two line ratios. The advantage over using the Brα/Brγ and Brα/Pfγ is that wind tracers (Brγ and Br12) and disc tracers (fluorescent FeII and CO bandheads) can be studied with just K and H –band spectra of MYSOs, reducing the required observing time and wavelength range significantly. In addition, the line to continuum ratio is much higher in shorter wavelength lines as the dust excess emission is weaker. However, the shorter wavelength of the Brγ and 12 transitions means they are faint relative to Brα due to dust extinction.

While in T Tauri stars Brγ is understood to arise from the recombination of electrons and protons in the accretion funnels (which is why this line can be used to measure accretion rates), the situation is far from clear in MYSOs. As explained above, the emission has been shown to be consistent with a wind origin. However, it is not obvious whether this wind has a stellar or disc origin. In addition, the Brγ line luminosity has been found to correlate with stellar luminosity across the mass range (Cooper *et al.* 2013). Accretion in MYSOs is unlikely to be aided by magnetic fields through funnels due to the lack of or weakness of the field. Instead, the likely origin of the correlation between Brγ and accretion luminosity is the connection between wind and accretion.

Other elements of the circumstellar environment of MYSOs can also be studied with NIR spectroscopy. The first overtone of ro–vibrational CO transitions (also known as CO bandheads) is indicative of hot (4000K), dense (10^{10}cm^{-3}) and neutral material. It was modeled by Chandler *et al.* (1995) as arising in an accretion disc in MYSOs, near to the star (3–30R$_{\odot}$), as a result of collisional excitation of CO molecules. The outer layers of the disc provide shielding to the inner layers, which creates the hot, dense and neutral medium required for CO bandhead emission. Blum *et al.* (2004) and Bik *et al.* (2006) observed samples of 4 and 20 MYSOs, respectively, at high resolution in the K–band. They find CO bandhead emission which is consistent with a Keplerian disc origin.

Ilee *et al.* (2013) modelled high–resolution CO bandhead observations of a larger sample of 20 MYSOs from the RMS database. They obtained good fits for Keplerian rotating discs, and the best temperature and density exponents of the discs suggest small scale–height (flat) circumstellar discs. However, the CO bandhead is not an ideal disc tracer, as not every MYSO shows these transitions, and high resolution data are required in order to reasonably fit the line emission and interpret the properties of the disc.

The fluorescent FeII line at 1.687 μm requires high–density, partially ionised gas, located close to a source emitting continuum Lyman photons. These conditions are typical of discs, as has been shown in AGNs by Baldwin *et al.* (2004) and Be stars by Zorec *et al.* (2007). Because of this, Lumsden *et al.* (2012) fitted the fluorescent FeII line with a Keplerian disc. The inclination and size of IR–emitting region was obtained from the fits and compared with previous interferometric data. The authors find good agreement with the interferometric data.

Outflows, and the shocks that they produce can also be traced with NIR spectroscopy. Several molecular hydrogen transitions, the strongest of which at 2.12 μm, as well as [Fe II] lines, such as that at 1.64 μm have been used to map outflows (Caratti o Garatti *et al.* 2013). Both of these types of transitions have a low transition probability, and arise in hot, dense conditions, such as in the wake of a shock front produced when an outflow impacts the ISM.

Atomic helium lines in MYSOs, such as that at 2.06 μm, are believed to arise at the base of the stellar wind (Brand & Blitz 1993). This is because a high excitation and temperature are needed to excite helium.

Atomic sodium (2.20 μm) and oxygen (1.32 μm) have also been detected in MYSOs (Porter *et al.* 1998). These are believed to be the result of fluorescent emission, although it is unclear whether they are formed in discs, winds or both.

The inference of discs from spectroscopy was confirmed by direct imaging by Kraus *et al.* (2010) around the 20 $M_\odot$ MYSO G310.0135. With K–band interferometry with AMBER they found a dust disc which was similar to those observed in low–mass star formation. They also found a molecular outflow and two bow shocks perpendicular to the disc, which lends significant support to disc accretion theories. Malbet *et al.* (2007) also resolved a disc around MWC297 with interferometric observations with AMBER at the VLT. However, due to the low sensitivity of recent instruments, this technique can be only applied to the nearest brightest targets.

Cooper *et al.* (2013) obtained the largest sample of low–resolution (R$\sim$500) spectra of MYSOs, on 180 targets from the RMS survey. These covered a wide range of luminosities (52 to $3\times10^5 L_\odot$) and extinctions (A_V=2.7–114). 39% were found to have a disc, either through CO bandhead or fluorescent FeII, and 56% an outflow through H_2 emission. Brγ was found in 75% of the sample, and a P Cygni profile (which indicates an outflowing wind) was present in 7% of those. The Brγ detection rates are similar to those found for low–mass T Tauri young stars (see Carr 1989), as well as for intermediate mass YSOs (from Ishii *et al.* 2001), which suggests that similar formation mechanisms could play a role for massive stars as for low and intermediate–mass stars.

In recent years, several studies of extragalactic MYSOs have been performed in the Magellanic Clouds. Following the discovery of the 20 $M_{\odot}$ MYSO IRAS 05328–6827 in the LMC by Van Loon *et al.* (2005) with thermal infrared spectroscopy, Oliveira *et al.* (2006) and Oliveira *et al.* (2013) have conducted targeted searches for MYSOs in the LMC and SMC respectively. By analysing the presence of ice absorption, silicate emission or absorption and PAH emission, they found a number of sources at different evolutionary stages from young deeply embedded MYSOs to compact H II regions. They also find evidence of sequential star formation driven by stellar feedback. Ward *et al.* (2016) and Ward *et al.* (2017) followed this up with K–band integral field observations of the LMC and SMC respectively. They find many similar emission features (Brγ, HeI, H_2) associated with Milky Way MYSOs, but almost no CO bandhead emission. In addition, the spectra reveal lower dust extinction values (median of A_V=14 mag in the SMC and 22 mag in the LMC compared to 44 mag from Cooper *et al.* 2013) and tentatively stronger accretion rates from Brγ compared to Galactic results. The authors suggest that these differences may be due to the lower metallicity of the Magellanic Clouds ($Z_{LMC} \approx 0.5\ Z_{\odot}$ and $Z_{SMC} \approx 0.2\ Z_{\odot}$).

1.7 Episodic accretion in MYSOs

As mentioned above, variability in low–mass pre–MS stars is a well known phenomenon. In fact, T Tauri stars were identified by Joy (1945) as a new class of variable stars. One of the best explanations for this observed behaviour is the inhomogeneity of the accretion process – rather than accretion at a constant rate, it is likely these stars undergo episodic bursts of high accretion (see Audard *et al.*

2014 for a review of episodic accretion in low–mass YSOs). Of the eruptive low–mass protostars, there are two main object types that stand out – FU Orionis and EX Orionis class stars. FU Ori stars are low–mass protostars that undergo strong accretion outbursts lasting up to a few decades, with a large increase in $\dot{M}$, from 10^{-7} to 10^{-4} $M_{\odot}$/year. EX Ori have more frequent but lower intensity bursts. It is believed that FU Ori–class objects are at an early stage between Class I and II, and EX Ori arise due to instabilities in the discs of Class II objects. This historic division between high and low intensity outbursts has recently been disputed by recent observations of intermediate objects such as V1647 Ori (Aspin *et al.* 2009), with an outburst timescale of just over 2 years.

Recent variability analysis of NIR all–sky surveys like UKIDSS and VISTA (Lucas & Jim 2017, Contreras-Peña *et al.* 2017) have shown that half or more of the K–band variable sources are YSOs, indicating that pre–MS stars undergoing episodic accretion dominate the NIR sky variability in the Galactic disc.

Connelley & Greene (2014) have studied the variability of the NIR spectrum of Class I protostars on timescales of days to years, between 0.85–2.45 μm. They found that all 19 observed targets and every one of their emission lines shows some degree of variability. However, the variability causes no change in the strength of the continuum or the presence or absence of any lines. The variability of lines arising from the same processes, like the shock tracers [FeII] 1.64 μm and the H_2 2.12 μm, do seem to correlate. However the variability of wind and accretion tracers are rarely positively correlated, which suggests a time delay between accretion and wind effects.

Studies of MYSO variability are fewer and further between than for low–mass protostars. Kumar *et al.* (2016) compared the Contreras Peña *et al.* (2014) variable star sample with ATLASGAL, searching for variable MYSOs by matching their location with massive submillimetre clumps. They found 13 of the variable stars in the Contreras Peña *et al.* (2014) to be MYSOs, with bolometric luminosities of 400–8000 $L_{\odot}$ and masses between 6–11 $M_{\odot}$ (as determined from SED fitting). The variability occurred on timescales of hundreds of days. The NIR variability correlates with similar behaviour in the 6.7 GHz methanol maser emission. The authors suggests that the variability is due to episodic accretion, with the 100 days timescale corresponding to the frequency at which gas reaches the MYSO from the disk.

Borissova *et al.* (2016) analysed MYSOs in young clusters with VVV, and found that 57% of MYSOs show at least low amplitude NIR variability.

Caratti o Garatti *et al.* (2017) found an accretion burst in the 20 $M_\odot$ MYSO S255 NIRS3. They found a 3.5 mag increase in H–band magnitude and 2.5 in the K–band compared to UKIDSS archival data. The K–band spectrum of the source itself showed a mostly featureless rising red continuum, due to the strong dust extinction. The lower extinction gas in the outflow cavities displayed more line emission than the source. Many of these emission lines (Brγ, H_2), as well as the continuum were significantly stronger compared to the quiescent spectrum. In addition, new lines like the CO bandhead, NaI and HeI were observed. These lines are also characteristic of outbursting FU or EX Oris, but in the case of this MYSO the line luminosities were up to four orders of magnitude higher, indicating that the accretion burst was of higher intensity. The bolometric luminosity increased during the burst from 2.9×10^4 to 1.6×10^5 $L_\odot$. This indicates that the accreted amount of material during this burst was 2 Jupiter masses, or 3.4×10^{-3} $M_\odot$ in 9 months, which is 4 orders of magnitude more than in low–mass protostellar eruptions. In a recent paper, Cesaroni *et al.* (2018) presented the results of a search for the thermal jet produced as result of this outburst in S255 NIRS3. They found an exponential increase in radio flux density at around 13 months after the NIR burst, which is consistent wth a simple expanding jet model. S255 NIR3 also showed a small increase in millimetre flux, which the authors modelled to arise from free–free emission.

Three–dimensional simulations of Kuiper *et al.* (2011) also find that, in the disk accretion massive star formation scenario, the accretion process in not continuous, but appears to be punctuated by strong outbursts, as in the low mass case. Meyer *et al.* (2017) improved on these simulations by including the self–gravity of the gas, as well as a more realistic treatment of the proto–stellar irradiation feedback. They also found that massive star formation is dominated by episodic accretion bursts in the MYSO phase. This occurs due to disc gravitational instabilities, with massive clumps of about 0.5 $M_\odot$ being accreted over a relatively short period of time. They find that these events repeat on a timescale of 2–2.5 kyr. The burst durations are short, approximately 10 years. This means that the

MYSOs spend approximately 0.5% of their assumed 30000 year phase lifetime in outburst.

If MYSOs spend 0.5% of the time in this phase in outburst, one would expect that at any given time we observe the complete sample of MYSOs in the Galaxy, 0.5% of them would be in outburst. Or, in other words, there is a likelyhood of 0.5% that any observed MYSO is in outburst. So, of the about 800 RMS observed MYSOs, only 4 targets should be in outburst at any given time. However, in order to determine whether an object is in outburst or not detailed observations over long time intervals at multiple wavelengths are required, as in the case of S255 NIRS3 discussed above.

1.8 Thesis outline

This Introduction has presented the current understanding of star formation, both at the low and high mass ends. There are still significant difficulties in bridging the gap between observations and theories of massive star formation. Research into the MYSO phase can provide answers to many of the current questions. This thesis makes use of near–infrared techniques to study large samples of MYSOs in order to improve our understanding of high–mass star formation. The aim of this research is to further our understanding of massive star formation by studying the latest embedded stage, the MYSO phase, where the mass of the star is set. This analysis helps answer questions such as: Do massive stars form in a similar fashion to low–mass stars, as predicted by monolithic collapse models, or in a completely different manner as predicted by competitive accretion? Can the MYSO phase be split into several subclasses like the T Tauri low–mass phase? How do their circumstellar environments (accretion disc, outflows, jets, etc.) compare to those of low–mass objects, and which models fit them best? How does the structure of MYSOs compare to that of MS and evolved stars? Are MYSOs formed as part of multiple systems, and if so what are the multiplicity properties of these systems, especially in contrast to low–mass pre–MS objects and MS stars? Whilst the wrok presented here does not solve these questions directly, it provides important new information to begin answering them.

Chapter 2 presents a low–resolution (R≈1500) spectroscopic survey using *K* and

H–band data obtained at the AAT as part of the RMS survey. Detection rates and line luminosity correlations are studied, as well as the behaviour of the MYSOs under the evolutionary sequence of Cooper (2013).

Chapter 3 presents a medium–resolution (R≈7000) NIR spectroscopic survey of 36 MYSOs from the RMS survey. By making use of hydrogen recombination lines, as well as other disc and wind tracers in these wavelength ranges, information about the circumstellar regions of MYSOs was obtained. Comparisons were drawn with lower–mass YSOs (T Tauri and Herbig Ae/Be stars), as well as with predictions from high–mass star formation simulations.

Chapter 4 contains a pilot search for binary and multiple companions of MYSOs with adaptive optics in the K–band. Statistical methods are employed to ascertain the likelihood of these being real companions rather than chance projections, and separation and mass ratio distributions are presented.

Chapter 5 summarises the findings of all previous chapters and present a discussion based on these, as well as proposed directions for future work.

Chapter 2

Evolutionary trends in MYSOs with low–resolution NIR spectra

2.1 Introduction

As explained in Chapter 1, there is a clear evolutionary sequence for low mass YSOs, with different stages going from the embedded Class 0 pre–main sequence star to the Class III which is fully formed and ready to join the ZAMS. Because massive stars have shorter Kelvin–Helmholtz timescales, their evolution proceeds much faster, and as such there is no clear equivalent to these classes for high mass stars. A massive star on the ZAMS is likely to be still embedded in its birth cloud. The MYSO phase can be seen as a massive equivalent of the pre–MS YSO classes, but there have not been many studies of different evolutionary stages within the MYSO class.

Early NIR surveys of MYSOs such as Bunn *et al.* (1995) identified differences between observed MYSOs based on HI recombination line ratios and proposed these may have an evolutionary origin. NIR spectra of a large sample of MYSOs in the Northern Hemisphere were taken as part of the RMS project as a final classification step. The spectra and analysis of the transitions probed by this data were presented in Cooper *et al.* (2013) (CLO13 from here), and further investigations of the evolutionary trends of MYSOs were shown in Cooper (2013) (C13 from here). In C13, the author identified an empirical evolutionary sequence of MYSOs, based on the presence or absence of certain lines. The transitions used

Table 2.1: Evolutionary sequence as identified by C13

	H_2	Brγ	Br10	fl. FeII
Type I	Strong	Absent	Absent	Absent
Type II	Present	Present	Weak/Absent	Absent
Type III	Weak	Strong	Present	Present
Type IV	Absent	Strong	Present	Present

to define the evolutionary classes were H_2 2.12 μm, Brγ, Br10 and fluorescent Fe II. Type I was defined as showing only H_2 lines, and Type III had weak or absent H_2 and strong Br series. The intermediate type II showed both Brγ and H_2 but no fluorescent FeII emission. In addition, type III was split into IIIa and IIIb based, respectively, on the presence or absence of the H_2 line. In this chapter, I adopt this classification, but refer to type IIIa as III and type IIIb as IV. The classification criteria are outlined in Table 2.1.

It is worth pointing out that this classification scheme is empirical. C13 found that most MYSOs can be split into these four classes, and through statistical tests discovered that these empirical classes form an evolutionary sequence. This is consistent with the origin of the lines, at least at a qualitative level. The least evolved objects are expected to be the most embedded, and as such their discs (as seen by fluorescent FeII) are hard to see. The ionisation is low in early stages, and so there is no recombination emission observed. The molecular material is shocked as a result of outflows, and as such strong H_2 emission is observed. As the MYSO evolves, the ionisation fraction increases (as a result of both outflow shocks and radiation from the central protostar). As such, molecular hydrogen emission gets slowly replaced by recombination emission. The higher energy Br10 is only observable at later stages as it requires a stronger incoming radiation field, as well as a less embedded stellar environment in order for the H–band to be visible. Outflows clear out cavities close to the central object, and the disc becomes more prominent, detectable through fluorescent FeII emission.

All but one of the 194 MYSOs in the C13 sample were classified under this scheme. Through K–S tests the author was able to exclude luminosity, distance, orientation or extinction as driving factors for the different classes. Type IIIs were found to have bluer MIR colours than Is, which was interpreted as evidence of evolution, with later types becoming less embedded. This was also confirmed by the inverse relationship between Brγ and H_2 EWs, with early type sources showing strong H_2 from outflows and shocks and weak HI, as they have yet to produce enough ionising radiation to create strong HI lines. [FeII] 1.644 μm shocked emission was also stronger in earlier types. HeI emission and P Cygni profiles had the highest detection rates for types III and IV, suggesting that the outflows are becoming more like MS winds.

These observational classes were associated with different stages of the Hosokawa *et al.* (2010) models. Type I sources were seen to be in the stage I of the model, undergoing adiabatic accretion, or at the beginning of the swelling in stage II. Type II sources are at the swollen up stage and may have started to contract. Type III MYSOs correspond to the latter part of the Hosokawa *et al.* (2010) stage III (contraction), whilst Type IVs are in the transition between stages III and IV (the beginning of the MS accretion).

In this Chapter and the following I test for correlations between different quantities such as pairs of line luminosities or fluxes by using the Pearson correlation coefficient. The coefficient takes a value between –1 and 1, with a value of 1 corresponding to a perfect correlation, –1 for an anti–correlation and 0 for no correlation. Generally, a Pearson factor between (–0.5,0.5) points to the lack of a correlation, but this does depend on the sample size. For a more accurate correlation test, I take the sample sizes into account by converting the Pearson coefficients into probabilities of false correlation using standard tables. I consider two quantities correlated when the probability of false correlation is lower that 0.05.

In this chapter I will describe a follow–up statistical survey of MYSOs in the Southern Hemisphere at the Anglo–Australian Telescope. The work presented here aims to answer questions about evolution across the MYSO phase, primarily by using NIR spectroscopy, but also combining this with MIR, submm and radio data. I investigate whether there is any difference between, or indeed if there is such a thing as, early or evolved MYSO. I study changes in embededness, disc, accretion activity and shocks throughout the MYSO phase, and provide explanations for the observed behaviour based on theoretical models. MYSOs are compared to lower–mass Herbig and T Tauri stars, in order to test different high–mass star formation paradigms.

The observations and reduction are described in Section 2.2. The following sections describe the photometry, astrometry (2.3) and extinction measurements (2.4). The results are presented in Section 2.5, including comparisons with other surveys. I classify the MYSOs according to the criteria outlined above, and analyse the trends with evolutionary classes in Section 2.6. The findings are summarised in Section 2.7.

2.2 Observations and data reduction

The data presented in this chapter was observed as part of the RMS project (Lumsden *et al.* 2013). The spectra were taken at the Anglo–Australian Telescope located at the Siding Spring Observatory in Australia. The instrument used was the IRIS2 camera (Tinney *et al.* 2004), which is a near–infrared imager and spectrograph. The spectra were taken in the long slit spectroscopy mode. The slit width is 0.9", the length 7' and the plate scale 0.45"/pixel. The spectral ranges covered are 1.46–1.81 μm in the H–band at R$\sim$2270 and 2.02–2.37 μm in the K–band at R$\sim$2250. These wavelengths and all following ones are in vacuum. Xenon arc lamp spectra are provided for wavelength calibration.

Main sequence stars of spectral types B8–G6 from the Bright Star Catalogue (Hoffleit & Jaschek 1991) were observed to correct for telluric absorption lines. These stars were chosen so as to be at similar airmasses to the science targets (0.1–0.2 airmass difference at most) and observed shortly before or after the YSO candidates for accurate correction. The telluric stars range between 3.9–6.5 magnitudes at K.

This survey consists of objects in the Southern Hemisphere (between –02 and –60° Declination and 7–18 h Right Ascension) from the RMS survey thought to be potential MYSOs. The targets, the dates they were observed on, slit position angles and zenithal distances are presented in Table A.1. They were observed between 2005–2011 over 20 nights. They are located at distances between 0.5–14.5 kpc, and have bolometric luminosities (determined as part of the RMS survey) of 50–300,000 $L_{\odot}$. Their magnitudes are between 4.9–14.4 at K and 7.5–16.5 at H. 152 targets were observed in the K–band and 101 in H. Some of the targets initially observed in K were not observed at H as well because they had already been classified as non–MYSOs or they were too faint to be observed at H, due to their embeddedness. 92 of the initial K–band targets and 70 of the H–band ones were given the final classification of MYSO. Non–MYSOs observed include Ultra–Compact HII regions (HII), evolved stars (ES), NIR point sources with considerable nebulosity (described by the RMS catalogue as ambiguous young or old sources, Y/O), or objects that do not fall into any other RMS category (described in the catalogue as 'Other', O). The reason for the relatively large fraction of non–MYSOs observed (40%) lies in the design of this survey. The earlier data (from 2005–2007) includes spectra of all RMS targets taken in order to establish their origin. The classification of objects is not the aim of this work, and was done as part of earlier RMS work. As MYSOs are the subjects of this research, all subsequent analysis is focused solely on the MYSO spectra.

A standard reduction procedure was applied using the Starlink software package (Currie *et al.* 2014), starting with the bias and dark current subtraction. Flat field frames were obtained at the start of observing nights in order to correct for pixel–to–pixel variations. Sky offset frames taken in the standard ABBA pattern were used in order to remove the sky background. One–dimensional spectra were extracted by summing over the seeing disc in the combined frames. The initial wavelength calibration from the Xe arc lamps was found to be inaccurate due to the low number of arc lines in the K–band. As such it was later recalibrated with OH night sky lines of Rousselot *et al.* (2000). The final calibration was found to be accurate within ≈25 km/s. The achieved resolution was measured to be 1500 in H and 2000 in K from the arc lines, equivalent to 150–200 km/s velocity resolution. The average resulting SNR of the calibrated spectra was 80 in K and 40 in H.

The telluric correction was complicated by the presence of strong intrinsic absorption HI features, which were often blended with the atmospheric absorption telluric lines. The blending made accurate removal of the intrinsic stellar features in the telluric standards difficult. This, along with artefacts from the flat fielding process caused by the IRIS2 detector led to a poor telluric correction, which resulted in an over–broadening of HI lines, as can be seen in Figure 2.1.

In order to mitigate their effects, I used the MOLECFIT package as described

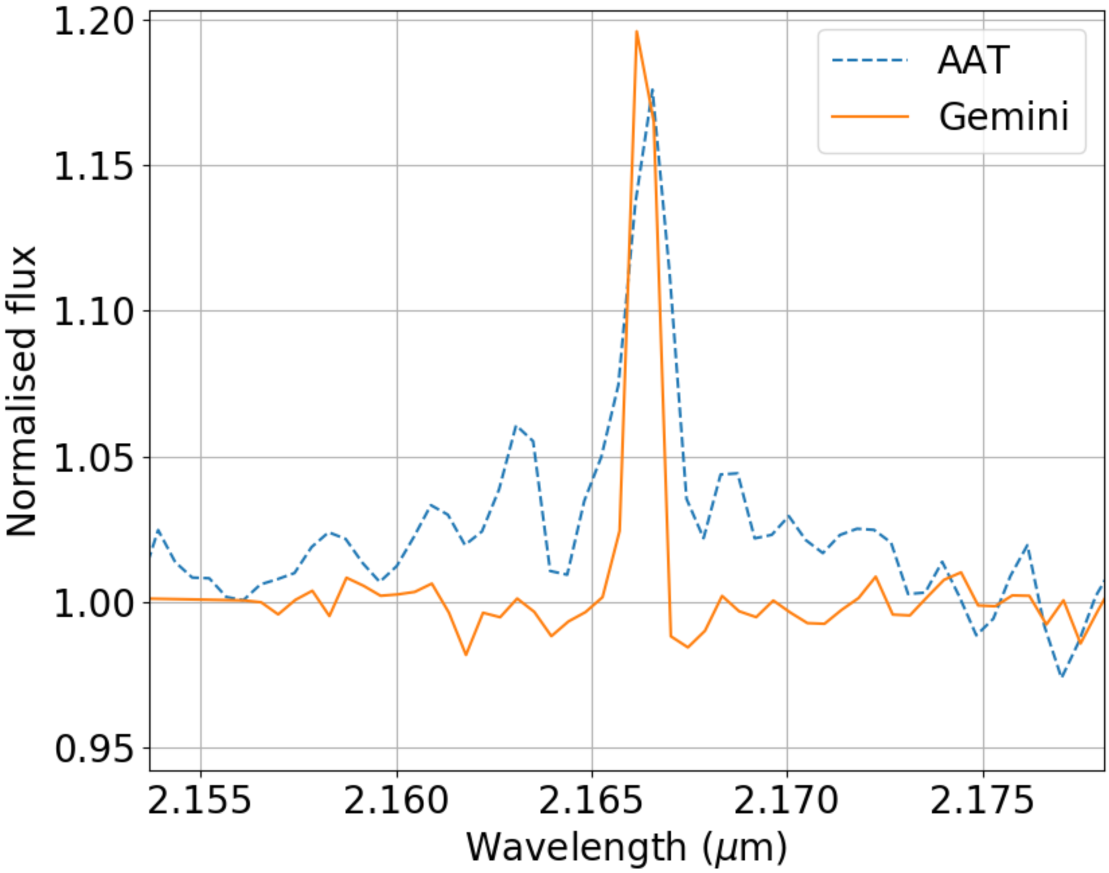

Figure 2.1: Comparison of the reduced spectrum of G010.8856 from AAT data (blue, dotted line) to the same MYSO from the Gemini data (orange, solid line) as shown in Chapter 3. Note how the incorrect telluric subtraction has caused the line to become considerably broader and have a different profile.

in Smette *et al.* (2015). This was developed by ESO in collaboration with the Institute for Astro– and Particle Physics in Innsbruck. It works by fitting synthetic transmission spectra from the LNFL/LBLRTM radiative transfer code to observed spectra. For a given telescope location and a set of abundances of relevant molecules (O_2, O_3, H_2O, CO, CO_2, CH_4, OCS, N_2O as well as several other trace gases), MOLECFIT predicts the observed telluric absorption spectrum. It also provides the option to recalibrate the wavelength solution, fit the line spread function of the spectrograph, the local continuum and the telescope background. The resulting telluric absorption spectrum can then be subtracted from the science spectrum. However, there are certain limitations to the performance of MOLECFIT. The developers advise that less accurate corrections are to be expected from spectra with a large number of intrinsic features (as our H–band spectra are expected to have), low SNR observations or low spectral resolution data. As such, the direct application of MOLECFIT to this data set is not able to solve the telluric absorption problem on its own.

The following method was adopted in order to obtain an approximate correction to the atmospheric absorption. First, the MOLECFIT routine was applied to the telluric standard star. This removes a great portion of the telluric absorption lines, leaving mostly the intrinsic features of the telluric standards. Then, the intrinsic stellar absorption lines are fit with either a Gaussian or Lorentzian profile. Dividing the initial telluric standard by the intrinsic feature fit leaves a corrected spectrum of telluric absorption features, which can be used to correct the atmospheric absorption in the science targets. This correction procedure is exemplified in Figure 2.2, for the intrinsic standard BS6331, along with the correction on G010.8856.

The measured FWHM from the spectra were corrected for the instrumental resolution. The intrinsic FWHM of a spectral line is given by:

$$FWHM = \sqrt{FWHM_{obs}^2 - FWHM_{instr}^2}, \tag{2.1}$$

where FWHM_{obs} is the measured width of the line and FWHM_{instr} is the instrumental resolution. There are two ways to measure the instrumental resolution – either from the width of the arc lines, or the OH night sky lines. Resolutions

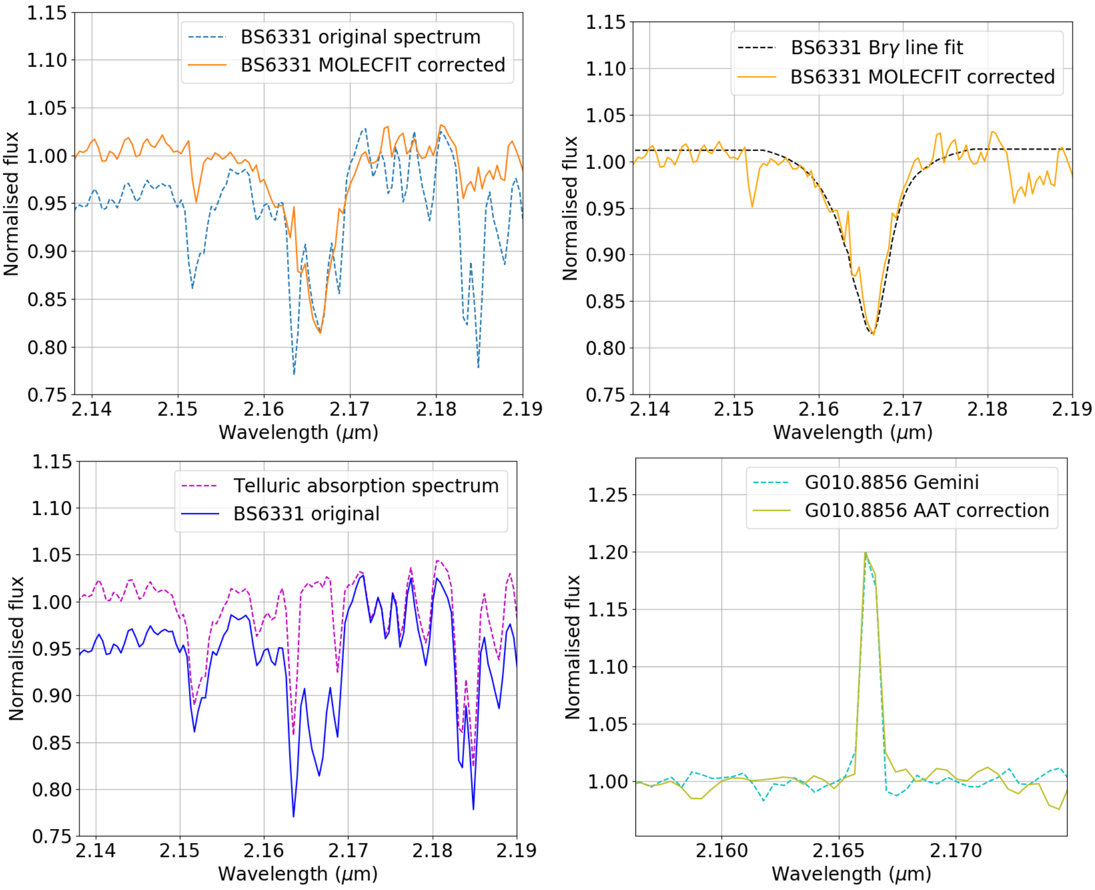

Figure 2.2: Example of the telluric correction using MOLECFIT. Top left – The original telluric star BS6331 (blue, dotted line) along with the MOLECFIT correction to this (orange, solid line); top right – the MOLECFIT correction and the intrinsic fit to the Brγ absorption line (black, dotted line); bottom left – the result of the correction (magenta, dotted line) along with the original BS 6331 spectrum (blue, solid line); bottom right – the spectrum of G010.8856 corrected in this manner (lime green, solid line), compared with the Gemini spectrum (light blue, dotted line).

measured from arc lines are 135±5 km/s for the H–band and 200±6 km/s for the K–band. OH night sky lines give similar instrumental resolutions – 142±4 km/s for the H–band and 221±19 km/s for the K–band. As such, I settle on the average value from the two methods as the instrumental FWHM, 138±5 km/s in the H–band and 211±15 km/s in the K–band.

2.3 Photometry and astrometry

The spectra were taken in non–photometric conditions, and without any flux standards. As such, direct flux calibration was not possible. Instead, the ratio of the science targets to the telluric stars was used for relative photometry. Accurate magnitudes for the telluric stars can be obtained from 2MASS (Skrutskie *et al.* 2006). The MYSO spectra were calibrated with the PyRAF reduction package as provided by Science Software Branch at STScI (2012). The first step was pairing up the telluric star with a standard star of the same spectral type with the PyRAF task *standard*. Then the sensitivity and extinction functions are computed by comparing the observed telluric to its assigned spectral standard with the task *sensfunc*. Next, the telluric spectrum flux is calculated with *calibrate*, and based on this the MYSO flux can be calculated relative to the telluric star by applying *calibrate* again. I show the result of the correction on G010.8856, compared to the Gemini flux calibrated spectrum in Figure 2.3. There is a disagreement of almost a factor two between the spectra in terms of the continuum flux, but it is worth noting that both of these surveys were performed under bad weather conditions. As such, it is likely that the flux calibrations are not as accurate as photometric surveys, but such accuracy is beyond the scope of these programs.

In order to asses the quality of the flux calibration, I measured the continuum fluxes from the spectra using the tools available in the PyRAF routine *splot*. 2MASS magnitudes are available for comparison for all of the targets in this survey, and VVV VISTA (Minniti *et al.* 2010) data also cover some of the targets. Whilst the VVV data has high spatial resolution (0.34” compared to 2” for 2MASS), it saturates for magnitudes brighter than 11 mag in the K–band. As many targets are brighter than this limit, the RMS catalogue adopts 2MASS

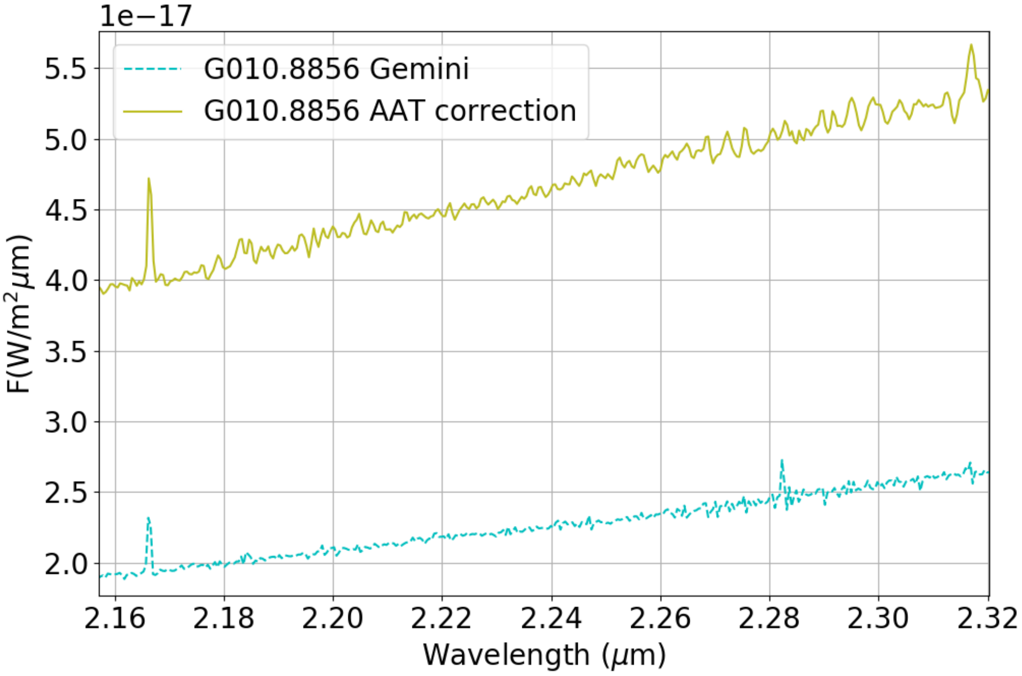

Figure 2.3: Final flux calibration of G010.8856 lime green, solid line) compared with that of Gemini (light blue, dotted line).

magnitudes for most of the objects presented here. Magnitudes measured from flux calibrated spectra are compared to these catalogue magnitudes. The continuum fluxes were measured between the ranges 2.035–2.328 μm in K and 1.540–1.750 μm in H, masking emission lines. These are similar to the passbands in the 2MASS survey. The continuum noise was measured in a region of 0.01 μm around 2.160 in K and 1.662 μm and H respectively. These correspond to the central wavelengths of the 2MASS survey, and are feature–free zones where the continuum is clearly visible. These continuum fluxes were converted to measured magnitudes with the 2MASS zero–points, $1.13\times\ 10^{-9}$ W/ m$^2\mu$m for the H–band and 4.28×10^{-10} W/ m$^2\mu$m for the K–band. The magnitudes from the spectra are compared to RMS catalogue values in Figure 2.4. The K–band magnitudes are spread equally about the $m_{obs} = m_{cat}$ correlation line within ±1 mag, with a best fit to the data of $m_{obs} = m_{cat}$. The H–band seem to be offset from this 1–1 correlation, with measured H–band magnitudes being brighter than the catalogue values by ≈1 mag. This may be due to the rising red continuum spectral slope of MYSOs, as the H–band filter is calibrated based on the spectrum of Vega which is flat. In addition, many sources were not observed at H. However, a Pearson correlation test shows correlation factors of 0.66 for H and 0.70 for K. This indicates that there is indeed a strong correlation in both bands, and the photometry obtained in this manner is usable.

In order to compare with the other RMS NIR spectroscopic surveys, I applied the photometry methods of CLO13. A correction factor given by $f_{obs}/f_{corr} = 10^{(m_{obs}-m_{cat})/2.5}$ was calculated, where m$_{cat}$ is the accepted RMS value, either from 2MASS or VISTA. All measured line fluxes were then corrected to catalogue values using this correction factor. Values for f_{obs}/f_{corr} are given in the Table B.1.

A number of targets showed more than one spectrum within the slit in close proximity. When extracted, these appeared to be distinct objects with different spectra. Often these extra sources would only be visible in one–band. As such, it was necessary to decide which of the multiple sources within the slit was the primary target, and determine the coordinates and magnitudes of the extra sources. For this, I analysed the 2D spectral images in order to determine the separation between the sources, and which one is the brightest. Combining this with the position angle and central coordinates of the slit and comparing with 2MASS images, the position of the slit on the sky could be determined. The extra sources were paired up with their respective 2MASS counterparts, bearing in mind that the IRIS2 plate scale is 0.45"/pixel. For a position angle of 0° (as measured in the standard way from N to E), the top source in the 2D spectral image of the slit is the southernmost one on the sky, and the bottom one will be to the north. An example of this determination for target G347.0775 is shown in Figure 2.5.

I identified the adopted RMS counterpart name from the catalogue. The other sources are given names according to their position on the sky relative to the main source (N, SW, etc.)

2.4 Extinction estimates

The amount of circumstellar extinction was estimated in a similar manner to CLO13, which is in turn based on the Draine & Lee (1984) interstellar extinction

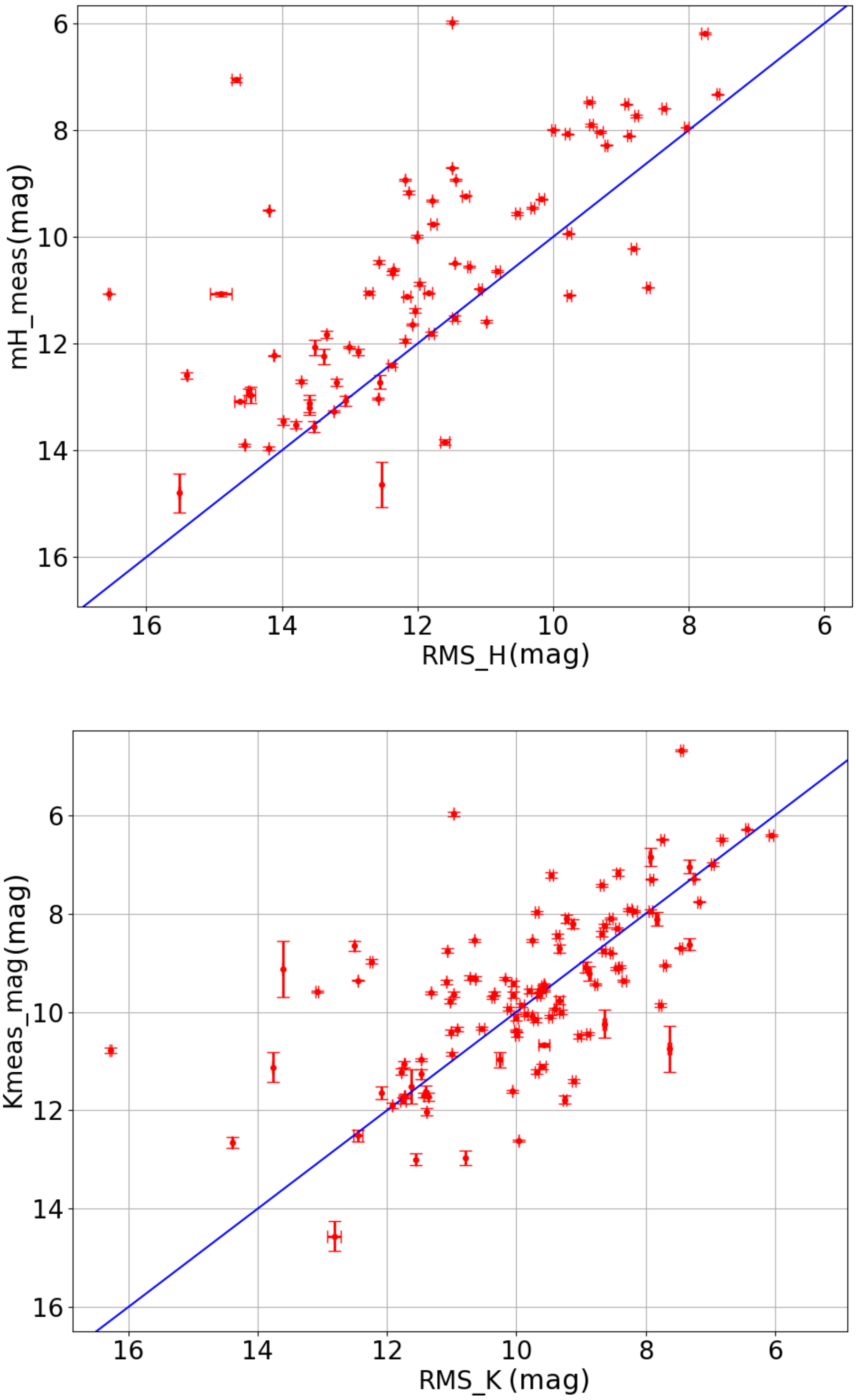

Figure 2.4: Magnitudes measured from the spectra as a function of catalogue magnitudes. *H*–band is on the top and *K*–band on the bottom. The 1–1 correlation is also displayed.

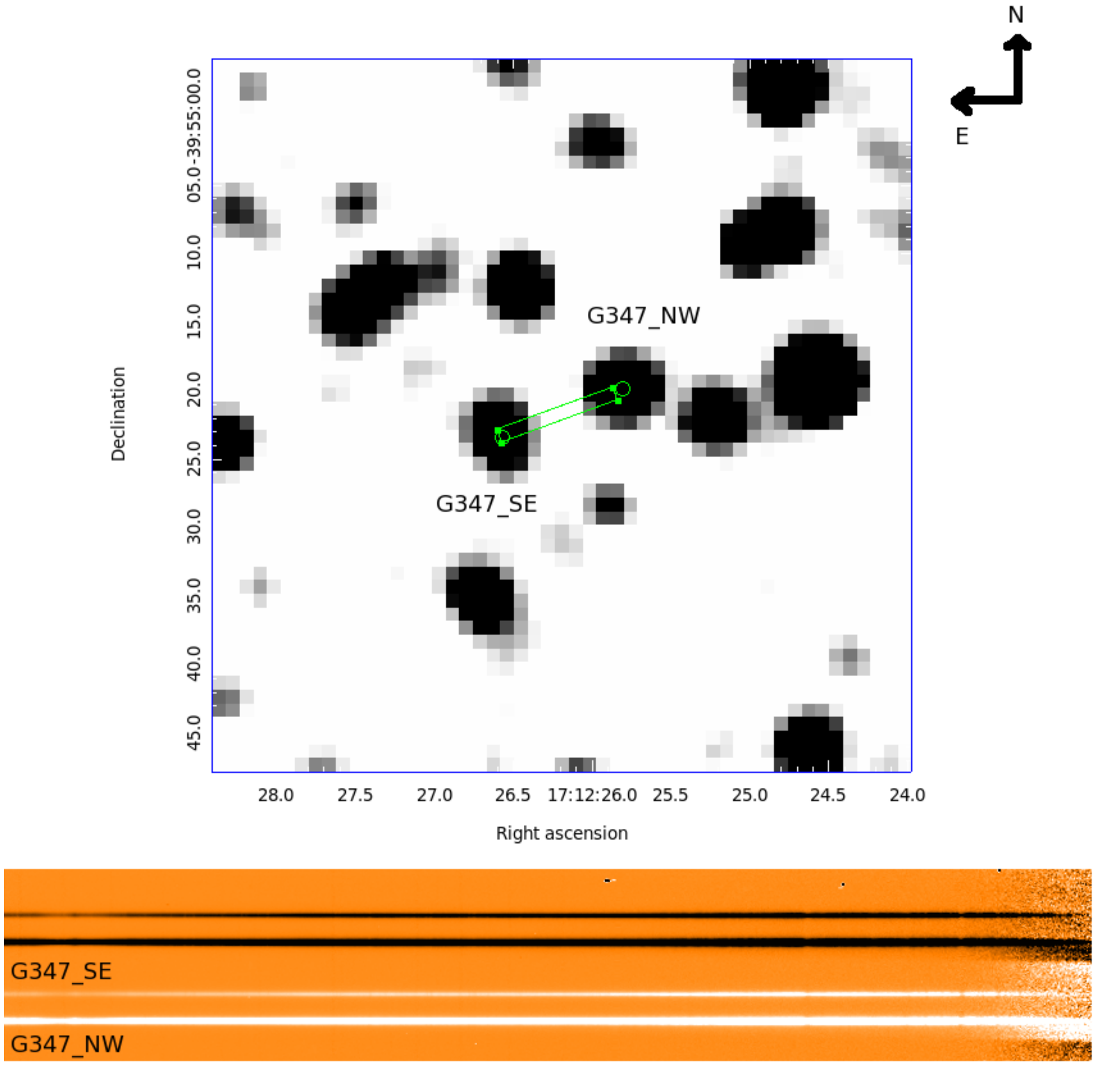

Figure 2.5: Example of the separation of two targets in the slit in the case of G347.0775. The top is the 2MASS K–band image of the field, along with the expected position of the slit and the two identified sources. North is up in this frame. Bottom is the 2D spectral image of the same target in the K–band. Two sources are seen, the brightest of which is the bottom one. 2MASS photometry confirms indeed the NW source is the brightest by 1.3 mags, and the difference between the two is 1.8 mags in the flux calibrated spectra. The NW source is at the adopted RMS position of G347.0775.

model. Assuming the MYSO has the intrinsic colours of a B0 Main Sequence star, the amount of visual dust extinction can be computed from the NIR colours. As such, the extinction can be determined from either the $J - H$ or the $H - K$ colours with the following formula:

$$A_V = \frac{m_1 - m_2 + CI_{int}}{0.55^{1.75}(\lambda_1^{-1.75} - \lambda_2^{-1.75})}, \tag{2.2}$$

where m_1/λ_1 and m_2/λ_2 are the magnitudes and central wavelengths of the J and H or H and K–bands, respectively. CI_{int} is the intrinsic colour index of a B0V star, as taken from Koornneef (1983), $J - H$ = –0.12 and $H - K$ = –0.05. The exponent 1.75 corresponds to the interstellar reddening constant of Draine & Lee (1984). The errors can then be calculated from:

$$\Delta A_V = \frac{\sqrt{\Delta m_1^2 + \Delta m_2^2}}{0.55^{1.75}(\lambda_1^{-1.75} - \lambda_2^{-1.75})} \tag{2.3}$$

H and K–band magnitudes were available for all the targets, but J–band magnitudes are only available for 31 objects. In this case, the J–band magnitude was taken as an upper limit at 16.8 mag (the detection limit of the 2MASS survey in this band) and the extinction from $J - H$ is reported as a lower limit based on this and the H–band magnitude. The extinction values are displayed in Figure 2.6. They are similar to the extinctions of the CLO13 sample, with the MYSOs in this survey having an average $\mathrm{A}_V(H - K)$ = 46 mags compared to 42 for the CLO13. The extinctions from $H - K$ colours range between 14–127 mags, whereas for the CLO13 MYSOs these are between 2.7–114 mags. The Pearson correlation factor between the extinctions from $J - H$ and $H - K$ in this sample is p=0.47, equivalent to a probability of false correlation of $1.8{\times}10^{-4}$.
The best fit equation is $\mathrm{A}_V(H - K) = 0.73\ \mathrm{A}_V(J - H) + 25$, compared to $\mathrm{A}_V(H - K) = 1.1\ \mathrm{A}_V(J - H) + 6.0$ for CLO13. The $H - K$ colours are mostly larger than those from $J - H$, so the extinctions from $H - K$ tend to be larger than those from $J - H$. The reason for the disagreement between extinction values from $J - H$ and $H - K$ was first discussed by Porter *et al.* (1998). Dust excess, along with Rayleigh–Jeans scattering affect these measurements. The excess is

strongest in the K–band, causing the $H-K$ colours to become redder, whilst scattering causes the $J-H$ to become bluer. For objects surrounded by large amount of dust, $H-K$ has a larger numerical value that $J-H$, causing the estimates of A_V from $J-H$ and $H-K$ to diverge considerably from the 1–1 correlation.

A colour–colour plot is useful to illustrate this point (see Figure 2.7). Most objects are 1–3 magnitudes above the 1–1 correlation in $H-K$ for a given $J-H$, due to the combined effect of dust excess and scattering.

I also calculate circumstellar extinctions by comparing the continuum slope of the MYSOs to the expected blackbody distribution ($F_\lambda \propto \lambda^{-4}$) through a chi–squared minimisation algorithm. The values obtained for extinction using the slope of the H–band continuum are generally lower than those from $H-K$ colours. The K–band is more sensitive to enhancements due to hot dust excess, and as such values for extinction from this band tend to be larger than those from the H–band continuum slope. The correlation between extinction from the H and K continuum slopes is weaker than for the GNIRS data in Chapter 3, with p=0.50 and probability of spurious correlation 7.5×10^{-5}.

The values from all these different circumstellar extinction measures do generally agree with each other within a 3σ–measure. The average scatter in extinction from the methods used is of the order ΔA_V=5 mag.

Finally, all sources will be affected by foreground extinction. Further away sources tend to have larger foreground extinction. Some lines of sight will have stronger extinction than others. I used the Galactic extinction maps of Neckel *et al.* (1980), as well as more recent estimates of Green *et al.* (2015) to estimate the values for foreground extinction for MYSOs in my sample. These are shown in Table B.1. The foreground extinction is, as expected, significantly lower than the circumstellar extinction, usually $\approx 5\% \times A_{Vcirc}$. The values for foreground extinction vary between 0.2 to 5.2 magnitudes in the V–band, with an average of 2.3 magnitudes.

Given all of this, I use extinctions determined from the $H-K$ magnitudes to correct observed line fluxes in the subsequent analysis. This allows for more accurate comparison with previous RMS data of CLO13, as the extinction was estimated in the same manner there.

2.5 Results

2.5.1 Line identification

Once the spectra had been reduced, the next step was to identify the spectral lines present and measure their parameters. Most of the lines found in the Gemini sample and previous surveys are also seen in this data. A line is considered detected if the peak line flux was 3σ or more above the continuum noise, $F_\lambda > 3\Delta F_{cont}$, and if the line had a full–width half–maximum larger than the resolution limit. ΔF_{cont} was measured from the root–mean–square variation of the continuum counts close to a given line but in a featureless area. This and line fluxes were both measured with the *splot* package in PyRAF.

The line flux was measured by integrating the line profile, and the full–width half–maximum by fitting a Gaussian curve to the profile. Upper limits were based on the quality of the spectra. It was found empirically that the minimum detectable EW is given by $\mathrm{ul}_{EW}(\text{Å})=\frac{15}{SNR}$, where the signal–to–noise ratio is taken as the average across the band.

An example spectrum for the MYSO G345.4938 is shown in Figure 2.8. The strongest emission is HI recombination of the Brackett series. The Brγ line (n=7–4 transition) is seen in the K–band, and the Br10–20 transitions in the H–band. Several molecular hydrogen transitions (H_2 in Figure 2.8) are also present in both H and K, the strongest of which is at 2.120 μm (detected by the CLO13 and Lumsden & Puxley 1996 surveys).

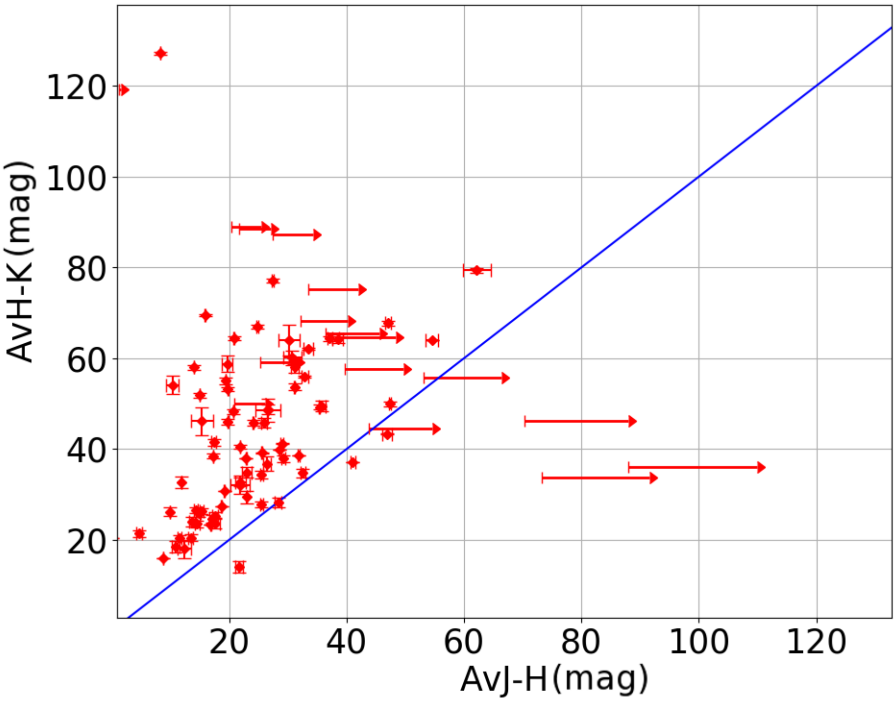

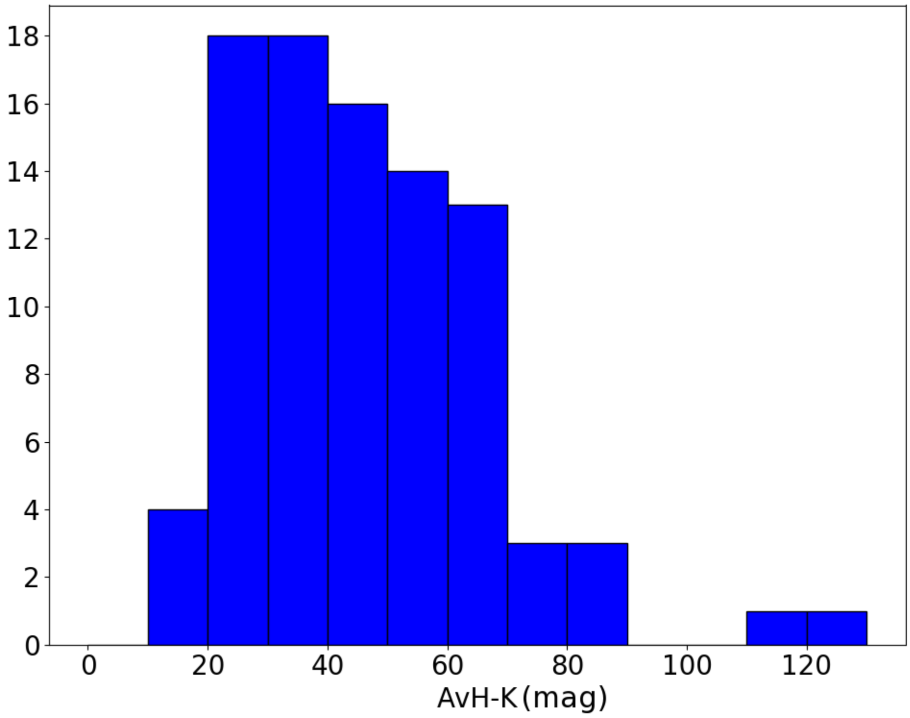

Figure 2.6: Top – extinction from the $H - K$ colours as a function of extinction from $J - H$. The 1–1 correlation line is also plotted. Bottom – histogram of the values of A_V from $H - K$ colours.

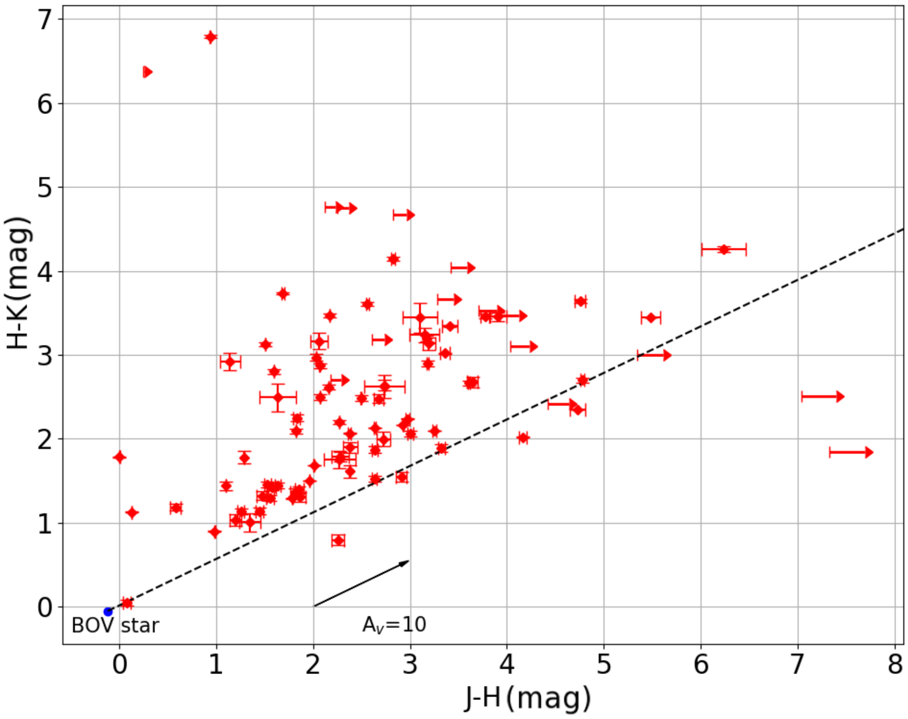

Figure 2.7: NIR colour–colour plot of MYSOs in this sample. The dotted line represents the expected extinction vector from a field B0V star, shown as a blue dot. An A$_V$ of 10 is displayed for comparison. The dust excess causes the $H - K$ colours to become redder, whilst scattering causes the $J - H$ to become bluer, resulting in the observed offset from the 1–1 correlation.

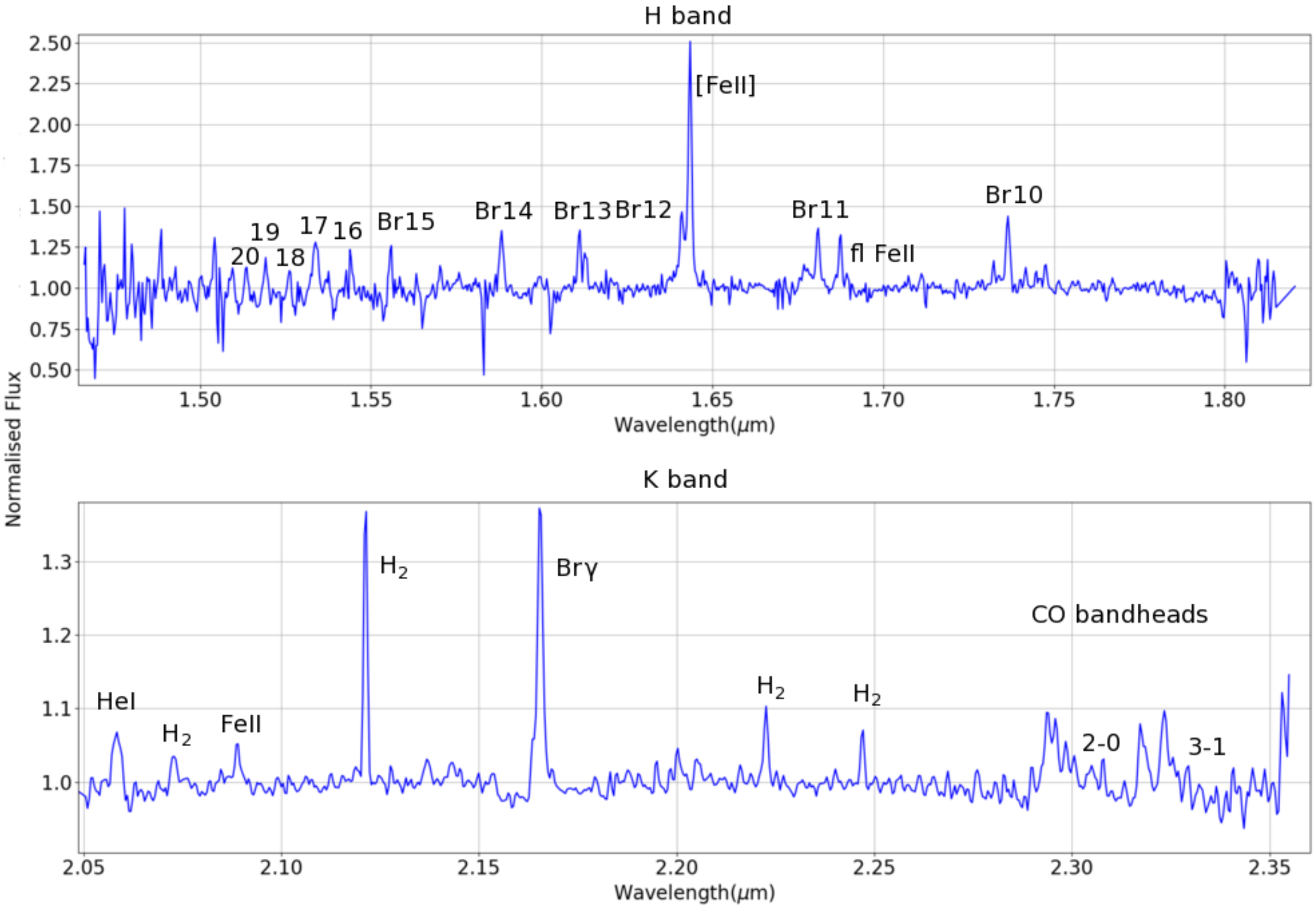

Figure 2.8: Example continuum normalised spectrum of MYSO G345.4938. The H–band is in the top panel and the K–band spectrum in the bottom. Identified transitions are marked, with Br corresponding to HI Brackett series, fl FeII to the fluorescent Fe line at 1.687 μm and [FeII] to the forbidden shocked Fe transition.

A number of FeII transitions are detected, such as the forbidden shock tracer transition at 1.644 μm (previously observed in massive pre–stellar objects by Lumsden & Puxley 1996 and CLO13) and the fluorescent transition at 1.687 μm, thought to originate in a disc (as modelled by Lumsden *et al.* 2012). The strongest HeI line is seen at 2.058 μm (previously observed in MYSOs by Porter *et al.* 1998 and Drew *et al.* 1993). The NaI doublet at 2.209 μm (seen in MYSOs by Porter *et al.* 1998) is also detected, as well as the first two CO ro–vibrational transitions (also known as 'bandheads', modelled to arise in discs by Chandler *et al.* 1995 and Ilee *et al.* 2013). The 1.690 μm line was identified by Lumsden *et al.* (2012) as an FeI transition. The lines at 1.746 and 2.110 μm were observed by Lumsden & Puxley (1996) as [FeII] and HeI, respectively. The same survey also identifies a line at 2.146 μm as [FeIII], although they were studying a UCHII. It is unlikely the same level of ionisation of Fe would be reached in MYSOs to give rise to this transition. Lumsden *et al.* (2001) identify the 2.073 μm transition as an H_2 line in their observations of planetary nebulae. MYSO observations of Porter *et al.* (1998) see the 2.090 μm line and identify it as an FeII line. They also observe a transition at 1.576 μm which is also present in this sample, but do not provide an identification for it. This line is present in 19 objects in this survey. 16 of these also show the [FeII] 1.644 μm line, and 8 show the H_2 line. As such, it may be tempting to identify this as an [FeII] line. However, this transition has not been identified as an [FeII] line in the Oliva (1987); Oliva *et al.* (1989) or any other surveys for Fe lines, and so the nature of this line is still unclear. The transition at 1.711 μm is identified by Oliva (1987) as a [FeII] line.

All detected lines, their central wavelengths and their detection rates are shown in Table 2.2.

The Brγ has the highest detection rate at 83.2%, as this is the lowest energy transition of the HI recombination lines observable in the K–band, and as such it has the highest transition probability. The detectability of further transitions decreases as the excitation level increases. This is probably a combined effect of the transition probability and the quality of the data. At wavelengths shorter than 1.6 μm the quality of the data is considerably lower, as telluric absorption is stronger. The extinction is also stronger and so the MYSOs are fainter in the blue part of the H–band. Also, the lines are a lot closer together than the rest of

Table 2.2: Lines observed in this sample and their respective wavelengths and detection rates. Rates in Br12 and [FeII] are given for unblended and also blended (with –B) in the low–resolution CLO13 survey

Line	Central λ (μm)	# of objects detected in	Detection Rate (%)	GNIRS detection rate	CLO13 detection rate
Br20	1.520	26	38.8		
Br19	1.526	26	38.8		
Br18	1.534	26	38.8		
Br17	1.544	29	43.3		
Br16	1.556	32	47.8		
Br15	1.571	33	49.3		
Br14	1.588	38	56.7		
Br13	1.611	39	58.2		
Br12	1.641	42	62.7	83	19/44–B
Br11	1.681	42	62.7	79	37
Br10	1.737	42	62.7	79	45
Brγ	2.166	74	83.2	97	75
?	1.576	19	28.3		
[FeII]	1.644	42	62.7	42	11/36–B
flFeII	1.687	50	74.6	61	26
FeI	1.690	35	52.2		
HeI	1.701	7	10.5		
[FeII]	1.711	20	29.9		
[FeII]	1.746	27	40.3		
HeI	2.058	15	16.9		15
H_2	2.073	27	30.3		
FeII	2.090	27	30.3		
HeI	2.113	4	4.5		
H_2	2.120	53	59.5		56
FeIII?	2.146	7	7.9		
NaI	2.209	8	9.0	37	
H_2	2.220	32	36.0		
H_2	2.240	27	30.3	21	9
CO (2–0)	2.295	11	12.3	34	17
CO (3–1)	2.324	11	12.3	34	

the Br series – 0.006 μm between Br19 and 20 as opposed to 0.056 μm between Br10 and 11.

The shock tracers [FeII] 1.644 μm and H_2 2.12 μm lines have similar detection rates of ≈60%. The two disc tracers CO bandhead and fluorescent FeII have significantly different detection rates (at 12 and 75%), although they are both expected to trace material arising from the disc. Recent modelling results of Ilee *et al.* 2018 show that the CO bandhead transitions only arise in objects of intermediate accretion rates, which may be why there is a lower detection rate of CO than of fluorescent FeII.

Three objects that had been classified in the RMS survey as MYSOs (G332.8256–00.5498_A, G348.7342–01.0359, G326.7249+00.6159) showed strong HII region–like spectral features – strong (>3×continuum) and narrow (FWHM<100 km/s) HI recombination lines and HeI 1.7 μm absorption. These objects may be in a transition phase between MYSO and HII region, as longer wavelength features confirm them to be MYSOs (weak/no radio emission, peak of SED in submillimetre), but NIR spectra suggest they are HII regions. As such, I do not use them in any of the following analysis.

2.5.2 Comparisons with previous surveys

The results can be compared with the previous RMS survey of CLO13, as well as the GNIRS data from Chapter 3. In the GNIRS survey I observed 39 MYSOs (including multiple sources) at a resolution of ≈7000, cross–dispersed in four bands between 1.07–2.33 μm. The *K* and *H*–band intervals were 2.147–2.335 and 1.611–1.752 μm. The CLO13 survey observed 131 MYSOs at a resolution of ≈500 between 1.395–2.506 μm. The AAT sample presented here contains 89 MYSOs observed in the *K*–band and 67 in the *H*–band. The resolution was R≈1500–2000, and the wavelength ranges were 1.463–1.812 μm in the *H*–band and 2.022–2.374 μm in the *K*–band. Although the spectral resolution varies between these surveys, the wavelength ranges are comparable, with 8 transitions observed in all 3 samples.

The Br10–12 and γ lines are at higher detection rates in this sample than in CLO13, but at a lower rate than in the GNIRS sample. However, it is worth noting that the Br12 and [FeII] lines were often blended in the CLO13 sample due to the low resolution of the spectrograph used. Both the unblended and total fractions of detections are quoted for these two transitions in Table 2.2. The fluorescent FeII line has the same detection rate in this sample and in GNIRS, higher than in the CLO13 survey. The [FeII] and H_2 2.240 μm lines are at their highest detection rates here. The HeI 2.058 and the molecular hydrogen 2.120 μm lines are at similar detection rates in this and the CLO13 surveys, although the HeI rate is slightly higher here. The CO bandheads and the NaI lines are at their lowest detection rates here.

The key reasons for the difference in detection rates between these samples is likely the different resolutions of the surveys, as well as the sample selection criteria. The CLO13 sample was taken as a final classification step for the RMS survey targets in the Northern Hemisphere. As such, it is representative of the full RMS sample. Gemini sources were selected to have the highest bolometric luminosities (and as such the highest masses). Because of this they are less embedded (and likely more evolved), with most objects visible at H–band and shorter. The AAT sample presented in this chapter contains the NIR brightest RMS targets in the Southern Hemisphere (as IRIS2 at the AAT had a lower sensitivity than UIST at UKIRT as used by C13). As such, they are less embedded than the CLO13 sources, but lower bolometric luminosity than Gemini. So, the AAT sources should have more evolved sources than CLO13, but less than Gemini. This is confirmed by the classification of MYSOs here according to the C13 evolutionary sequence (see Section 2.6), 17% of the CLO13 sample are the least evolved Type I MYSOs, whereas only 7% of AAT sources and none of the Gemini sources are Type I.

The Brackett series are expected to trace winds and outflows in MYSOs (Simon *et al.* 1981), as well as low density nebular ionised gas in more evolved sources (Drew *et al.* 1993). The CLO13 survey contained a larger fraction of earlier MYSOs (according to the evolutionary sequence described in C13) than this sample. Combined with the lower resolution of the CLO13 survey, this would explain why the detection rate of the Brackett series transitions is at its lowest there. Comparing the detection rates of the HeI line in this and the CLO13 sample agrees with this idea – the AAT sample has a larger proportion of evolved

MYSOs which display the MS–like winds producing the HeI line. The similar level of detection of the molecular hydrogen 2.120 μm in this and the CLO13 survey points to the fact that we both observe a similar number of objects with shocks. The more frequent detection of [FeII] here than in CLO13 is probably linked to the blending of this line with the Br12 line in the previous survey. Also it is possible that the [FeII] line arises from shocks caused by ionised jets, as it requires a higher ionisation level than H_2. Similarly, the H_2 2.240 μm line is at its lowest detection rate in CLO13 as it is weaker than the 2.120μm line and so harder to detect with lower resolution spectra. Another reason for the difference in detection rates between the 2.120 and 2.240 H_2 μm lines is the fact that the 2.240 μm line has a higher excitation energy than the 2.120 μm line. The difference in resolution also plays a part in detecting the fluorescent FeII line, at its lowest rate in the CLO13 survey. Also, this line is only found in the most evolved sources, of which there are fewer in the CLO13 survey. The CO bandhead detection rate is at its lowest value in this survey. This may be because the GNIRS survey was explicitly constructed to contain several sources known to have CO bandhead emission (S106IRS1, V645 Cygni, etc.)

Other theoretical (Meyer *et al.* 2017) and observational (Caratti o Garatti *et al.* 2017) results suggest that accretion in MYSOs may be episodic, with frequent accretion bursts driving the birth of massive stars. This could also lead to a large variation in the detection rates of CO bandhead, Brackett series, and many other spectral transitions, as different surveys may contain different fractions of quiescent or bursting MYSOs. Some spectral lines (like the HI recombination lines) would be stronger and easier to detect in MYSOs undergoing an intense accretion episode. Others, like the CO bandheads may not be detected during an accretion outburst, as this would produce continuum emission that is stronger than the bandhead emission.

2.6 MYSO evolutionary classes

I separated the MYSOs in this sample according to the classes described in C13 (see Table 2.1). The primary classification criterion was the presence or absence of a given line, as defined by C13. The strength of a given line, in terms of the description of C13 of 'Absent/Weak/Present/Strong' was a secondary classification criterion. 68 of the 89 YSOs in this survey could be unambiguously classified under this scheme. 5 targets showed HI lines in absorption and as such could not be fit into any of the classes. These absorption lines likely have a photospheric origin (see Section 3.9), which are only visible when the dilution by dust excess is low. As such, it is possible that these objects are in a more evolved state than Type IV MYSOs, where much of the circumstellar dust has been cleared out. A further 16 YSOs showed no or insufficient emission lines to be classified according to the scheme. In this case, it is possible that the strong dust excess masks the emission lines. This would mean that these objects are in an earlier evolutionary state than Type I MYSOs.

It is worth pointing out that all these 92 sources are YSOs according to the RMS criteria. All the objects with absorption lines or with insufficient lines to be classified do have good quality spectra, with average SNRs similar to those of MYSOs of Types I–IV. YSO classifications of the objects in this survey according to the C13 scheme are given in Appendix B.1.

5 objects are classified as Type I, 13 as Type II, 27 as Type III and 23 as Type IV. As such, 7% of the classified sample are Type I, 19% Type II, 40% Type III and 34% Type IV. For comparison, in the C13 sample, 17% of the sources were Type I, 38% Type II, 18% Type III and 27% Type IV. This confirms that most objects in this sample are evolved MYSOs (Type III and IV), as opposed to the C13 sample where the majority of sources are the less evolved Type I and IIs.

2.6.1 Luminosity and distance distributions

Through Kolmogorov–Smirnov tests, C13 finds no segregation with bolometric luminosity or distance between the different MYSO classes. The author explains that this shows that neither luminosity nor distance are the drivers of the differences between classes. This gives support to the idea that this is a real evolutionary sequence. Under the Hosokawa *et al.* (2010) models, less evolved type I MYSOs of the same luminosity as an older type IV star at the time of observation will go on to accrete more material and form a more massive star than the type IV MYSO. A Type I MYSOs will be swollen up and, through accretion reach a higher mass than its current. In a type IV, accretion may still be ongoing, but not for much longer, and the current mass of the MYSO is similar to the final mass of the object arriving on the ZAMS.

The K–S test provides a probability that two given samples are drawn from the same initial distribution. The result of the test is the distance between the cumulative distribution function of two samples, or the D–value. The closer this is to 0, the more likely the two samples are drawn from the same initial distribution. Depending on the result of the test and the size of the samples, a p–value can be deduced representing a probability that the samples are drawn from the same initial distribution. A p–value larger than the limiting value of 0.05 signifies the tested samples arise from the same initial distribution.

I perform the same analysis as C13 on the MYSOs in the AAT sample in order to determine whether distance or luminosity are the drivers of the segregation between classes. Whilst distance is not expected to affect the evolution of MYSOs, it is worth checking whether there is any pattern in the distances of objects of different classes. The resulting histograms do not look significantly different between the different classes, for either luminosity (Fig 2.9) or distance (Fig 2.10). Kolmogorov–Smirnov tests confirm this, with all the p–value statistics above 0.05 when comparing all the classes to one another, as well as to the histogram of all the YSOs (see Table 2.3 and 2.4). The p–value of the K–S test between type II and IV YSOs in terms of distance is the lowest, at p=0.05. This is likely caused by the shift of the central peak from 4 kpc in type II to 3 kpc in type IV, as well as the larger number of sources at <2 kpc in type IV. However, the p–value is still above the limiting value, indicating the two distributions are drawn from the same sample. This points to the fact that the distributions are similar, and luminosity or distance are unlikely to be the driving factors behind the existence of the different classes, confirming the results of C13.

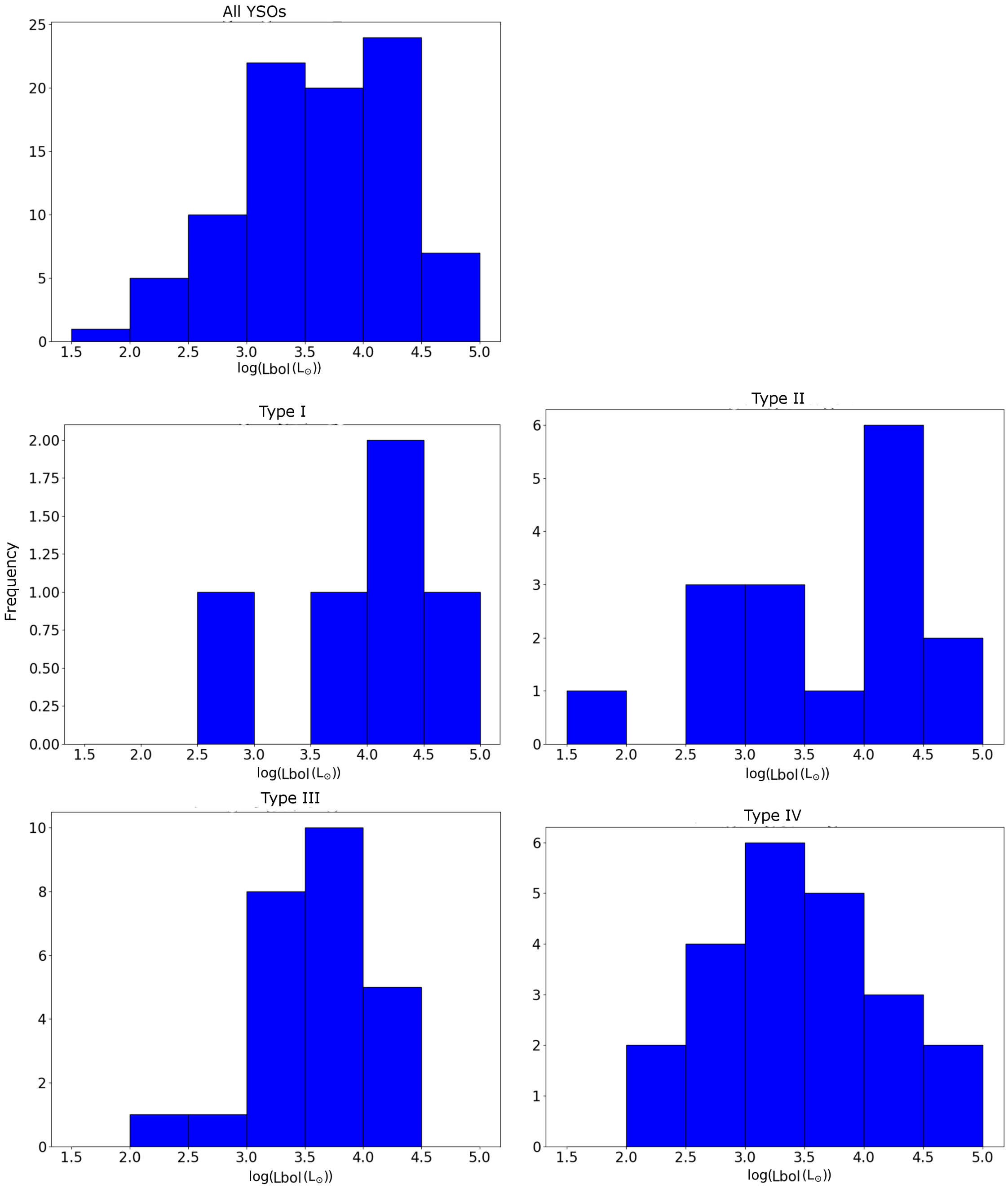

Figure 2.9: Top – Histogram of bolometric luminosities of all YSOs in the AAT sample. Middle left to bottom right – Histograms of the bolometric luminosities of the four different classes of YSO.

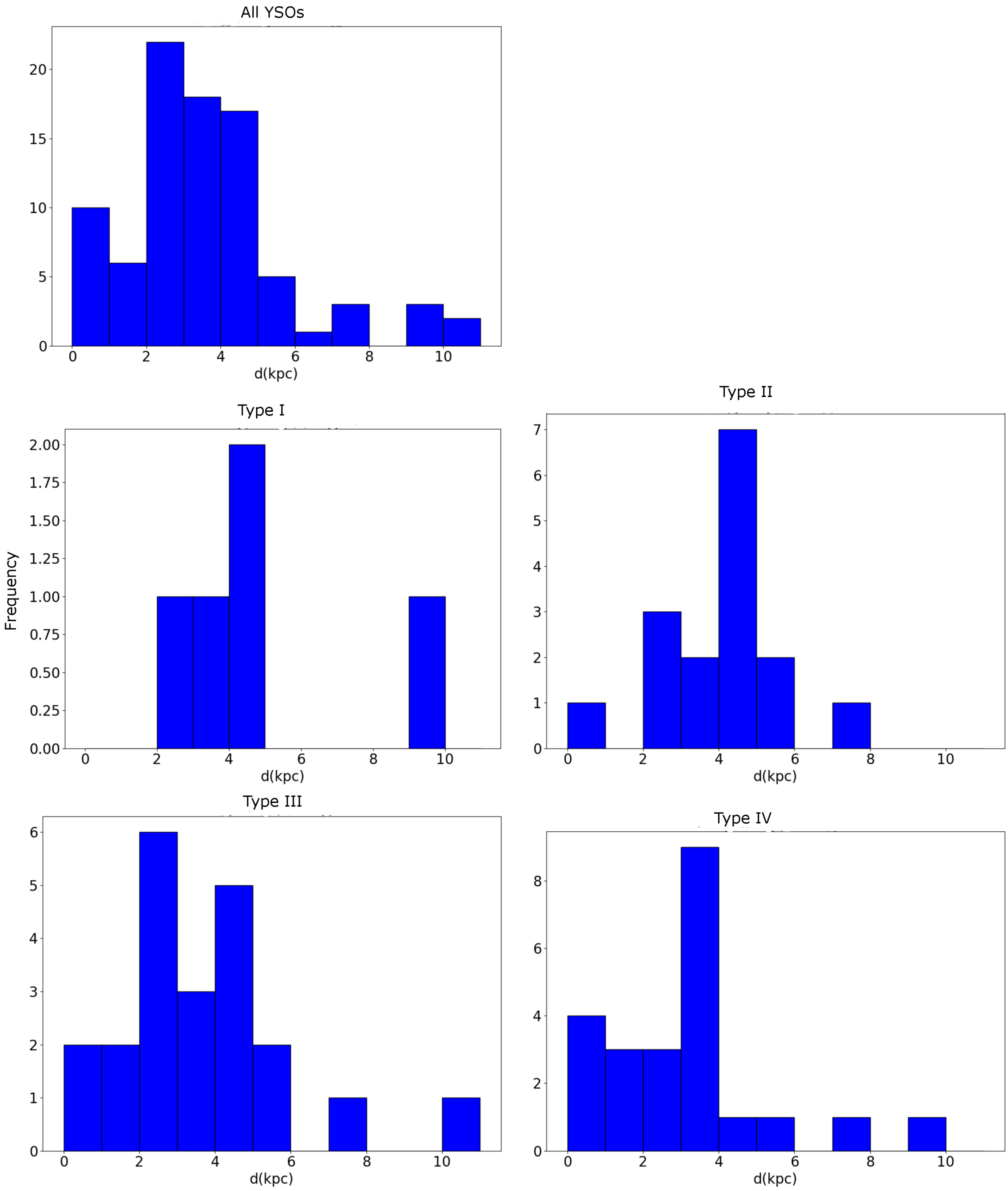

Figure 2.10: Top – Histogram of distances to all YSOs in the AAT sample. Middle left to bottom right – Histograms of the distances to objects in the four different classes of YSO.

Table 2.3: K–S test of bolometric luminosities of different MYSO classes.

Bolometric luminosity K–S test	D–value	P–value
All MYSOs vs Type I	0.33	0.57
All MYSOs vs Type III	0.16	0.85
All MYSOs vs Type III	0.11	0.97
All MYSOs vs Type IV	0.12	0.94
Type I vs Type II	0.30	0.81
Type I vs Type III	0.41	0.38
Type I vs Type IV	0.39	0.44
Type II vs Type III	0.27	0.41
Type II vs Type IV	0.21	0.75
Type III vs Type IV	0.22	0.52

Table 2.4: K–S test of distance of different MYSO classes

Distance K–S test	D–value	P–value
All MYSOs vs Type I	0.25	0.89
All MYSOs vs Type III	0.19	0.69
All MYSOs vs Type III	0.14	0.84
All MYSOs vs Type IV	0.23	0.27
Type I vs Type II	0.29	0.85
Type I vs Type III	0.19	0.99
Type I vs Type IV	0.39	0.44
Type II vs Type III	0.25	0.53
Type II vs Type IV	0.42	0.05
Type III vs Type IV	0.29	0.19

2.6.2 Colours and extinction

As discussed in Section 2.4, colours can be used as a measure of dust embeddedness. Stars redder than field MS objects are located in cocoons of dust, which affect bluer wavelengths strongest, so the continuum flux at longer wavelengths appears enhanced. Given this, it is possible that extinction would trace age, seen as pre–stellar objects are still embedded in their birth clouds. This would result in the less evolved MYSOs (type I) to be more embedded than the more evolved sources (type IV).

However, it is possible that this scenario is complicated by the unknown inclination of the objects. Even at an earlier stage, MYSOs oriented pole–on towards our line of sight may appear less embedded than those oriented edge–on. This is because for a pole–on source we are looking straight into a cavity which has been cleared by the outflowing material (a by–product of the accretion process). This degeneracy between visual extinction and inclination is difficult to break with the current data set, as measurements of inclination require multi–wavelength observations for accurate determinations.

Figure 2.11 shows a NIR colour–colour plot and extinction from $H-K$ against extinction from $J-H$ plot, colour coded for the four different spectral classes of MYSOs. There is no evidence of segregation, with MYSOs of all spectral types being located across the range of colours and extinctions. This proves that extinction/NIR colours are not a good tracer of MYSO evolution. One explanation for this may be that the type Is are indeed dustier, but distance and direction of the line of sight through the Galaxy, as well as the inclination of the MYSO may play a significant role in the colours and extinctions seen.

Whitney *et al.* (2003a,b) present 2D radiative transfer models of low mass YSOs under different inclinations. They show that embedded Class 0 sources can appear as blue as Class III sources due to the effect of inclination, with an average effect at NIR colours of as much as 1 magnitude difference. I show the effect these would have in the colour–colour $J-H$ vs $H-K$ plot, as well as the resulting spread in extinctions, 10 magnitudes in A_{VJ-H} and 18 in A_{VH-K}. Whilst the effect is likely to not be this large for most sources, even a fraction of the average effect would explain the lack of segregation.

NIR colours may also be affected by variability due to accretion burst. During an accretion outburst, a large amount of dust may be heated up, resulting in strong dust excess, which would cause the H–K colour index to appear redder. Alternatively, strong outflows may be produced as a result of intense accretion, which would cause the MYSO to appear less embedded, and the colours bluer. Finally, most of the JHK magnitudes presented here come from 2MASS survey data, which can be unreliable in some cases. For sources in crowded fields, as some of the MYSOs in this survey are, source confusion is likely to play a significant role. In addition, 2MASS saturates for K–band magnitudes brighter than 8 mag. Whilst not many of the targets here are brighter than the saturation limit, it is possible that some will be affected by the non–linear response of the 2MASS detector close to the saturation limit.

It is interesting to investigate the colour–colour plots for MIR wavelengths for MYSOs in our sample, based on data from the RMS survey, which was compiled with fluxes from the MSX satellite. The MYSO classes segregate more in the MIR colour–colour plots than in the NIR ones (see Figure 2.12).

The type I and IVs (right side of Figure 2.12) appear to be segregated. This shows that the younger type I sources seem to be more embedded, although it is again worth noting that there are considerably fewer type I sources than all the other classes. Relatively few type IV sources have large colour indexes, indicating they are less embedded than their younger type I and II counterparts. This is confirmed by the averages, with type Is having an average $F_{21}/F_8=22$, type IIs 11.2, type IIIs 7.3 and type IV 4.2. The whole sample average is 8.8, which shows that the type I and IIs are more embedded than the average MYSO. This is expected if type III and IV are more evolved MYSOs, closer to an HII region than a pre–stellar core. In a type IV source much of the dust in the region will have been evaporated by the ever increasing ionising flux from the YSO. The collimated jets and outflows are expected to have removed a significant amount of dust from the circumstellar region of evolved MYSOs.

2.6.3 Line detections and widths

In this section I analyse the differences between spectral classes in terms of the detection rates of different transitions, line luminosities, FWHM and EW correlations. The detection rates of observed lines in the different MYSO evolutionary classes are presented in Figure 2.13

The presence or absence of Brγ, Br10, fluorescent FeII and H_2 2.120 μm in different types is a result of the definition of the classification scheme. The detection rates of the Br series increase with decreasing excitation level of the transition (from Br20–10) in each of the spectral classes, similar to the overall detection rate. As discussed in Section 2.5.1, this is due to a combination of transition probability and separation of transitions in wavelength increasing with decreasing excitation.

C13 suggests that the 2.06 μm HeI line is expected to trace MS–like winds based on the rarity of H_2 detection in sources with HeI. The detection rate of this line in the AAT sample is consistent with this idea, as it is larger for later MYSO Type III and IVs and not present in Types I and IIs.

The [FeII] 1.64 μm detection rate seems to increase from types I through to III, and then becomes less frequent but still detected in type IV. This is similar to the result of C13, who explained this by inaccuracies in detecting objects blended with the Br12 line. None of the lines in this sample show a blend between Br12 and [FeII], so the increased detection of [FeII] with MYSO class must be a real effect. This increase may be due to the [FeII] tracing shocks caused by ionised jets, which require a relatively strong UV photon flux from the central source, as expected from more evolved sources. The decrease in detection rate of [FeII] in Type IVs may be due to a decrease in shock activity as a result of lower accretion.

Both CO bandhead transitions observable in this sample have a maximum of detections in MYSO Type II, with a detection rate almost three times larger in II than in Type III and IVs. This is similar to the findings of C13, although the differences between evolutionary classes in terms of CO bandhead detection are smaller there. This may be a reflection of the evolutionary state of the MYSO – the contraction of the swollen up central star begins in Type IIs, and the circumstellar region is less embedded than in Type I. As such, the disc is at its strongest and easiest to see in Type II.

Another possibility is that the required accretion rates may be only found in Type II objects. Type I objects may be swollen up as a result of high accretion rates. In this case, the continuum dust excess would overwhelm the CO bandhead emission, as shown by Ilee *et al.* 2018. The circumstellar material will be optically thick, and the disc will not be present to higher radii, possibly causing the CO bandhead to go into absorption (although CO absorption is not detected in this data). On the other hand, if the accretion rates are lower in evolved MYSOs, the disc surface density will also be too low to detect CO bandhead emission. If the accretion rates changes with evolution this would explain why there is a decrease in CO detection from Types II–IV.

It is also possible that MYSOs undergo episodic accretion (Caratti o Garatti *et al.* 2017, Meyer *et al.* 2017), in which case the intermediate accretion rates required for the production of CO are only available in a small fraction of any given observed sample, hence the lower CO detection rate compared to the other disc tracer, fluorescent FeII.

Next, I investigate differences in the line profiles with evolutionary class. Specifically, how the broadening of a line changes with evolutionary class. As explained in Chapter 1, HII regions are expected to show strong (2–5×continuum level) and narrow (30–40 km/s) Brackett emission series, as opposed to MYSOs which show weaker (1.2–2×continuum level) and broader lines (≈100s of km/s). The reason for this is that by the HII region stage the nebular recombination line emission dominates the observed Brγ flux. Also, the accretion activity decreases, and with it the fast outflows which give rise to the broad HI lines. The pre–stellar object settles into a less collimated stellar wind, akin to the mass–loss processes of MS stars. Given this, one would expect to see a decrease in line broadening with MYSO evolutionary class.

I analyse the widths of Brγ and 11 lines with evolutionary type to assess this. Br11 is preferred to Br10 as the profile of the latter transition is badly affected by telluric absorption lines, and as such the FWHM of Br10 is not as reliable as that of the Br11 line.

I compare the FWHM from Brγ to that of Br11 in Figure 2.14. As expected, they show a correlation, indicating that these two transitions do trace the same

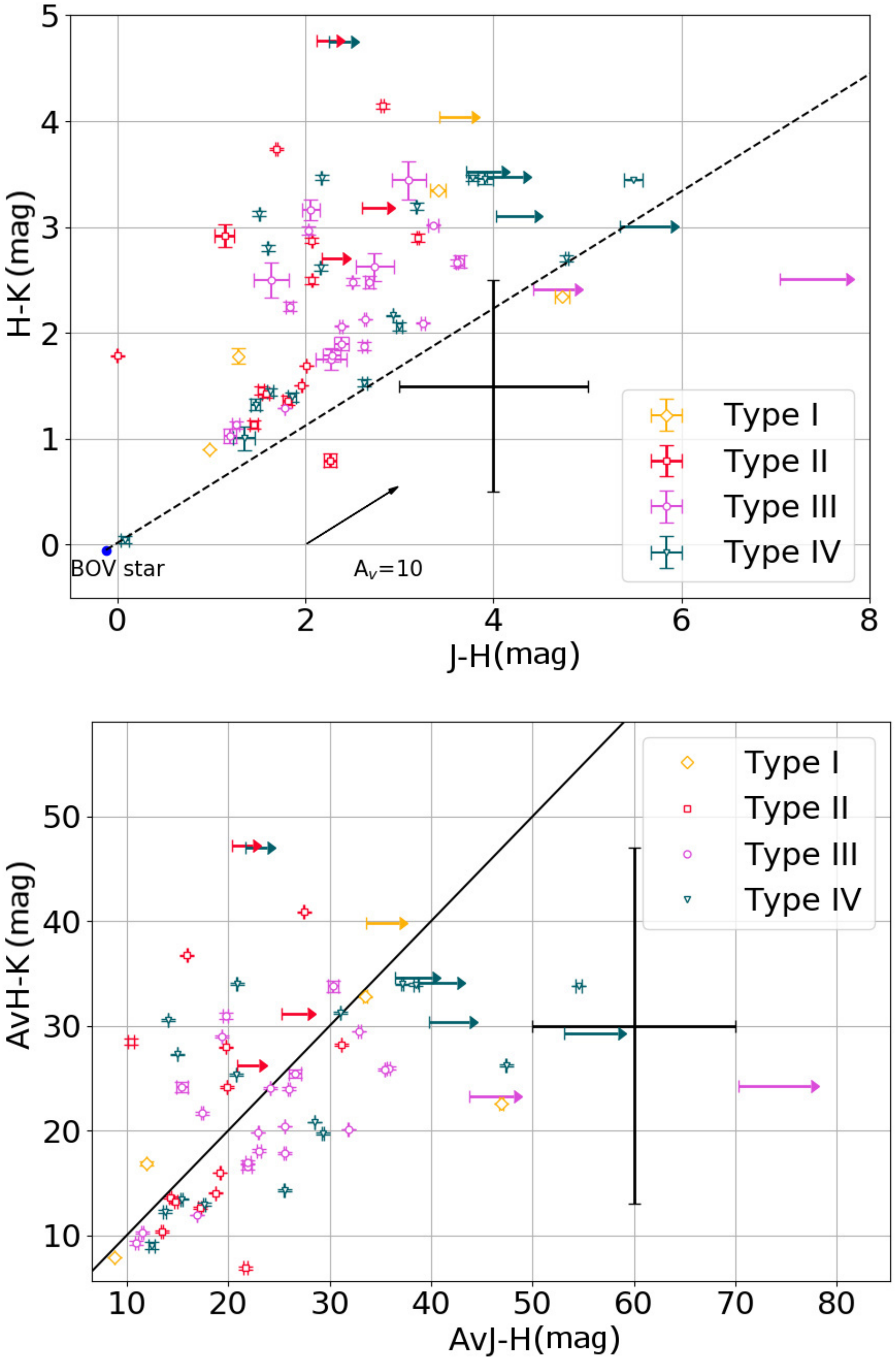

Figure 2.11: Top – $H-K$ colour as a function of $J-H$ colour. A B0V star (blue circle), its reddening vector (dotted line) and the effect of A_V=10 mag (arrow) are also plotted. Bottom – extinction from the $H-K$ colours as a function of extinction from $J-H$. The 1–1 correlation line is also plotted. MYSO evolutionary classes are colour–coded. The black data point with error bars is a representative uncertainty expected from changes in orientation as discussed by Whitney *et al.* (2003a,b)

material at similar optical depths. There is not much segregation with type. The correlation factor is p=0.39, indicating a probability of spurious correlation of 0.02.

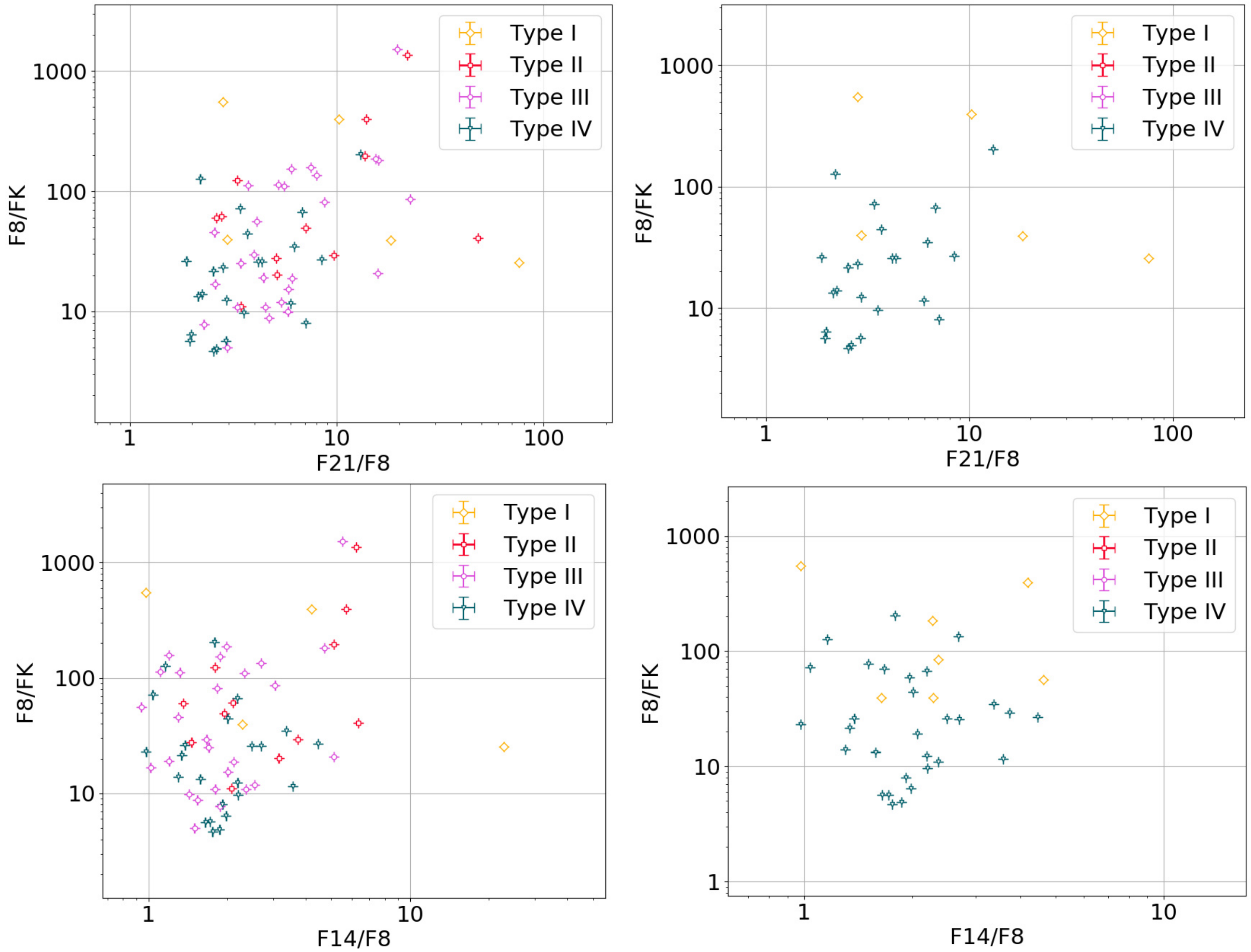

Figure 2.12: Plots of MIR flux ratios from MSX data. Flux densities are taken from the RMS catalogue and are measured in Janskys. Top left – $F_{8\mu m}/F_K$ as a function of $F_{21\mu m}/F_{8\mu m}$ for all YSOs, colour coded for the different classes as above. Top right – $F_{8\mu m}/F_K$ as a function of $F_{21\mu m}/F_{8\mu m}$ for only Type I and IVs. Bottom left – $F_{8\mu m}/F_K$ as a function of $F_{14\mu m}/F_{8\mu m}$ for all YSOs, colour coded for the different classes. Bottom right – $F_{8\mu m}/F_K$ as a function of $F_{14\mu m}/F_{8\mu m}$ for only Type I and IVs.

The behaviour of line width with luminosity and colour is investigated (see Figure 2.15). The Brγ FWHM is used, as all targets had been observed at K and this gives a larger sample than Br11, and the FWHM from the two lines agree with one another, as shown in Figure 2.14. There is no segregation between the different types, with either colour or bolometric luminosity. There is also no correlation, with Pearson correlation factors of p≈–0.01. There are a few possible explanations for this.

It may be that the objects undergo episodic accretion, in which case the outflows and winds traced by the Brγ FWHMs would not be reflective of the evolutionary state of the MYSO. Different inclinations of the objects in the sample may add to this, with the outflow appearing stronger and so the Brγ line becoming broader in sources viewed pole–on.

In their survey of Class I protostars, Connelley & Greene (2010) find an inverse relationship between Brγ and H_2 EWs, with most targets of low veiling having strengths weaker than –5 Å in Brγ and –3 Å in H_2 2.120 μm. In addition, they found their objects to obey the relation $|\mathrm{EW}_{Br\gamma}| < |\frac{50}{EW_{H_2}}|$. C13 finds these constraints apply to some MYSOs, but a significant fraction do not follow the constraints from low–mass YSOs. Veiling by dust excess should affect both H_2 and Br γ by a similar amount, so stronger veiled sources should have lower EW in both lines, and as such be located in the upper right part of a H_2 against Br γ EW plot. The author also states that if the Brγ vs H_2 equivalent width plot can be used as a measure of veiling, Type I YSOs seem to have more veiling than Type IIIs, which is what one would expect if Type IIIs were more evolved, so have less dust to veil them. This relation does apply to sources in the AAT sample (see Figure 2.16), with few sources having $|\mathrm{EW}_{Br\gamma}| > |\frac{50}{EW_{H_2}}|$. However, a few of the Type II and III YSOs have Brγ EW stronger than –5Å and H_2 EW stronger than –3 Å. The many outliers reflect the fact that using this plot, and EW in general as a measure of veiling is not accurate. This may be because of contamination from wider nebular components (as in the HI line profiles of S106IRS1 in Drew *et al.* 1993), or contribution from stellar absorption lines to the HI profiles (see Section 3.9.4).

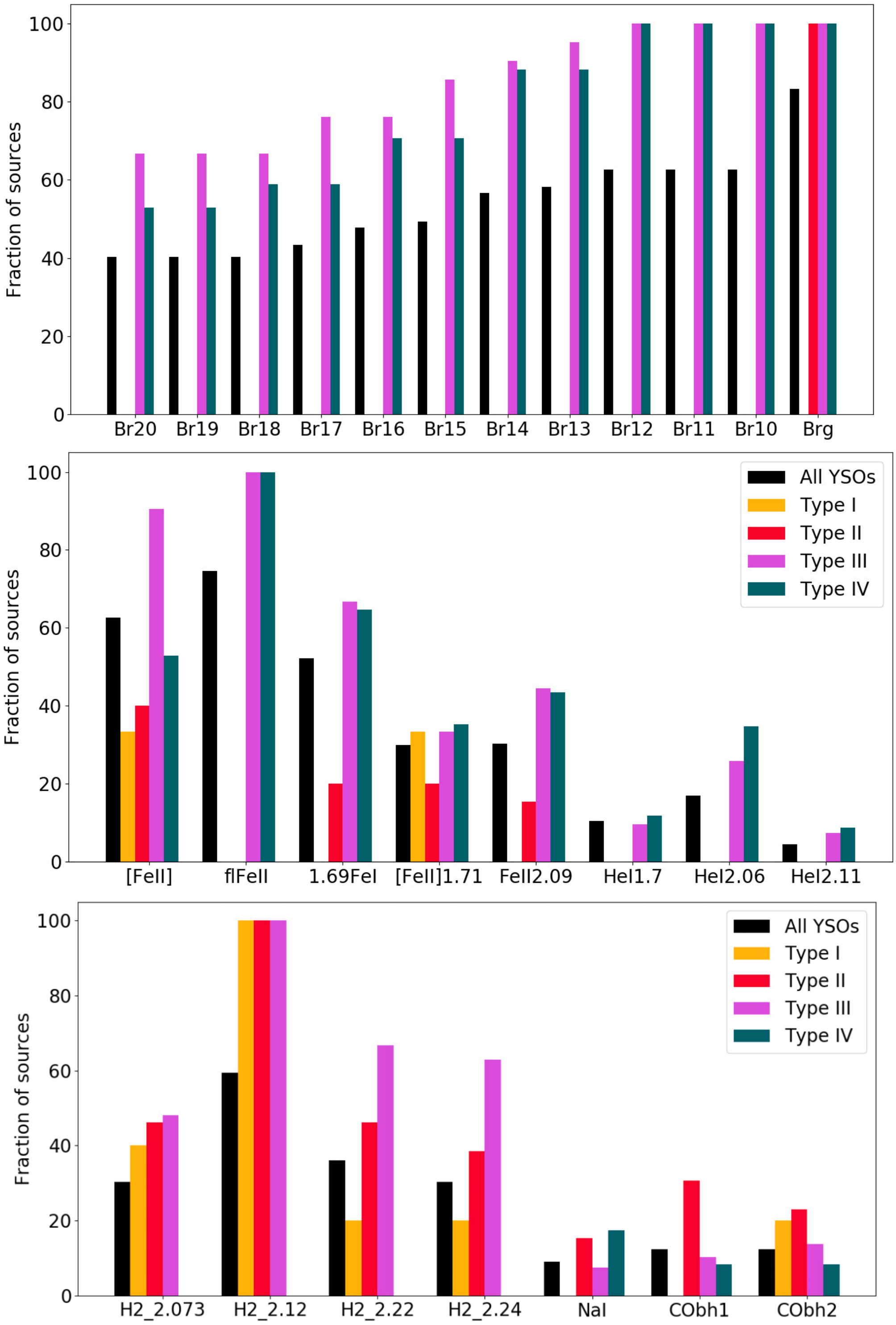

Figure 2.13: Detection rates of different spectral lines with MYSO evolutionary classes, colour coded as above. Top – Br10–20 and γ, middle – He and Fe lines, bottom – H_2, CO and Na transitions.

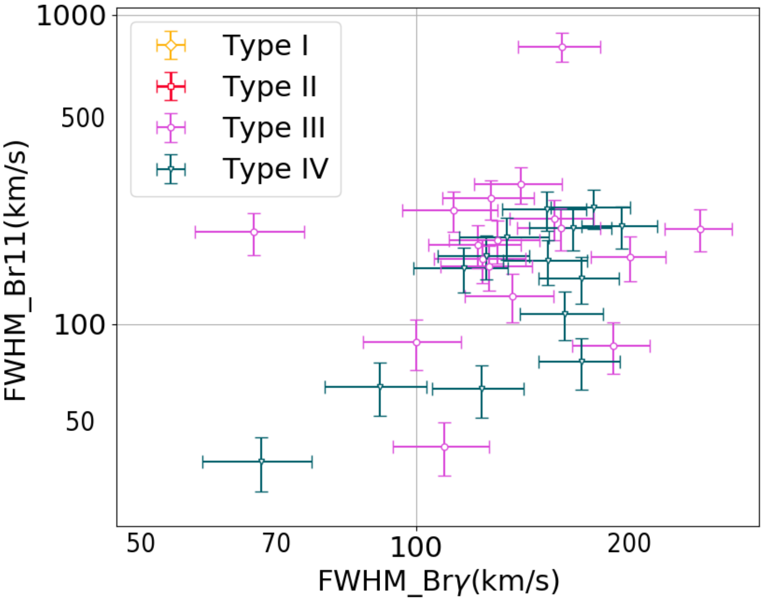

Figure 2.14: FWHM from Br11 as a function of FWHM from Brγ, colour coded for spectral classes as above. There is a clear correlation between the two, as expected as they arise from the same material.

2.6.4 Line correlations

I also checked for a correlation between the two shock tracers [FeII] and H_2 (see Figure 2.17). A strong correlation is present in luminosity space. The correlation factor was p=0.85, with a probability of chance correlation of 1.1×10^{-6}. The EW correlation is weak, with p=0.37, and a probability of false correlation of 0.05. There is no clear segregation between the different MYSO classes in the EW plot. The Type IV sources with [FeII] emission show a similar spread in EW as the earlier sources. Similarly, there is not much segregation in the luminosity plot. The lack of segregation may again be due to a stronger continuum affecting the EW, or due to hot dust excess or stellar continuum emission. A stronger continuum results in a smaller equivalent width. As such, equivalent widths are likely less accurate estimators of line properties in MYSOs compared to line fluxes or luminosities.

C13 concludes that the luminosity correlation is evidence of the shock origin of the [FeII] line. I would urge caution in inferring this, as in this sample most of

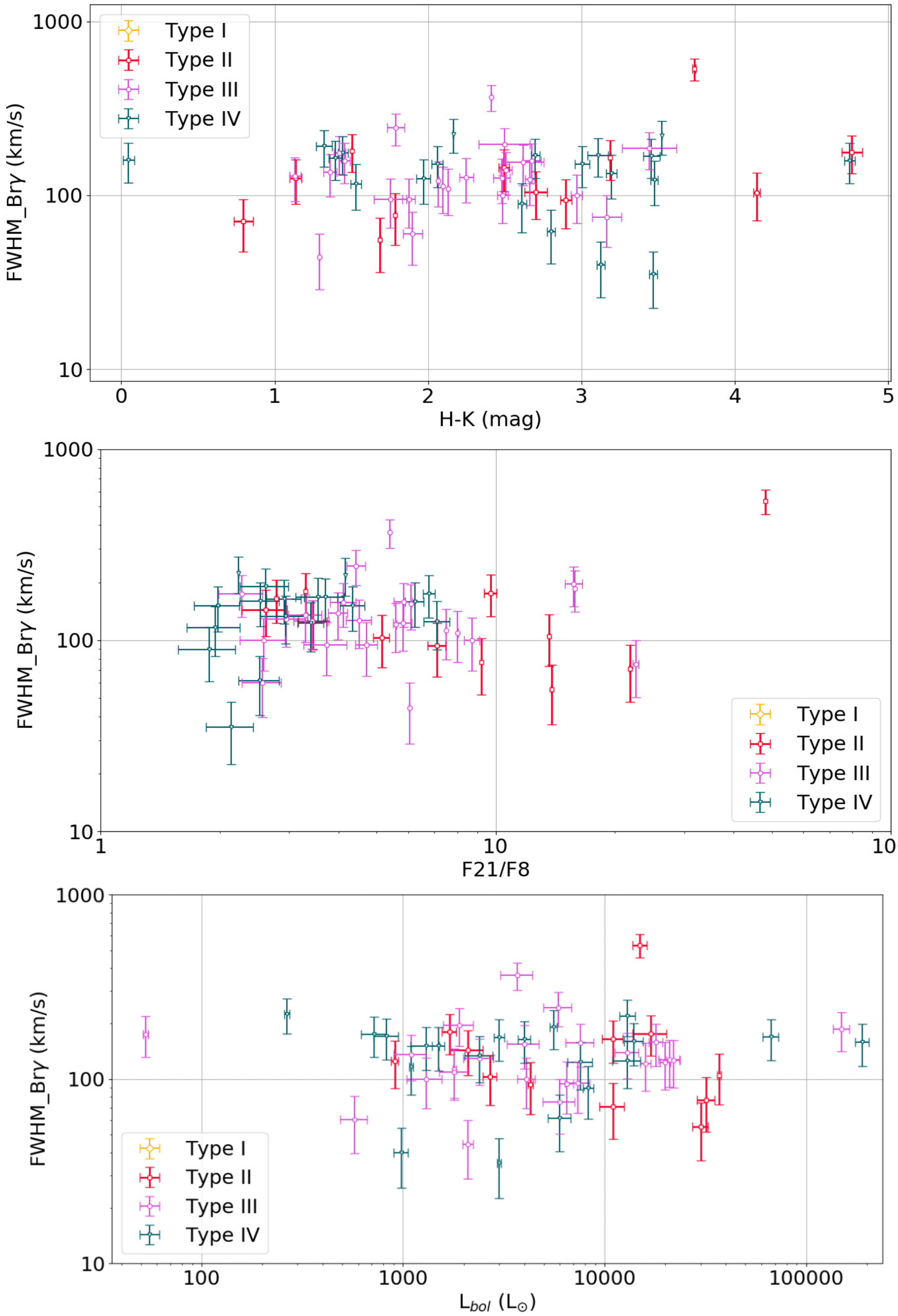

Figure 2.15: Top – Plot of $H-K$ colour as a function of Brγ FWHM. Middle – MIR flux ratio of 21 μm / 8 μm as a function of FWHM. Bottom – Bolometric luminosity as a function of FWHM.

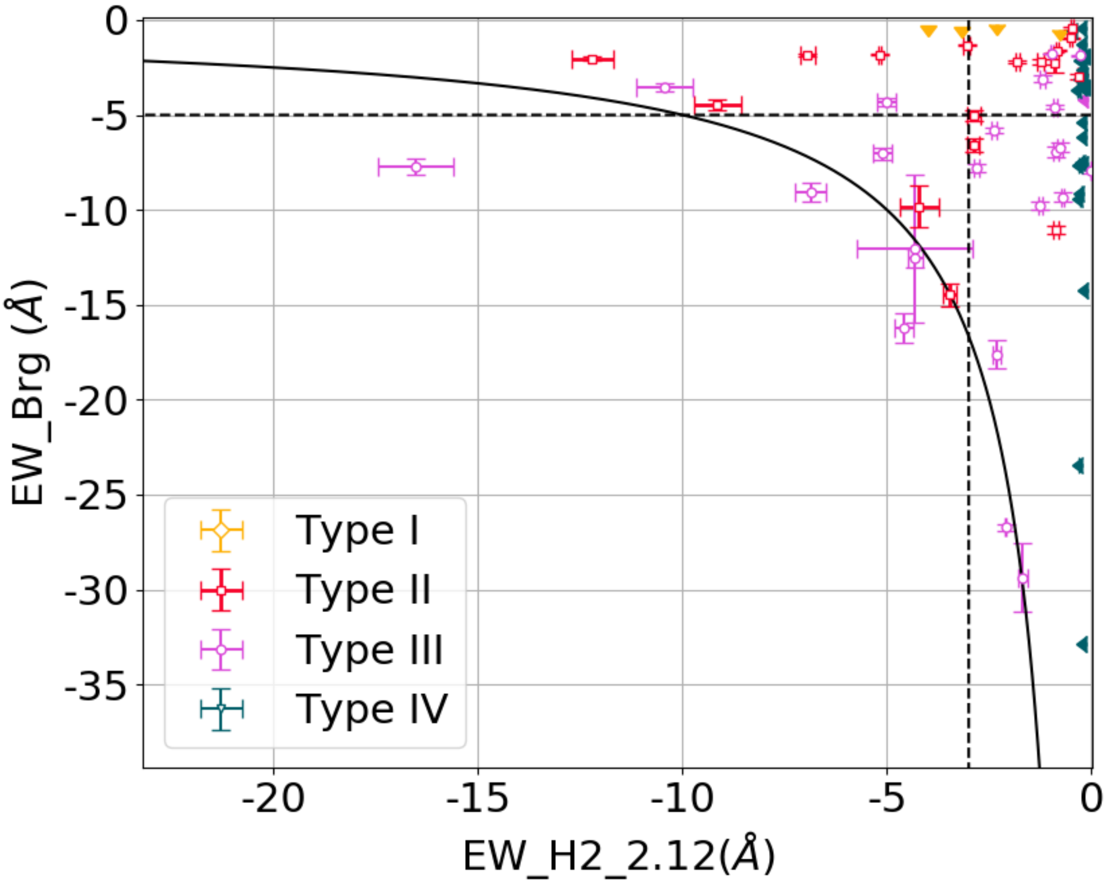

Figure 2.16: Equivalent width from Brγ against EW from H_2 2.12 μm, colour coded for the different MYSO classes. The solid black line shows the Connelley & Greene (2010) relation of $EW_{Br\gamma}$ =50/EW_{H_2}. The dotted black lines show the limits for low veiling sources of $EW_{Br\gamma}$ =–5 Å and EW_{H_2} =–3 Å

Table 2.5: Pearson correlation p–values for different line fluxes for MYSOs in this sample. N/A corresponds to lines detected together in only two objects or less, for which the correlation could not be studied. HeI corresponds to the line at 2.06 μm, and H_2 to the transition at 2.12 μm

Line	Br10	[FeII]	flFeII	HeI	H_2	Brγ	NaI	CO
Br10		0.87	0.88	0.87	0.52	0.7	0.52	–0.18
[FeII]	0.87		0.72	0.88	0.53	0.55	0.37	0.35
flFeII	0.88	0.72		0.85	0.22	0.71	0.76	0.04
HeI	0.87	0.88	0.85		0.85	0.95	N/A	N/A
H_2	0.52	0.53	0.22	0.85		0.67	0.85	0.67
Brγ	0.70	0.55	0.71	0.949	0.67		0.90	0.76
NaI	0.52	0.37	0.76	N/A	0.85	0.90		0.99
CO	–0.18	0.35	0.04	N/A	0.67	0.76	0.99	

Table 2.6: Pearson probabilities of false correlation for different line fluxes for MYSOs in this sample. N/A corresponds to lines detected together in only two objects or less, for which the correlation could not be studied.

Line	Br10	[FeII]	flFeII	HeI	H_2	Brγ	NaI	CO
Br10		<0.01%	<0.01%	0.05%	1.31%	<0.01%	36.91%	81.50%
[FeII]	<0.01%		2.85%	0.09%	0.50%	0.15%	75.87%	49.12%
flFeII	<0.01%	2.85%		0.40%	30.64%	0.01%	28.40%	50.46%
HeI	0.05%	0.09%	0.40%		0.75%	<0.01%	N/A	N/A
H_2	1.31%	0.50%	30.64%	0.75%		<0.01%	15.30%	4.83%
Brγ	<0.01%	0.15%	0.01%	<0.01%	<0.01%		0.10%	2.86%
NaI	36.91%	75.87%	28.40%	N/A	15.30%	0.10%		0.05%
CO	81.50%	49.12%	50.46%	N/A	4.83%	2.86%	0.05%	

the line fluxes are correlated with one another (see Tables 2.5 and 2.6). 75% of the pairs of line fluxes are correlated at a level of probability of false correlation of lower than 5%. Most of the non–correlations are related to NaI or CO bandhead, which are detected in a low number of sources. In addition, all the Brackett series in the H–band (Br10–20) are strongly correlated, as expected, with p–values of above 0.96, which corresponds to a null probability of false correlation.

As an additional check, I also computed correlation factors when normalising the line flux by bolometric flux, total flux in spectral band (H or K, depending on where the line is) or Brγ flux. Whilst some of the correlation factors between normalised line fluxes decrease (relative to non–normalised correlation factors), others increase, and the end result is that 70% of the normalised line fluxes also correlate (similar to the 75% of the non–normalised fluxes as discussed above). The average difference between normalised and non–normalised correlation factors is 17% of the numerical value of the factors. In conclusion, normalising the line fluxes by bolometric, band or Brγ flux still leads to most line fluxes correlating to one another. Similarly, in the GNIRS sample of Chapter 3 I found most NIR line luminosities correlate with one another, even when using statistical tests to ensure the correlations are not caused by flux or distance biases.

It is more likely that the line correlations in the NIR are caused by a scaling effect, as line luminosities are proportional to the stellar mass. In order words, a bigger star will have stronger accretion resulting in more powerful outflows and a larger accretion disc, as has been discussed by Mendigutía *et al.* (2015).

I also compare the luminosities of the Brγ and first CO bandhead lines (Figure 2.18). There is a strong correlation between these two as well, in spite of their different origins, one from the disc and the other from the wind. The detections have a Pearson coefficient of 0.84, corresponding to a probability of false correlation of 0.005. The best fit was $\log(L_{CO}) = (0.7\pm0.2)\log(L_{Br\gamma}) -- (0.1\pm0.6)$. This agrees with the best fit correlation found by Ilee *et al.* (2014) for the lower mass Herbig Ae/Be stars, who reported $\log(L_{CO}) = (0.6\pm0.2)\log(L_{Br\gamma}) -- (0.8\pm0.5)$. Upper limits also are also well correlated, with a correlation coefficient of 0.85, corresponding to a null probability of false correlation. The best fit for upper limits is $\log(L_{CO}) = (0.8\pm0.5)\log(L_{Br\gamma}) -- (1.3\pm0.8)$, lower than the one for the detections.

The Brγ line has been shown to be a proxy for accretion in low mass T Tauri and intermediate mass Herbig Ae/Be stars. Here I use the relation between Brγ line luminosity and accretion luminosity from lower mass YSOs to obtain an estimate for accretion luminosity. Mendigutía *et al.* (2011) obtain a best fit for:

$$log(L_{acc}/L_{\odot}) = 0.91 log(L_{Br\gamma}/L_{\odot}) + 3.55 \tag{2.4}$$

Bolometric luminosities can be converted to stellar masses and radii using the ZAMS stellar parameters of Davies *et al.* (2011), which are in turn based on the hydrostatic stellar models of Meynet & Maeder (2000). Estimates of stellar parameters are given in Table 1 of Davies *et al.* (2011). For example, a ZAMS star of 1000 L$_{\odot}$ will have a mass of 6 M$_{\odot}$, and radius of 3 R$_{\odot}$, whereas a star of 3700 L$_{\odot}$ will have a mass of 9 M$_{\odot}$, and radius of 3.9 R$_{\odot}$. Parameters for stars of luminosities between those given in Davies *et al.* (2011) are determined through interpolation.

With these assumptions, the mass accretion rate can be determined from:

$$\dot{M} = \frac{L_{acc} R_{*}}{G M_{*}} \tag{2.5}$$

CLO13 found that most Brγ luminosities are between L$_{Br\gamma}$=$10^{-7} - 10^{-5}$ L$_{bol}$, similar to values for T Tauri and HAe/Be stars. They also found that L$_{acc}$= 0.01 – 1 L$_{bol}$, which is also in agreement with results from lower mass YSOs. As shown in Figure 2.19, similar trends are found in the AAT MYSOs, confirming the findings of CLO13. In addition, the mass accretion rates also agree with results from lower mass sources, with most MYSOs between $10^{-7.5}$–$10^{-5.5}$ M$_{\odot}$/yr (see Figure 2.19).

The models of Hosokawa *et al.* (2010) predict that MYSOs are swollen up compared to ZAMS stars, with stellar radii up to three times larger than expected from the models of Davies *et al.* (2011). This increase in radius would produce accretion rates that are three times larger than those shown in Figure 2.19 (as per Formula 2.5). As a result, the accretion rates of MYSOs would be much larger than those of the lower mass pre–MS stars, similar to the trend seen by Beltrán & de Wit (2016) and Fairlamb *et al.* (2017) between Herbig Ae stars and their higher mass Be counterparts. The accretion rates of higher mass Herbig Be stars

Table 2.7: Average values of accretion luminosity and rate, as well as accretion luminosity normalised by bolometric luminosity and accretion rate normalised by stellar mass

	L_{acc}	L_{acc}/L_{bol}	M_{acc}	M_{acc}/M_*
All	3.7E+4	0.9	3.3E–4	8.4E–6
Type I	N/A	N/A	N/A	N/A
Type II	6.1E+3	0.6	7.0E–5	5.3E–6
Type III	4.7E+3	0.9	5.5E–5	4.8E–6
Type IV	6.1E+4	1.1	4.5E–4	1.5E–5

are consistent with a steeper $\dot{M}$–M_* fit than Herbig Ae, so it would be expected that MYSOs are fitted by an even steeper law. This lends support to scaling theories of high–mass star formation.

Table 2.7 presents the average values of accretion rate and luminosity, as well as accretion luminosity normalised by bolometric luminosity and accretion rate normalised by stellar mass for the different MYSO evolutionary classes. The accretion rate and luminosity averages are larger in Type IV than Type II, but lower in Type III than in Type II. The same trend is seen for normalised accretion rates. The normalised accretion luminosity does, however, seem to increase with evolution. Visually, in Figure 2.19, the different MYSO evolutionary class do not appear to segregate, in terms of accretion rate or luminosity. One possible explanation for the lack of segregation may be that the Brγ line may not be tracing just the accretion in evolved sources, but also contain nebular elements. It is also possible that accretion is episodic at all stages. An outbursting MYSO would in principle show a stronger Brγ flux as the resulting wind emission would increase due to the stronger accretion activity. As such, a quiescent Type II MYSO could have the same Brγ line flux, and resulting accretion rate as an outbursting Type IV. However, the continuum level emission from hot dust excess will also increase as the accretion shock radiation heats up the dust. So the equivalent width may actually decrease due to the increased continuum level. The combined effect of the continuum level and line flux increase under high accretion rates is not clear, and it is likely more simulations are needed to investigate this.

I investigate the evolution of accretion rates with NIR and MIR colours (see Figure 2.20). There is no correlation between $F_{21\mu m}/F_{8\mu m}$ and accretion rate, with a

Pearson coefficient of p=0.04, equivalent to a probability of spurious correlation of 0.37. There is a strong correlation between accretion rates and NIR $H-K$ colour, with p=0.64 and probability of spurious correlation of ≈0. The NIR colours trace hot dust excess emission, which is correlated with accretion, as dust gets heated up due to accretion shocks. MIR data on the other hand was taken with MSX, which has a larger beam size than the 2MASS NIR data, and as such is less sensitive to accretion. This may be why MIR flux ratios do not correlate with accretion rates, but NIR colours do. The NIR results are consistent with the idea that the most embedded and least evolved objects are the strongest accretors, similar to the low mass YSOs.

I also investigate the presence of P Cygni and inverse P Cygni features in the Brγ and the 2.06 μm HeI line. P Cygni–like self–absorption arises in gas in outflowing motion towards the observer, whilst an inverse P Cygni will be seen when an inflow of gas is directly observed. 9 objects show a Brγ P Cygni profile, 10 a HeI P Cygni and 2 an inverse P Cygni in Brγ. Three of the Brγ P Cygni profile objects did not fit the classification scheme. Aside from those, there were 1 type II object, 3 type III and 2 type IV objects with Brγ P Cygni. There were also 3 Type III objects and 7 type IV objects with HeI P Cygni, as well as 2 Type II objects with an inverse P Cygni in Brγ. The detection rates are given in Table 2.8.

P Cygni profiles in the HeI line are only seen in evolved MYSOs, with significantly more in Type IV than III. This is expected as more evolved objects have less collimated, MS–like winds, which are more likely to give rise to P Cygni profiles as shown by Drew *et al.* (1993).

These sources are also bluer in MIR colours than sources without a P Cygni profile, as seen in Figure 2.21. The average $F_{21\mu m}/F_{8\mu m}$ for all MYSOs is 8.8, whereas for P Cygni Brγ sources it is 5 and for P Cygni HeI 2.06 μm sources it is 6.8. Similarly, the average $F_{8\mu m}/F_K$ is 180 for the whole sample, 54 for P Cygni Br γ sources and 49 for P Cygni HeI sources. Inverse P Cygni profiles, indicative of infall, are also only seen in the early Type II MYSOs. This points to younger MYSOs being more favourable for the detection of infall activity, possibly due to accretion being stronger at earlier stages.

The bluer MIR colours of MYSOs with P Cygni profiles is expected if they are less embedded, more evolved objects. The Brγ line strengths of objects with PC profiles in this line are higher than the average of the sample. This may be due to a stronger stellar continuum or a nebular optically thin gas component in recombination lines.

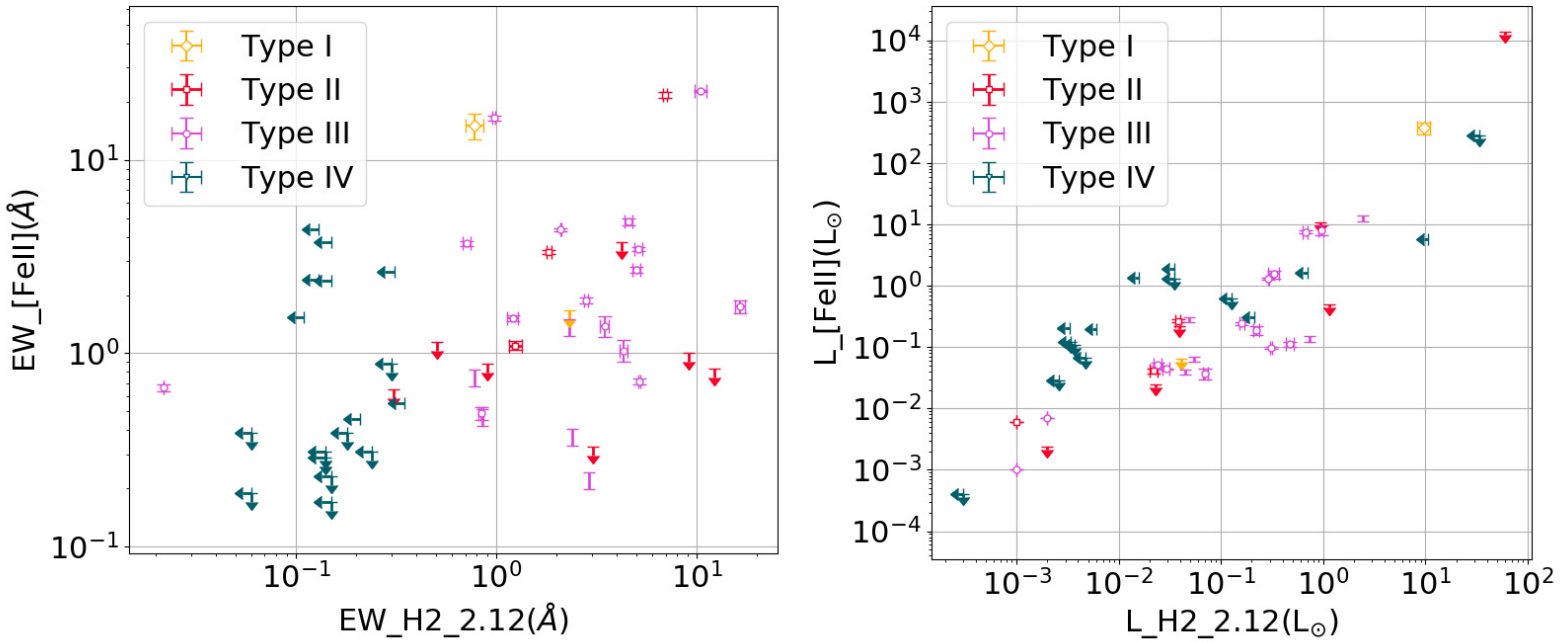

Figure 2.17: Left – EW from the 1.644 μm [FeII] emission line as a function of H_2 2.120 μm EW. Right – Luminosity of [FeII] line as a function of H_2 2.120 μm luminosity. Colour coded as above.

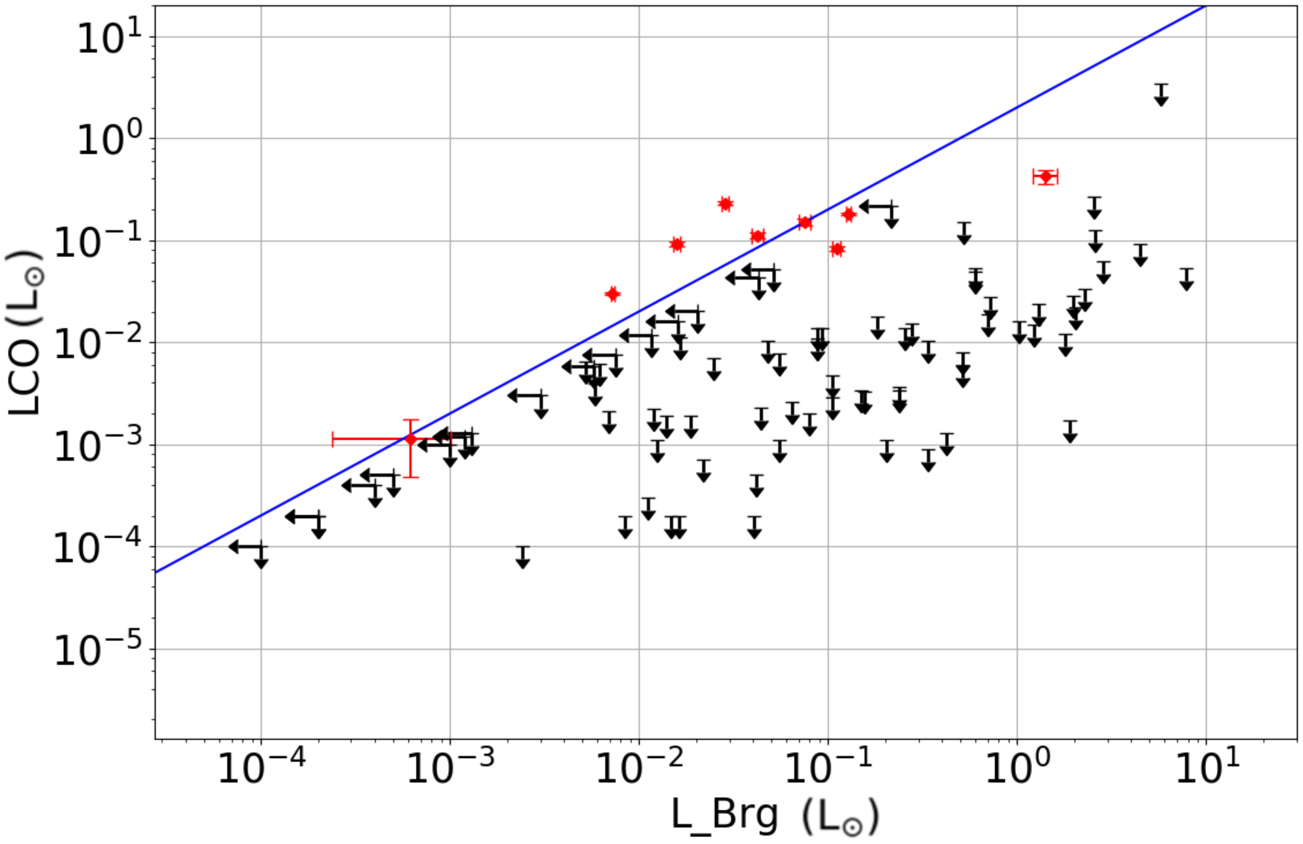

Figure 2.18: Luminosity of the CO bandhead first transition as a function of Brγ line luminosity. Upper limits for non–detections are also included, as well as the a best fit line (solid blue line).

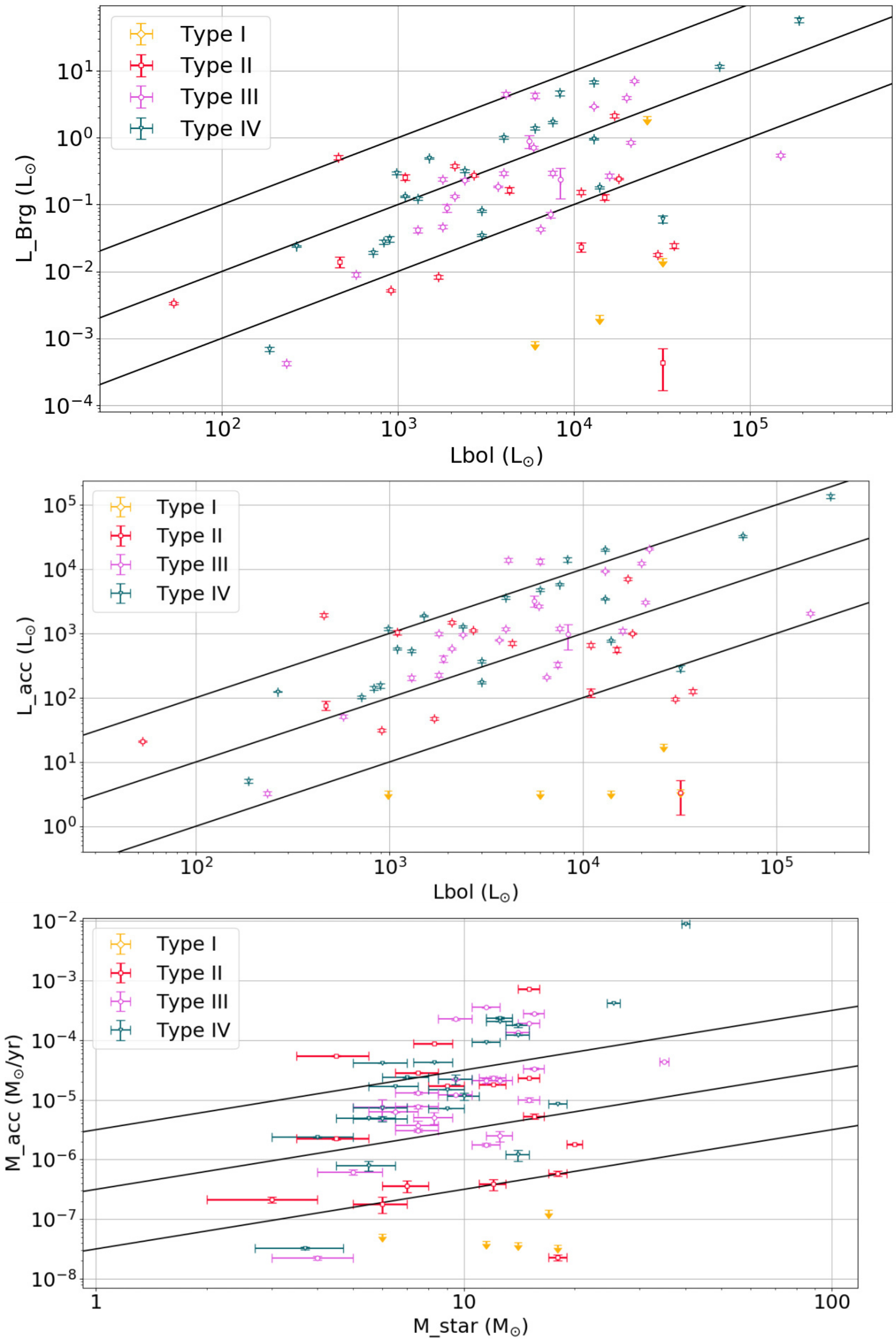

Figure 2.19: Left – Brγ luminosity as a function of bolometric luminosity. The black solid lines are $L_{Br\gamma}=10^{-5}$,10^{-4} and 10^{-3} L_{bol}, as in CLO13. Middle – Accretion luminosity determined with the Mendigutía *et al.* (2011) relation as a function of bolometric luminosity. The black solid lines are L_{acc}=0.01, 0.1 and 1 L_{bol}. Right – Mass accretion rate as a function of stellar mass. The black solid lines are $10^{-7.5}$,$10^{-6.5}$ and $10^{-5.5}$ M_*.

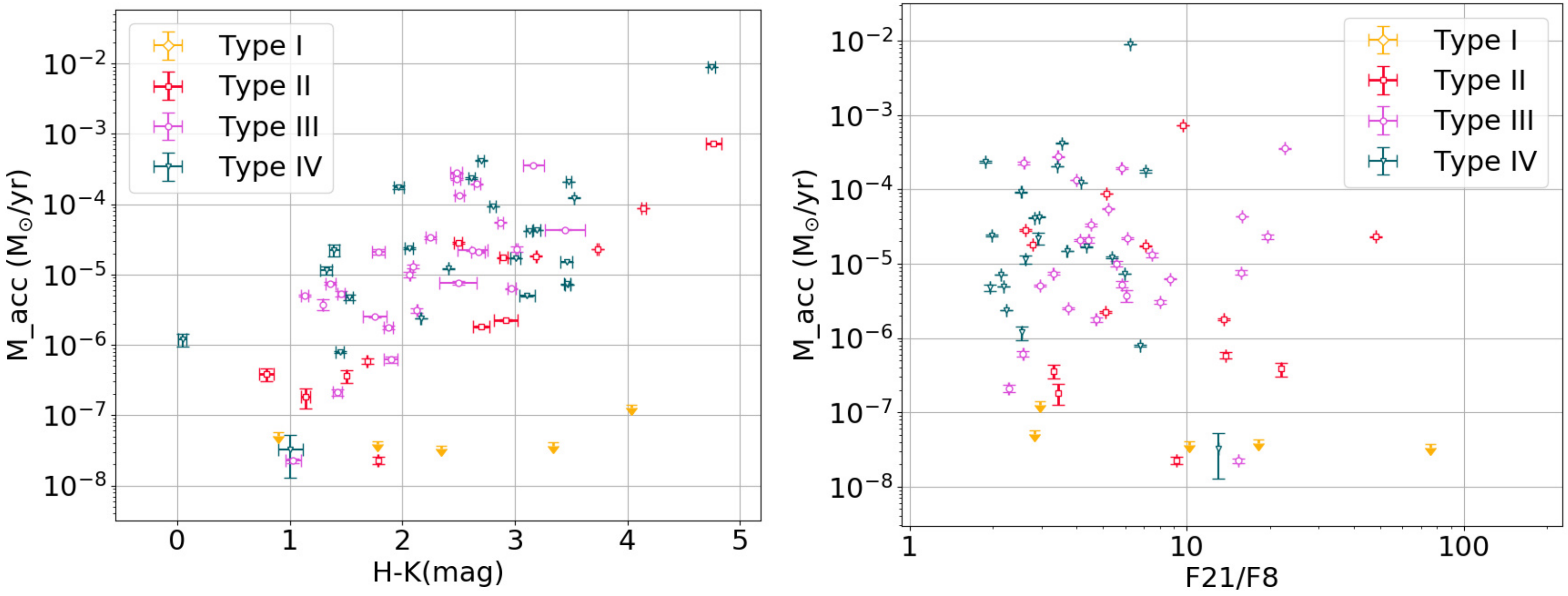

Figure 2.20: Left – Accretion rate from Brγ as a function of NIR $H-K$ colours. Right – Accretion rate as a function of $F_{21\mu m}/F_{8\mu m}$.

Table 2.8: P Cygni (PC) and inverse P Cygni (IPC) detection rates (in %) in Brγ and HeI with MYSO class

	PC Brγ	PC HeI 2.06	IPC Brγ	Uncertainties
All YSOs	9.8 ±	10.9	2.1	1.1
Type I	N/A	N/A	N/A	20.0
Type II	7.7	N/A	15.3	7.7
Type III	10.3	10.3	0.0	3.4
Type IV	8.3	29.2	0.0	4.2

2.6.5 Comparisons with surveys at other wavelengths

2.6.5.1 Ionised radio jets

I compare the results of this survey with the ionised jet survey of Purser *et al.* (2016), which covered a similar area of the Galaxy with ATCA observations at 5–22 GHz to look for ionised jets in MYSOs. 19 objects, or 27% of this sample were also classified by Purser *et al.* (2016). Of these, 10 objects had jet detections.

Of the 19 objects with jet observations, 3 were Type I, 5 Type II, 5 Type III and 6 Type IV, so a split between the classes similar to the average split in the sample. Jets were found in 2/3 Type I objects, 2/5 Type II, 4/5 Type III and 2/6 Type IV.

Although the numbers are very small, the Type IV objects have the lowest jet detection rates. Table 2.9 shows the detection rates of various lines in the Purser *et al.* (2016) objects with and without jets. There is not much difference between objects with or without jets in HI or CO bandhead detection rates. However, there are significantly higher detection rates of [FeII] but also fluorescent Fe II in objects with jets compared to targets without jet detections. H_2 detection rates are also slightly increased in objects with jets. One would expect the increases in the shock tracers H_2 and [FeII] as jets entrain the interstellar medium and give rise to shocks. As for the fluorescent FeII, sources with detected jets probably undergo strong accretion and as such have more developed accretion discs which give rise to the observed increased fluorescent FeII detection rates. A histogram of the values of accretion rates for objects with or without jet detections does look significantly different (see Figure 2.22). Jet objects do seem to have stronger ac-

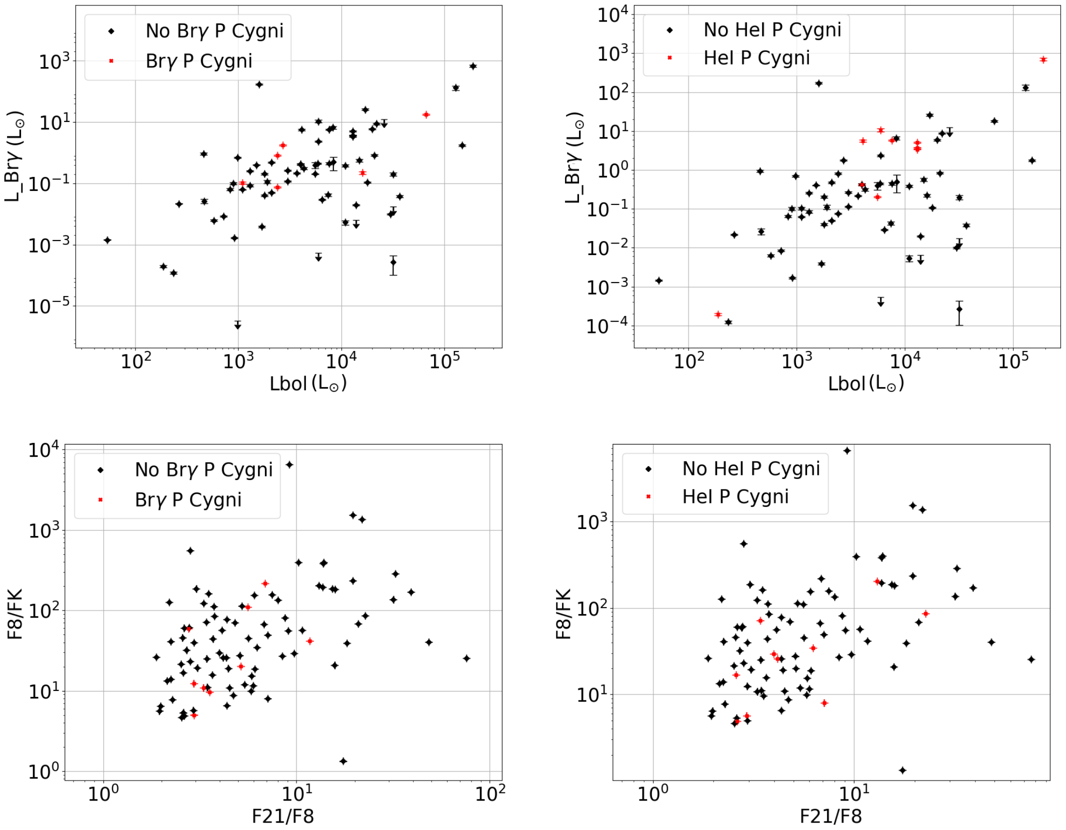

Figure 2.21: Top left – Brγ line luminosity against bolometric luminosity, with objects with P Cygni in the Brγ line (red) and without (black) colour coded. Top right – Brγ line luminosity against bolometric luminosity for objects with or without P Cygni profiles in HeI. Bottom left – $F_{8\mu m}/F_K$ as a function of $F_{21\mu m}/F_{8\mu m}$ for objects with or without a P Cygni profile in Brγ. Bottom left – $F_{8\mu m}/F_K$ as a function of $F_{21\mu m}/F_{8\mu m}$ for objects with or without a P Cygni profile in HeI.

Table 2.9: Detection rates of different lines in objects with or without jets from the Purser *et al.* (2016) sample. Uncertainties are of order 10%.

	Brγ	Br10	CO	H_2	[FeII]	fl Fe
YSOs with jets	70%	60%	20%	70%	60%	60%
YSOs without jets	88%	55%	22%	55%	33%	33%

cretion rates (average 7.7×10^{-5} $M_\odot$/yr) than non–jets (average 3.2×10^{-5} $M_\odot$/yr) as expected.

However, the differences in accretion rates between jet and non–jet sources are not at a significant level, a K–S test giving a statistic of 0.42 and a p–value of 0.51, which shows the two distributions are drawn from the same initial sample. Investigations of a larger sample than the current 19 objects with jet measurements are required in order to obtain better statistics to determine whether MYSOs with ionised jets have stronger accretion rates than those without.

2.6.5.2 Submilimetre clump masses

ATLASGAL (Schuller *et al.* 2009) was a large area survey of the southern sky taken at 870 μm with APEX, in order to measure continuum dust emission through the Galaxy. One of its main uses has been in star formation, with Urquhart *et al.* (2014) matching RMS sources to ATLASGAL targets to derive clump masses, virialised masses and H_2 column densities for many of the sources in this sample. The clump mass is given by the following formula, as described by Hildebrand (1983):

$$M_{clump} = \frac{D^2 S_\nu R}{B_\nu(T_d)\kappa_\nu}, \tag{2.6}$$

where D is the distance, S_ν the 870 μm flux, R the gas–to–dust mass ratio, taken as 100, κ_ν the opacity coefficient (1.85 cm^{-2}g) and $B_\nu(T_d)$ the Planck function at the given dust temperature, assumed to be 20 K. Combining this with evolutionary tracks of Molinari *et al.* (2008), they find that there is little difference between MYSOs and HII regions in clump structure or where the embedded star is. This suggests that the clump is formed before the onset of star formation, and it does not change significantly during this process. A strong correlation was seen between clump mass and bolometric luminosity of MYSOs, suggesting that

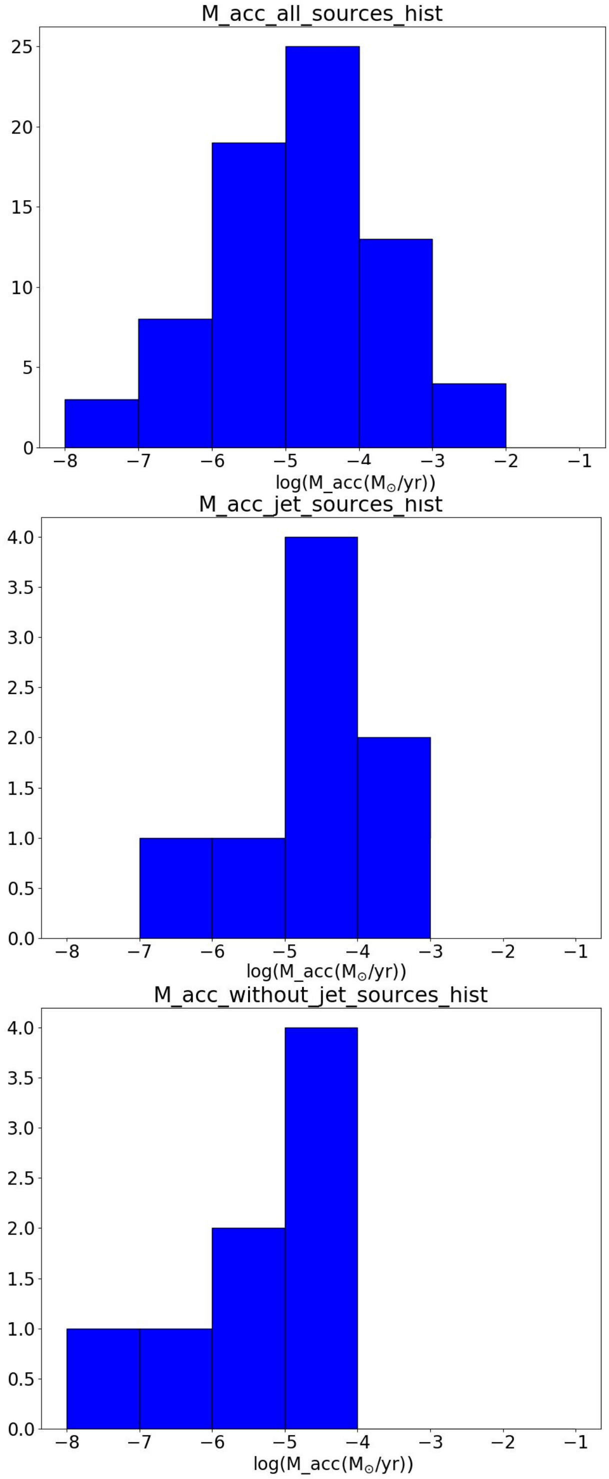

Figure 2.22: Top – Histogram of accretion rates for all YSOs. Middle – Histogram of accretion rates in sources with ionised jet detections. Bottom – Histogram of accretion rates for sources without jet detections. Two sources with jet detections and one without jet detection had no Brγ emission and as such the accretion rate could not be determined, so they are not shown in the histograms.

the most massive stars form in the most massive clumps. Using L_{bol}/M_{clump} as a proxy for age they find that methanol masers are an earlier evolutionary stage than MYSOs and HII regions.

I used their clump masses, where available (50 objects in this sample) to perform a similar analysis on the MYSOs surveyed (see Figure 2.23). There is a strong correlation between clump mass and bolometric luminosity, with a Pearson coefficient of p=0.55 and a probability of false correlation of 2×10^{-5}. One would expect that the most massive clumps are those harbouring Type I objects, as in the early stages the material has not been processed from the clump to the core and onto the pre–stellar object at this stage yet. More evolved objects like Type IV should have the lowest clump masses, as much of the clump material will have been processed onto the protostar by this stage. The average clump masses per type confirm this; the whole sample average is 1900 $M_\odot$, for Type Is 4800 $M_\odot$, for Type II 2000 $M_\odot$, for Type III 2400 $M_\odot$ and for Type IV 870 $M_\odot$. Almost all of the MYSOs in this sample are in the accretion phase (the vertical climb) according to the evolutionary models of Molinari *et al.* (2008), and the clump has yet to become depleted or dispersed (the horizontal part of the tracks). Using L_{bol}/M_{clump} as a tracer of age shows that Type I objects are indeed at an earlier evolutionary stage than type IV objects. The average L_{bol}/M_{clump} for the whole sample is 20 $L_\odot/M_\odot$, for Type Is 7 $L_\odot/M_\odot$, for Type IIs 11 $L_\odot/M_\odot$, for Type IIIs 17 $L_\odot/M_\odot$ and for Type IVs 34 $L_\odot/M_\odot$.

One might expect that dust temperature may be significantly higher than the 20 K assumed in determining the clump mass due to MYSO evolution. It is worth considering whether this could lead to enough of a change in clump mass in order for the bolometric luminosity–clump mass correlation to dissapear. The SED of all observed MYSOs peaks in the FIR, indicating that the strongest part of the emission comes from cold dust, justifying the 20K assumption of temperature. In addition, Urquhart *et al.* (2011a) see extended emission from NH_3 towards all MYSO clumps, which would not be present should the dust temperatures be much higher than 20 K. Urquhart *et al.* (2014) determine kinetic temperatures from NH_3 line widths, and find that the mean temperature for the centre of the clump is 23K. Observations of ammonia of UCHIIs (objects at a later evolutionary stage than MYSOs) of Urquhart *et al.* (2011b) find them to have an average kinetic temperature of 22.1 K. As such, even objects at a later evolutionary stage have a similar dust temperature to MYSOs. 80% of the sources are located between 15–25 K in Figure 10 of Urquhart *et al.* (2014), so an error of ±5 K is reasonable. As the authors discuss, this would lead to a change of 50% in determined clump masses. However, a change of at least factor 3–5 would be required in order to remove the correlation in Figure 2.23. As such, I conclude that inaccuracies in the assumption of 20 K dust temperature in determining the clump masses are unlikely to lead to a loss of the $M_{clump} - L_{bol}$ correlation.

I also checked for correlations or segregation between L_{bol}/M_{clump} and colour. Figure 2.24 shows plots of L_{bol}/M_{clump} as a function of $H - K$ and $F_{21\mu m}/F_{8\mu m}$. There is no correlation with NIR colour, with a Pearson factor of 0.37 and a probability of false correlation of 0.05. There is no correlation with the MIR flux ratio either, with p=–0.09, giving rise to a probability of spurious correlation of 0.25.

There is also no correlation between accretion rates and L_{bol}/M_{clump}. The correlation coefficient is p=–0.05 and the probability of spurious correlation of 0.33. This may be due to contamination by elements other than accretion in the Brγ line flux such as stellar continuum or optically thin nebular gas, especially for evolved MYSOs.

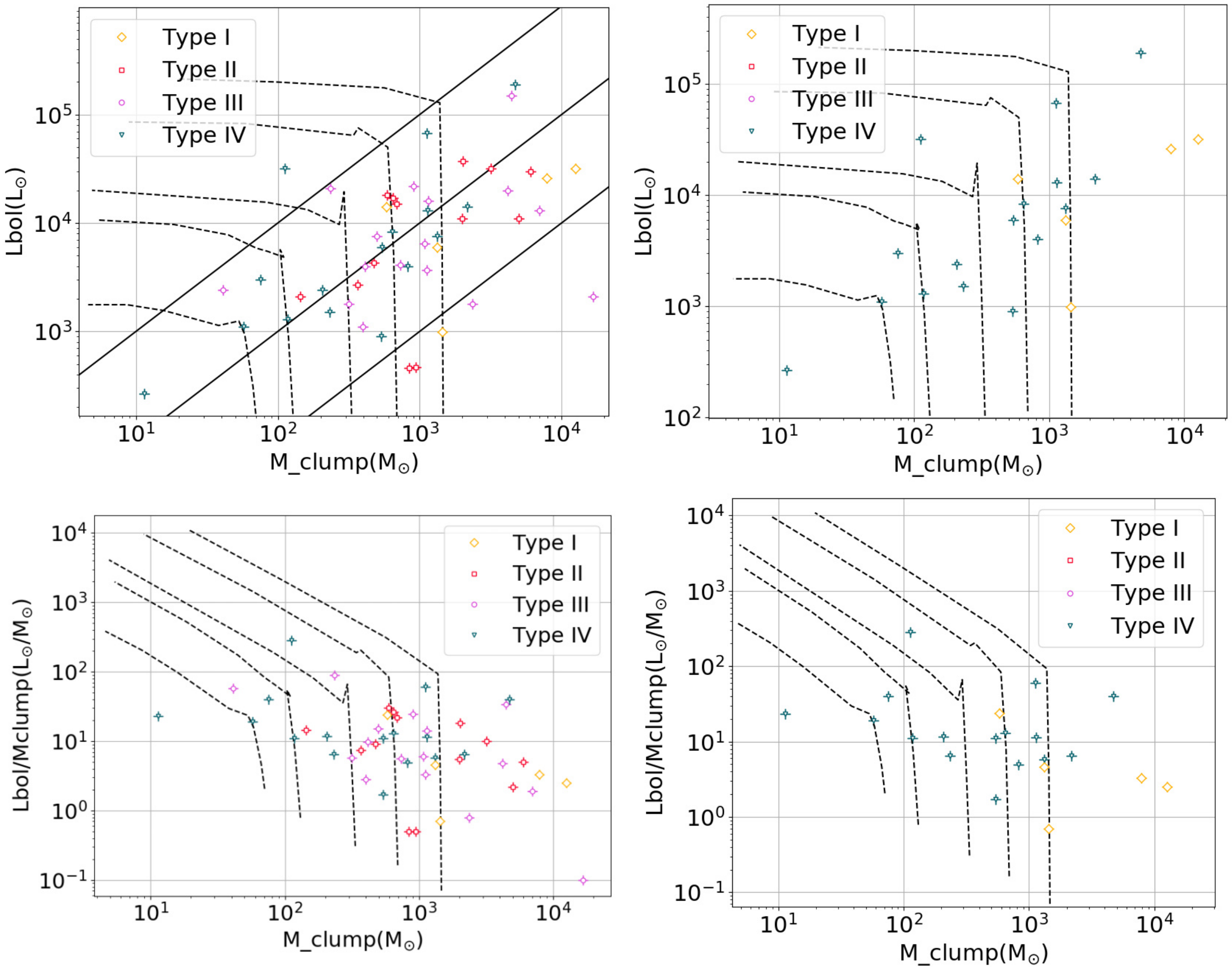

Figure 2.23: Top left – Bolometric luminosity of MYSOs as a function of clump mass, colour coded for MYSO class. Solid lines are L_{bol}=0.01, 0.1 and 1 × M_{clump}. Dotted lines are evolutionary tracks from Molinari *et al.* (2008), for clump masses of 80, 140, 350, 700 and 2000 $M_\odot$. Top right – same plot but only for Type I and IV MYSOs. Bottom left – L_{bol}/M_{clump} as a function of M_{clump}, with evolutionary tracks and colour coded. Bottom right – same plot but only for Type I and IV MYSOs.

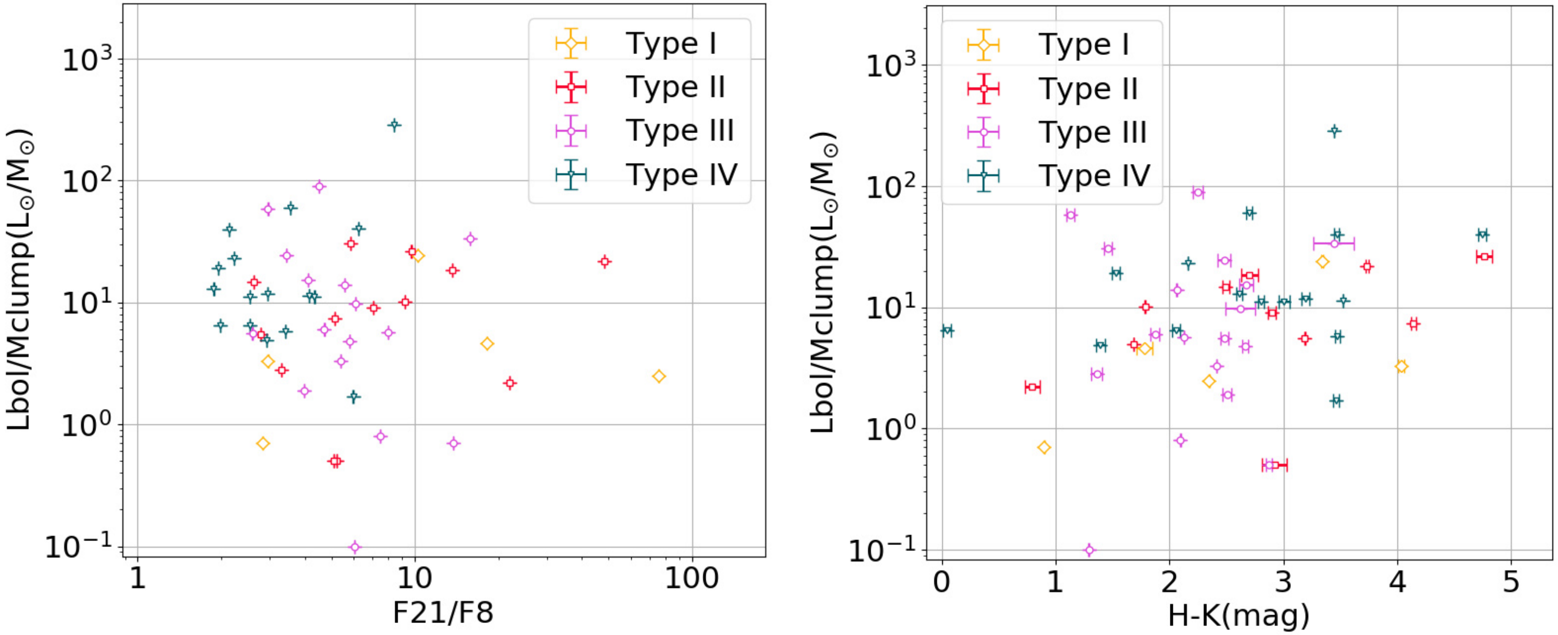

Figure 2.24: Left – L_{bol}/M_{clump} as a function of $F_{21\mu m}/F_{8\mu m}$, colour coded for MYSO types. Right – L_{bol}/M_{clump} as a function of $H - K$ colours

2.6.6 Assessment of classification criteria

In C13, the MYSO subclasses are defined based on the presence or absence of a given line. It is worth assessing whether these criteria can be constrained more accurately based on relative strengths of different lines. Given that many of the objects have been observed only in the K–band, it would be useful to base some of the classification solely on K–band transitions. For example, one cannot decide if an object is a class II or III with K–band spectra only. Clear quantitative criteria would help formalise the evolutionary sequence. As the line fluxes may be affected by the scaling effect discussed in Section 2.6.4, I analysed the behaviour of flux ratios of lines used to define the classifications scheme.

The Brγ line is expected to be stronger relative to H_2 in Type III than in Type II objects. Also, the strength of the Br10 relative to Brγ or Br10 to fluorescent FeII may change with evolutionary class. Table 2.10 shows the average values for line ratios for these lines. Significant differences are seen. The H_2 line is the strongest relative to Br γ in Type II. The relative strength of Br10 to Brγ increases with MYSO class, reaching a maximum in Type IV. The fluorescent FeII line is also at its strongest relative to Brγ in Type IVs.

The average Brγ/H_2 line flux ratio is almost 7 times as large in Type III than in Type II. In addition, 85% of the line flux ratios are lower than 2.5 in Type II, and 70% of the Type III ratios are above 2.5.

Histograms of the flux ratios of Brγ to H_2, Br10 and fluorescent FeII for the different evolutionary classes of C13 are presented in Figure 2.25. These confirm the trends seen in the averages, with Brγ becoming stronger relative to H_2 in Type III as opposed to Type II. Br10 and fluorescent FeII both become stronger relative to Brγ when going from Type III to IV. However, there is no clear segregation or limit in terms of either of these line ratios between the different types. K-S tests confirm this, resulting in a D–value of $\approx$0.3 for all three line ratios presented in the histogram. This indicates that the distributions of line ratios from different types are drawn from the same initial sample.

The lack of a clear quantitative separation between evolutionary classes may be due to the insufficient resolution of the data, or contamination due to nebular components, particularly in the HI emission lines. It is possible that by using

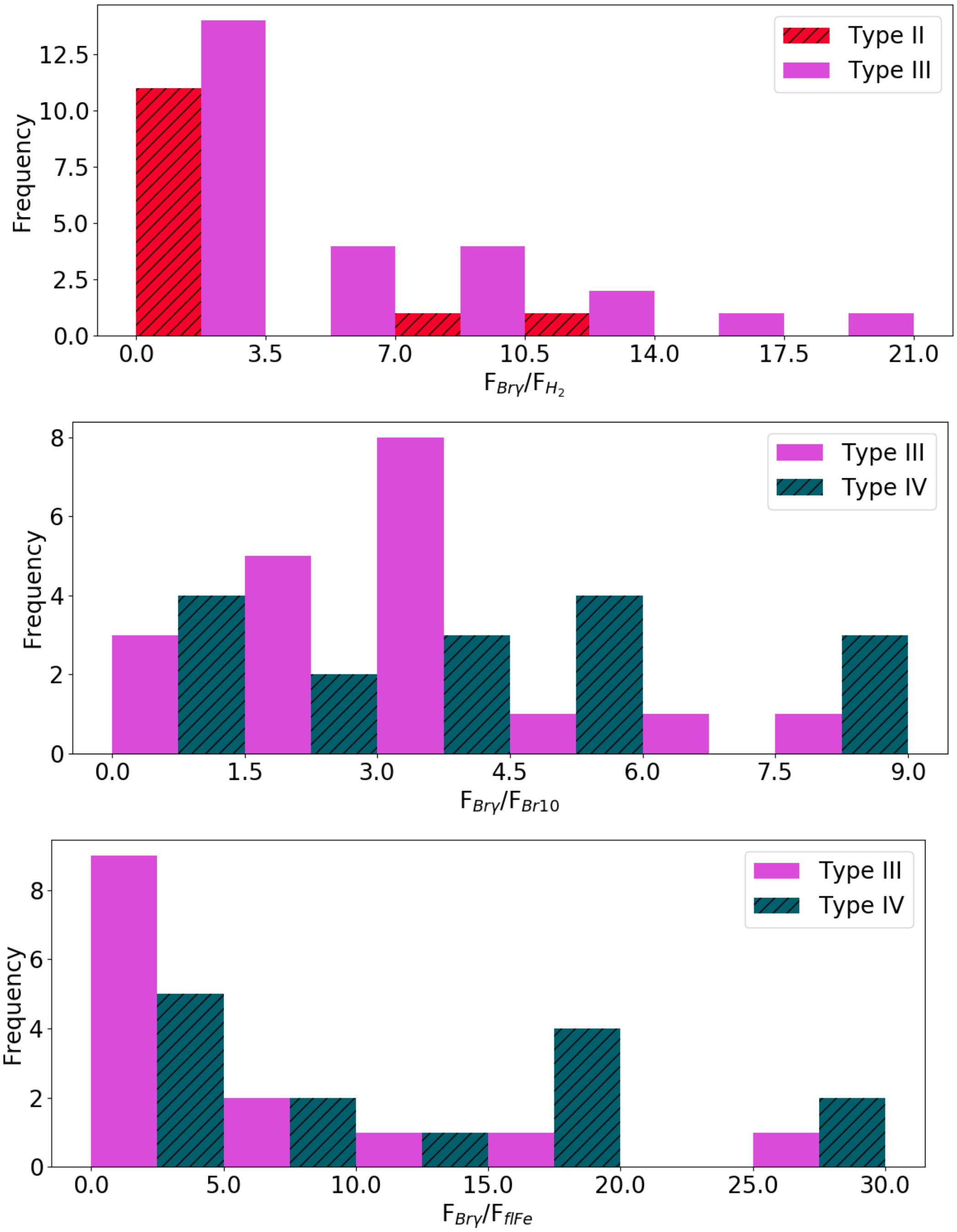

Figure 2.25: Top – Histogram of line flux ratios of Brackett γ to H_2, colour coded for type. Middle – Histogram of Brγ/Br10 flux ratios. Bottom – Histogram of Brγ/fluorescent FeII flux ratios.

Table 2.10: Average values of line flux ratios for Br10, Br γ H_2 and fluorescent FeII. Uncertainties determined as standard error on the mean.

Flux ratios	Brγ/H_2	Br10/Brγ	Brγ/flFe	# of sources in class
All YSOs	14.5 ± 1.4	0.4 ± 0.0	17.9 ± 0.9	68
Type I				5
Type II	2.8 ± 0.3			13
Type III	18.3 ± 2.5	0.4 ± 0.0	16.8 ± 1.8	27
Type IV		0.7 ± 0.1	19.2 ± 1.7	23

multi–wavelength data, and line transitions from other parts of the MYSO SED differences between the evolutionary classes of MYSOs can be constrained more accurately.

2.7 Conclusions

Near–IR spectra were obtained and reduced for 152 objects selected from the RMS survey, 89 of which were MYSOs. This data has a resolution of ≈2000, and contains spectra of all the objects in the *K*–band and of 70 MYSOs in the *H*–band. The YSOs observed range between 50–300,000 $L_\odot$ and 14–127 mag of visual dust extinction. 68 of the YSOs in this sample were classified under the evolutionary scheme of C13. 5 objects were found to be Type I MYSOs, 13 Type II, 29 Type III and 24 Type IV.

Kolmogorov–Smirnov tests confirmed that there is no difference between the evolutionary classes in terms of luminosity and distance are drawn from the same sample, so these properties are not what gives rise to the different classes.

MYSOs were split into these classes based on the presence or absence of certain spectral lines. Multi–wavelength data confirmed that this is a real evolutionary sequence. Type I and II MYSOs were found to be the most embedded and consistent with having the strongest shocks as a result of intense accretion. Results from Type III and IVs are possibly indicating that in evolved MYSO stages jets and outflows have cleared out a significant part of the surrounding dust, leaving the MYSO less embedded.

Changes in the accretion activity were studied by Brγ line flux changes. I compared these with results from the lower mass Herbig and T Tauri stars. Results showed that MYSO accretion rates scale with protostellar mass in a similar fashion to the scaling relations for lower mass YSOs. This suggests that there are similarities in accretion between high mass and low mass stars, which indicates that massive stars form in a similar manner to low mass stars. There is no clear trend of average accretion rate or luminosity with evolutionary type. There is also no clear segregation in accretion strength between the different MYSO classes, as seen from plotting the accretion rate as a function of stellar mass. This may be due to episodic accretion across the MYSO phase, or contamination of the Brγ line profile by wider, optically thin nebular components.

By comparing with submillimetre data, I showed that the earliest MYSOs are located in the largest clumps, and that more evolved MYSOs have already processed much of the clump mass onto the protostar through a disc, and as such are located in less massive clumps. Radio data comparisons show that the ionised jets trace accretion activity, as expected as jets are a byproduct of accretion. Evolved MYSOs have the lowest jet detection rate. Infall motion, as traced by inverse P Cygni profiles, is only detected in early MYSO types, with outflows, as traced by P Cygni profiles, being most prevalent in evolved, least embedded MYSOs. These observational results are all consistent with a decrease in accretion activity as the objects approach the UCHII region phase.

Based on the current data, I was not able to define a more quantitative separation between the evolutionary classes, in terms of either line flux, strength or ratios of these quantities.

The data presented here, together with the subsequent analysis present a picture of a dynamic MYSO phase, and provide evidence for a split of MYSOs into evolutionary classes based on NIR line tracers. The MYSO phase marks a turning point in the process of formation of a massive star, during which the pre–stellar object transforms from a deeply embedded core with strong shock and infall activity into a protostar which has cleared the dust around it and is almost revealed at optical wavelengths as an HII region. The high–mass star formation process seems be similar to the low–mass process, as the monolithic collapse/core accretion models suggest (with significant differences in terms of the timescale of the formation process).

Chapter 3

The circumstellar environment of MYSOs: intermediate resolution Gemini NIR spectroscopy

3.1 Introduction

As explained in Chapter 1, there are still gaps in the science of how massive stars form. Low–mass star formation is thought to result from the monolithic collapse of a cloud followed by accretion through the circumstellar disc, and is in general reasonably well understood as per the description of Shu *et al.* (1987).

The theory needs to be adapted if it is to be applied to the formation of objects that are more massive, as there is considerably stronger stellar feedback than for low–mass stars. In addition, high–mass protostars lack a stellar magnetic field, making magnetospheric accretion unfeasible.

Although disc accretion seems therefore to be a main contender for the formation of massive stars, little is known about the precise accretion mechanism. Even the most recent, sophisticated star formation models (Rosen *et al.* 2016) are not able to simulate the fine detail required to probe the accretion process from parsec scales via the disc to the stellar surface. This is due to the idealised nature of these simulations, which do not include effects such as magnetic field or outflows.

Current evidence for pre–Main Sequence Herbig Ae/Be stars suggests the transition in disc accretion mechanism occurs around the A–B spectral type boundary

(Mottram *et al.* 2007b, Ababakr *et al.* 2017). One of the few models put forward to explain the accretion mechanism in massive Herbig Be stars is the boundary layer where the circumstellar disc extends to the surface of the central star. For example, through modelling the UV spectra of a sample of Herbig Ae/Be stars, Blondel & Djie (2006) suggested these intermediate to massive stars could be accreting via a boundary layer.

Next to the theoretical considerations, massive star formation poses a considerable observational challenge due to the rarity and amount of dust extinction in massive prestellar objects. The Massive Young Stellar Object phase (MYSO) offers a unique opportunity in understanding massive star formation. An overview of the class of MYSOs can be found in 1.4.2.

Near–infrared (NIR) techniques can be particularly useful to study the inner 100s of au of MYSOs, where an accretion disc is expected to be found. This can be traced with transitions such as the CO ro–vibrational lines ('bandheads') at 2.3μm (Ilee *et al.* 2013) or the fluorescent FeII line at 1.687 μm (Lumsden *et al.* 2012). Stellar winds are traced by hydrogen recombination lines, particularly the Brackett series (Simon *et al.* 1981). The hydrogen recombination profiles provide clues about the line emitting region (Drew *et al.* 1993). This is possible due to the difference in the optical thickness of the various lines.

Thus far, the NIR spectrum of MYSOs has been studied either in small samples at high spectral resolution, but small wavelength coverage (e.g. Ilee *et al.* 2013 observed a dozen objects at $R \sim 30,000$ across CO 2.3 μm; Blum *et al.* 2004 observed 4 MYSOs at $R \sim 50,000$ across the same region; Bik *et al.* 2006 studied 20 MYSOs in the K–band (between 2.08–2.18 and 2.28–2.40 μm) at $R \sim 10,000$) or in large samples of low resolution at broader wavelength coverage (e.g. CLO13 observed around 250 objects at $R \sim 500$ in H and K).

In this chapter I present medium resolution (R$\sim$ 7000) near–infrared spectra of 36 MYSOs selected from the RMS catalogue described by Lumsden *et al.* (2013). This is the largest NIR spectral sample of MYSOs at this resolution studied in this manner to date. The resolution allows for studies of the line profiles and for the detection of fainter features when compared to the lower resolution observations while the larger wavelength coverage allows for the study of a range of lines with varying excitation properties. This type of analysis offers insights into the circumstellar environment of MYSOs. Specifically, massive protostars are compared to their intermediate and low–mass counterparts and to predictions of theoretical models. The work in this chapter provides clues to the type and strength of accretion processes taking place in MYSOs, as well as to the resulting winds and outflows. In addition, the spectral type of at least one MYSO is determined, and compared to predictions from simulations.

Section 3.2 describes the sample, observations, and data reduction. The photometry methods used are described in Section 3.3. In Section 3.4 I present an assessment of dust extinction. The contribution of the dust excess is analysed in Section 3.5. Sections 3.6 – 3.9 contain the main analysis of this study: MYSO spectral type measurements, correlations between different line luminosities and features of the H recombination line profiles. Also included is an investigation into the effect dust excess and the intrinsic photospheric absorption lines on HI emission line ratios in 3.9.4. In section 3.10 I present the conclusions of this research. A spectral atlas with line parameters can be found in the Appendix C. Plots of the spectra are available in the Appendix D.

3.2 Observations

The data were obtained between 18 February and 23 July 2011 using the NIR spectrograph GNIRS on the Gemini–North telescope. 36 objects were observed over 20 nights in service mode. The cross–dispersed mode was used, coupled with the 'short' 111 l/mm camera, and a 2 pixel wide slit. Each pixel is 0.15", giving a slit width of 0.3" and length of 7". The average seeing was 0.75". Since the objects are bright at K, the data were taken as a bad–weather programme. As such, the conditions were not photometric. The observed wavelength ranges are set up in orders and centred around the positions of the K, H, J and X photometric bands. The K–band ranges between 2.1472 and 2.3355 μm, the H–band between 1.6107 and 1.7519 μm, the J–band between 1.2888 and 1.4017 μm and the X–band between 1.0741 and 1.1682 μm. These and the following wavelengths for spectral lines are in vacuum. Because the sources are red, the photon count and thus the SNR is highest at longer wavelengths.

Most of the observed sources were selected from the RMS database (Lumsden *et al.*, 2013). Two objects (G106.7968 and G213.7040) are not in the RMS database as they are located at a high galactic latitude, and hence not covered by the MSX satellite, but they are still interesting for the purposes of this survey. For these, the distance and bolometric luminosity are taken from Simon *et al.* (1981). The selection criteria included source classification as MYSO, observability from Gemini–N, and being bright enough at K to result in good SNR spectra at these wavelengths.

Emphasis was put on obtaining data from the most luminous objects fulfilling those criteria. All observed targets have bolometric luminosities of L>3000 $L_{\odot}$ and radio flux<0.5 Jy at 5 GHz. In addition, most (90%) of the observed objects are very bright (L>8000 $L_{\odot}$) and radio–quiet. As such, the MYSOs studied here have likely not yet started to ionise the ISM and produce an HII region (see Section 3.9.3 for a discussion on this). The sample properties are described in the Table 3.1.

Most of the targets are compact enough to allow nodding along the slit in an ABBA sequence to remove the sky background. For extended sources a sky region outside of the nebula was used. Spectra of nearby stars of spectral types B9V–A4V were obtained in order to correct for atmospheric telluric absorption. The airmass difference between these and the science targets was always less than 0.1. Stars with these spectral types were used as they have few intrinsic absorption features in the wavelength ranges of interest to this work. Where necessary, their intrinsic HI absorption features were fitted and removed prior to telluric line correction. A standard reduction procedure was applied to all the spectra, using the *PyRAF* package (Science Software Branch at STScI 2012). The bias and dark subtraction are done in the pre–reduction phase at the telescope. Pixel–to–pixel variations were corrected for by using flat–field frames. The sky background was removed with the standard ABBA subtraction. One–dimensional spectra from each order were then extracted.

Table 3.1: Source list, including date, exposure time, position angle of the slit and known properties. 1 –Magnitudes from 2MASS; 2 – extinctions from H–band continuum slope derived in this work; 3 – LSR velocities from Urquhart *et al.* (2011b); distances from Urquhart *et al.* (2011a), they carry an uncertainty of order 1 kpc; bolometric luminosities calculated by Mottram *et al.* (2011b); uncertainties on bolometric fluxes are of the order 20%, combined with distance uncertainties they result in errors in bolometric luminosity of order 10^4 L$_\odot$. * – sources not in RMS database, distances and luminosities from Simon *et al.* (1981). ** – As the binarity of G110 is a new discovery and the slit was oriented E–W, one cannot accurately pinpoint the declination of the two objects. I believe the distance between them to be no more than 0.75" as given by the seeing. Luminosities, distances and LSR velocities for visual binaries given as for the whole system.

Date (2011)	RMS name	Exp. (s)	RA (J2000)	Dec. (J2000)	PA	m_J^1	m_H^1	m_K^1	A_V (mag)^2	$V_{\rm LSR}$ (km/s)^3	Dist. (kpc)	L_{bol} (10^3L$_\odot$)^5	Other name
20.04	G010.8411-02.5919	960	18:19:12.10	-20:47:30.90	90	16.3	13.2	9.7	55±3	12.3	1.9	24	GGD 27
29.06	G010.8856+00.1221	960	18:09:08.00	-19:27:24.00	90	15.6	12.9	9.6	51±4	19.7	2.7	5.5	
16.05	G012.9090-00.2607	960	18:14:39.60	-17:52:02.30	60	15.3	13.2	9.2	30±3	36.7	2.4	32	W33A
16.05	G014.9958-00.6732	64	18:20:19.50	-16:13:29.80	90	12.7	9.8	7.3	39±14	19.4	2	13	M17SW IRS1
29.06	G015.1288-00.6717	480	18:20:34.60	-16:06:28.20	90	12.9	10.5	8.9	25±2	19	2	12	
29.05	G017.6380+00.1566	64	18:22:26.40	-13:30:12.00	90	15	12.7	7.3	93±3	22.1	2.2	100	AFGL 2136
18.06	G018.3412+01.7681	960	18:17:58.10	-12:07:24.80	0	15.3	12.9	9.3	53±7	33.1	2.8	22	
9.07	G023.3891+00.1851	304	18:33:14.30	-08:23:57.40	90	15.8	11.6	8.4	47±3	75.5	4.5	24	
16.07	G025.4118+00.1052_A	480	18:37:16.90	-06:38:29.80	90	17.2	15.7	12.9	61±1	95.3	5.2	9.7	
23.07	G026.2020+00.2262	456	18:38:18.50	-05:52:57.40	90	14.2	10.6	8.3	37±4	112.4	7.5	3.6	
20.07	G026.3819+01.4057_A	480	18:34:25.70	-05:10:50.20	90	13.1	10.8	9.1	33±6	42.1	2.9	17	
22.07	G027.7571+00.0500	960	18:41:48.00	-04:34:52.90	90	16.7	13	9.3	59±16	99.6	5.4	13	
29.06	G029.8620-00.0444	960	18:45:59.60	-02:45:06.50	50	15.1	12.5	9.8	43±5	101.2	4.9	28	
20.05	G030.1981-00.1691	960	18:47:03.10	-02:30:36.10	90	17	12.6	9.3	53±4	103.1	4.9	30	
20.05	G033.3891+00.1989	64	18:51:33.80	00:29:51.00	90	13	9.6	7.2	33±4	85.3	5	13	GGD 30 IRS 3
20.07	G033.5237+00.0198	960	18:52:26.70	00:32:08.90	90	15.8	12	8.9	45±4	103.5	7	13	

22.07	G034.0500-00.2977_A	304	18:54:31.90	00:51:32.60	90	14.1	12.2	11	11±3	11.5	12.9	23	
22.07	G034.0500-00.2977_B	304	18:54:32.30	00:51:33.20	90	11	9.6	8.4	21±4				
23.07	G034.7123-00.5946	960	18:56:48.30	01:18:47.10	90	18.4	13.4	9.2	59±4	44.5	2.9	9.7	
22.04	G056.4120-00.0277	160	19:36:21.50	20:45:17.90	90	12.5	9.9	8.1	31±2	-4.4	9.3	22	
10.06	G073.6525+00.1944	960	20:16:22.00	35:36:06.20	55	13.9	11.5	9.6	31±7	-73.4	11.2	100	
25.06	G073.6952-00.9996	120	20:21:18.90	34:57:50.90	0	12.9	10.6	8	47±5	-31.3	7.4	17	
16.07	G076.3829-00.6210	24	20:27:26.80	37:22:47.70	90	10.4	7.7	5.9	31±5	-1.7	1.4	40	S106 IRS1
10.06	G077.4622+01.7600_A	480	20:20:39.30	39:37:58.50	150	12.8	10.6	8.9	39±4	2.1	1.4	3.1	
24.06	G078.8867+00.7087	40	20:29:24.00	40:11:19.40	0	14.3	10.8	6.6	65±2	-6	3.3	200	AFGL 2591
23.06	G094.3228-00.1671	960	21:31:45.10	51:15:35.30	90	15.4	12	9.8	47±18	-38.4	4.4	5.7	CPM 15
16.07	G094.6028-01.7966	48	21:39:58.30	50:14:20.90	90	10.9	9.2	6.8	29±3	-43.9	4.9	43	V645 Cygni
21.07	G102.3533+03.6360	48	21:57:25.20	59:21:56.60	90	12.3	9.6	7.2	39±2	-88.6	8.4	110	CPM 36
22.07	G106.7968+05.3121*	24	22:19:18.20	63:18:47.00	64			8.1	6.1	59±1	0.9	13	S140 IRS1
21.07	G110.1082+00.0473B_A	480	23:05:10.20	+60:14:42.7**	90	10.7	10	10.1	3±3	-52.1	4.3	17	
21.07	G110.1082+00.0473B_B	480	23:05:10.30	+60:14:42.7**	90	9.8	9.5		3±1				
26.06	G111.2348-01.2385	960	23:17:21.00	59:28:48.00	10	14.1	11.3	9.6	73±3	-54.4	4.4	42	
21.07	G111.5234+00.8004A	96	23:13:32.40	61:29:06.20	45	11.1	9.7	7.8	35±3	-58.6	2.6	5.6	NGC7538IRS4
25.06	G111.5423+00.7776	200	23:13:45.40	61:28:10.30	80	14.6	11.6	8.5	91±3	-57.2	2.6	210	
21.07	G120.1483+03.3745	48	00:23:57.00	66:05:51.50	90	11.8	9	7	33±4	-68.9	5.6	21	CPM 1
18.02	G151.6120-00.4575	48	04:10:11.90	50:59:54.40	90	10.9	8.9	7.1	27±3	-49.7	6.4	61	CPM 12
18.02	G213.7040-12.5971_A*	80	06:07:47.80	-06:22:56.20	14	13.1	11.4	7.2	31±2	0.95		25	MonR2IRS3A
18.02	G213.7040-12.5971_B*	80	06:07:47.90	-06:22:55.40	14	9.5	7.3		31±2				MonR2IRS3B
18.02	G233.8306-00.1803	24	07:30:16.70	-18:35:49.10	60	10.9	8	6.1	35±14	44.6	3.3	13	

Argon lamp spectra and telluric absorption lines from the solar spectrum of Hinkle *et al.* (1995) were used to perform the wavelength calibration. The resulting calibration was assessed by measuring the wavelengths of telluric lines. The wavelength calibration was found to be accurate to ∼5 km s^{-1}. The resolution of the spectra as measured from the arc calibration lines is in the range 35–49 km s^{-1}, corresponding to R≈7000. The K and H–band spectra have high SNR (>100 for most spectra), while 66% of the J and 50% of the X–bands have SNR>30.
The intrinsic absorption features of the telluric standards were removed by using Voigt profiles. This proved particularly difficult for the Br10 line at 1.737 μm, as a number of telluric lines are blended with this HI line. As such this recombination line was not used in the analysis. The calibrated target spectra were then divided by the telluric standard (with the intrinsic features removed), in order to remove the atmospheric absorption features. The result is multiplied by a blackbody of the temperature of the telluric standard star to retrieve the relative photometric shape of the target spectra. The spectra were not obtained in photometric conditions, as accurate flux calibration was not the main aim of the observations.
I measured wavelength shifts of line centres of the Brackett transitions from laboratory wavelengths. These shifts can then be transformed to observed velocities, and then to LSR velocities, using the PyRAF routine *rvcorrect*. I compare these to values from the RMS database deduced from mm NH_3 observations, as reported by Urquhart *et al.* (2011b). The velocity from the Br12 line is shown in Figure 3.1. The deduced LSR velocities agree very well with the RMS LSR velocities, with a Pearson correlation factor of 0.89. The other recombination lines yielded similar results. This shows that the NH_3 gas does indeed trace material associated with the MYSO.

3.3 Photometry

In order to determine whether the quality of the spectra allows for flux calibration, the following tests were performed. The continuum level counts in the spectra (normalised by exposure time) should reflect the flux density $F_\lambda = F/\Delta\lambda$.

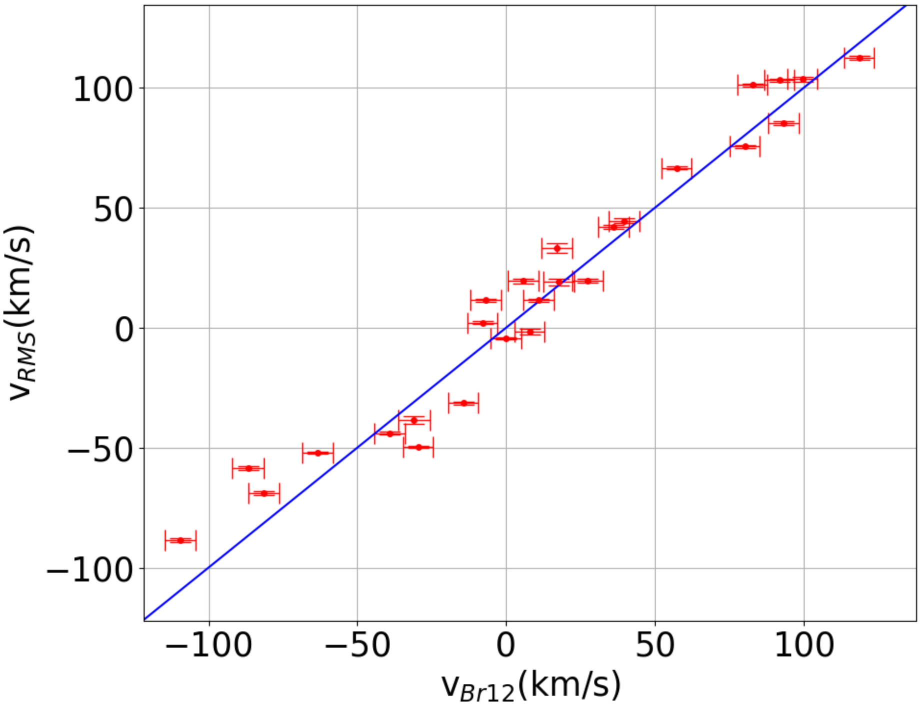

Figure 3.1: Plot of deduced LSR velocity from the Br12 line against LSR velocity from Urquhart *et al.* (2007a). A 1–1 correlation is also included.

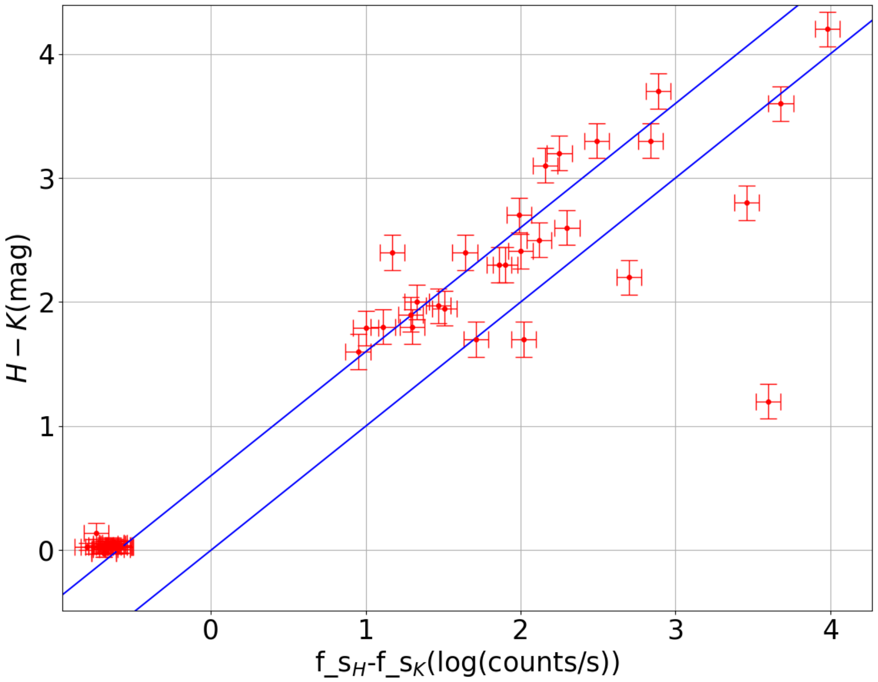

Figure 3.2: Plot of $H-K$ colour as a function of normalised H/K–band counts for MYSOs and telluric stars in the sample. A 1–1 correlation, as well as a $H-K$=(f_s$_H$–f_s$_K$)+0.6 line are also included (in blue).

As such, the quantity f$_s$=–2.5log(counts/t$_{exp}$) should be proportional to the photometric magnitude of an object in a given band. However, when plotting f$_s$ as a function of 2MASS magnitude in a given spectral band, I found that the gradient and intercept of the best fit for MYSOs in a given band vary from one night to another. There was no photometry solution that reconciles both the telluric stars and the MYSOs. The reason for the low spectrophotometric quality of the data is probably the observing conditions, the spectra having been taken under a bad weather program.

I carried out a similar test to determine whether ratios between counts in different bands can be used to estimate colours, comparing f$_{sH}$–f$_{sK}$ to m$_H$–m$_K$, where the catalogue magnitudes are taken from 2MASS. There is good agreement between these two quantities for MYSO and telluric standard stars (see Figure 3.2). The telluric stars are located in the bottom left part of the plot, close to $H-K$=0.

As they are MS stars, their magnitudes are accurately known. The SNR of the telluric spectra is high as they were bright, and so their count ratios closely agree with the colours. The MYSOs show a much larger spread from the line of best fit, but they do correlate well with each other and with the values from the telluric stars. In conclusion, the count ratios of MYSOs can be used to estimate colours to an accuracy of 0.6 mag.

Also, the MYSO magnitudes were estimated by comparing their spectral counts with those of a telluric standard star in a given band. As the magnitude of the telluric star is generally known more accurately, this can be used to estimate the MYSO magnitude. Comparison between magnitudes estimated in this manner and catalogue values show good agreement, within 0.5 magnitudes.

The fact that relative count rates return fairly good estimates of the colours allowed for the calculation of continuum fluxes of MYSOs in the X–band (1.09 μm). A scaling factor between X and J was derived from the relative count rates in the science targets. This was then compared with the respective $X - J$ colour of the telluric standard stars (whose continuum flux at 1.09 μm were obtained by interpolating between their fluxes at the J and I photometric bands). The MYSO X–band spectra were then scaled at the given 2MASS central band wavelengths.

I used 2MASS photometry to scale the flux counts of the MYSOs in this sample to known catalogue magnitudes. UKIDSS (Lucas *et al.*, 2008b) was also considered, but using photometry from this survey results in an discontinuous spectrum between different orders for a large fraction of the sample. The reason for this is the sensitivity of the UKIDSS survey. Many of the targets have $m_K < 10$, which often leads to saturation in UKIDSS. Where 2MASS data was not available, the MYSO magnitudes were estimated from the telluric star magnitude, with the caveat that the fluxes carry large error bars – 0.5 magnitudes in the K–band.

I conclude from these tests that whilst the spectral counts in one band cannot be used on their own to estimate magnitudes and fluxes reliably, making use of the ratio between the MYSO counts and the telluric standard stars results in a reasonable estimate. Also, ratios between different bands of the same object are a good estimate of the colour. Where 2MASS data was not available, ratios of counts between the MYSOs and their respective telluric standards were converted to magnitude differences, and the MYSO magnitudes were estimated from the telluric star magnitudes. The spectra were scaled at the given 2MASS central band wavelengths.

3.4 Extinction

The determination of the dust extinction to the target objects, and the subsequent correction for it, are problematic in the case of MYSOs. As explained in the introduction, these regions are considerably affected by dust. In the sample of CLO13 of 135 MYSOs, the extinctions found ranged between 2.7<A_V <114.

3.4.1 From NIR colours

The first method for calculating the extinction follows the description of section 3.5 of CLO13 which was applied for the AAT sample in the previous chapter (see Section 2.4). Intrinsic near–IR colours of MYSOs are approximated to those of a B0 star, which are given by Koornneef (1983) as $J-H$=–0.12 and $H-K$=–0.04. By comparing observational colour indices (from 2MASS) with intrinsic colours, the extinction at the V–band (A_V) can be deduced.
A_V was calculated from $J-H$ and $H-K$ colours, and a plot of one against another for objects in the sample is shown in Figure 3.3. It is clear that the plot is not consistent with A_{HK}=A_{JH}, or indeed with a straight line fit. The reason why different values are expected for the extinction from the two different colours is, as was explained by Porter *et al.* (1998), that the K–band flux is strongly affected by dust excess, while the J and H by scattering. This causes extinction estimates from the $H-K$ colours to be significantly overestimated, as shown by Figure 3.3.
Another possible explanation for the departure from the 1–1 correlation is that the assumption of an MYSO being comparable to a B0 main–sequence star does not hold. From the simulations of Hosokawa *et al.* (2010), it was found that that MYSOs may actually swell up due to accretion. This may cause them to have a configuration similar to a red giant star rather than a main–sequence star, and so also a different intrinsic colour. Koornneef (1983) gives intrinsic red giant colours

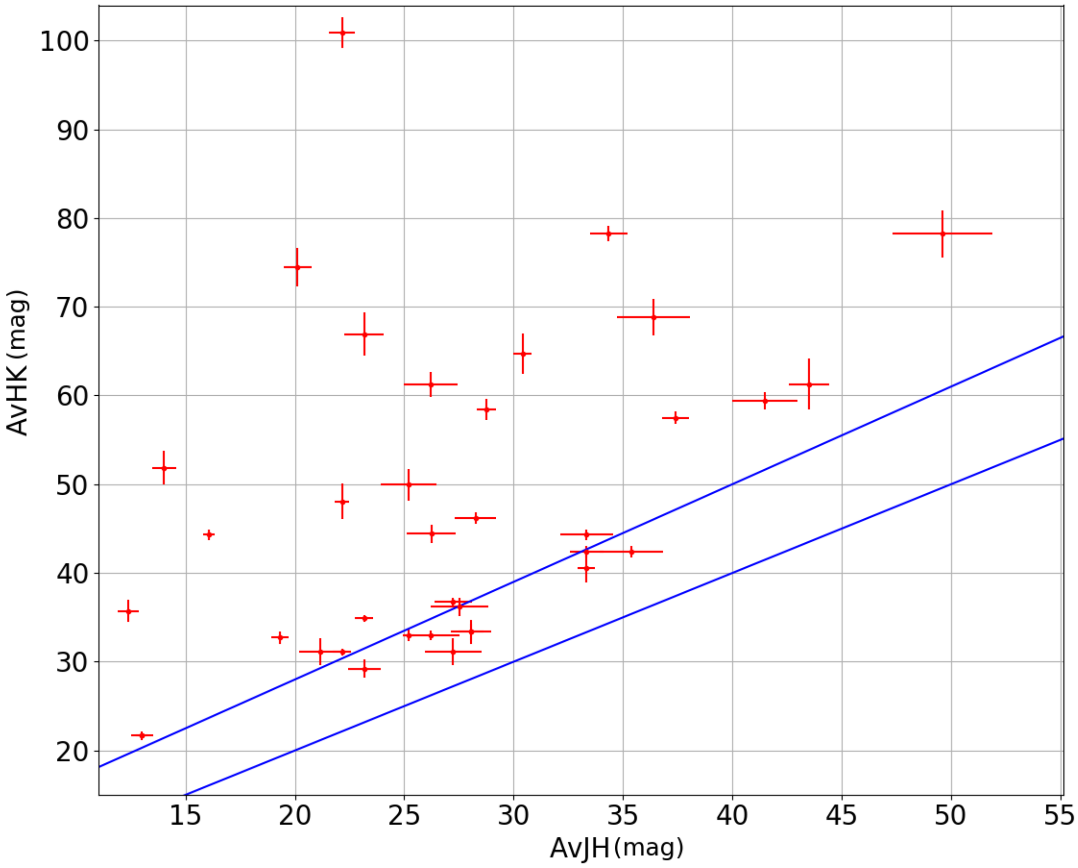

Figure 3.3: Plot of extinction obtained from $H - K$ vs from $J - H$. The straight lines are the best fit of CLO13, (A$_{VHK}$=1.1 A$_{VJH}$+6) as well as A$_{VHK}$= A$_{VJH}$

of $J-H$=0.65 and $H-K$=0.15. However, using red giant rather than B0 colours will not cause the extinctions from $J-H$ and $H-K$ to agree.

In addition, the emission may not only arise from the central star itself. A significant fraction of the light in the NIR may come from an accretion disc, which is not taken into account when calculating A_V in this manner.

Finally, NIR colours may also be affected by variability. During an accretion burst, large quantities of dust may be heated up, resulting in strong dust excess, causing the $H-K$ colour index to appear redder. Also, strong outflows resulting from intense accretion, could result in the MYSO to appear less embedded, and hence the NIR colours to be bluer.

3.4.2 From line flux ratios

Another method for determining extinction makes use of the ratio of fluxes of hydrogen recombination lines present in the data, as shown by Porter *et al.* (1998). The calculated fluxes of the HI lines are normalised to a percentage of the Brγ flux. The flux of the Brγ line can then be predicted from each of the other HI transitions by using the theoretical case B ratios given by Hummer & Storey (1987), assuming that the gas producing the lines is optically thin. Due to extinction affecting bluer wavelengths stronger, the predicted Brγ flux will be most underestimated at short wavelengths. The predicted Brγ fluxes should lie on a straight line when plotted against $(\lambda/0.6)^{-1.7}$ (the reddening law A_λ/A_V), if the optically thin assumption holds. The gradient of this line will be –0.4A_V (the factor of conversion from flux to magnitude). The survey of Porter *et al.* (1998) and the Gemini data set have one object in common – G014.9958–00.6732, or M17SW IRS1. As such, I attempt to reproduce their results, but normalising fluxes to Brγ (rather than to Brα as Porter *et al.* 1998 had done), as it is the longest wavelength HI line in the sample. However, the Porter *et al.* (1998) survey covered a larger wavelength range and so had a larger number of H recombination lines available (Brγ, 10–12, 16–18 and Paγ, β, δ) whereas the GNIRS data only shows Brγ, 10–12 and Paγ, with the latter only for a limited number of objects (there is no X–band data so no Paγ for G014.9958). By using the fluxes available for G014.9958 from the GNIRS data (Brγ, 10, 11 and 12), the extinction obtained is A$_V$=2.8 mag. Porter *et al.* (1998) deduced a value of A$_V$=26.4 through this method for M17SW IRS1. However, by using their data for just Brγ, 10, 11 and 12 (the lines available in the GNIRS data), the predicted extinction will be A$_V$=1.6 mag. This shows that Paschen lines are necessary for accurate use of this method. This is similar to the findings of Porter *et al.* (1998). They suggest that this is due to the optical thickness being higher than what is predicted under the case B assumption.

Figure 3.4 also highlights this problem. G056.4120–00.0277 is an object that shows emission in Brγ, Br 10–12, as well as Paγ. When taking into account just the Brackett series HI lines, the extinction is 1.58 mag at V, much lower than the average MYSO A$_V$ value. Adding Paγ to the analysis results in an extinction value of 25.0 mag. By comparison, the extinction for this object from the H–band continuum slope is found to be A$_V$=31.3±0.7 mag.

I apply this method to all the objects in the sample with data in the K and H–bands. The results are displayed in Figure 3.5, compared to the extinctions from the H–band continuum slope, determined as detailed in the following paragraph. The extinctions determined with this method are likely incorrect, as a large number of them are negative, or much lower that what is expected from the continuum slope, or indeed the NIR colours method. This is likely due to the fact that the optically thin approximation is not necessarily accurate for a number of sources in the sample (see Figure 3.12). Also, the wavelength range covered is not large enough, so Paschen transitions which are needed to constrain the value of A$_V$ more accurately are lacking for many sources.

3.4.3 From continuum slope

I also estimate the extinction using the continuum slope of the spectrum, in a similar manner to Porter *et al.* (1998). The spectra of MYSOs show a rising red continuum, which is caused by a combination of reddening of the stellar photosphere by dust extinction on the one hand and thermal emission by dust on the other hand. Martin & Whittet (1990) derive that $A_\lambda \propto \lambda^{-1.8}$ between

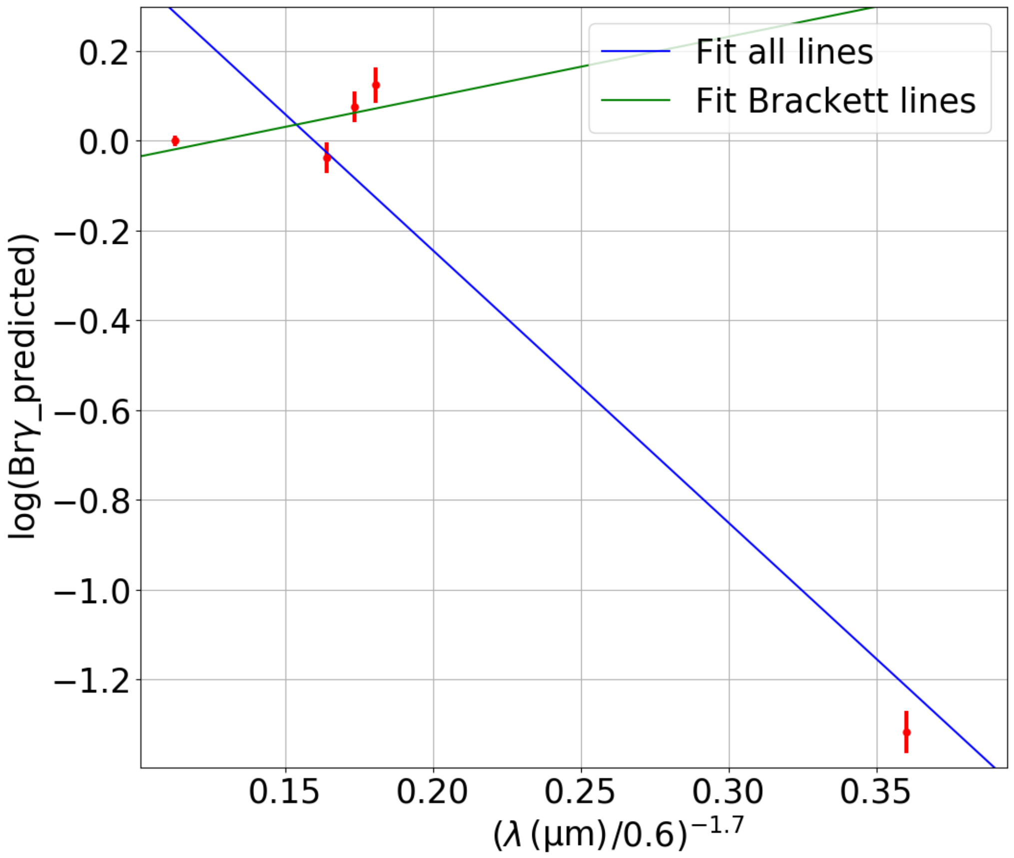

Figure 3.4: Plot of predicted line fluxes for Brγ (obtained under the assumption of case B optically thin gas) against the extinction law for G056.4120–00.0277. The points are obtained from Brγ, 12, 11, 10 and Paγ from left to right. The two straight lines are extinctions A_V=–3.35 and 15.25 mag (corresponding to slopes of 1.34 and –6.07 respectively). They are best fits from using just K and H–band transitions (green, first four data points) and K, H and X lines (blue, all the data points). It is obvious that the absence of the Paγ line affects the resulting extinction significantly.

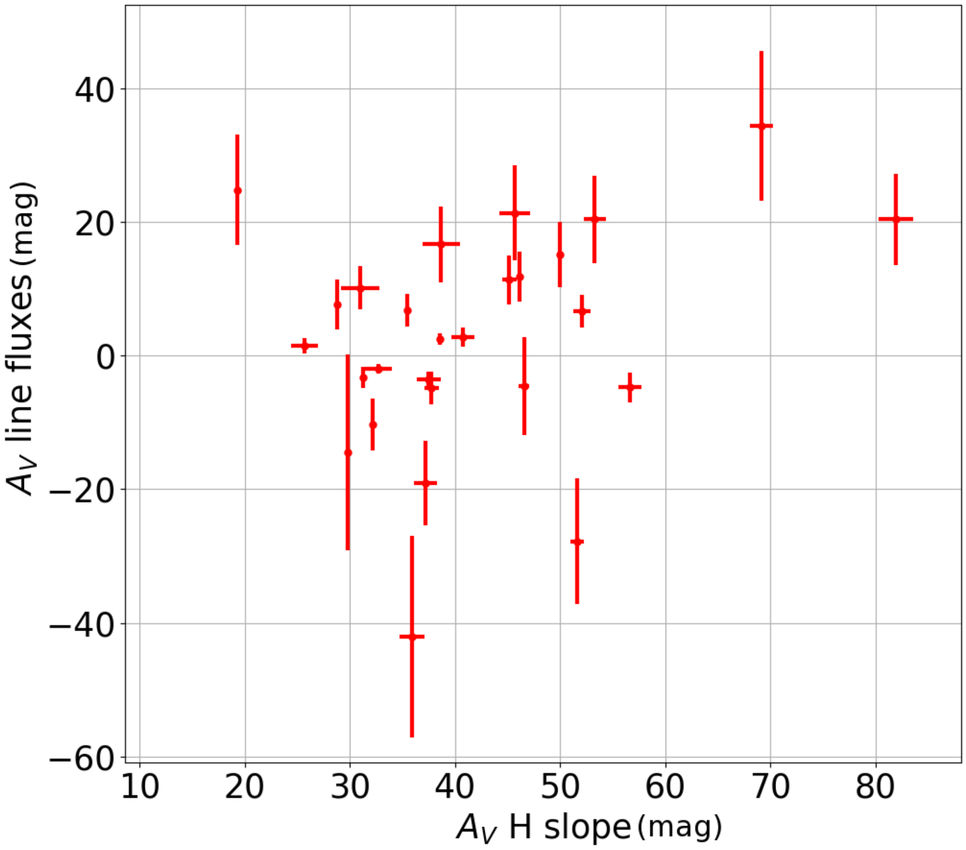

Figure 3.5: Plot of extinctions from predicted Brγ fluxes against extinctions from the H–band continuum slope. Most of the values for the extinction from line fluxes are negative, or low. The correlation factor is also low, 0.31, showing the disagreement between the two methods.

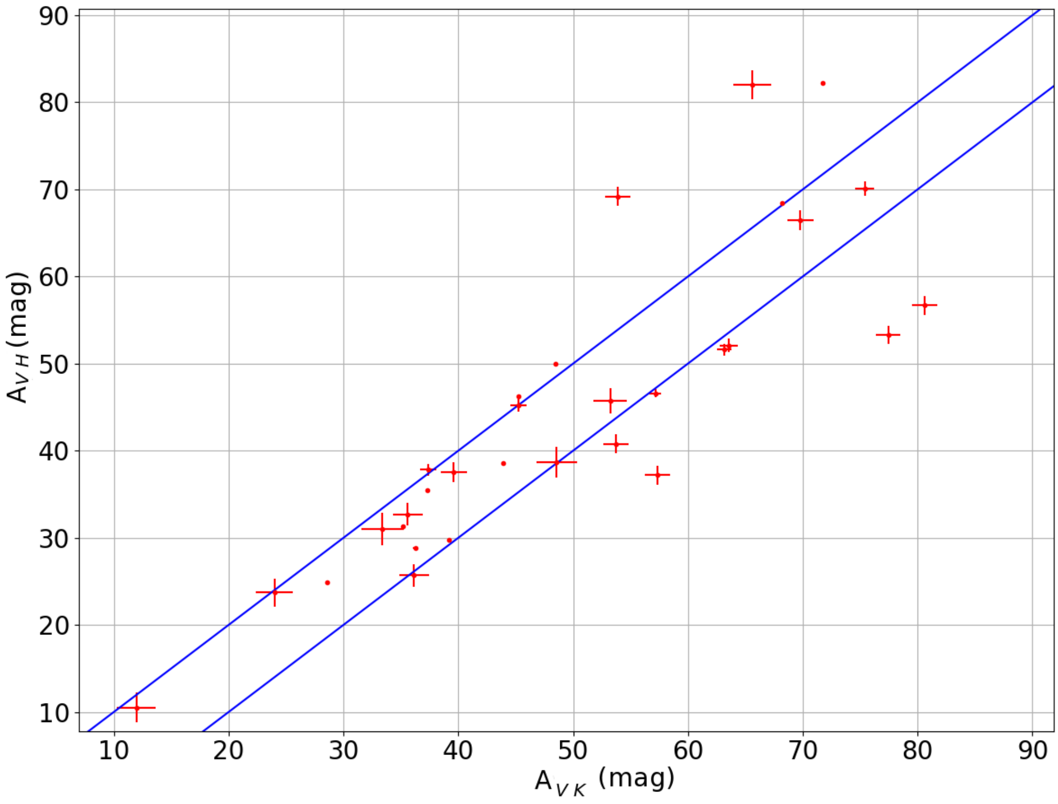

Figure 3.6: Extinction obtained from H−band continuum shape against that from K−band continuum shape. The straight lines are A_{VH}=A_{VK} and A_{VH}=A_{VK}−10

1–4μm (see also Moore *et al.* 2005 for the case of high A_V). The Rayleigh–Jeans (RJ) approximation can be used for a blackbody at NIR wavelengths, i.e. $F_\lambda \propto \lambda^{-4}$. I determine the value of the extinction that produces a dereddened spectrum with a slope closest to that of the RJ approximation through chi–squared minimisation. This gives values for A_V from each of the spectral bands of an object. The errors are determined from the chi–squared analysis. The K–band yields the highest value for A_V. This is most likely due to dust emission starting to contribute significantly at these wavelengths. Porter *et al.* (1998) demonstrated that extinctions derived from the continuum slope at the shorter J and H–bands are in agreement with those from the line fluxes of the hydrogen lines assuming case B recombination. Most of the sources in this sample are too embedded to be detected in the X or J–bands, or spectra in these two shortest wavelength bands have too low an SNR for extinction estimations from the continuum slope.

As the spectra are cross–dispersed, results from the K and H–band continuum slopes are well correlated, with a Pearson correlation factor of 0.85 (see Figure 3.6). This indicates that for this data set, this method produces similar results when using data from different bands, unlike the extinctions determined from NIR colours. However, as the effect of hot dust excess is strongest in the K–band, most objects are closer to the A_{VH}=A_{VK} – 10 line than to the 1–1 correlation.

The line flux ratio method requires a wider range of spectral lines than available in this survey for accurate results. Using the NIR colours produces different results depending on which photometric colours are used. In addition, quite a few of the sources in this sample are inconsistent with the optically thin approximation, as a plot of Br12 vs Brγ line luminosity shows (Figure 3.12). However, the values of A_V deduced from the slope of continuum in different bands produce results that agree with one another. I therefore choose to use the extinction obtained from the spectral slope of the H–band continuum in all of the following analysis, as the effect of hot dust excess is considerably lower than in the K–band. The values are listed in Table 3.1.

3.5 Dust excesses

Another way through which dust affects MYSO spectra is excess emission from hot dust. The excess will affect spectral energy distribution, as well as the strength of photospheric stellar lines. As such it is important to obtain an estimate for the strength of the excess.

Just as with dust extinction, the parameters that influence the amount of excess are not readily determined from observations. Hence, SED modelling techniques were employed. I chose the object S106 IRS1 (G076.3829 in the RMS denomination) as the starting point of the investigation, a well studied MYSO (see Drew *et al.* 1993) at a high inclination (∼80°). Observational fluxes were fit with the command line tool developed by Robitaille *et al.* (2007). The predictions of these models were then used with the Hyperion package (explained in Robitaille 2011) in order to separate the dust and stellar contributions to the observed emission.

The results of the best fitting model at 80° are presented in Figure 3.7. Because of the inclination, the direct stellar emission is practically invisible (∼30 orders of magnitude lower than the other components). The strongest component of the observed emission comes from scattered stellar photons at less that 1 μm (in green in Figure 3.7), direct dust emission at longer than 4 μm (red), and scattered dust emission at 1–4 μm (yellow). The value of the excess can be determined from the Hyperion results directly, as the total dust emission divided by the total stellar (source in the plots) emission. The total dust emission is the sum of the direct and scattered dust emission components, and the total stellar emission is, similarly the sum of the direct and scattered stellar emission components. The strength of the excess is 0.05 × the continuum at H and 3.6 in the K–band for the best fitting model. It is worth noting that this best–fitting model predicted that the MYSO has no accretion disc. The next best fitting model (which had a similar chi–squared to the best fit, but unlike the best fitting model also had a disc component) gave 76 × the continuum at H and 250 in K. In conclusion, the SED fits suggest the excess is either high at both H and K or low at K and almost zero at H. I will come back to these measurements later, in Section 3.9.4.

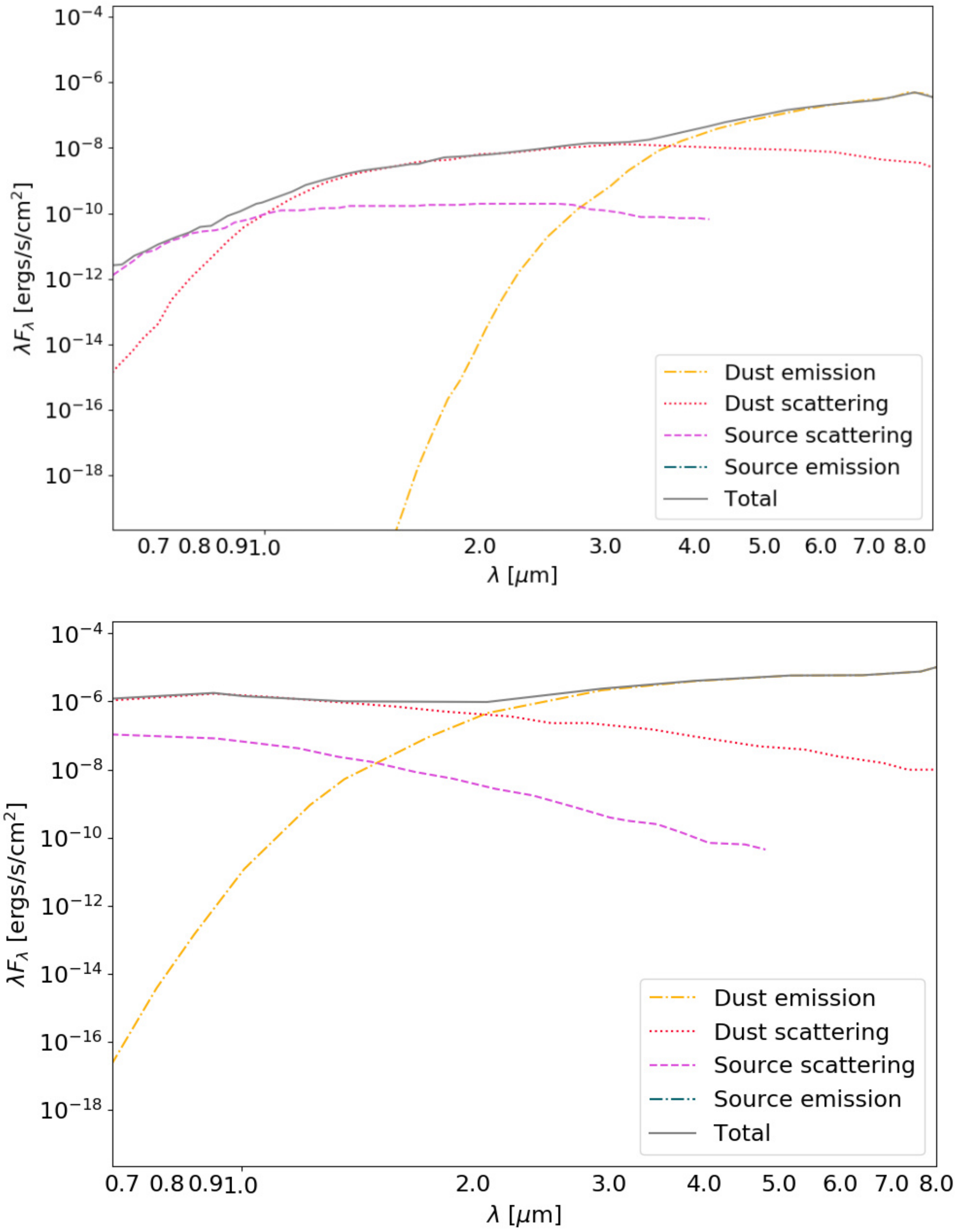

Figure 3.7: Hyperion simulation of the SED of S106IRS1, at an inclination of 80^o, between 0.6–10 μm, for the disc–less model (top) and disc model (bottom). The dust emission and scattering components are displayed in the yellow dot–dashed line and red dotted line, respectively, and the stellar scattering in the pink dashed line, with the source emission in dot–dashed dark green. The grey solid line represents the total emission.

3.6 Description of spectra

I have compiled an atlas of the spectral features found in the data (presented in Appendix C). A spectral line is considered a detection if it has a peak flux $F_\lambda > 3\Delta F_{cont}$, and a full–width half–maximum larger than the resolution limit. ΔF_{cont} is given by the root–mean–square variations of the continuum counts. Most of the continuum normalised lines were fitted with Gaussian profiles, which provided similar results to the integration of line profiles. The only exception was the CO bandhead emission, for which fluxes were measured by integrating the profile.

An example spectrum, of G056.4120–00.0277, is presented in Figure 3.8. The HeI transition at 1.083μm, as well as the Paγ hydrogen recombination line at 1.094 μm are present in the X–band. Strong telluric absorption hinders the detection of spectral lines in the red part of this band. Strong telluric absorption also minimises the use of the J–band past ∼1.35μm. The only J–band transitions in the observable range are the OI line at 1.316μm, which is seen towards some sources, as well as a strong Diffuse Interstellar Band (DIB) absorption at 1.318μm. The H–band spectrum is marked by three strong Brackett series transitions – 12–4 at 1.641 μm, 11–4 at 1.681 μm and 10–4 at 1.737μm. A number of Fe transitions are also present, such as the shocked [FeII] transition at 1.644 μm, the fluorescent FeII transition at 1.687 μm, as well as another FeI line at 1.711 μm. The strongest feature in the K–band is the Brγ line at 2.166 μm. Other transitions observed in the K–band are the NaI doublet at 2.206 and 2.209 μm, and the shocked H_2 transition at 2.24 μm. The strongest H_2 transition at 2.12 μm is unfortunately not covered in the GNIRS cross–dispersed mode. Finally, the first two CO first–overtone bandhead transitions, located at 2.29 and 2.32 μm are also observed.

The detection rates of various lines are presented in Table 3.2. Virtually all objects have Brγ in emission. The detection rate of the higher series Brackett lines is slightly smaller, which can be attributed to the fact that these lines are intrinsically weaker, and therefore harder to detect.

Overall, the detection rates of HI recombination lines and fluorescent FeII are higher than in CL013 and the AAT sample of Chapter 2. This can be explained by the superior spectral resolution employed here, facilitating the detection of

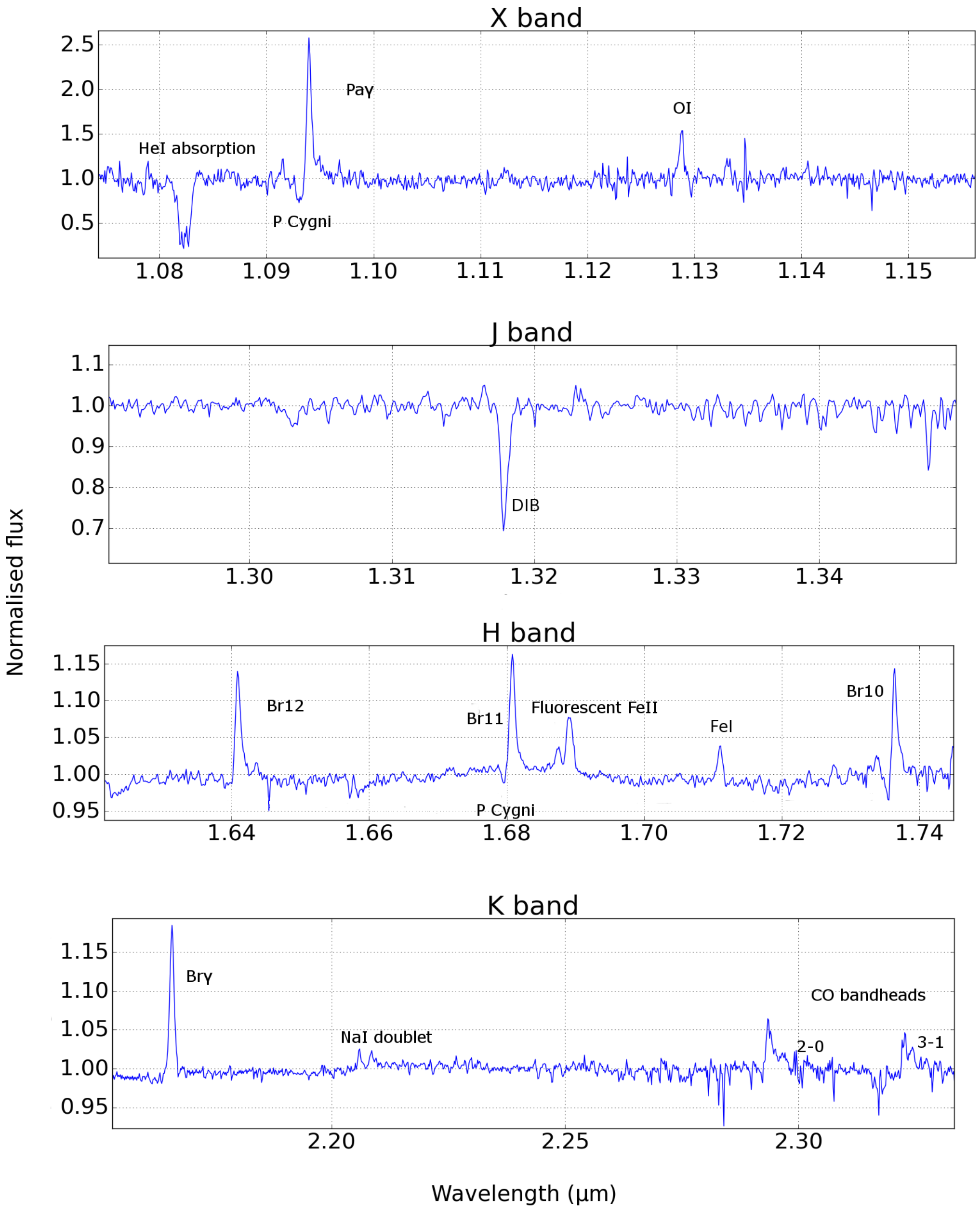

Figure 3.8: Example spectrum of G056.4120–00.0277, continuum normalised. From bottom to top, the data correspond to the *K*, *H*, *J* and *X*–bands respectively.

Table 3.2: Detection rates of various features observed in the sample, compared to their respective values in the CLO13 survey. A number of the transitions were not detected in the previous survey. The higher spectral resolution allows for fainter lines to be detected.

Spectral line	Brγ	Br12	Br11	Br10	Paγ	H2	NaI	CO
Wavelength (μm)	2.166	1.641	1.681	1.737	1.094	2.240	2.206	2.295
Detection rate	97%	82%	79%	79%	26%	21%	37%	34%
CLO13 rate	75%	44%	37%	45%	N/A	9%	N/A	17%
AAT rate	83%	63%	63%	63%	N/A	30%	9%	12%

Spectral line	[FeII]	fl. FeII	OI	HeI
Wavelength (μm)	1.644	1.687	1.316	1.083
Detection rate	42%	61%	21%	24%
CLO13 rate	34%	26%	N/A	N/A
AAT rate	40%	75%	N/A	N/A

weaker lines that were unresolved by CLO13, and marginally resolved with the AAT. NIR spectra from the CLO13 sample were used to classify all MYSOs in the Northern Hemisphere in the RMS survey, whereas the AAT sample was used to classify the brightest Southern MYSO candidates. As such, the CLO13 sample is more representative of the whole RMS survey, and of the Galactic MYSO population. In addition, the sources in this sample are likely to be more evolved MYSOs than in the CLO13 or AAT samples. None of the targets in this chapter are Type I sources (under the C13 classification scheme), and only 10% are Type II sources. 17% of the CLO13 sample is made up of Type I sources, and 38% Type II, whereas 7% of the AAT sample is Type I and 19% Type II. This explains why the [FeII] line has a lower detection rate in this sample than in the AAT sample, as this is a shock tracer. The fact that the [FeII] is at the lowest detetion rate in the CLO13 sample is due to the blending of this line with Br12. Three objects (G034.0500–00.2977, G110.1082+00.0473B and G213.7040–12.5971) showed two separate spectra within the slit, which, when extracted, appear to be different objects, and which may thus form a binary system. G034.0500 is referred to in the RMS database as a binary source, whereas the binarity of G213.7040 and G110.1082 are new findings. However, in the absence of other data to confirm binarity it is possible that these are visual binaries rather than bound systems.

3.7 Absorption lines

3.7.1 Spectral typing

The stellar parameters cannot be determined in the usual manner as the targets are invisible at optical wavelengths – the classical wavelength regime for spectral typing. At near–infrared wavelengths the MYSO photospheres are heavily veiled by dust emission, and spectral typing is difficult as well. In practice, spectral types of MYSOs are usually estimated using the temperature derived from Spectral Energy Distribution (SED) fitting.

Traditionally, MYSOs have been found to have luminosities similar to those of OB stars. Spectral types have rarely been determined directly in MYSOs, and not at all in the case of RMS MYSOs. Previously, Kendall *et al.* (2003) observed *H*–band spectra of three MYSOs, IRAS 17175–3544, 17441–2910 and 18079–1756 at intermediate resolution (R∼5000). They found photospheric absorption lines in IRAS 18079–1756 and IRAS 17175–3544, and assigned spectral types of B3V and O7–8V respectively to these two objects.

Most of the MYSOs in this sample show strong, broad HI emission, due to a stellar wind (see also Section 3.8). However, two of the objects in this sample (G015.1288–00.6717 and G034.0500–00.2977_A) display absorption in the Br10, Br11 and Br12 lines. There are also hints of absorption in Brγ and Paγ, alongside the dominant emission in these two objects. The RMS survey quotes G015.1288 as having L_{bol}=13,000 $L_{\odot}$. This corresponds to a spectral type of B0.5 for a Zero–Age Main–Sequence star, using the values from Straizys & Kuriliene (1981).

The *H*–band absorption profiles of G015.1288 were compared with spectra of normal stars from the surveys of Hanson *et al.* (2005) and Meyer *et al.* (1998). A spectral type of F or later would be hard to reconcile with the MYSO data, as F stars have a large number of metal lines. In addition, early O spectral types do not match either, as their Brackett lines are weaker and narrower than observed for G015. Late O and B1–5 stars show a HeI line at 1.70 μm, at comparable or higher strength than the hydrogen absorption lines, and this transition is not present here.

It is worth noting that the near–infrared spectral surveys of Meyer *et al.* (1998)

and Hanson *et al.* (2005) do not have complete spectral and luminosity type coverage. The only B type sample spectra available are those for B1, B5 and B8. So, given the observed spectrum, a spectral type later than B5 and earlier than A9 would be expected for G015.1288. However, the Br10–12 absorption in the B5–A9 stars is much stronger than observed for G015.1288. It is possible that a significant amount of excess could veil the HI absorption to a comparable level to the observations. This is illustrated in Figure 3.10, which zooms in on the Brackett lines in the H–band spectra of a number of normal B8–A7 stars with added excess continuum emission. The excess is added as an extra term of constant value across the H–band (as the wavelength range is small enough in order to ensure no variation in excess across the band). The value of the excess is chosen such that the strengths of the diluted Brackett lines in G015.1288 match the strengths of the absorption lines in MS stars. Overplotted on these are the GNIRS data for G015.1288, rebinned to the same resolution as catalogue spectra. A B8 star with added excess does not match the observed HI profiles, as the lines in this star are considerably narrower than in G015.1288. In addition, the HeI line is still strong enough to be observed. The A0Ib profiles match the observations in strength, but are narrower. An A0V star has broader wings in the Brackett lines than G015.1288. The A5III HI profiles with added excess are also similar to the observed MYSO lines, but the A2IV and A7III spectral types are not a good match for G015.1288. In the absence of more observational spectra to compare this data with, based on visual comparison, I conclude that G015.1288 has the spectrum of an early A giant or supergiant, with an excess continuum added to the stellar photosphere corresponding to 4 × the continuum at H.

A similar analysis was applied to the Br10–12 absorption lines in the spectrum of G034.0500–00.2977_A. In this case the lines are considerably broader, and the best fit is that of an A0V (MS–like) star, as can be seen in Figure 3.11. In contrast, the spectrum of G034.0500_B shows the usual NIR rising red continuum of MYSOs with strong HI emission lines. Source A is brightest in the H–band. The two sources are not resolved in 2MASS, but they are in UKIDSS. The separation is 0.7”, which is within the seeing limit of the observations, so it is likely source A in the GNIRS observations is the UKIDSS source A. Source B shows a red colour index in UKIDSS as well, but source A only has a magnitude in the H–band. A full study of the binary system is beyond the scope of this work. However, given that a lower mass object will be in an earlier evolutionary stage than a higher mass object of the same age, it is more likely that G034.0500–00.2977_A is a Main Sequence star located in the same direction as source B, rather than a lower mass star–forming object associated with a MYSO.

In summary, the (only) observed absorption spectrum of a MYSO in the present sample can be reproduced by an A–type object with a relatively low surface gravity. A continuum excess emission of a factor of a few is needed in order to match the lower depth of the lines. This excess is due to radiation from hot dust, and does not affect the spectral classification itself, as that is based on the line widths and relative strengths of absorption lines, both of which do not change after the addition of a continuum excess. As shown in Section 3.5, it is possible MYSOs have considerable amounts of dust excess emission at both H and K. For a typical temperature of 10,000 K of an A0 star and an observed luminosity of 13,000 $L_{\odot}$, I infer a stellar radius of order 70 $R_{\odot}$ for G015.1288.

The fact that the star is cooler and larger than what might be expected based on its total luminosity can be understood in terms of the high accretion expected in massive star forming objects. Models of Hosokawa *et al.* (2010), as well as more recent hydrodynamic simulations done by Haemmerlé & Peters (2016) show that a pre–MS star accreting at a constant rate of 10^{-3} $M_{\odot}yr^{-1}$ can swell up to 40–300 $R_{\odot}$. At constant luminosity, this puffing up will cause a decrease in temperature of a factor ~3. A puffed up late–O/early–B type star will have a temperature and structure similar to an A–type giant or supergiant star. This might explain why MYSOs have yet to ionise their surroundings and form an HII region, as the UV flux of an A star is considerably lower than that of a B star. Furthermore, the winds of an A star have considerably lower expansion speeds than those of B stars (cf. Hoare & Franco 2007).

3.7.2 Other absorption lines

Turning to other absorption lines, as can be seen in Figure 3.8, the strongest absorption feature in the spectrum is located at 1.318μm. I identify this absorption with the λ=13175 (Å) Diffuse Interstellar Band (Cox *et al.* 2014; Hamano

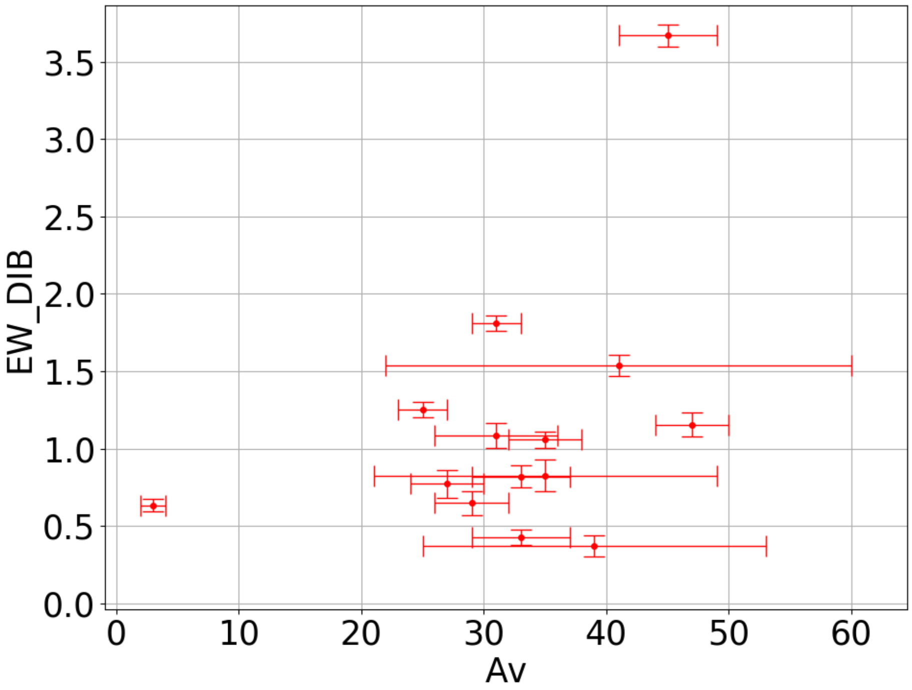

Figure 3.9: Equivalent width of DIB 13175 Å as a function of circumstellar extinction in the V–band. EW are in Å and extinctions in magnitudes.

et al. 2015). It is detected in most objects for which usable J-band data were obtained, and the equivalent widths are measured to be up to several Å. The lines in the MYSOs are much stronger than reported thus far in the literature and this can be partly understood due the fact that the extinction towards the targets is much larger than those sampled in Cox *et al.* (2014) and Hamano *et al.* (2015), whose highest extinction lines of sight have an A_V of 10. These authors also determine the slope of the relationship between the EW of DIB and A_V. The EWs of the band in the MYSOs do not follow these relationships however; the lines are weaker than the A_V values would imply (see Figure 3.9).

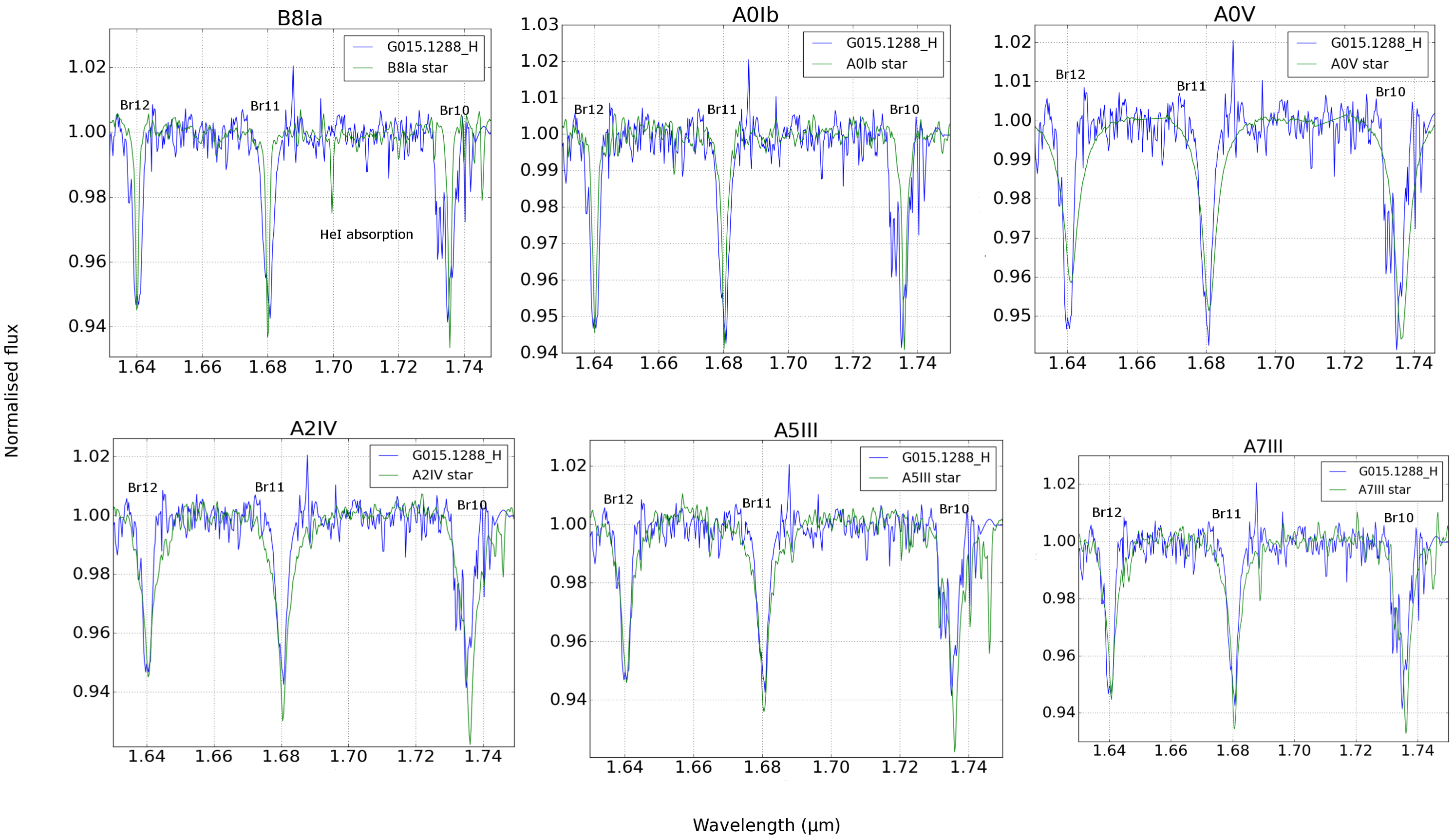

Figure 3.10: Br10–12 profiles in G015.1288–00.6717 (blue) compared with normal stars with added continuum dust excess (green). Data from Meyer *et al.* (1998) and Hanson *et al.* (2005). See text for details.

To understand this finding, it is important to consider that the total extinction towards the targets is a combination of foreground (interstellar) extinction and extinction due to the dust in the parental molecular cloud and circumstellar envelopes. It had been observed previously that the DIBs do not trace circumstellar material as efficiently as they trace the interstellar material. This could be due to different excitation conditions in these respective environments, the net effect is that the line–EWs are indeed lower than the total A_V would suggest (Oudmaijer *et al.* 1997).

Finally, CO bandhead absorption lines are also detected, which are expected to originate from a further out, colder component than its emission counterpart (Davies *et al.* 2010). Studies of CO bandhead absorption are used to measure the properties of the outer, cooler envelope of MYSOs. However, this type of analysis is beyond the scope of this study.

3.8 Emission lines

3.8.1 Line luminosities and accretion rates

I will first discuss the line luminosities, which are computed using the distances,the measured Equivalent Widths and the dereddened continuum fluxes.

The lines in the Brackett series form in similar conditions. For example, in the case B approximation, the ratio Brγ/Br12 $\simeq$ 5±1, for temperatures between 3000–30000K and electron densities 10^4–10^9 cm^{-3}. In the optically thick case, the Rayleigh–Jeans approximation applies and the ratio is given by:

$$F_{Br\gamma}/F_{Br12} = (\lambda_{Br12}/\lambda_{Br\gamma})^{-4} S_{Br\gamma}/S_{Br12}, \tag{3.1}$$

where S is the projected surface area the line is emitted from. If both lines are emitted from an area of the same size, the ratio becomes 0.33, the lowest expected value. The Br12 and Brγ luminosities indeed correlate, as shown in Figure 3.12. Most points lie between the optically thin and optically thick approximations. Information about the optical thickness of these regions can be obtained from analysing the ratio of the line profiles in velocity space, which I will return to in Section 3.9.2.

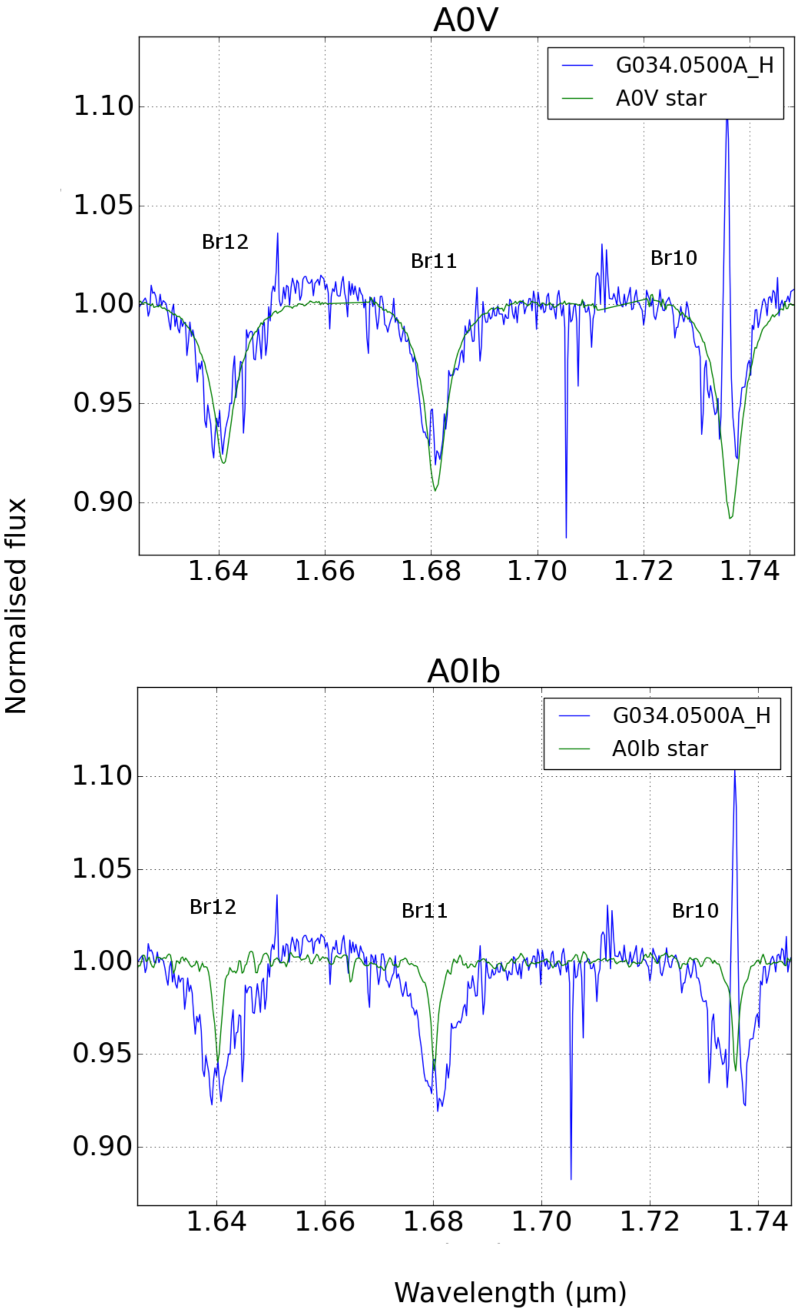

Figure 3.11: Spectral typing of G034.0500_A. The Brackett absorption lines are too broad compared to what would be expected of a A0Ib star, they are more like an A0V.

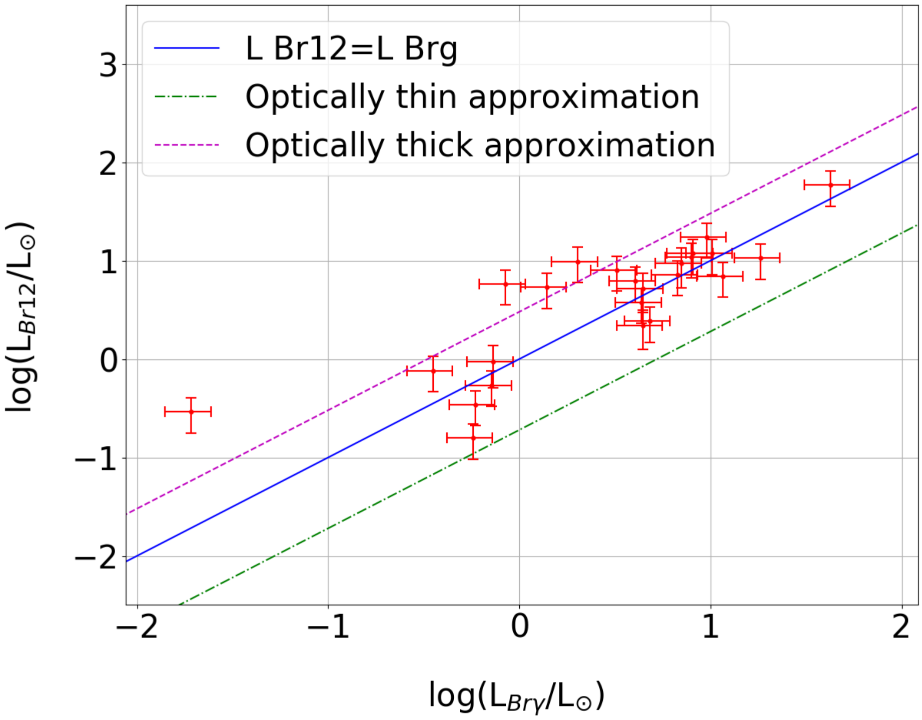

Figure 3.12: Br12 luminosity as a function of Brγ, with optically thin and optically thick approximations, and an equal luminosity line.

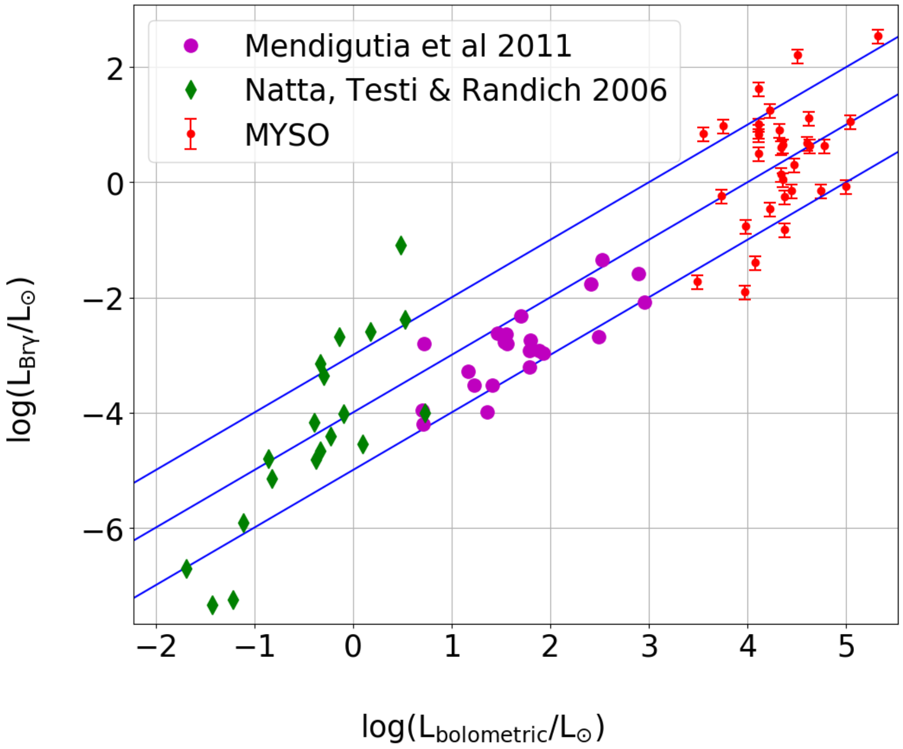

Figure 3.13: Log–log plot of the luminosity in the Brγ line against bolometric luminosity. Green diamonds are T Tauri stars, while purple circles are Herbig stars, objects of a lower and intermediate mass, respectively, believed to be at a similar evolutionary stage as MYSOs. The solid lines correspond to $L_{Br\gamma}$=10^{-3}L$_{bol}$, 10^{-4}L$_{bol}$ and 10^{-5}L$_{bol}$

CLO13 found that Brγ luminosities lie between log(L$_{Br\gamma}$) = log(L$_{bol}$)–3 and log(L$_{bol}$)–5. This result is confirmed by the GNIRS data, as can be seen in Figure 3.13. I also plot data of intermediate mass pre–Main Sequence Herbig Ae/Be stars from Mendigutía *et al.* (2011) and low mass T Tauri stars from Natta *et al.* (2006) for comparison with lower mass sources. These seem to also lie within the same range as the MYSO data, indicating that there is some degree of continuity across the mass range of different pre–Main Sequence objects.

The luminosity of the Brγ line, and many other emission lines, has been shown to be a proxy for the accretion luminosity in low and intermediate–mass YSOs (Mendigutía *et al.* 2011; Natta *et al.* 2006). This stems from the observed corre-

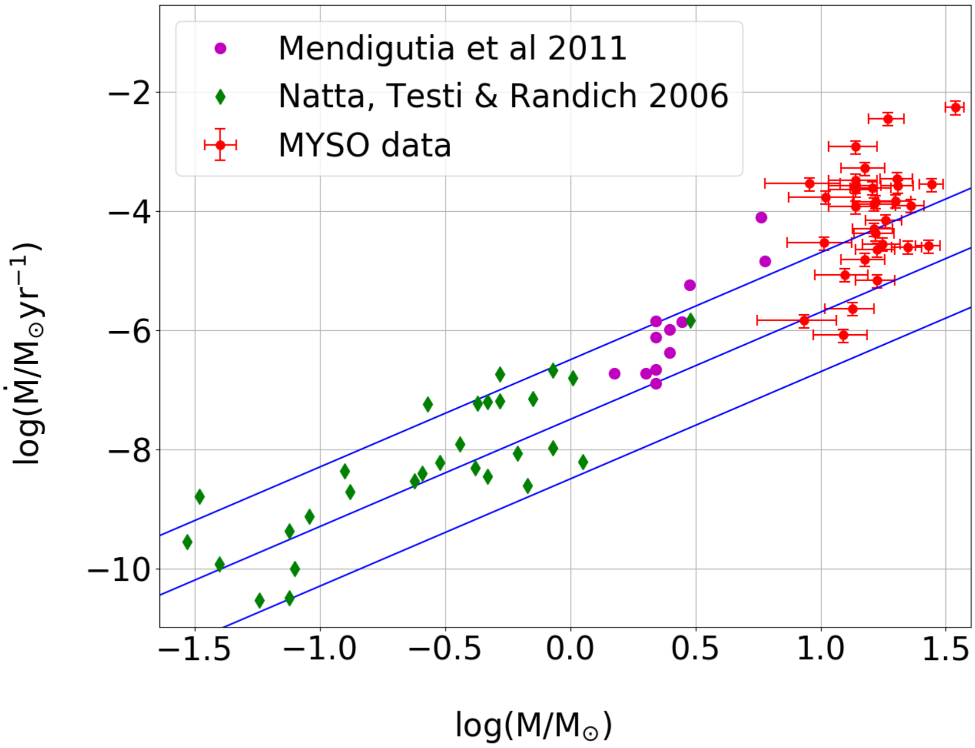

Figure 3.14: Log–log plot of the mass accretion rate against stellar mass. The symbols are as the previous figure. The solid lines correspond to $\log(\dot{M}) = -8.5 + 1.8\log(M_*)$, $\log(\dot{M}) = -7.5 + 1.8\log(M_*)$ and $\log(\dot{M}) = -6.5 + 1.8\log(M_*)$

lation between the Brγ line luminosity with the accretion luminosity – which is essentially the kinetic energy of the infalling material converted into radiation in the accretion shock. The hydrogen recombination line emission is seen to originate in the accretion funnels in the lower mass T Tauri stars, whereas it appears to trace winds in the higher mass Herbig Be stars (see e.g. Fairlamb *et al.* 2015). This might appear counterintuitive – why would stellar winds trace accretion for both T Tau and Herbig stars? The reason for this is that the hydrogen is ionised by the radiation emerging from the accretion shock region, leading to a relationship between accretion and hydrogen recombination emission. In principle, therefore, one can exploit the correlation and proceed with computing accretion luminosities from the Brγ lines.

Following CLO13, I calculate accretion luminosities from Brγ. To this end I use the Mendigutía *et al.* (2011) relation:

$$\log(L_{acc}/L_{\odot}) = (3.55 \pm 0.80) + (0.91 \pm 0.27)\log(L_{Br\gamma}/L_{\odot}) \tag{3.2}$$

This results in accretion luminosities of MYSOs in the range L_{acc} =0.01–1 L_{bol}. The mass accretion rates can be determined from the accretion luminosities, if the masses and radii of the star are known, with the following formula:

$$\dot{M}_{acc} = \frac{L_{acc}R_*}{GM_*} \tag{3.3}$$

Masses and radii are estimated from the bolometric luminosities using the Zero Age Main Sequence relations as tabulated by Davies *et al.* (2011), (M $\propto \mathrm{L}_{bol}^{0.33}$, R $\propto \mathrm{L}_{bol}^{0.2}$). Figure 3.14 shows the resulting accretion rates against stellar mass. The mass accretion rates lie above $\log(\dot{M}_{acc}) = -8.5 + 1.8\log(M_*)$, similarly to lower mass objects, but also extend to above the $\log(\dot{M}_{acc}) = -6.5 + 1.8\log(M_*)$ line, unlike the low mass sources. It would appear that the results for the MYSOs follow the trend of increasing mass accretion rate with mass as observed for the lower mass T Tauri and Herbig Ae/Be stars, a trend that was also pointed out by Beltrán & de Wit (2016). However, the mass–accretion rate relation for MYSOs can be fit by $\log(\dot{M}_{acc}) = (-7.0 \pm 1.4) + (2.4 \pm 1.2)\log(M_*)$, which is a steeper line than $\log(\dot{M}_{acc}) = -7.5 + 1.8\log(M_*)$, which was the best fit for the low–mass T Tauri stars. The accretion rates deduced for MYSOs are between 10^{-6} and

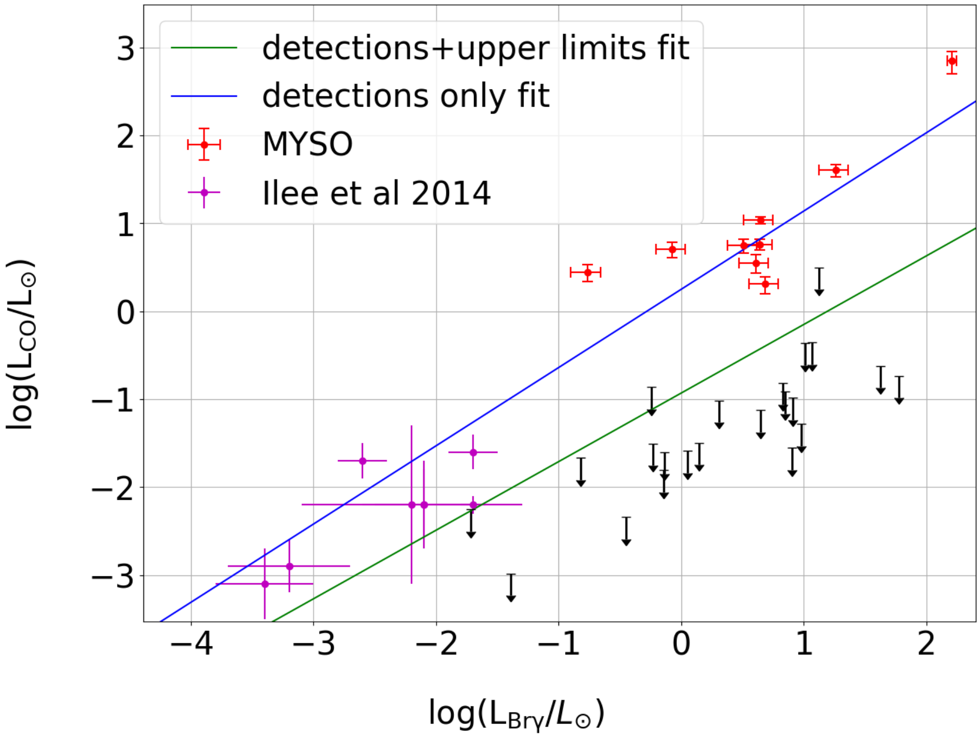

Figure 3.15: Log–log plot of the CO bandhead luminosity as a function of Brγ luminosity, with data from GNIRS and Ilee *et al.* (2014)

4.5×10^{-3} M$_\odot$/yr. This range of accretion rates and luminosities agree with the results of CLO13, as well as those from the AAT survey presented in Chapter 2. These accretion rates were derived assuming MYSO have a similar configuration to MS stars. However, it is possible that MYSOs have an A giant or supergiant configurations, from simulations of Hosokawa *et al.* (2010) as well as the observational results in Section 3.7.1. As the stars are larger, the gravitational potential being released per unit mass will be smaller. Accounting for this effect will thus result in accretion rates that will be about an order of magnitude higher.

3.8.2 Other line luminosities

Not only the Br12 and Brγ line luminosities correlate (Figure 3.12), 75% of the lines' luminosities studied here correlate with one another with a probability of false correlation of under 1% (see Tables 3.3 – 3.4). In order to asses whether any distance or continuum flux biases are present, I performed a Pearson partial correlation test (Wall & Jenkins 2003). 70% of the observed correlations still hold even under a partial correlation test (see Tables 3.5 – 3.6). Moreover, many of the pairs of lines that do not correlate likely do so because the given two lines are only detected together in a small number of objects. For example, CO bandhead emission and [FeII] are both detected in only four objects, and the probability of false correlation of their line luminosities is 9%. In addition, there are a few pairs of lines, like [FeII] and Paγ that are only detected together in two objects or less. In these cases, a correlation factor cannot be determined, and they have been labelled 'N/A' in the tables.

For example, the CO bandhead, when in emission, and the Brγ luminosities strongly correlate (see Figure 3.15, in agreement with the results of Ilee *et al.* 2014). The best fit line to detections is $\log(L_{CO}) = (0.49 \pm 0.11) + (0.80 \pm 0.09)\log(L_{Br\gamma})$, and when including upper limits, this becomes $\log(L_{CO}) = (-0.95 \pm 0.12) + (0.85 \pm 0.11)\log(L_{Br\gamma})$. The scaling from lower mass Herbig Ae/Be starts seems to apply to the correlation between these two lines as well.

There are two issues that must be highlighted here. Firstly, the CO bandhead emission arises from the warm, dense circumstellar disc material which is not necessarily directly associated with the ionised wind or present–day accretion flows. It is thus curious that the luminosity of emission lines originating from these very different regions are correlated. A logical further step is that the correlation itself will also allow one to derive the mass accretion rates from the CO bandhead emission, despite the fact that the line forming region does not need to have a direct relationship to the accretion process. Secondly, the correlation is very strong when the CO bandhead is in emission, but a large fraction of the stars in the sample do not have (detected) emission. The upper limits to the line luminosities for the non–detections lie in some cases several orders of magnitude below those of the detections, which prompts the question why the detections themselves would correlate with the Brγ line luminosities at all.

The fluorescent FeII line at 1.687 μm was found by CLO13 to correlate with both bolometric and Brγ luminosity for detections only. The best fit lines were $\log(L_{fl.FeII}) = -4.1 + 0.82\log(L_{bol})$ and $\log(L_{fl.FeII}) = -0.79 + 0.8\log(L_{Br\gamma})$. I find no correlation of fluorescent FeII with bolometric luminosity, the factor being R=0.04. The flourescent FeII does however correlate with Brγ, with a best fit line of $\log(L_{fluor.FeII}) = 0.06 + 0.61 \log(L_{Br\gamma})$, with R=0.75. I also investigated the correlation between the forbidden FeII line at 1.644 μm and the fluorescent FeII line. The best fit line is $\log(L_{flFeII}) = 0.59 + 4.69 \log(L_{[FeII]})$. The correlation factor here is R=0.76. This is again unexpected, because the fluorescent and forbidden FeII lines are believed to be formed in separate environments – the former in tracing discs and the latter shocks resulting from outflows and jets.

The luminosity of the OI line does not correlate with bolometric luminosity (R=0.02). Still, there is a strong correlation (R=0.89) with Brγ, given by $\log(L_{OI}) = 1.44 + 0.53 \log(L_{Br\gamma})$.

A first conclusion of this would be that there may be an underlying relation between these lines causing their luminosity to correlate. In the case of the Brγ line, which is more likely to be formed in a wind rather than in an accretion funnel (see the discussion later on line profiles), it could be argued that accretion and outflows are intimately linked as winds can be accretion powered and thus correlated with the accretion rates. However, many lines arise from different regions and it will be hard to apply this explanation to all lines. Indeed, in a recent study on Herbig Ae/Be and T Tauri stars, Mendigutía *et al.* (2015) have shown that line correlations with accretion luminosities are caused by both of these quantities being correlated with stellar luminosity. This may well be the case for MYSOs too, with correlations seen being a scaling effect as the emission line strengths are proportional to the stellar luminosity. Hence brighter, more massive, stars will have stronger emission lines, as well as a stronger continuum flux.

The observed correlations may also arise due to selection effects. Line luminosities lower than those on the best fit correlation line may be hard to detect due to the SNR of the data, as shown by the upper limits in Figure 3.15. As for luminosities above the values on the best fit line, the transitions may not be able to reach a level of excitation required to produce luminosities stronger than those on the best fit line.

Whatever the reason might be for the observed correlation, it is worth bearing in mind that they cannot be used to indicate causality. In other words, just because

Table 3.3: Pearson correlation factor R between different lines in the sample. N/A corresponds to less than three objects showing a detection of pair of lines. In this case a correlation factor cannot be determined. Bol corresponds to correlations of line luminosities with bolometric luminosity.

Line	Brg	Br12	Pag	NaI	CO	flFe	[FeII]	OI	Bol.
λ (μm)	2.166	1.641	1.094	2.206	2.295	1.687	1.644	1.316	
Brg		0.89	0.89	0.78	0.87	0.75	0.61	0.89	0.40
Br12	0.89		0.92	0.87	0.93	0.79	0.77	0.93	0.24
Pag	0.89	0.92		0.98	0.97	0.13	N/A	0.89	0.77
NaI	0.78	0.87	0.98		0.84	0.51	0.64	0.78	-0.49
CO	0.87	0.93	0.97	0.84		0.88	0.99	N/A	-0.15
flFe	0.75	0.79	0.13	0.51	0.88		0.76	0.9	0.04
[FeII]	0.61	0.77	N/A	0.64	0.99	0.76		0.68	0.48
OI	0.89	0.93	0.89	0.78	N/A	0.90	0.68		0.02
Bol.	0.40	0.24	0.77	-0.49	-0.15	0.04	0.48	0.02	

Table 3.4: Probability of false correlation between different lines in the sample.

Line	Brg	Br12	Pag	NaI	CO	flFe	[FeII]	OI	Bol.
λ (μm)	2.166	1.641	1.094	2.206	2.295	1.687	1.644	1.316	
Brg		<0.01%	0.06%	0.02%	0.65%	<0.01%	0.93%	0.06%	2.10%
Br12	<0.01%		0.12%	0.01%	0.62%	<0.01%	0.02%	<0.01%	22.70%
Pag	0.06%	0.12%		0.06%	3.00%	78.00%	N/A	1.30%	0.92%
NaI	0.02%	0.01%	0.06%		0.45%	11.00%	12.00%	12.00%	77.00%
CO	0.65%	0.62%	3.00%	0.45%		0.89%	9.00%	N/A	67.98%
flFe	<0.01%	<0.01%	78.00%	11.00%	0.89%		0.10%	0.23%	85.61%
[FeII]	0.93%	0.02%	N/A	12.00%	9.00%	0.10%		0.12%	5.10%
OI	0.06%	<0.01%	1.30%	12.00%	N/A	0.23%	0.12%		96.12%
Bol.	2.10%	22.70%	0.92%	77.00%	67.98%	85.61%	5.10%	96.12%	

Table 3.5: Pearson partial correlation factor R when controlling for distance and continuum flux for all the different lines in the sample.

Line	Brg	Br12	Pag	NaI	CO	flFe	[FeII]	OI
λ (μm)	2.166	1.641	1.094	2.206	2.295	1.687	1.644	1.316
Brg		0.88	0.95	0.79	0.79	0.80	0.59	0.96
Br12	0.88		0.95	0.88	0.85	0.80	0.72	0.98
Pag	0.95	0.95		0.98	0.99	0.38	N/A	0.95
NaI	0.79	0.88	0.98		0.87	0.72	0.63	0.89
CO	0.79	0.85	0.99	0.87		0.98	0.79	N/A
flFe	0.80	0.80	0.38	0.72	0.98		0.7	0.96
[FeII]	0.59	0.72	N/A	0.63	0.79	0.70		0.97
OI	0.96	0.98	0.95	0.89	N/A	0.96	0.97	

Table 3.6: Probability of false correlation when controlling for distance and continuum flux for all the lines in the sample.

Line	Brg	Br12	Pag	NaI	CO	flFe	[FeII]	OI
λ (μm)	2.166	1.641	1.094	2.206	2.295	1.687	1.644	1.316
Brg		<0.01%	<0.01%	0.02%	0.01%	<0.01%	1.20%	<0.01%
Br12	<0.01%		0.03%	<0.01%	7.50%	<0.01%	0.08%	0.04%
Pag	<0.01%	0.03%		0.06%	0.10%	40.00%	N/A	4.30%
NaI	0.02%	<0.01%	0.06%		0.22%	1.20%	12.00%	4.30%
CO	0.01%	7.50%	0.10%	0.22%		0.01%	42.00%	N/A
flFe	<0.01%	<0.01%	40.00%	1.20%	0.01%		0.37%	0.02%
[FeII]	1.20%	0.08%	N/A	12.00%	42.00%	0.37%		0.62%
OI	<0.01%	0.04%	4.30%	4.30%	N/A	0.02%	0.62%	

a line correlates with another, it does not mean that they are produced by the same physical process or within the same region in the MYSOs.

3.9 Line profiles

3.9.1 Profile shapes

One of the main advantages of this data set is its spectral resolution. This allows for a detailed analysis of the line profiles. Following the prescriptions of Cauley & Johns-Krull (2015), who performed an analysis of line profiles in Herbig Ae/Be stars, I divide the profile features into 6 different categories: E – single–peaked emission, A – absorption, PC – P Cygni profile, IPC – inverse P Cygni profile, D

– double peaked profile and N – non–detection. The results are presented graphically, for the main observed lines, in Figure 3.16.

For most lines, single–peaked emission is the most frequent feature type. The relative proportion of different feature types is similar for all HI recombination lines. Blueshifted P Cygni–type (PC) absorption, indicative of outflowing material, is fairly rare; it is seen in all HI lines in three MYSOs, only in Br10–12 in two other objects, and in HeI in 2 objects. Redshifted inverse P Cygni–like (IPC) absorption, indicative of infall, is seen in three objects in Brγ and two in HeI. The occurrences of P Cygni and inverse P Cygni lines are 13% and 8% respectively. These are lower than the values found by Cauley & Johns-Krull (2015) for Herbig Ae/Be stars, which in turn were found to be lower than those for T Tauri stars. They also found that more Herbig Ae than Herbig Be stars show IPC lines, which they take as indication of the differences between the dominant accretion processes involved in these objects. Effectively the accretion switches from magnetically–controlled for T Tauri and Herbig Ae stars to disc accretion in the case of Herbig Be stars. The MYSO fractions of PC and IPC profiles show that this trend continues to higher mass MYSOs. Another likely cause for the lower detection rates of PC and IPC–like absorption profiles is dilution by the dust excess, which is higher in MYSOs than in TTaus and HAe/Bes. Most of the Brγ PC velocities extend as far as 600–800 km/s, and IPC up to 200–300 km/s. Brγ is found in emission in all but one source, G078.8867, where it displays absorption. There are also hints of absorption (possibly stellar) alongside the emission in 2 other sources. One source (G029.8620) shows a double peaked profile. At least 5 sources are not well fit by a single Gaussian component, possibly due to the presence of a nebular recombination term. In addition, 7 objects display a profile asymmetry, with either the blue or the red wing extending to a larger velocity than the other side of the profile.

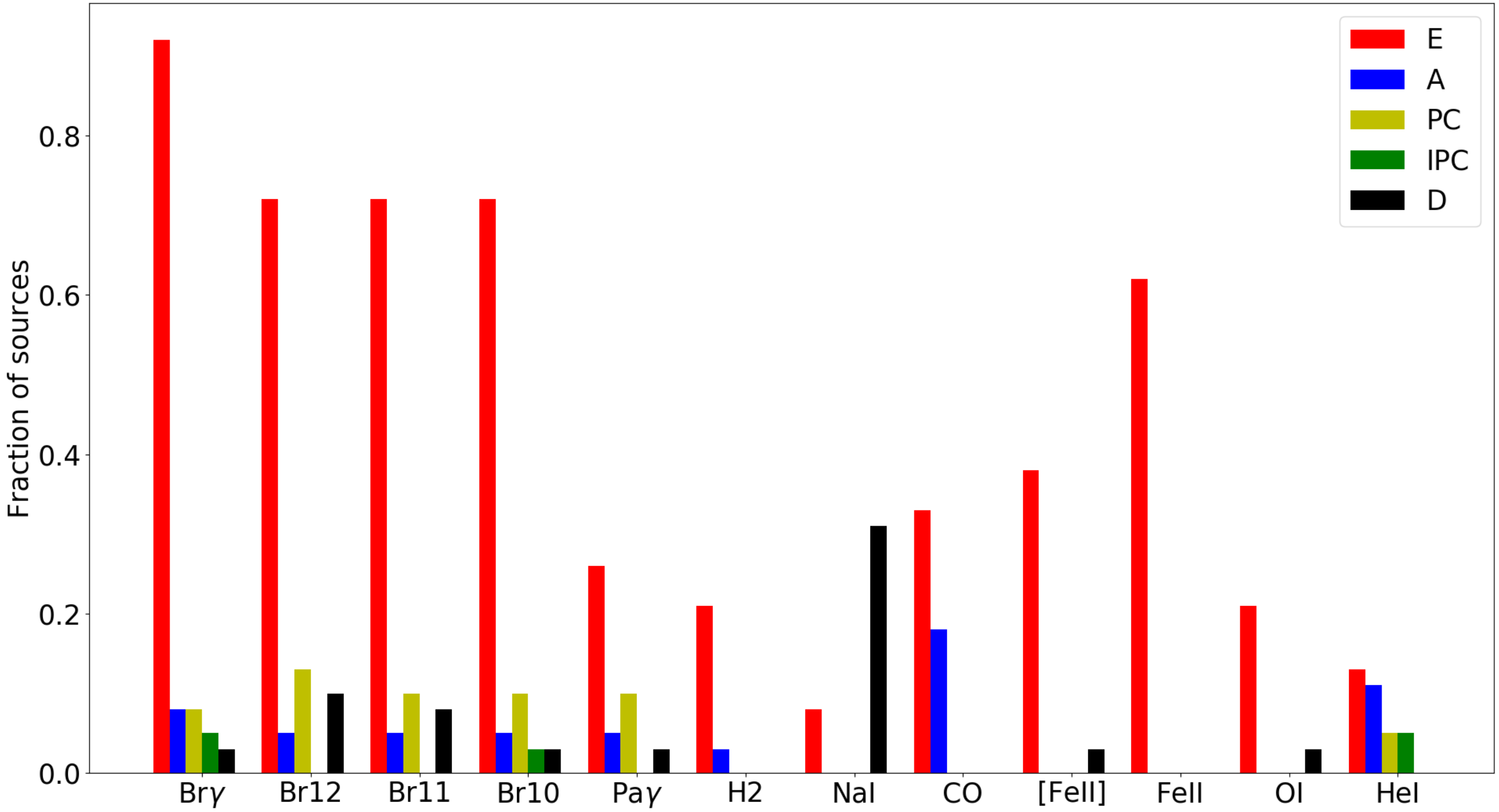

Figure 3.16: Detection rates of different features, with different profile types. E=single–peaked emission, A=absorption, PC=P Cygni profile, IPC=inverse P Cygni and D=double peaked

5 objects show a P Cygni profile, which generally extends to 600–800 km/s. One of the PC profiles extends to only 300 km/s and one other to 1000 km/s. 4 other objects display hints of an inverse P Cygni emission, extending to 200–300 km/s. The average FWHM of the Gaussian fits to the Brγ profiles is 150±7 km/s, and the strength relative to continuum 1.43±0.12. Examples of the Brγ profiles can be seen in Figure 3.17.

The profiles of the Br10, 11 and 12 lines in the H–band are similar for most objects, and their behaviour mirrors that of the Brγ line. Two objects display Br10–12 in absorption as discussed in Section 3.7.1. Six Br10–12 profiles are not well fit by a single Gaussian profile. Almost all of these multi–component profiles also show similar behaviour in Brγ. Five objects display an asymmetry in the line profile. A P Cygni profile is seen in five targets. However, the terminal velocity of the outflow producing this feature in Br10–12 is slightly lower than in Brγ in three targets, ≈400 km/s. None of the sources display an inverse P Cygni profile, and three sources display a double peaked profile in Br10–12. The average FWHM is 170±35 km/s. The average strength is 1.35±0.01 relative to the continuum.

The Paγ line displays emission along with hints of intrinsic stellar absorption in half of the sources (4 targets) where it is detected. This may be due to the lower excess in the X–band. Three of the sources show a Paγ P Cygni profile, with velocities up to 400–700 km/s. These sources also display a similar feature in the Brackett emission lines. The average FWHM of the Paγ line is 137±14 km/s, and the average strength 2.04±0.24 × the continuum.

The red component of the NaI doublet is stronger than the blue one for almost all of the sources, but by less than 5%. Only two objects display this transition as a single rather than double profile. The average FWHM of this line is 208±15 km/s, and its strength 1.04±0.01 relative to the continuum.

The CO bandhead displays a blue shoulder, indicative of emission from an edge–on disc, in 4 objects, a third of the total number of sources with CO emission. The average strength of this feature is 1.08±0.01 × the continuum.

The fluorescent FeII line displays one of two different type of profiles. 75% of them have a profile similar to the HI lines, wide (>100 km/s) and relatively weak (>1.2×continuum), whilst the others have a strong and narrow profile (see

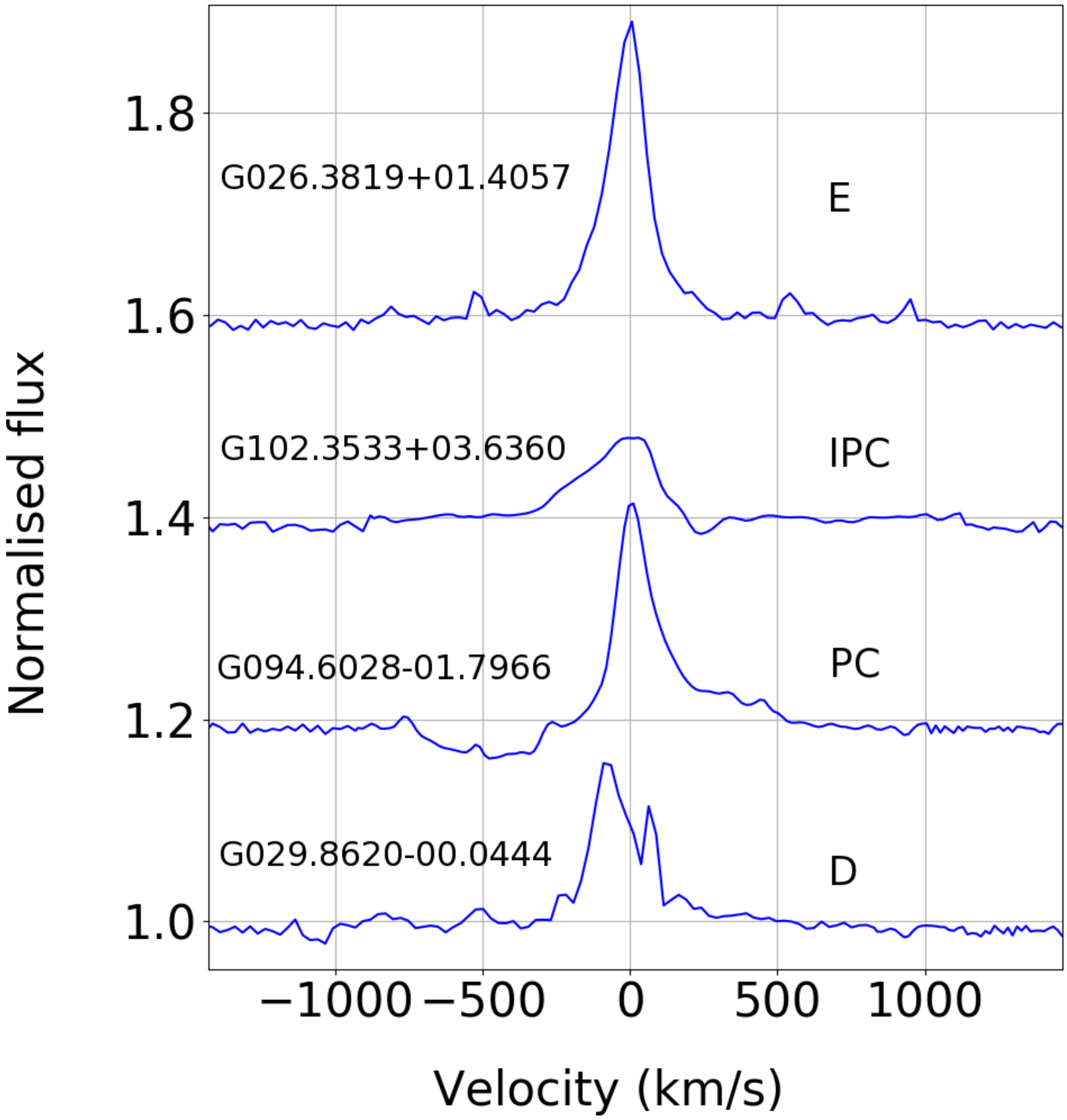

Figure 3.17: Examples of Brγ profiles from the sample. From top to bottom: single–peaked emission G026.3819; inverse P Cygni absorption G102.3533; P Cygni absorption G094.6028;

Figure 3.18). In addition, 9 objects show both fluorescent FeII and CO bandhead emission. All but one of the sources with the CO blue shoulder feature show fluorescent FeII emission. Sources with the CO blue shoulder also display a weak and wide FeII profile. The average FWHM of the fluorescent FeII profile is 108±13 km/s, and the average strength 1.28±0.08 × the continuum.

The [FeII] line profile at 1.644 μm is resolved in most MYSOs. In two objects the [FeII] and Br12 lines form a blend. In addition, this line is weaker than Br12 in all but one object. The profiles are quite narrow, with an average FWHM of 78±8 km/s and strong, 1.22±0.08 relative to continuum. This line is symmetrical in most cases, with Gaussian profiles providing good fits.

The OI line shows a similar split in feature types to fluorescent FeII, with profiles being either strong and narrow or weak and wide (see Figure 3.18). Objects where both of these lines are seen show a similar profile in OI as in the Fe line. However, one MYSO (G014.9958) does not fit in either category, having a strong and wide OI profile. Most OI profiles are symmetrical, and are fit well by a single Gaussian profile. The average FWHM of the OI line is 100±13 km/s and the strength 2.22±0.5 × the continuum.

Nine objects show a HeI feature at 1.083 μm. In five objects this line is in emission and four in absorption. P Cygni features are seen in two objects, and inverse P Cygni in another two. Both the blueshifted emission and absorption features extend up to 600 km/s and are often stronger than similar features in Brγ or Br10–12, with the absorption being up to 80% of the continuum. This is again indicative of the lower excess in the X–band. The average FWHM of HeI profiles is 228±57 km/s and an average strength of 1.56±0.78 relative to the continuum level.

3.9.2 Hydrogen line profile ratios

As explained in Section 3.9.1, many observed HI recombination line profiles show asymmetries, suggesting that there are multiple components giving rise to the observed emission. In order to disentangle these, I analyse the recombination line ratios. These can provide clues on the formation mechanism and kinematics of the wind emission. As explained earlier, the value of the Brγ/Br12 line ratio increases with decreasing optical depth.

The spectral dependence of this ratio can help distinguish between different wind components of different accelerations that give rise to the observed emission. In the earlier work of Drew *et al.* (1993) and Bunn *et al.* (1995) ratios of Brα/Brγ and Brα/Pfγ were studied. The Brγ/Br12 ratios are expected to be comparable with those as the absorption cross sections of these lines have similar values to those of lines they used (see also Lumsden *et al.* 2012).

The procedure for computing the ratios is as follows. A region of ±500 km/s from the velocity centre of the line is selected, and the spectra are rebinned to correct for differences in resolution between the K and H–bands. The extinction correction is then applied and the continuum is fitted with a 2$^{\mathrm{nd}}$ order polynomial fit and subtracted. Finally, the two lines are divided. The chosen extinction value only affects the numerical value of the ratio, but trends in shape of the ratio profile remain unchanged. A number of different features can be distinguished in the ratios, as shown in Figure 3.19. Some line ratio profiles are flat, others show a dish shaped profile. Central peaks are also seen, either narrow (FWHM≈50–80 km/s) or wide (FWHM≈80–100 km/s). Other objects display a central dip, blue or red asymmetries. Often two or more of these different types are all seen in a line ratio. Their relative fractions are shown in Table 3.7. Even though the rates of features in Brγ/Br12 and Brγ/Br11 are not the same, the relative detection rates of different features are similar. As such, I will focus on the Brγ/Br12 ratio profile features in the following discussion.

Some of these features have been seen in other line ratio surveys. Drew *et al.* (1993) reported a dish shaped profile in S106IRS1 in their Brα/Brγ spectral line ratio, which they interpret as an accelerated wind, while Lumsden *et al.* (2012) find a peak in the Brγ/Br12 ratio for most of their targets.

A dish shaped profile indicates optically thin gas expanding faster than the optically thick central material. Drew *et al.* (1993) also see a narrow central peak in the S106IRS1 Brα/Brγ ratio, which they interpret as an optically thin nebular gas region.

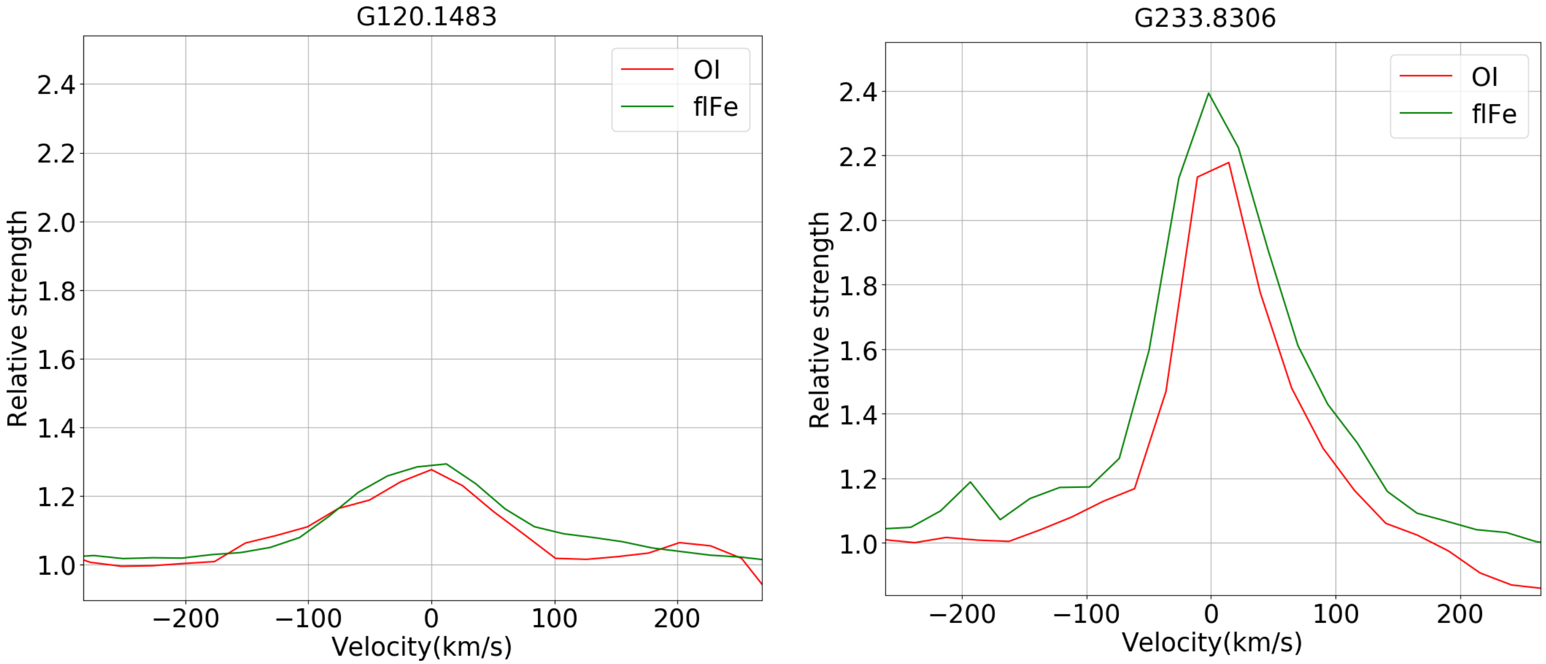

Figure 3.18: Fluorescent FeII (green) and OI (red) profile types. Left – weak and wide profiles, right – strong and narrow.

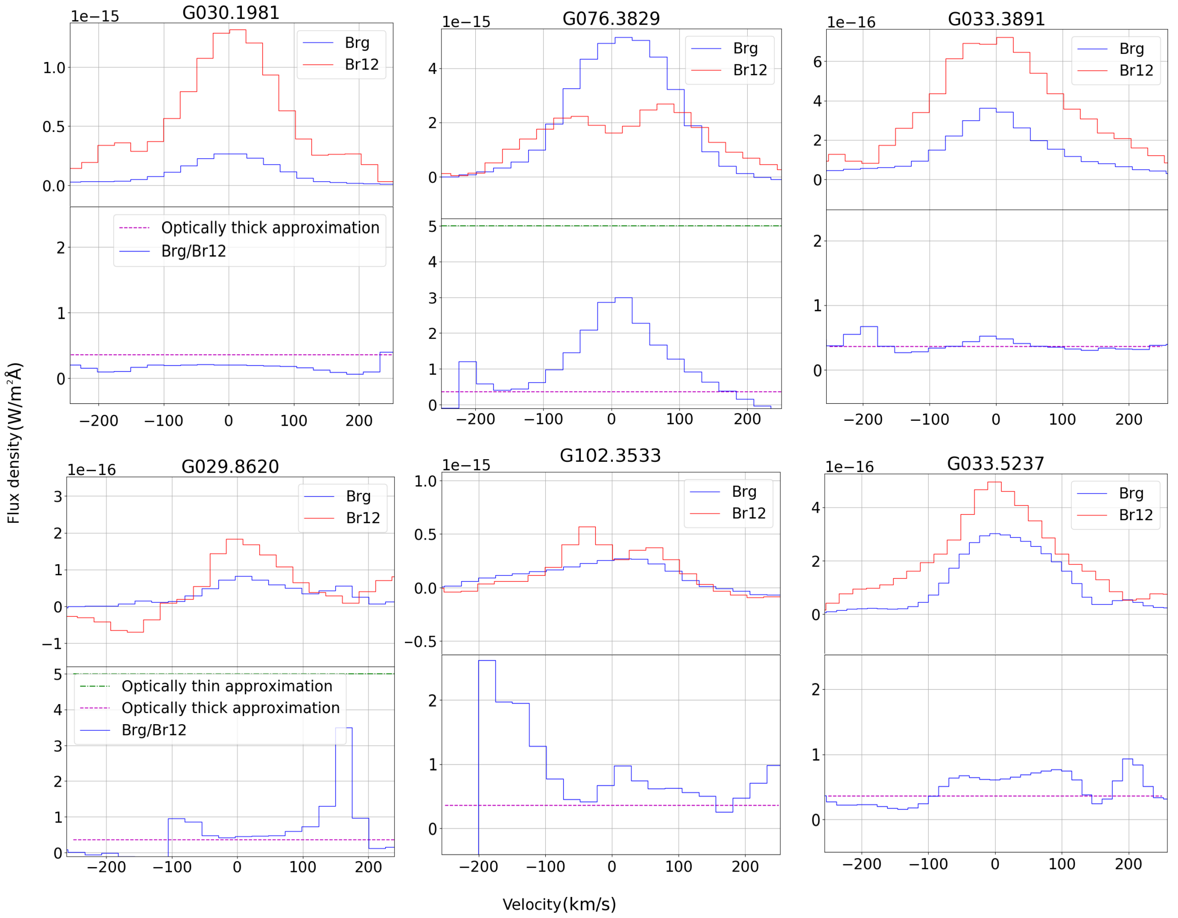

Figure 3.19: Examples of different types of profile ratio in Brγ/Br12. The horizontal axis denotes the velocity. Top (left to right): Flat ratio, Wide peak, Narrow peak. Bottom(left to right): Dish shape, Dish shape+central peak, Central dip. The optically thin limit is at a ratio of 5, which is not shown on several panels

Table 3.7: Fraction of objects with different type of profile features in Brγ/Br12 and Brγ/Br11. Sources can display more than one type of feature

	Brγ/Br12	Brγ/Br11
Flat	21%	41%
Wide peak	28%	21%
Narrow peak	17%	17%
Dish	14%	17%
Dish + peak	10%	3%
Central dip	17%	10%
Red asymmetry	14%	24%

By the same logic, a weak and wide peak can be seen as an inverted dish shape, where the optically thin gas is expanding slower than the optically thick gas. This can be interpreted as a decelerating wind. A central dip within a wider peak can be seen as a decelerating wind combined with a larger, optically thick nebular region. A flat ratio simply shows all regions expanding at the same acceleration, irrespective of optical thickness. Asymmetries are suggestive of infall (on the red side) or outflow (on the blue side). In addition to compiling a catalogue of the different features observed in the Brackett emission line profile ratios, I have also checked for patterns between the presence of other spectral lines, bolometric luminosity and these features. Table 3.8 summarises the findings.

Fewer sources with wide peaks or flat profile ratios show CO bandhead emission than sources with narrow peaks and/or dish shaped profile ratios. The H_2 line seems to be present only in sources with either a wide peak or a central dip in the profile ratios, and in a higher fraction of objects in the latter. This could also be due to the fact that this line has a low detection rate. The forbidden FeII line is at a minimum detection rate in sources with a narrow peak profile ratio, whilst the fluorescent FeII line is ubiquitous in the objects from this sample. However, there are slightly fewer objects with a narrow peak or a dish shape profile (separately) that show the latter line.

There are no clear correlations between the features and bolometric luminosity, near–IR or mid–IR colours. This casts doubt on the idea presented by Bunn *et al.* (1995) that the range of profiles may be corresponding to an evolutionary

Table 3.8: Brγ/Br12 profile ratio feature detection rates in MYSOs with different spectral transitions. Also shown in the last column is the average bolometric luminosity of objects with different spectral features. E corresponds to emission and A to absorption

Brγ/Br12	CO E	CO A	NaI	H_2	[FeII]	fl. FeII	OI	HeI	Avg. L_{bol}
λ (μm)	2.295	2.295	2.206	2.240	1.644	1.687	1.316	1.083	($10^3 L_\odot$)
Flat	0%	50%	17%	0%	67%	83%	17%	0%	17
Wide peak	17%	17%	58%	25%	67%	83%	33%	17%	30
Narrow peak	80%	20%	80%	0%	33%	80%	0%	20%	16
Dish shape	43%	29%	57%	0%	71%	86%	29%	43%	31
Dish + peak	50%	50%	50%	0%	75%	100%	0%	25%	50
Central dip	40%	20%	60%	40%	60%	100%	40%	20%	21
Red asymm.	50%	50%	50%	25%	75%	100%	25%	25%	14
Blue asymm.	50%	25%	50%	25%	50%	100%	25%	25%	21

Table 3.9: K–S test of the line profile ratio feature of different MYSO classes under the CLO13 sequence

Bolometric luminosity K–S test	D–value	p–value
All MYSOs vs Type II	0.23	0.96
All MYSOs vs Type III	0.14	0.99
All MYSOs vs Type IV	0.10	0.99
Type II vs Type III	0.33	0.85
Type II vs Type IV	0.33	0.70
Type III vs Type IV	0.17	0.99

sequence.

I analysed whether the different features seen in the line ratios correlate with the C13 evolutionary sequence. However, it is difficult to classify objects in this sample according to the C13 evolutionary sequence as the GNIRS K spectral band only starts at 2.147 μm. Due to this, the H_2 2.12 μm line cannot be detected, which is paramount for the C13 classification scheme. Regardless of this, I have classified the GNIRS objects according to this scheme by using the Br and fluorescent FeII transitions, and the H_2 2.240 μm line in lieu of the 2.12 μm line, as well as adopting classifications from C13 or Chapter 2 where there were targets in common. The profile ratio features seen were assigned classes from 1–6, corresponding to central dip, wide peak, flat, dish shape, dish + narrow peak and narrow peak respectively. There were no Type I objects found in this sample. Figure 3.20 shows histograms of the types of wind features seen in objects in each of the Type II, III and IV evolutionary classes. Type II objects seem to display only wide peak line ratio profile features, although this may be because the relatively low number of Type II objects in this sample. Although the histograms do look relatively different, K–S tests (see Table 3.9) show there is no significant difference between the C13 types in terms of profile ratio features, with all histograms being drawn from the same initial distributions as the p–values are larger than 0.05.

It is possible that the profile rations arise due to inclination effects. In other words, the more accelerated the wind profile is seen in the ratios, the higher the inclination angle of the disc. In a face–on MYSO one would see the outflow cavity directly, and the wind would be accelerated, whereas in an edge–on system the wind would appear decelerated as the material towards the line of sight would be optically thicker in this case. The simulations of Krumholz *et al.* (2005) find MYSOs develop bubbles around their poles where radiation pressure escapes, and winds from these regions would be seen as accelerated. However, there are few objects that have been directly imaged and for which inclinations with respect to the line of sight are available. So, testing whether the profile ratio features observed are caused by the range of inclinations of MYSOs is not possible at the present time.

3.9.3 HII region contributions to recombination lines

In the previous sections all of the Brγ line luminosity was attributed to accretion. However, this assumes that there is no contribution from low density ionised gas like that of an HII region. Here I assess the plausibility of this assumption by analysing the possible presence of an HII region in the sample objects.

Firstly, one would expect a much stronger Brγ line (4–5×continuum level) than what is observed in this survey, where the average Brγ strength is 1.3×continuum. Recombination lines in HII regions are also narrower compared to the sample average of 150 km/s (typical FWHM of 30–40 km/s e.g. Lumsden & Puxley 1996, Burton *et al.* 2004).

In addition, another means of revealing the presence of an HII region is by detecting strong free–free emission at 5 or 9 GHz. Most of these MYSOs are undetected at these radio frequencies at the 0.5 Jy level (Urquhart *et al.* 2009b, or in subsequent RMS database observations).

Several of the sources have been observed at high–resolution in the sensitive radio observations of Rosero *et al.* (2016). Their morphologies show little evidence of an HII region structure. Instead, the radio continuum is dominated by jet emission. Following Purser *et al.* (2016) I produce a plot of radio flux as a function of bolometric luminosity in Figure 3.21 and compare the MYSOs with expected values for HII regions from Davies *et al.* (2011) and jets from Anglada (1995). Given their bolometric luminosity, almost all of the sources are too faint in the radio to be an HII region. Four objects are detected at 9 GHz (G110.1082B, G076.3829, G111.5423 and G010.8411), with only G110.1082B being close to the HII region line. However, this MYSO is located 5” away from an HII region (G110.1082A), and the radio flux is integrated over both A and B sources.

Given the above, I conclude that the contribution of HII region emission to the total Brγ flux is minimal for MYSOs in the GNIRS sample.

3.9.4 Intrinsic photospheric absorption effects

Following from the identification of absorption lines in a number of targets (see Section 3.7.1), I investigate the effect of intrinsic stellar photospheric absorption lines on the observed Brγ/Br12 wind line ratios.

The previous surveys of HI line ratios in MYSOs have considered that the emission seen in these lines is dominated by the wind. Given the structure of the MYSO, it is likely that its atmosphere also produces HI absorption lines. However, these have not been taken into account previously. The reason for this is that most other surveys studied the Brα/Brγ ratios, and at their respective wavelengths strong hot dust excess emission is present. This would dilute the effect of any intrinsic absorption to the point where it would be unobservable. However, when studying the Brγ/Br12 ratio, it is likely that while at the K−band excess due to hot dust emission will be strong, the H−band excess will be smaller. In addition, as detailed in Section 3.7.1, some MYSOs are likely to be swollen up due to accretion, which would cause them to be more like A supergiants, which have HI absorption lines $\sim$3 times stronger than OB stars. Two objects displayed only absorption in HI, and a few others showed clues of both emission and absorption. As such, I investigate the effect that photospheric absorption lines have on HI line ratios, with a focus on the object S106IRS, for which the excesses has been calculated in Section 3.5.

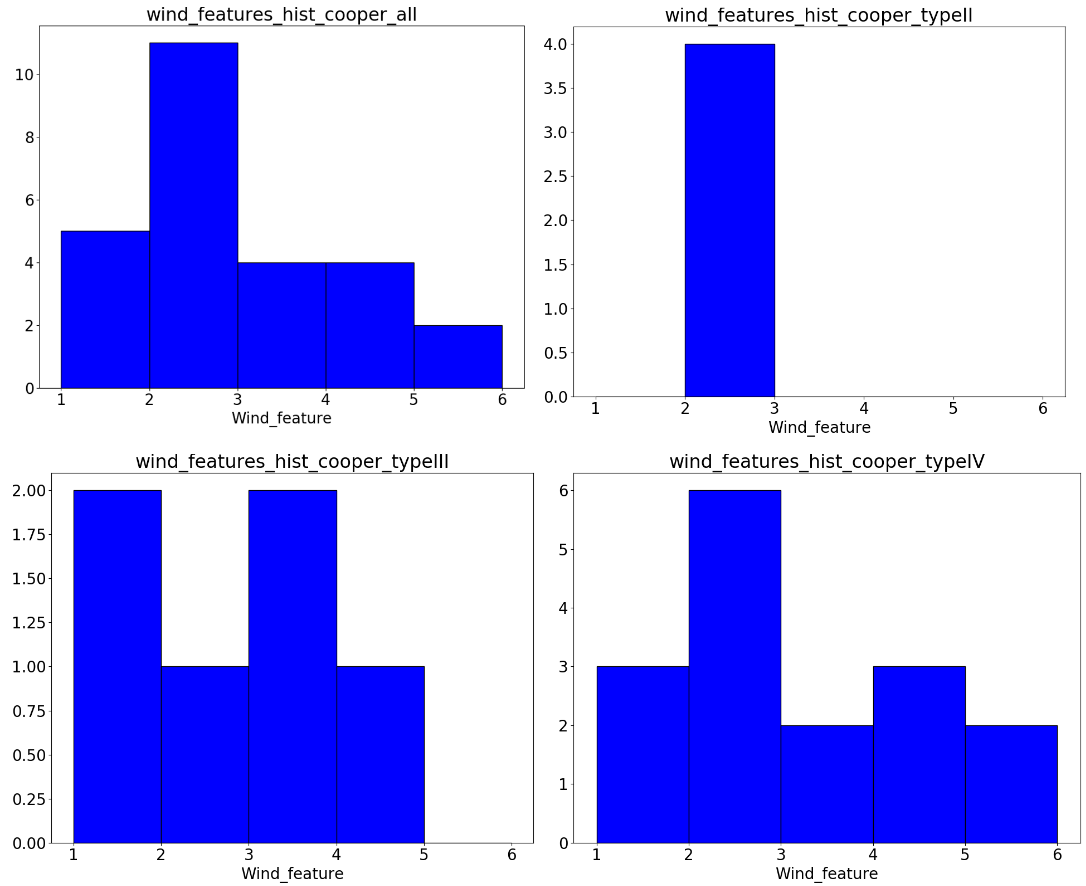

Figure 3.20: Histograms of line profile ratios in Brγ/Br12 with CLO13 evolutionary types. The line profile ratio features correspond as follows: 1– central dip; 2 – wide peak; 3 – flat; 4 – dish shape; 5 – dish shape with a narrow peak; 6– narrow peak. Top left – all MYSOs classified under the CLO13 scheme. Top right – CLO13 Type II MYSOs. Bottom left CLO13 Type III MYSOs. Bottom right – CLO13 Type IV MYSOs.

Three elements that give rise to the observed HI profile are considered: emission from winds, photospheric absorption and hot dust excess emission. I choose both the emission and absorption to follow a Lorentzian profile, with the same shape for Brγ and Br12. Their line ratio would then be flat for pure wind emission, making it easier to see differences arising due to the presence of intrinsic photospheric absorption. The emission lines are defined as formed in the optically thin regime (Brγ=5×Br12), and with a FWHM of 200 km/s (matching the observed emission FWHM). The absorption dips to 0.9×continuum with a FWHM of 200 km/s, similar to spectral profiles of normal stars. The continuum is defined as that of a blackbody, and so as per the RJ approximation the ratio of the flux density in the H–band (for Br12) to that in the K–band (for Brγ) will be proportional to λ^{-4}. So the continuum will be three times stronger in the H–band than in the K–band. The excess is chosen to be flat across a line profile, as the dust emission will not vary significantly over the 2000 km/s range over which Brγ and 12 are respectively studied. The top two best SED–fitting models for G076.3829 predicted a stellar radius of 152.2 and 7.4 $R_\odot$, temperatures of 5563 and 37410 K, luminosities of 1.9 and $9.7\times10^4 L_\odot$ and masses of 17.2 and 26.32 $M_\odot$ respectively. The first model predicts a disc–less object, whereas the second one has a disc of mass of 0.15 $M_\odot$, extending from 33–1017 au. I will be referring to these two models as the disc–less and the disc models respectively. The strengths of the excesses are chosen as determined for the two top best fitting models of G076.3829, as 0.05 × the continuum at H and 3.6 × the continuum at K for the disc–less model, and 76 and 250 × continuum at H and K respectively for the disc model. In addition, the strength of the emission is chosen such that the resulting final peak strength of Brγ is 2 × stellar continuum at K and that of Br12 is 1.2 × stellar continuum at H, which are the observed line–to–continuum ratios in S106 IRS1.

After adding all the three components, the continuum is subtracted, and the ratio of Brγ and Br12 is plotted in velocity space (see Figure 3.22), similar to the method used to produce Figure 3.19 in Section 3.9.2. Figure 3.22 shows the effect of intrinsic stellar absorption lines for G076.3829 for the case of no extinction, with the three figures representing the resulting Brγ/Br12 ratio for no excess, excess as given by the disc–less model and excess from the disc model. The three plots are relatively similar, with the final ratio showing a minimum of varying

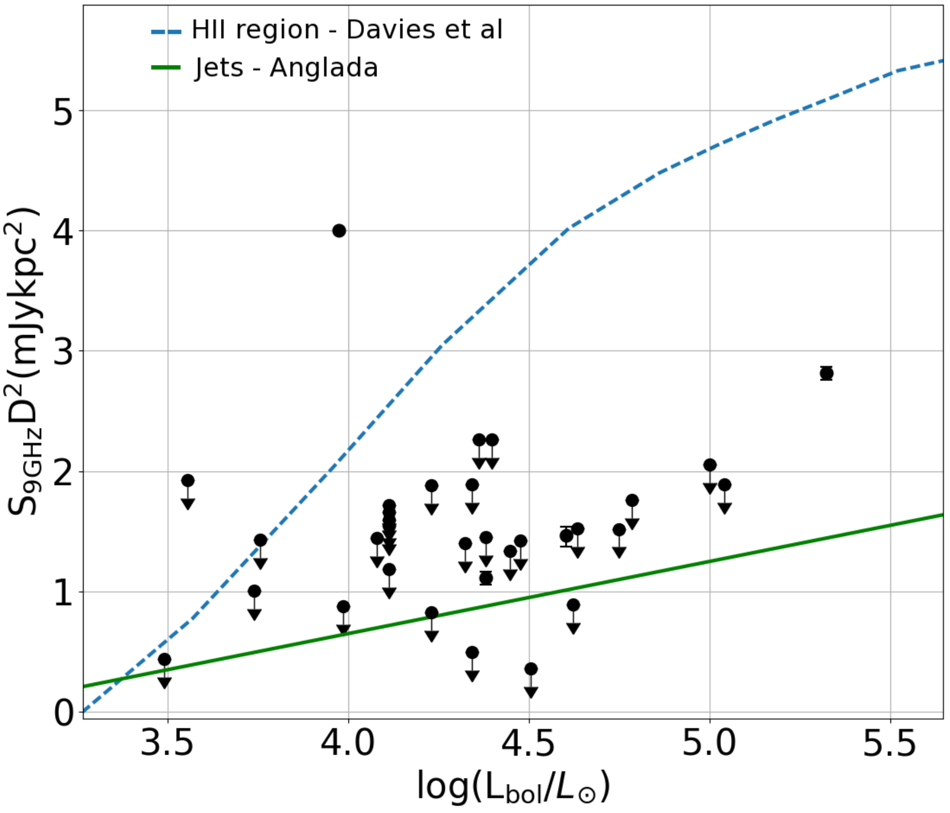

Figure 3.21: Radio flux at 9 GHz of the GNIRS MYSOs, taken from the RMS database when available, as a function of bolometric luminosity. HII regions are expected to be found close to the dashed blue curve, as per the models of Davies *et al.* (2011), whereas MYSO that should be jets are closer to the green line, resulting from a fit to observations by Anglada (1995).

strength relative to the intrinsic Brγ/Br12 ratio. The relative peak strength of this minimum varies, from 5% of the base level of the ratio for the disc–less case to 0.05% for the disc model. For comparison, if no excesses were present, the effect would be a minimum of 4–5%. In the disc–less model, the relative absence of H–band excess coupled with the presence of a relatively low K–band excess means the effect is not much different than that when no excess is present. In the disc case, the excess is so high that the resulting line–continuum strength increases considerably for both lines. This dilutes the effect of the intrinsic absorption by a factor of almost 10.

The next step was to quantify the effect of dust extinction, by dereddening the Brγ and Br12 profiles before producing the ratio. I looked at how the line ratio changes for moderate (A_V=10 mag, 3.23) and high (100 mag, 3.24) extinction. For the disc–less model, the resulting effect at moderate extinctions is similar to what was observed for no extinction (5% minimum), and increases to $\sim$ 10% for high extinction (see top panels of Figures 3.23 and 3.23). In the disc case, the effect becomes a wider parabola across the observed range, which changes shape at high extinction (see Figure 3.23). The parabola arises due to the increase in the line–continuum strength, more so in the wings than the core, due to the high excesses. The change in the shape of the ratio comes across as the continuum–subtracted Br12 becomes stronger than the Brγ when correcting for a high extinction. The numerical value of the ratio is much lower in the high extinction case (Brγ/Br12=0.0125 in the core), as Br12 becomes unrealistically strong relative to Brγ due to the large extinction correction applied.

Another interesting result is that, for a given excess, the acceptable ranges of A_V can be predicted. Given that the optically thick limit for the ratio is 0.33 and the the optically thin limit is 5, any values of extinction that lead to ratios outside this range are clearly not realistic. For the disc–less model one would expect the extinction to be between 30–70 mag at V, and for the disc model between 2–50 mag. The value of extinction determined from the H–band continuum slope for G076.3829 from this data set was 31 ± 5 mag, in agreement with ranges from either of the disc or disc–less models. So, the extinction and excess have a complementary effect in reducing the numerical value of the line ratio. It is worth noting that it is difficult to estimate either the extinction or the excess without

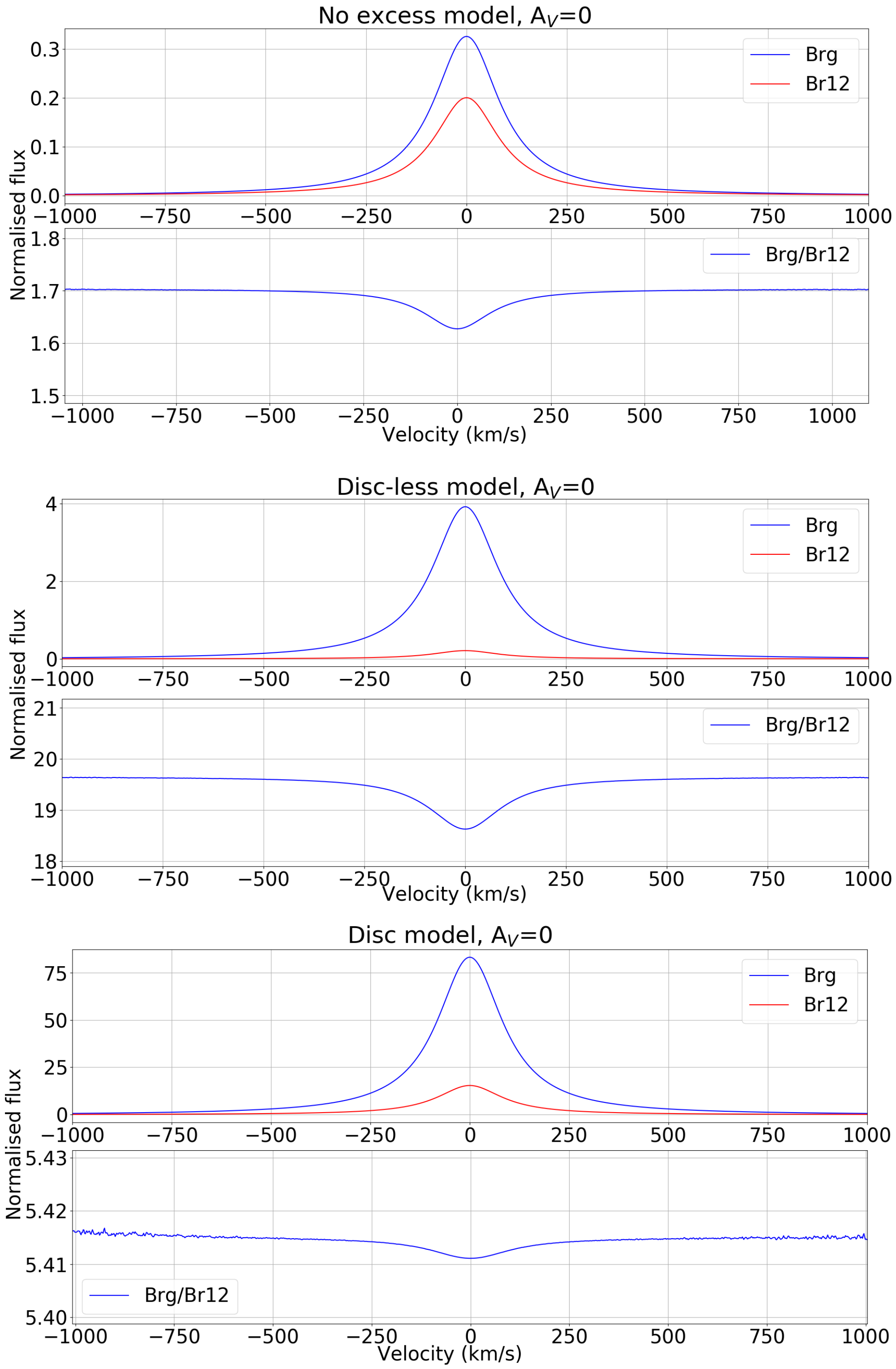

Figure 3.22: Investigation on the effects of photospheric absorption lines on HI line ratios. The top subpanel is the continuum subtracted Brγ – blue and Br12 – red. Bottom subpanel is the ratio of these two. The top plots show the zero excess case, the middle the disc–less model and the bottom the disc model

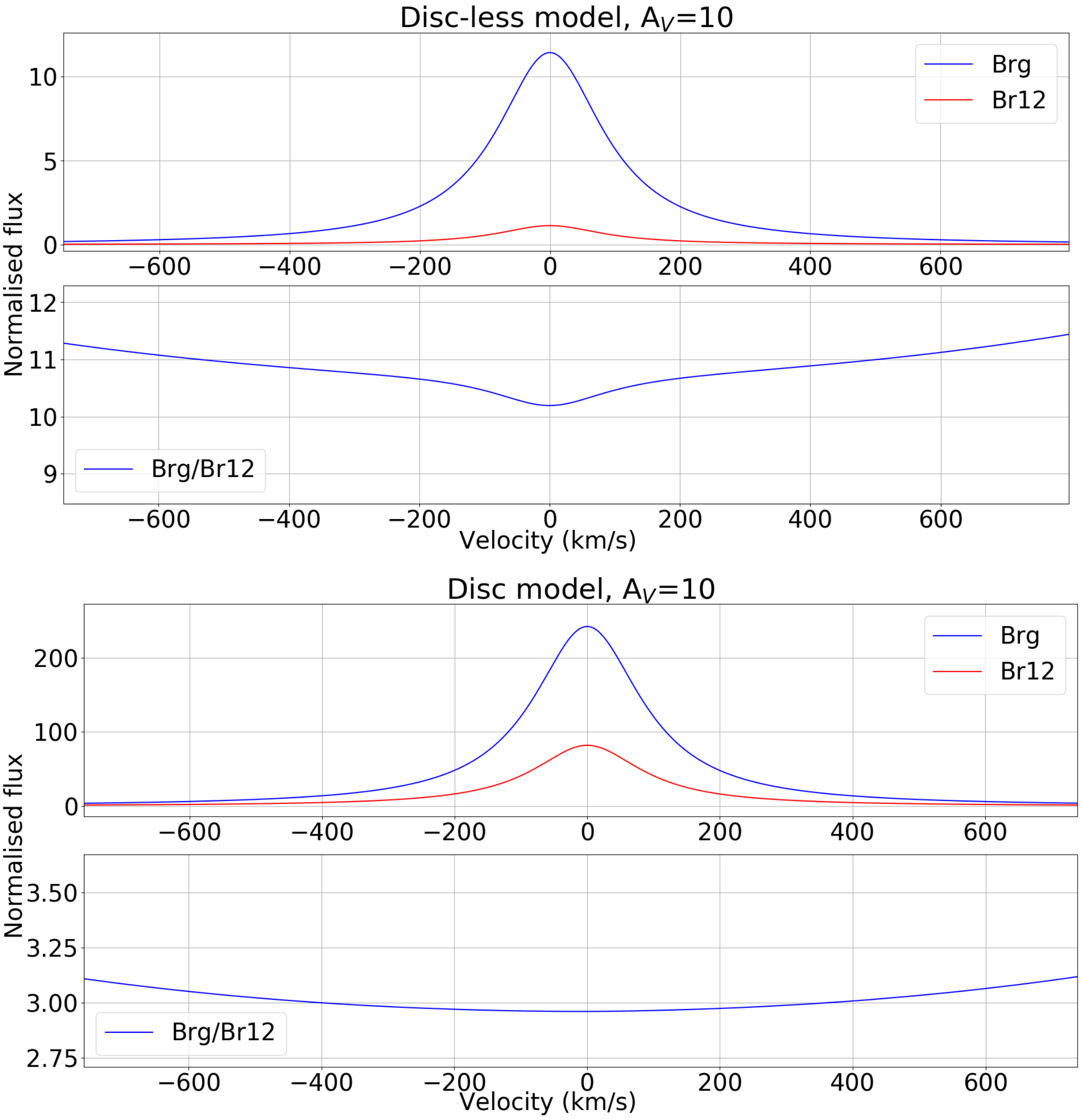

Figure 3.23: Investigation on the effects of photospheric absorption lines on G076.3829 Brγ/Br12 line ratios, adding an extinction correction of A_V=10 mag. Top subpanel is continuum subtracted Brγ – blue and Br12 – red. Bottom subpanel is the ratio of these two. Top plots are for the disc–less model, bottom ones the disc model.

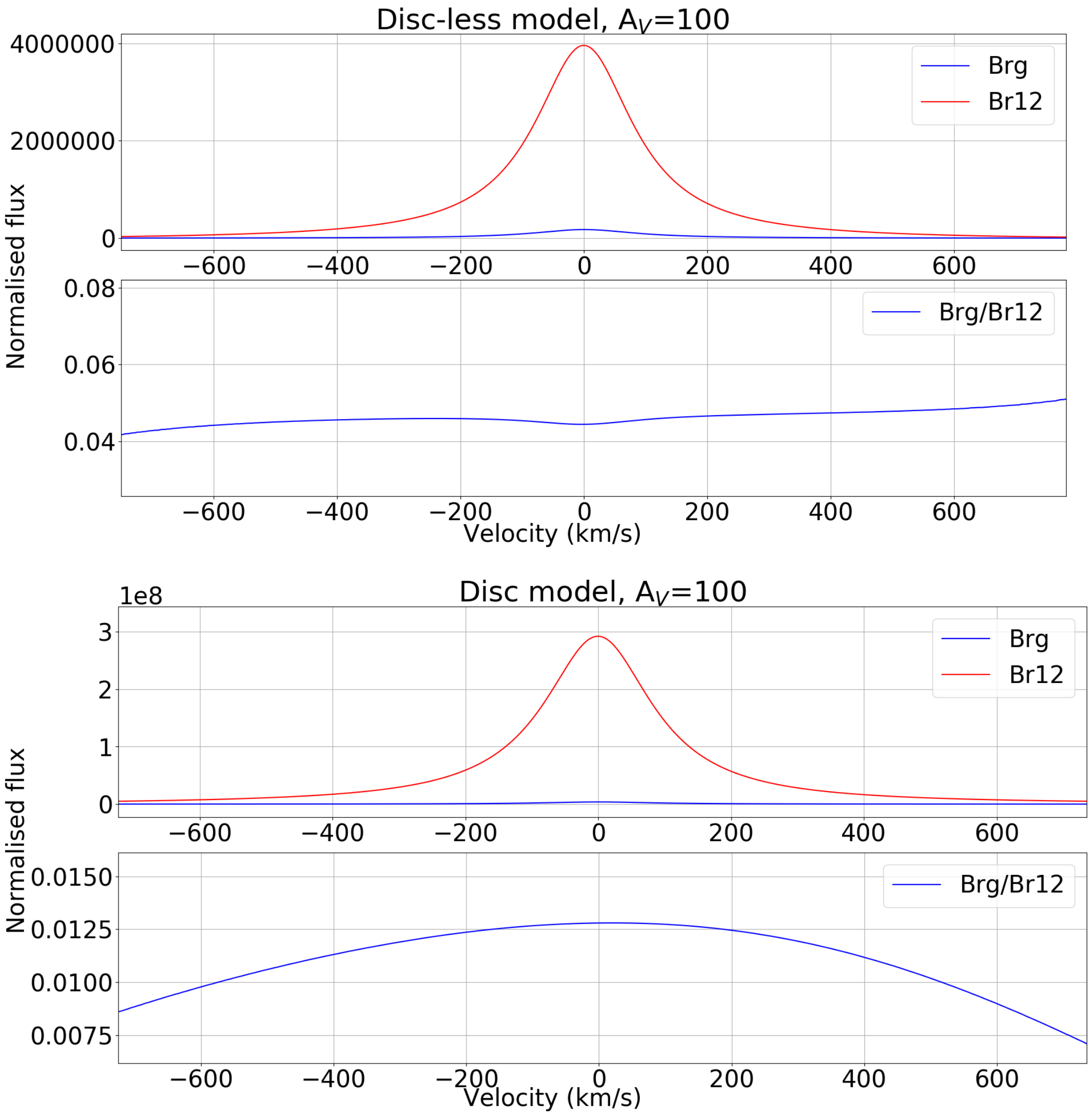

Figure 3.24: Investigation on the effects of photospheric absorption lines on G076.3829 Brγ/Br12 line ratios, adding an extinction correction of A_V=100 mag. Top subpanel is continuum subtracted Brγ – blue and Br12 – red. Bottom subpanel is the ratio of these two. Top plots are for the disc–less model, bottom ones the disc model.

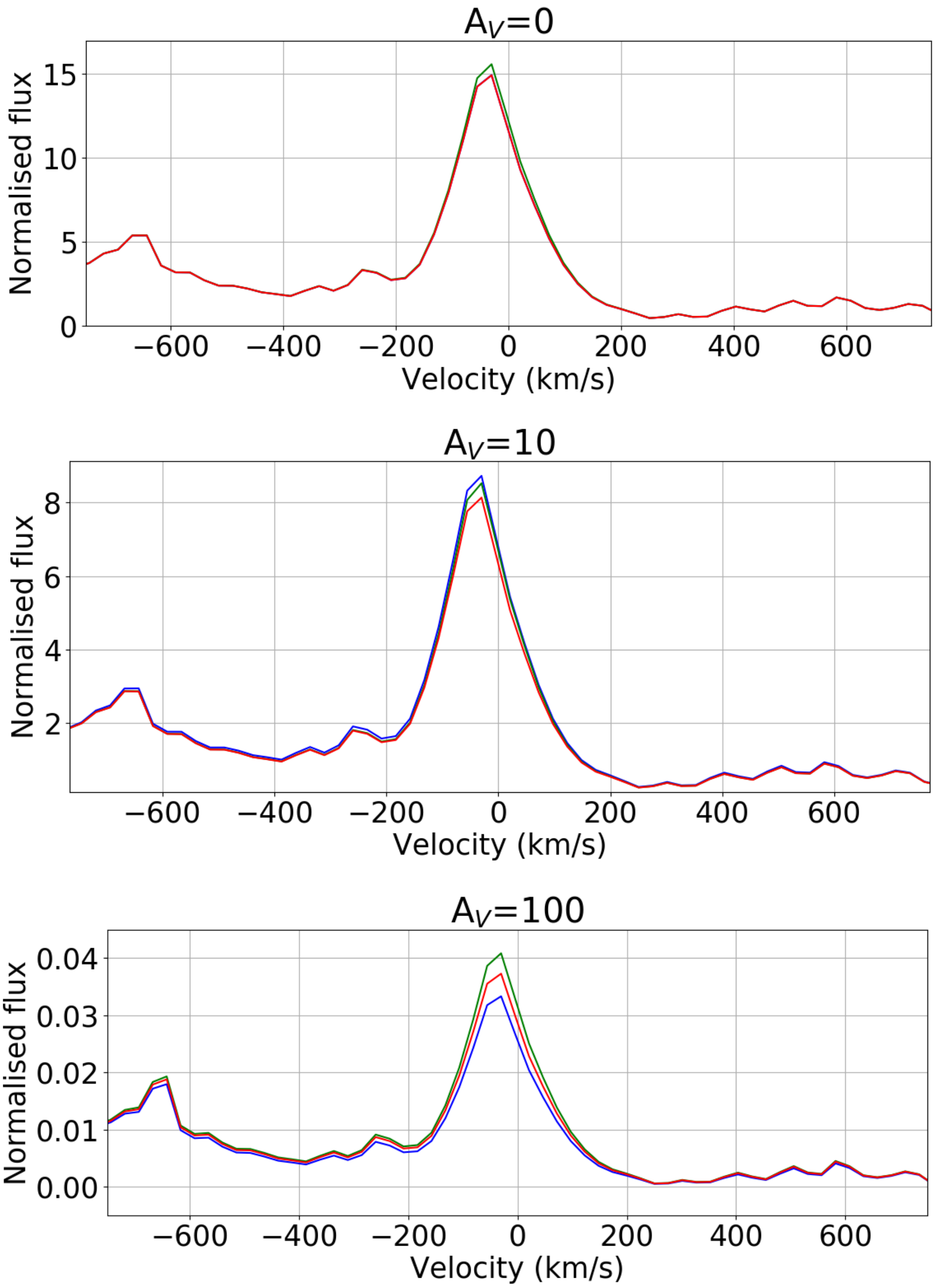

Figure 3.25: Investigation on the effects of photospheric absorption lines on G076.3829 Brγ/Br12 line ratios. The Brγ/Br12 ratio from the observed spectra is divided by the intrinsic absorption effect, as displayed in Figures 3.23–3.24. Top plot is no extinction, middle is A_V=10 mag and bottom is 100 mag. The red line is the initial observed ratio, the blue line correcting with the effect deduced from the disc model at the given extinction, and the green line from the disc–less model.

knowledge of the other parameter, as they are strongly intrinsically connected. The final step is quantifying the effect of the intrinsic absorption on the measured HI line ratios in G076.3829. The observed ratio of Brγ/Br12 in G076.3829, as plotted in the middle of the top panel of Figure 3.19, is divided by the intrinsic absorption line ratio effect (as plotted in Figures 3.22–3.24), for both the disc–less and disc models, for different extinction values. The results are displayed in Figure 3.25, with the initial observed ratio in G076.3829 plotted in red, the correction in the disc–less model case in green and in the disc case in blue. The three panels represent the three regimes of extinction considered, none, moderate and high. It is easy to see that the central peak of the observed ratios is still there for any choice of extinction or excess. The numerical values of the ratio at the peak may change by as much as 10%, but the profile of the ratio, and as such any broad conclusions that are to be drawn will be the same even if the effect of intrinsic photospheric lines are present. I conclude that as long as observed line ratio features are stronger than 10% of the continuum, the effect of the intrinsic photospheric absorption is unlikely to affect observed features.

3.10 Conclusions

This chapter has presented medium–resolution echelle NIR spectroscopic data for 36 MYSOs from the GNIRS instrument on the Gemini–North telescope. Nearly a third of these constitute the first NIR spectra taken for these objects. This is the largest sample of MYSOs studied at this resolution at these wavelengths of MYSOs to date. Dust extinction is estimated from the slope of the continuum in the H–band. The main findings are as follows:

- I have found photospheric absorption lines for one object, G015.1288. These lines indicate that this source is best described by an A giant or supergiant. An MYSO with such a configuration is consistent with the simulations of swollen up MYSOs of Hosokawa *et al.* (2010) and Haemmerlé & Peters (2016). This is the first observational detection of a swollen up MYSO to date.

- The detection rates of P Cygni and inverse P Cygni profiles in HI recombination lines are 13 and 8% respectively, lower than values reported for Herbig Ae/Be stars. The significantly lower detection rates of P Cygni and inverse P Cygni features than in Herbig stars may be due to higher dust excess emission in MYSOs, which results in a dilution of the P Cygni absorption features. This is consistent with the accretion changing from a process moderated by the stellar magnetic fields in TTaus and HAes to a different mechanism in HBes and MYSOs.

- The accretion luminosities and rates from Brγ agree with results for lower mass sources, providing tentative evidence for a continuity of star formation processes across a large mass range.

- 75% of the lines of interest studied in this survey correlate with one another in terms of luminosity. This may be due to correlations with stellar luminosity.

- Brγ/Br12 line profile ratios show a wide variety of features, possibly corresponding to a range of wind properties. Ratios corresponding to accelerated, constant or decelerated wind characteristics are seen, as well as traces of wider regions of different optical thickness.

- There is no correlation between line ratio features and luminosity, NIR colours or Cooper (2013) MYSO Types. The observed variety of features may be caused by inclination effects.

- The effects of intrinsic photospheric absorption on the line ratios in S106IRS1 were analysed for both none, moderate and high dust extinction and excess. The effect is the strongest for the largest amount of dust extinction and excess. However, it is never more than 10% of the value of the line ratio. This suggests that Brγ/Br12 features that are less than 10% stronger than the base ratio value may be arising due to photospheric HI absorption lines rather than the stellar wind.

The results presented in this chapter provide a wealth of information about the circumstellar region of MYSOs, highlighting the value of using NIR spectroscopy in understanding this class of objects and massive star formation in general. These observations are consistent with a picture of high–mass star formation that is similar to the low–mass case, as predicted by the monolithic collapse model. Most MYSOs seem to have a circumstellar disc which facilitates accretion, with jets and outflows removing angular momentum. The accretion process itself is likely proceeding through the disc, perhaps in a manner similar to the boundary layer accretion in Herbig Be stars. There is now evidence for at least some MYSOs being swollen up, as predicted by the models of Hosokawa *et al.* (2010).

Chapter 4

A search for MYSO binaries with K–band adaptive optics imaging

4.1 Introduction

As discussed in Chapter 1, the way in which massive stars form poses a number of challenging problems. A large binarity of the MYSOs is a by–product of both the monolithic collapse and competitive accretion scenarios. This binarity could be due to disc fragmentation (Krumholz *et al.* 2009), capture (Moeckel & Bally 2007), or as a result of the dense environment in competitive accretion (Bonnell & Bate 2006). Whereas the monolithic collapse scenario predicts binary separations of order 1000s of au (Krumholz *et al.* 2012), the captured binaries in competitive accretion quickly become close at separations of less than 10 au (Bonnell 2005). Knowing the binary properties of massive young stars is particularly important as the study of massive stars has seen a step change over the past decade. Since the final gaps in binary parameter space were filled in by Sana *et al.* (2012) and Chini *et al.* (2012) it has become clear that the binarity of massive stars is not only ubiquitous with a binary fraction close to a 100%, but also that binarity will significantly affect the evolution of massive stars: the companions of 70% of these massive stars are sufficiently close for binary interactions to occur. Sana *et al.* (2012) also found that 33% of the stars in binary systems will lose a significant fraction of their envelope through accretion by a companion. This figure agrees with results from supernova counts (as discussed by Williams 2015), 38% of which are type Ib, Ic or IIb. All of these supernova types are the end point in the evolution of stars with a hydrogen–poor atmosphere, consistent with stripping by a binary companion. As a result the evolution and fate of a massive star is also governed by its binary properties, rather than only by its initial mass as in the single star evolutionary scenarios (see eg. Smith & Tombleson 2015).

However, observationally nothing is known about the binary statistics of young massive stars. The binary frequencies alluded to above have only been measured for Main Sequence stars. These will not reflect the primordial binary properties as they will have been affected by secular evolution such as dynamical processes (see the review by Kratter 2011). An important question to address however is how these binaries were formed and evolved. As of now, we know hardly anything about the binary properties of massive pre–Main Sequence stars. Such studies have been few and far between, and only scarce information on individual targets has been published (Varricatt *et al.* 2013, Caratti o Garatti *et al.* 2015), but no targeted surveys have been conducted. It is interesting to note that although as mentioned above, various theories are capable of forming binaries, they have not been put to the test using observations and they have not even been informed by observations.

Baines *et al.* (2006) performed a targeted multiplicity survey of Herbig Ae/Be stars and found a binary fraction of 70% for separations $0.1 - 1.5$ arcseconds. and Wheelwright *et al.* (2010) determined that the mass ratios are close to unity, so equal mass binary systems are favoured for these intermediate mass stars. This agrees with simulation results of Bate *et al.* (2002), which produce most binary systems with equal mass ratios. The separations measured in these studies of intermediate mass stars are too large for the companion star to influence the evolution of the primary. However, dynamical interactions will lead to tighter binaries over the stars' lifetime. Binaries born at separation of order 10s of au can evolve to become close, tight binaries (Kratter 2011). Triple systems are expected to be stable in a hierarchical configuration, where the ratio of separations of inner and outer components is at least 10. Non–hierarchical triple systems are unstable over ≈100 crossing times, and result in a tight binary system and the ejection of the third companion. Reipurth *et al.* (2014) point out that given the observed binary fractions of protostars, it is possible that most protostars start out in multiple systems, and interactions in non–hierarchical triple systems lead to the observed multiplicity fraction of field stars (most field stars are single, the multiplicity fraction for field solar mass stars is 46% as found by Raghavan *et al.* 2010). Given all of this, it is very important to obtain the statistics of the binarity of Massive Young Stellar Objects (MYSOs).

This chapter describes a pilot adaptive optics survey aimed at searching for MYSO binary companions. This is the first step of a larger project to determine the binary statistics of young pre–stellar objects. It will be followed by an interferometric study with GRAVITY to find tight binaries and IFU observations in order to obtain spectra of observed companions. Section 4.2 describes the sample selection and the data reduction process. Section 4.3 presents the initial results – an analysis of the completeness limits of the survey, the methods employed to eliminate visual binaries and preliminary binary statistics. A discussion on the multiplicity fraction, mass ratios, period distributions, disc–binary orbit alignment and whether the binaries are special is presented in Section 4.4. The conclusions of this work are presented in Section 4.5

4.2 Observations and data reduction

4.2.1 Sample selection

This sample of MYSOs is drawn from the Leeds Red MSX Source Survey (RMS, Lumsden *et al.* 2013), which was a galaxy–wide search for massive young stars (for a description of the survey see Section 1.4.2.1). I selected the targets based on bolometric luminosity and distance cuts, as well as declinations accessible from the ESO–Very Large Telescope (VLT). There are 58 MYSOs in the RMS survey with L>3500 $L_\odot$, d<5 kpc, $\delta < 10^o$, and K<10.5 mag. The magnitude cut was chosen such that the targets could be their own guide stars for adaptive optics (AO) corrections with NaCo. As MYSOs are located in dusty environments, most nearby stars are too faint to be used as reference for AO. The final selection of 32 targets was chosen based on right ascension in order to increase observability during the observing semester, with 6h<RA<17h.

The K–band was chosen as this is the shortest wavelength (allowing the highest spatial resolution) at which all of the heavily extincted MYSOs are still visible. It is also the shortest wavelength at which much of the emission is still due to the star itself and not completely diluted by emission from surrounding hot dust.

The survey aimed to probe the separation range from the diffraction limit of ∼70–80 mas out to the full field of view of 14×14 arcseconds. For the average MYSO distance of targets in this sample of 3.3 kpc (compared to the average RMS MYSO distance of 4.5 kpc as per Chapter 1), this means binaries with separations 230 – 23000 au can be resolved. For comparison, the separation of the MYSO binary from simulations of Krumholz *et al.* (2009) and Krumholz *et al.* (2012) was 1590 au, while the observations of Varricatt *et al.* (2013) indicate an orbital distance of 2500 au. The average K–band magnitude of the targets is 9 mag. For $\Delta K = 6$ for Main Sequence stars, companions up to 15 times less massive can be recovered (as per Fig. 4 of Oudmaijer & Parr 2010). However, this can be affected by differential dust excess emission and extinction between binary system components, so in practice the limiting mass ratio is likely lower than 15.

4.2.2 Observations

The observations were carried out in service mode between 20th Dec 2015 – 17th March 2016, with the AO system NaCo (Lenzen *et al.* 2003, Rousset *et al.* 2003) on the Nasmyth A focus of the UT1 (Antu) of the VLT at ESO. The data were taken in the K–band. This configuration results in a diffraction limit of 0.0057" or 57 mas. NaCo has a 1024×1024 pixel InSb camera, with a pixel size of 27 μm. In order to obtain the highest spatial resolution, the S13 camera mode was used, with a plate scale of 13.27 mas/pixel, resulting in a field of view of 13.6×13.6 arcsec^2.

The Ks broadband filter was chosen in order to probe down to the lowest possible limiting magnitude in the shortest exposure times. This filter is centered on 2.18 μm and has a width of 0.35 μm. Due to a technical fault during the observing period, 1 in 8 columns in the lower left quadrant of the NaCo detector had no signal. As such, the targets were centered in the upper right quadrant, achieving full coverage only for distances ∼3" away from the main source. As it turned out, the fault in the 4th quadrant did not hamper the detection of companions in this part of the image. For each of the targets, two object frames were taken in auto–jitter mode with a box size of 2.5×2.5 arcsec^2. Two other jittered sky frames were taken at 6" away from the main target. The detector integration times were 80s per frame for targets of magnitude K >7.5, and 60s for brighter targets , split over 4 exposures in order to avoid saturation. With the addition of the overheads, the total time spent per target was 17 minutes. I observed a total of 32 targets, which add up to just over 9 hours of NaCo time for the whole programme. The seeing (in the V–band) was 1.7" or smaller, with an average of 1.1". The average airmass was 1.3, which ensured good AO corrections. Information about the observations is presented in Table 4.1.

The data were reduced with the ESO pipelines interfaced through the GASGANO software. Bad pixel maps, dark, twilight and lamp flat–field frames were provided for each observation. The dark current subtraction and flat field division were performed first, followed by bad pixel correction and sky subtraction. I cross–checked the GASGANO pipeline reduction with manual PyRAF routines, and the results from these two methods were consistent.

The quality of the AO correction is quantified in terms of the Strehl ratio (SR), usually given as a percentage between 0–100%. This parameter is given by the ratio of the peak intensities of the AO–corrected point–spread function (PSF) and the uncorrected PSF. The AO correction effectively sharpens the peak of the PSF and so increases the PSF core–wing ratio. The resulting images are therefore sharper (useful for detecting faint companions) but of lower photometric quality. The record for SR achieved is 80%, with the best achievable in K–band is usually 35–60% under ideal photometric observing conditions (see Davies & Kasper 2012 for a review of AO).

The average FWHM of the point sources is 0.12", and the average Strehl ratio 18%. Because the data were taken in bad weather, and the AO correction was performed using NIR rather than optical data, the SR achieved are not very high. An example of the data is shown in Fig 4.1.

Table 4.1: Source list, including observation conditions and quality. 1 – Magnitudes from 2MASS; 2 – distances from Urquhart *et al.* (2011a), they carry an uncertainty of order 1 kpc; 3 – luminosities calculated by Mottram *et al.* (2011b); uncertainties on bolometric fluxes are of the order 20%, combined with distance uncertainties they result in errors in bolometric luminosity of order 10^4 $L_\odot$; 'Mult?' indicates whether the targets have any detected companions, SR is the Strehl Ratio of the given observation.

Date	Object name	Mult?	Texp (s)	RA (J2000)	Dec (J2000)	*J*	*H*	*K*	D (kpc)	Lbol ($L_\odot$)	Mass ($M_\odot$)	Airm. (”)	Seeing mag	SR	Lim mag
20.12.2015	G212.0641-00.7395	N	160	06:47:13	+00:26:06.5	14.3	12	10	4.7	16000	14.5	1.33	0.75	5.3%	13.5
20.12.2015	G221.9605-01.9926	Y	160	07:00:51	-08:56:30.1	14.2	11.4	9.2	3.2	5500	10	1.22	0.67	14.7%	13.4
25.12.2015	G231.7986-01.9682	N	120	07:19:36	-17:39:18.0	9.2	7.8	6.4	3.2	5600	10.1	1.4	1.6	25.1%	14.5
25.12.2015	G232.0766-02.2767	Y	160	07:19:00	-18:02:41.6	13.4	12	10.4	3	5000	9.7	1.01	1.1	4.7%	13.3
27.12.2015	G232.6207+00.9959	N	160	07:32:10	-16:58:13.4	13.1	12.4	8.3	1.7	11000	12.5	1.21	0.75	21.4%	14.8
25.12.2015	G233.8306-00.1803	N	120	07:30:17	-18:35:49.1	10.9	8	6.1	3.3	13000	13	1.02	1.1	25.0%	13.9
22.12.2015	G268.3957-00.4842	Y	160	09:03:25	-47:28:27.5	15.7	11.8	8.3	0.7	3000	7.8	1.22	0.71	21.2%	15.3
27.12.2015	G282.2988-00.7769	Y	120	10:10:00	-57:02:07.3	10.2	8.4	7	3.7	4000	8.6	1.19	1.5	50.0%	14.5
04.01.2016	G287.3716+00.6444	Y	160	10:48:05	-58:27:01.5	10.4	8.9	7.5	4.5	18000	14.9	1.21	0.85	40.0%	14.3
04.01.2016	G290.3745+01.6615	Y	160	11:12:18	-58:46:20.8	12.2	10	8.6	2.9	15000	14	1.21	1.3	20.4%	13.4
10.02.2016	G293.5607-00.6703	N	160	11:30:07	-62:03:12.8	14.9	12.2	9.5	3.4	4000	8.6	1.27	1.2	3.0%	12.7
10.02.2016	G300.1615-00.0877	N	160	12:27:09	-62:49:44.2	15.7	12.1	9.3	4.2	5600	10.1	1.39	1.3	13.7%	14.9
10.02.2016	G300.3412-00.2190	N	160	12:28:36	-62:58:35.4	13.3	10.7	8.7	4.2	6000	10.8	1.46	1.4	19.6%	14.9
10.02.2016	G301.1726+01.0034	N	160	12:36:32	-61:49:02.8	12.7	10.2	7.9	4.3	21000	15.8	1.27	1.55	23.1%	14.3
10.02.2016	G301.8147+00.7808A	Y	160	12:41:54	-62:04:14.6	12	9.3	6.8	4.4	22000	16.1	1.29	0.95	24.9%	14.2
10.02.2016	G305.2017+00.2072A	N	160	13:11:10	-62:34:38.6	14.2	11.7	9.4	4	30000	18	1.27	0.9	12.4%	13.8
10.02.2016	G305.3676+00.2095	Y	160	13:12:36	-62:33:32.3	14.8	13.1	10.4	4	16000	14.5	1.27	1.2	4.8%	14.4
10.02.2016	G305.5610+00.0124	N	160	13:14:26	-62:44:30.4	15.7	12.6	9.7	4	12000	12.8	1.28	0.85	10.3%	12.3
10.02.2016	G305.6327+01.6467	N	120	13:13:48	-61:06:28.8	8.6	7.5	7.2	4.9	16000	14.5	1.3	1.1	24.6%	14.4
12.02.2016	G309.9796+00.5496	N	160	13:51:03	-61:30:14.1	15.9	12.4	9.7	3.5	7600	11.2	1.28	0.9	10.1%	13.5
10.02.2016	G310.0135+00.3892	Y	191	13:51:38	-61:39:07.5	11.8	7.6	4.9	3.2	67000	23.6	1.45	1.1	24.9%	15.1
12.02.2016	G311.4402+00.4243	N	160	14:03:07	-61:15:27.9	14.3	10.3	7.8	3.6	7100	10.9	1.25	1.05	23.5%	12.7
10.02.2016	G320.1542+00.7976	N	160	15:05:17	-57:31:40.0	11.2	10.3	9.8	2.5	5400	9.5	1.38	1.7	9.2%	13.8
10.02.2016	G326.4755+00.6947	Y	160	15:43:19	-54:07:35.4	15.4	12.4	9.3	1.8	4100	8.6	1.49	1.5	13.7%	13.9

10.02.2016	G327.9455-00.1149	N	160	15:54:35	-53:50:42.1	15.8	12.5	10	3.1	4300	9.3	1.38	1.4	5.3%	13.4
20.03.2016	G331.3576+01.0626	N	160	16:06:26	-50:43:22.0	12.6	11.1	9.6	4.5	18000	15	0.7	1.33	11.8%	15.1
10.03.2016	G332.0939-00.4206	N	120	16:16:16	-51:18:25.2	15.3	9.6	5.9	3.6	93000	28	1.28	1.4	25.1%	13.5
17.03.2016	G332.9868-00.4871	N	160	16:20:38	-50:43:49.6	17.6	13.7	9.3	3.6	18000	15	1.24	1.25	12.8%	13
20.03.2016	G334.7302+00.0052	N	160	16:26:05	-49:08:41.8	15.5	13	9.6	2.5	3800	8.5	1.48	0.9	2.6%	14.1
17.03.2016	G336.4917-01.4741B	N	160	16:40:01	-48:51:52.4	11.7	10.3	8.8	2	12000	14	1.24	1.2	19.1%	14.1
17.03.2016	G339.6816-01.2058	N	160	16:51:06	-46:15:52.4	13.1	10.4	8.5	2.4	6500	11	1.21	1.1	20.5%	13.6
17.03.2016	G344.8889+01.4349	N	120	16:57:52	-40:33:26.7	14.1	10.2	7.4	2.4	7000	11.3	1.16	1.1	24.4%	14.5

Table 4.2: All detected companions, along with their separation and position angles relative to the primaries, relative K–band magnitudes and 2MASS and VVV K–band magnitudes where previously detected. 'δm' is the difference in magnitudes between the secondary and the primary. The 2MASS magnitude flag is a three-letter code (for the J, H and K–bands) which indicates the photometric quality of the observation. 'A' corresponds to detections with valid measurements at a 10σ level, 'B' at 7σ, 'C' to 5σ and D to a measurement with no σ requirement. 'U' is an upper limit on the magnitude.

Object name	Sep (")	ΔSep (")	PA (°)	ΔPA (°)	K (mag)	ΔK (mag)	δm (mag)	2MASS K (mag)	2MASS flag	VVV K (mag)
G221.9605-01.9926B	0.60	0.26	75	25	10.8	0.1	1.6			
G221.9605-01.9926C	0.70	0.26	254	21	10.6	0.1	1.4			
G221.9605-01.9926D	1.10	0.26	60	13	10.2	0.1	1.0			
G221.9605-01.9926E	1.20	0.26	254	12	11.3	0.1	2.1			
G232.0766-02.2767B	3.13	0.24	178	4	9.6	0.2	1.7	9.8	AEU	
G232.0766-02.2767C	5.58	0.24	153	2	9.3	0.2	1.4	11.3	UUE	
G232.0766-02.2767D	4.30	0.24	206	3	7.5	0.1	2.5	10.8	UUE	
G232.6207+00.9959B	6.43	0.17	77	1	13.3	0.1	5.0	10.1	UDU	
G232.6207+00.9959C	6.66	0.17	125	4	10.9	0.1	2.6	11.2	UUE	
G268.3957-00.4842B	1.92	0.12	350	1	11.7	0.2	3.4			
G268.3957-00.4842C	4.75	0.12	3	1	14.3	0.1	6.0			
G268.3957-00.4842D	8.70	0.12	94	1	14.4	0.1	6.1			
G268.3957-00.4842E	8.91	0.12	95	1	12.5	0.1	4.2	12.3	AAA	
G282.2988-00.7769B	1.57	0.12	306	4	14.0	0.1	7.0			
G282.2988-00.7769C	2.71	0.12	200	3	14.5	0.1	7.5			
G287.3716+00.6444B	1.27	0.11	121	5	12.3	0.1	4.8			
G287.3716+00.6444C	1.48	0.11	112	4	13.5	0.2	6.0			
G287.3716+00.6444D	1.82	0.11	257	3	14.7	0.2	7.2			
G287.3716+00.6444E	1.90	0.11	28	3	12.7	0.1	5.2			
G290.3745+01.6615B	0.70	0.12	153	10	11.1	0.1	2.4			
G290.3745+01.6615C	1.88	0.12	156	4	11.9	0.1	3.2			
G290.3745+01.6615D	4.06	0.12	244	2	13.2	0.1	4.5			
G293.5607-00.6703B	5.69	0.29	339	3	11.1	0.2	1.5	11.1	AEE	

G293.5607-00.6703C	4.60	0.29	90	4	13.7	0.1	4.1			
G300.3412-00.2190B	7.41	0.18	163	1	12.3	0.1	3.7	11.7	AAA	11.9
G301.8147+00.7808A_B	2.88	0.14	115	3	13.9	0.2	7.1			
G301.8147+00.7808A_C	3.91	0.14	155	2	12.5	0.1	5.7			11.3
G305.3676+00.2095B	0.88	0.15	288	10	12.7	0.1	2.3			
G310.0135+00.3892B	2.56	0.15	41	3	11.2	0.2	6.3			
G320.1542+00.7976B	2.95	0.21	162	4	10.4	0.1	0.5	9.8	UUA	
G326.4755+00.6947B	2.19	0.23	179	6	13.5	0.1	4.2			
G327.9455-00.1149B	7.35	0.21	143	2	14.5	0.2	4.5	13.7	CAA	13.9
G331.3576+01.0626B	3.80	0.17	54	2	13.4	0.1	3.8			12.8
G331.3576+01.0626C	7.80	0.17	193	1	12.4	0.1	2.8	12.0	AAA	12.5
G331.3576+01.0626D	11.25	0.17	133	1	12.9	0.1	3.3	12.0	AAA	12.6
G331.3576+01.0626E	11.41	0.17	109	1	12.5	0.1	2.9	12.2	AAA	12.1
G332.9868-00.4871B	9.14	0.23	201	1	12.1	0.1	2.8	11.4	AAA	11.5
G334.7302+00.0052B	5.79	0.24	157	2	12.9	0.1	3.3	12.0	UAA	12.3
G336.4917-01.4741B_B	4.88	0.21	98	2	12.4	0.1	3.6	11.7	CAB	12.2
G339.6816-01.2058B	8.59	0.15	85	1	12.7	0.1	4.2	13.2	UUB	13.1

4.2.3 Companion detection

I used the SExtractor software (Bertin & Arnouts 1996) in combination with the GAIA–STARLINK package to identify sources in reduced frames. If a pixel has a number of counts that is 3σ above the standard deviation of the image and it is surrounded by 8 other pixels with counts$>3\sigma$, it is considered to be part of a detected source. SExtractor provides an estimate of the magnitude of an object (MAG_AUTO), based on the first moment method of Kron (1980).

Magnitudes can also be estimated by manually defining an aperture around the source in GAIA. The results from SExtractor and aperture photometry were found to be consistent. The magnitudes presented in the following analysis are all from SExtractor.

The magnitudes of the MYSOs in the RMS database were taken from 2MASS (Skrutskie *et al.* 2006). The magnitudes of the newly detected companions were computed relative to the brightness of the main sources. Although the VISTA Variables in the Via Lactea (VVV, Minniti *et al.* 2010) survey data was also available for two–thirds of the sources, I opted for 2MASS photometry as VVV saturates for magnitudes brighter than 11 in the K–band due to the more sensitive instruments used than on 2MASS and the longer integration times. All of the targets are brighter than 10.5 magnitudes, so 2MASS primary magnitudes are more reliable. However, comparisons with VVV can still be drawn for secondary fainter sources present in this catalogue.

The astrometry is calibrated relative to the RMS catalogue coordinates of the main source. The initial astrometry solution resulting from the GASGANO data reduction requires shifts of 1–3" to reconcile with the RMS coordinates, to correct for the pointing of the telescope.

4.3 Results

The list of detected candidate companions is presented in Table 4.2. I find a total of 40 secondary sources in the NaCo images, 21 of which are new detections, not available in either 2MASS or VVV survey data. The new discoveries are fainter (average δm=4.4 mag) and closer to the primary companions (average separation 2.0") than the companions that had already been seen in the survey data (average δm=3.3 mag, average separation 6.4"). This highlights the effectiveness of adaptive optics observations over large–scale surveys for detecting new, close and faint companions.

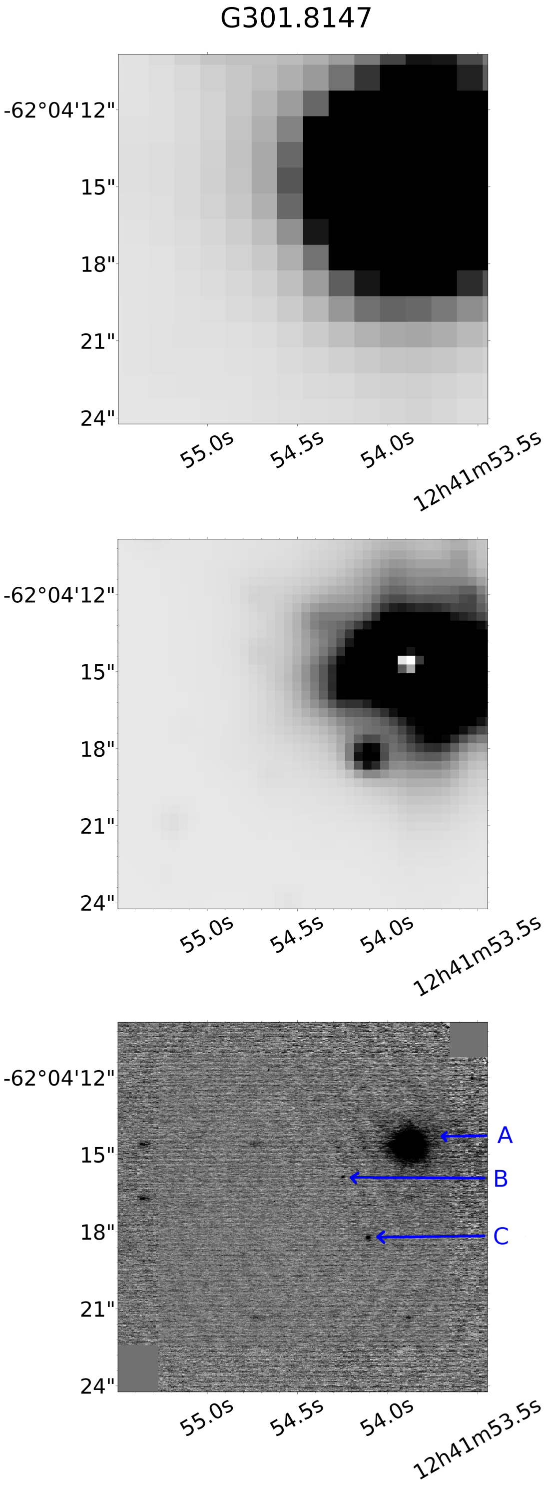

Figure 4.1: Top – 2MASS image of MYSO G301.8147A. Middle – the same image from the VVV survey; Bottom – corresponding reduced image from NaCo. The three companions in the NaCo image are indicated by blue arrows. Other black lines visible are image artefacts. Note the new companion previously undetected in VVV or 2MASS.

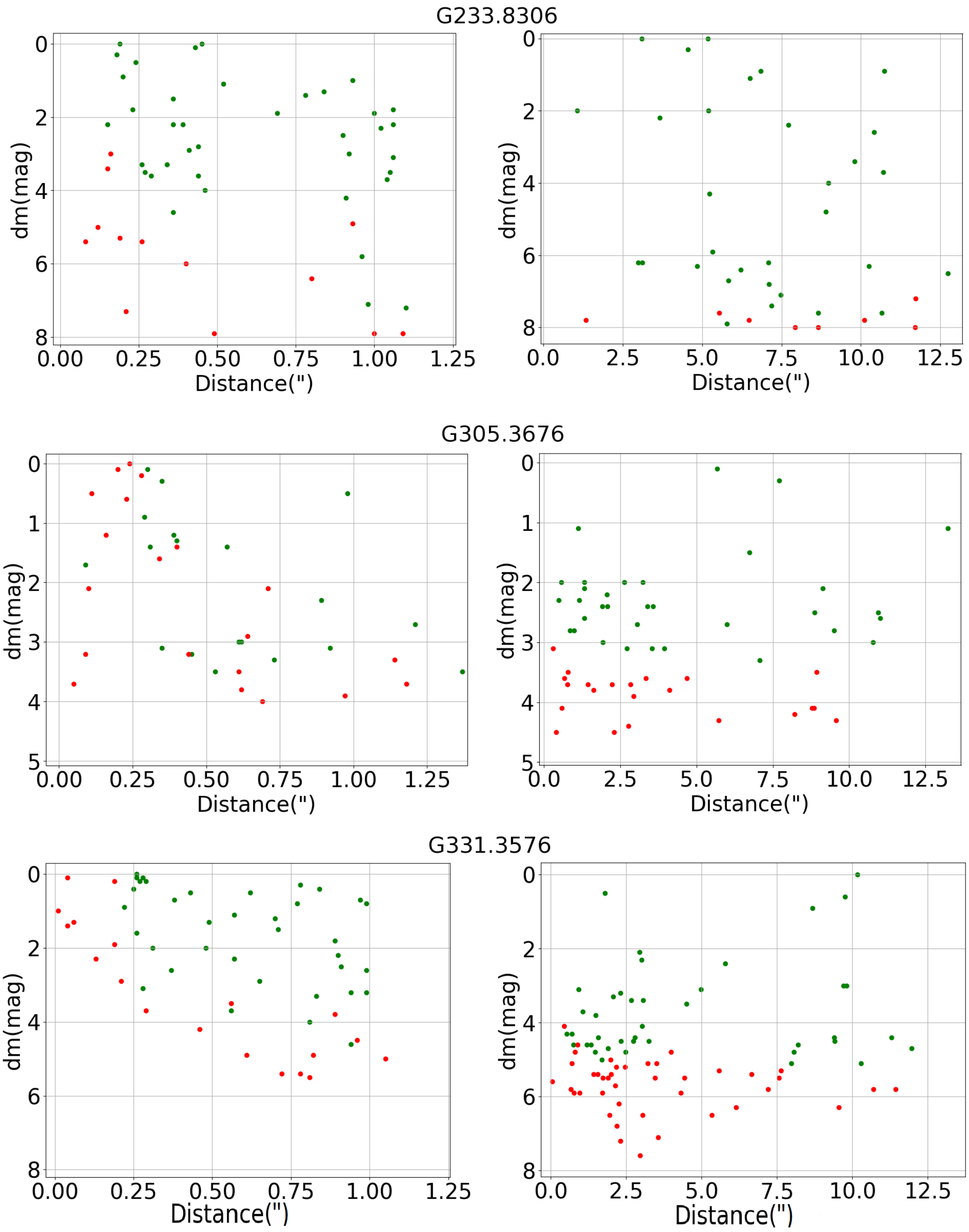

Figure 4.2: Limiting magnitude artificial source tests for G233.8306 (top), G305.3676 (middle) and G331.3576 (bottom). Red points correspond to artificial sources not detected by SExtractor at a 3σ level, and green to detected ones. Right panels show changes across all images, whereas left panels focus on the inner 1". The y–axis values are the differences in magnitudes between the artificially introduced companions and the primary source, and the x–axis the distance in arcseconds between these two.

4.3.1 Completeness analysis

The first step in analysing the completeness of the data was to calculate the limiting magnitude of the observations. This was done by placing an artificial 2D Gaussian source of the same FWHM as the main target at the center of the image. For this I used the Gaussian2DKernel function in the AstroPy.convolution package (Astropy Collaboration *et al.* 2013). The minimum flux at which the artificial source was detected at the 3σ level by SExtractor was taken as the limiting flux. The limiting magnitude was then calculated by comparing the limiting flux to the primary flux with 2MASS photometry.

The limiting magnitudes are presented in Table 4.1. The average is 14 mag, close to the 2MASS survey limits, but not quite as deep as VVV. The data probe 5.5 mag fainter than the main source on average, but at higher spatial resolution than both VVV and 2MASS.

The minimum separation at which companions can be detected is determined by the quality of the AO correction. In addition, some of the sources show extended emission due to the dusty environments they are located in. In order to determine the detection limit, I placed sources of random brightness at random distances and position angles around the main target. Three different MYSO observations were used for this, G233.8306 (FWHM of 0.08" and δm=7.5), G331.3576 (FWHM=0.11", δm=5) and G305.3676 (FWHM=0.18", δm=3). They were chosen as they are representative of the range of FWHM and magnitude differences of this survey. The results are shown in Figure 4.2, with detected artificial sources in green and non–detections in red. The limiting magnitude (that had been determined by placing an artificial source at the centre of the image) stays constant at distances larger than 1". At shorter distances, the limiting magnitude becomes brighter, with an empirical fit given by δm=(3.0±0.7) d + (2.3±0.5), where d is the separation from the main target in arcseconds and δm is the difference between the limiting magnitude and the magnitude of the primary . The minimum distance at which objects can be detected depends on the FWHM, and can be empirically quantified by $d_{\rm lim}$=1.5×FWHM.

I searched the 2MASS and VVV point source catalogues for other sources that were not detected in the NaCo image as a consistency check. Most of the missed secondary objects are either fainter than the limiting magnitude, close to the edges of the NaCo field, or untrustworthy detections as indicated by survey qual-

ity flags. 13 sources did not fit any of the above criteria, and as such were visually inspected. All of these were either part of extended emission or close enough to the limiting magnitude to explain their non–detection in the NACO images.
In conclusion, the limiting magnitudes ranges between K=12–15 mag for distances up to 1". At closer separations the limiting magnitude decreases, until d$\approx$1.5$\times$FWHM, which is the minimum distance at which a companion object can be observed. The sample is complete for ΔK=5 mag at 1–3" and ΔK=3 mag at 0.3–1".

4.3.2 Eliminating chance projections

It is important to discern whether the detected secondary sources are physical companions or simply visual binaries due to chance projection. The most conclusive way to settle this is by measuring relative motions with multi–epoch observations. Alternatively from multi–wavelength data, colour–colour and colour–magnitude diagrams can be constructed which may indicate whether secondary sources are located at the same distance as the primaries.
As only single–epoch and single wavelength data is available, I employed statistical methods to determine which objects are likely to be bound companions. Densely crowded fields are more likely to give rise to spurious companions. For their sample, Oudmaijer & Parr (2010) argue that if the density of background sources is >20 arcminute^{-2}, one would expect to find at least one chance projection in the NaCo field of 13.6$\times$13.6 arcsec^2. Correia *et al.* (2006) add distance from the primary source as a factor in determining the probability of an object being a chance projection. Assuming the distribution of unrelated sources is random and uniform over the observed field, the probability of chance alignment is given by an exponential decay with area from the primary:

$$P = 1 - e^{-\pi d^2 \rho}, \tag{4.1}$$

where ρ is the background source density, in arcsec^{-2}, and d the separation between the primary and potential companion in arcsec. I determined the background density of sources brighter than the limiting magnitude using the 2MASS point–source catalogue, with a square aperture of 1 arcminute centred on the main target, converting source densities from the measured sources per arcminute^2 to sources per arcsecond^2. Background counts from VVV differ by only 10–15% from 2MASS. As mentioned before, most of the sources of this sample are saturated in

VVV images, so 2MASS was preferred, in spite of its lower resolution. One can also use either a circular or annular aperture; the difference in background source counts between a square aperture and a circular or annular apertures is less than 20%, with the largest discrepancies found for sources in dense clusters. The source densities and probabilities of chance projections are presented in Table 4.3. I set the limit between a chance projection and a real companion at P_{chance} <20%. In addition, I only consider companions at separations <3" in order to ensure 100% completeness.

4.3.3 Binary statistics

4.3.3.1 Bound companions

Based on the procedure in Section 4.3.2, it is expected that no more than 20% of the detected companions at small separations (<3") are chance projections (3.6 out of 18 secondaries). As a test, one can look for the number of sources detected at a random location in the image. For example, if the target on the image was not in the upper right quadrant, but at the bottom left, how many objects would be found by chance alignment in that quadrant? In order to test this, I calculated the separation of all detected sources (including the target MYSOs) from the centre of the bottom left quadrant, at the opposite side of the image.

These can then be plotted onto a histogram to determine whether the prediction that 20% of the companions are chance projections is accurate (right panel of Figure 4.3). Three objects are indeed found to be located by chance in the opposite quadrant, close to the estimate for spurious binaries, 4.4. This test was repeated for the other quadrants of the image, as the bottom left was affected by the technical fault mentioned in Section 4.2.2. Similar numbers of chance companions are found by focusing on the other image quadrants.

All of this evidence points to the fact that the most likely bound companions are located within the same quadrant of the image as the target (at separations of <3") and with a low probability of chance projection ($P_{spurious}$ <20%). Applying these selection criteria results in a master sample of 18 physical companions. Of these, only one was previously detected by 2MASS and none were detected by VVV, again highlighting the value of AO surveys for binary analysis.

Table 4.3: Separations from primary, background source densities (BSC) and probabilities of chance projections of all detected companions.

Companion name	Separation (")	BSC (arcm^{-2})	P$_{chance}$ (%)
G221.9605-01.9926A	0.6	13	0.4
G221.9605-01.9926B	0.7	13	0.6
G221.9605-01.9926C	1.1	13	1.4
G221.9605-01.9926D	1.2	13	1.6
G232.0766-02.2767B	3.1	12	9.8
G232.0766-02.2767C	4.3	12	28
G232.0766-02.2767D	5.6	12	18
G232.6207+00.9959B	6.4	37	74
G232.6207+00.9959C	6.7	37	76
G268.3957-00.4842B	1.9	10	3.2
G268.3957-00.4842C	4.8	10	18
G268.3957-00.4842D	8.7	10	48
G268.3957-00.4842E	8.9	10	50
G282.2988-00.7769B	1.6	14	3.0
G282.2988-00.7769C	2.7	14	8.6
G287.3716+00.6444B	1.3	16	2.2
G287.3716+00.6444C	1.5	16	3.0
G287.3716+00.6444D	1.8	16	4.5
G287.3716+00.6444E	1.9	16	4.9
G290.3745+01.6615B	0.7	24	1.0
G290.3745+01.6615C	1.9	24	7.1
G290.3745+01.6615D	4.1	24	29
G293.5607-00.6703B	5.7	8	20
G293.5607-00.6703C	4.6	8	14
G300.3412-00.2190B	7.4	28	74
G301.8147+00.7808A_B	2.9	26	17
G301.8147+00.7808A_C	3.9	26	29
G305.3676+00.2095B	0.9	34	2.3
G310.0135+00.3892B	2.6	31	16
G320.1542+00.7976B	2.9	60	37
G326.4755+00.6947B	2.2	23	9.2
G327.9455-00.1149B	7.4	17	55
G331.3576+01.0626B	3.8	54	49
G331.3576+01.0626C	7.8	54	94
G331.3576+01.0626D	11.3	54	100
G331.3576+01.0626E	11.4	54	100
G332.9868-00.4871B	9.1	7	40
G334.7302+00.0052B	5.8	50	77
G336.4917-01.4741B_B	4.9	34	51
G339.6816-01.2058B	8.6	24	79

Table 4.4: Properties of candidate companions within 3" and with a probability of chance alignment of<20%; Masses and mass ratios with the foreground (fg) and circumstellar (circ) extinction estimates are provided. $P_{spur.}$ 2MASS is the probability of chance projection based on 2MASS source counts.

Name	Sep. (")	ΔSep (")	Physical sep.(au)	Δ Phys. sep.(au)	$P_{spur.}$ 2MASS	M_fg ($M_\odot$)	ΔM_fg ($M_\odot$)	M_circ ($M_\odot$)	ΔM_c ($M_\odot$)	q fg	Δq fg	q circ	Δq circ
G221.9605-01.9926A	0.6	0.3	1920	960	0.4	9.6	0.7	52.3	3.6	1.00	0.07	5.45	0.38
G221.9605-01.9926B	0.7	0.3	2240	960	0.6	10.4	0.4	56.8	2.4	1.08	0.05	5.92	0.25
G221.9605-01.9926C	1.1	0.3	3520	960	1.4	12.3	0.8	67.0	4.3	1.28	0.08	6.98	0.45
G221.9605-01.9926D	1.2	0.3	3840	960	1.6	7.8	0.2	42.5	0.9	0.81	0.02	4.43	0.09
G232.0766-02.2767B	3.1	0.2	9390	600	9.8	10.8	0.5	33.6	1.4	1.16	0.05	3.62	0.15
G268.3957-00.4842B	1.9	0.1	1344	70	3.2	1.6	0.1	23.5	1.6	0.20	0.01	3.03	0.21
G282.2988-00.7769B	1.6	0.1	5809	370	3.1	3.1	0.2	7.8	0.5	0.36	0.02	0.91	0.06
G282.2988-00.7769C	2.7	0.1	10027	370	8.6	2.5	0.1	6.3	0.3	0.29	0.01	0.74	0.03
G287.3716+00.6444B	1.3	0.1	5715	450	2.2	7.0	0.4	20.4	1.0	0.47	0.02	1.36	0.07
G287.3716+00.6444C	1.5	0.1	6660	450	3.1	4.2	0.2	12.4	0.5	0.28	0.01	0.83	0.03
G287.3716+00.6444D	1.8	0.1	8190	450	4.5	2.6	0.1	7.5	0.3	0.17	0.01	0.50	0.02
G287.3716+00.6444E	1.9	0.1	8550	450	4.9	5.9	0.2	17.2	0.7	0.40	0.02	1.15	0.05
G290.3745+01.6615B	0.7	0.1	2030	290	1.2	8.0	0.4	19.3	1.0	0.57	0.03	1.38	0.07
G290.3745+01.6615C	1.9	0.1	5452	290	7.1	5.7	0.2	13.8	0.6	0.41	0.02	0.99	0.04
G301.8147+00.7808A_B	2.9	0.1	12672	440	17.2	3.7	0.2	22.5	0.9	0.23	0.01	1.40	0.06
G305.3676+00.2095B	0.9	0.2	3520	800	2.3	5.0	0.2	39.8	1.8	0.35	0.02	2.78	0.12
G310.0135+00.3892B	2.6	0.2	8192	640	16.2	7.6	0.5	60.6	4.4	0.32	0.02	2.57	0.19
G326.4755+00.6947B	2.2	0.2	3942	360	9.2	1.9	0.1	19.1	0.8	0.22	0.01	2.21	0.09

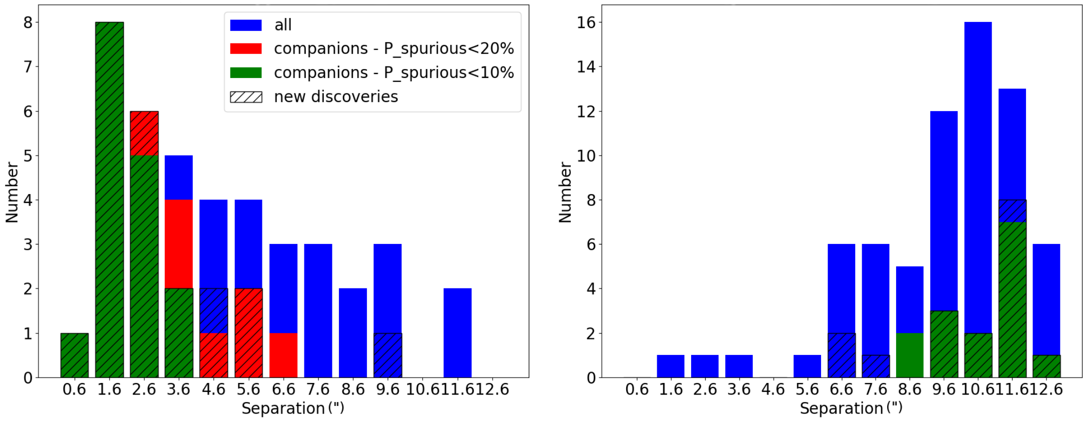

Figure 4.3: Histograms of the separations of companions from the main target (left) and from the centre of the fourth quadrant (right). On the left plot, most of the companions are located at 1–3" from the targets, as this region has 100% completeness. This corresponds to a separation of 9–12" from the centre of the fourth quadrant. Only three targets (just under 20%) are located by chance within 3" of the centre of the fourth quadrant as predicted by the statistical methods employed.

In order to compare these results with other surveys, I calculate the companion and multiplicity fractions (CF and MF). These are given by the following formulae: MF=$\frac{N_m}{N_t}$ and CF=$\frac{B+2T+3Q+...}{S+B+T+Q+...}$, where N_m is the number of multiple systems, N_t is the total number of observed systems, S is the number of single systems, B is the number of binary systems, T is the number of triple systems and Q of quadruple systems. As there are 32 systems, with 10 multiples, of which 6 binaries, two triples, one quadruple and one quintuple, the resulting values for the fractions are MF=31±3% and CF=53±3%.

4.3.3.2 Angular separations

Figure 4.3 presents a histogram of the angular separations of all the initial 38 companions. The overplotted red histogram shows objects with a probability of false correlation of <20%, whilst the green histogram shows objects with $P_{spurious} < 10\%$. New detections are hatched. This histogram shows a peak at small separations (≈1.6") followed by a rapid decrease. There is also only one companion in the 0.6" bin. This is likely due to the effects discussed in Section

4.3.1, as the limiting magnitude is fainter at separations shorter than 1" of the main target than in the rest of the image, making companions closer than 0.5" hard to detect. The histogram is mostly flat from 6.6–9.6", likely because in this range the histogram probes the uniform distribution of field stars. There are no detections in the 10.6" bin, or past 11.6". This is likely because the coverage is reduced to ≈40% at 11". Due to the set–up of the observations, with the primary targets at the centre of the top right quadrant of the image, the coverage is incomplete at separations larger than 3", as shown in Figure 4.4. The average coverage decreases from 80% at 5" to 30% at 15". This can be roughly fit by the function C(%)=–5.2 d(") + 110 (see Figure 4.5). Applying this coverage correction results in a flat angular separation distribution between 3.6–11.6" (see Figure 4.6). This flat distribution is similar to what one finds for background sources – similar amounts of sources in each 1" bin. This indicates that most secondary sources past 3" are unlikely to be real, bound companions.

Most of the companions with a low probability of chance projection are close to the primary source, partly due to the design of the probability formula which takes into account the distance from the primary. As mentioned earlier, newly detected companions form half of the total secondaries and they are closer to their primaries than objects in the field that had been already detected by survey data. This fact highlights again the resolving power of NaCo and adaptive optics in general.

The separations of the most likely physical companions (within 3" and with $P_{spurious}$ <20%) are well correlated with the magnitude difference to the primary (see Figure 4.7). All companions are above the detection limit determined empirically in Section 4.3.1 (blue solid line). The separation–magnitude correlation may be a result of observational biases, rather than indicate a physical effect.

4.3.3.3 Physical separation

Using distances from the RMS survey, the companion separations in arcseconds can be converted into physical separations in au. These are provided in Table 4.4. The physical separations range from 1344–12600 au, with an average of 5700 au. Their histogram (Figure 4.8) shows a peak around 3000 au and another at 9000 au. A histogram for the companions with the lowest probability of chance projection (<5%) is overplotted in green in Figure 4.8. This has a similar shape to the histogram for all bound companions, with a sharp peak at 3000 au. It

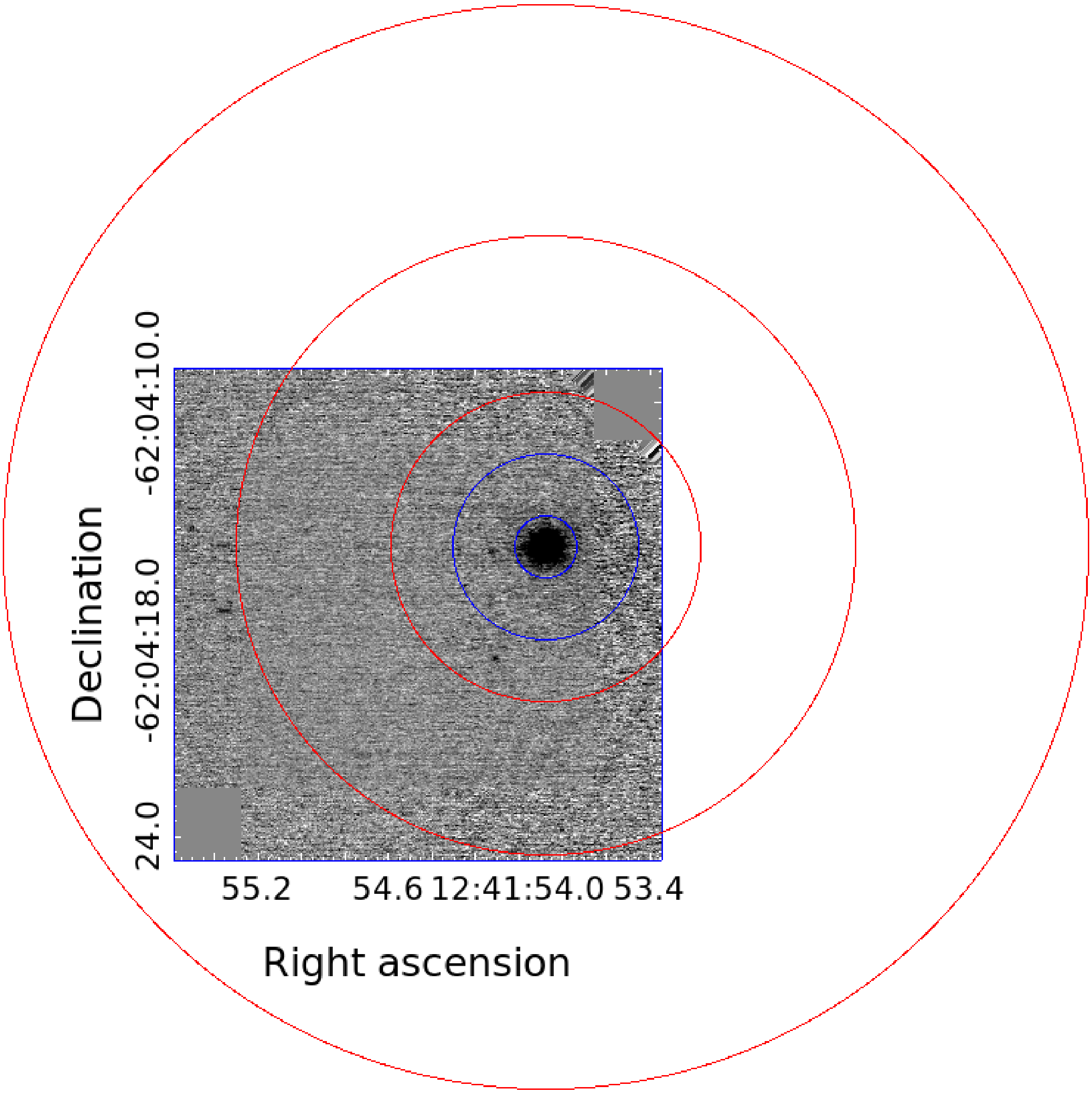

Figure 4.4: The completeness at different distances from the central object, illustrated for the image of G301.8147A. The concentric circles have radii of 1, 3 (blue), 5, 10 and 17.5 (red) arcseconds from the target. Any sources within 3" can be detected by the set–up of the NaCo images in this survey. However, at larger distances, potential companions can only be detected if they are located to the south–east of the main target. The probability of detection decreases with increasing distance, as shown in Figure 4.5.

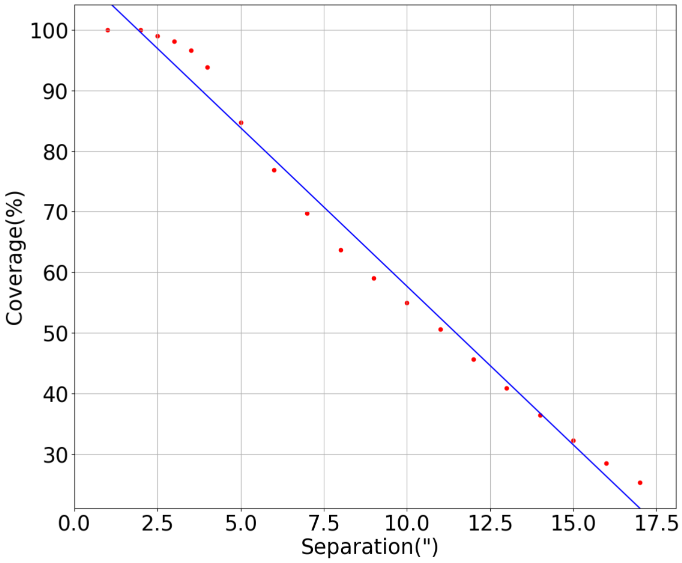

Figure 4.5: Average fraction of the area around the primary target that is covered by the NaCo observations as a function of separation from the primary target. The blue line is the best fit to the observed data, given by C(%)=–5.2 sep(") + 110.

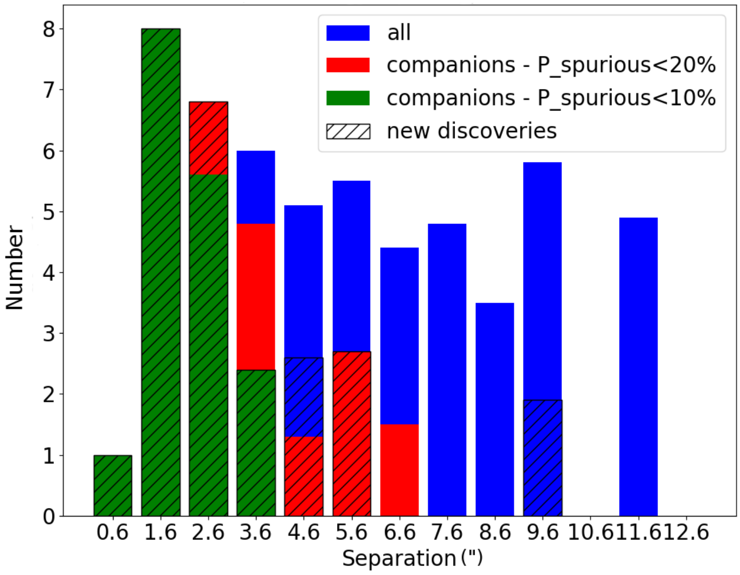

Figure 4.6: Histograms of the separations of companions from the main target, multiplied by a correction factor for the incomplete coverage at 3–15", as determined in Figure 4.4. Note the distribution now flattens up for 3–10".

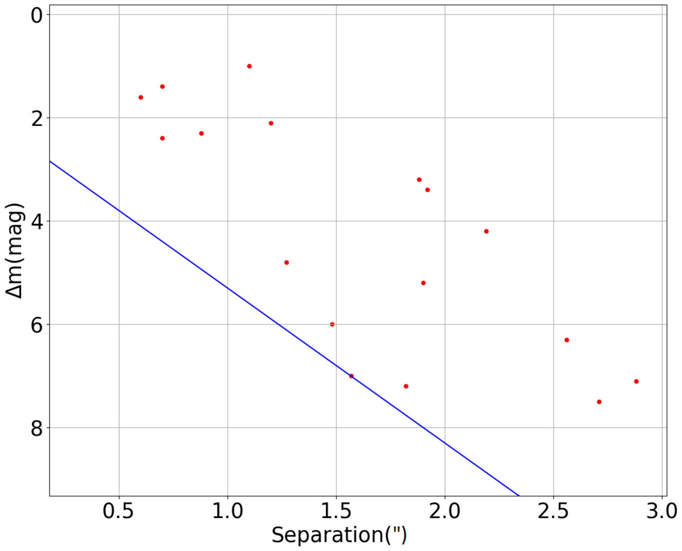

Figure 4.7: Magnitude difference between the secondary and primary companions as a function of the angular separation. The blue line is the detection limit of the survey, as determined in Section 4.3.1, given by δm(mag) = 3.0 d (") + 2.3.

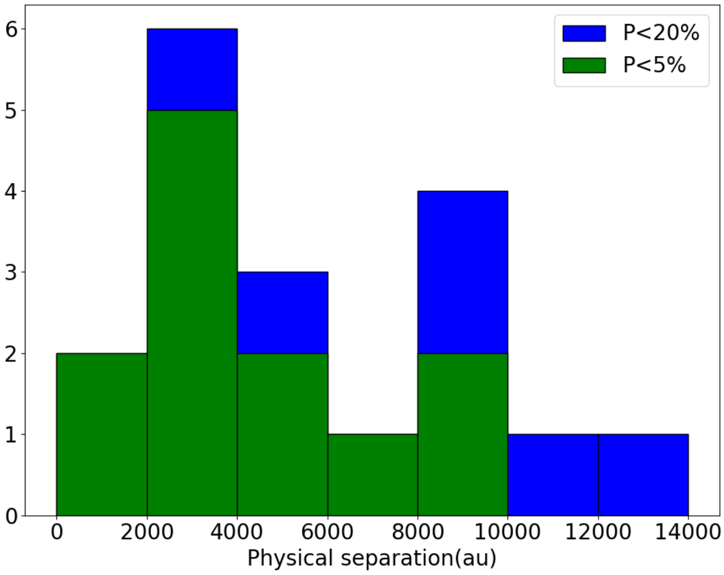

Figure 4.8: Histograms of the physical separations of companions within 3" and with a probability of chance projection<20% (blue) and with the probability between 0–5% (green)

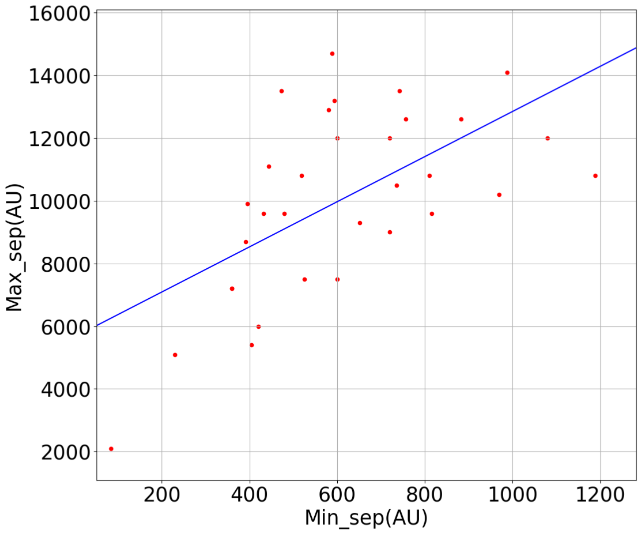

Figure 4.9: Maximum separation from the primary as a function of minimum separation in au. This shows the range of physical separations available to this survey – from hundreds to thousands of au. The blue solid line is the best fit line, given by Max_sep (au) = 7.5 Min_sep (au) + 5500.

it worth noting that given the 1 kpc order of uncertainty on distances noted by Urquhart *et al.* (2011a), the resulting average uncertainty on physical separations is likely to be of order 1500 au. Given the relatively small size of the sample and the completeness and uncertainty constraints it is unclear whether the observed peak is real or simply an artefact due to observational biases.

Taking 3" as the maximum observable separation from the main target, and 1.5 × FWHM (") as the minimum, I calculate the limits in au between which potential companions could be detected. These are displayed in Figure 4.9. The minimum physical separations range between 180–1200 au, and the maximum between 2000–15000 au. Therefore, the average range probed in this sample is 600–10000 au.

This shows that the range of physical separations probed by this survey corresponds to the widest binaries. The sources that are first detected in this survey are located at small angular separations to the primaries, thanks to the resolving power of NaCo. New detections also have the highest probability of being physical companions.

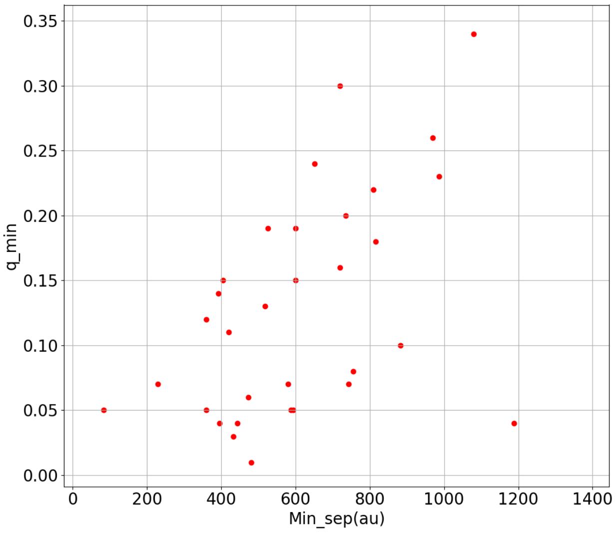

Figure 4.10: Minimum mass ratio of companions detectable as a function of minimum physical separation detectable in au.

4.4 Discussion

4.4.1 Multiplicity and companion fractions

The resulting multiplicity fraction is MF=31±3% and the companion fraction is CF=53%±3%. The multiplicity fraction does not differ significantly over distance and luminosity ranges or degree of embededness: there are 8 MYSO primaries within <2.5 kpc, and 24 systems further away than 2.5 kpc. The multiplicity fractions are 25±13% and 33±4% for the near and far MYSOs, respectively. There are 16 MYSOs with a bolometric luminosity under 10,000 $L_{\odot}$, and another 16 brighter than 10,000 $L_{\odot}$. For both of these ranges the multiplicity fraction is 31%. Finally, there are 16 MYSOs with a dust extinction (estimated from H–K photometry) of less than 40 magnitudes, and 16 with extinction over 40 magnitudes. The multiplicity fraction for both of these ranges is also 31%. This indicates that the binarity properties of MYSOs are homogenous throughout the Galaxy, with no environmental effects leading to a larger multiplicity in certain regions, or for more massive primaries.

The overall multiplicity and companion fractions are lower than the values quoted in the literature for massive stars and some low mass young stars. T Tauri stars are reported to have CF=64–79% depending on their mass range (Kraus *et al.* 2011) for the separation range 3–5000 au, whereas Class I embedded protostars have CF=37% according to Connelley *et al.* (2008b). O and B Main Sequence stars have been found to have CF=130 and 100% and MF=70 and 52% respectively (Sana *et al.* 2012) for separations 2–200 au.

However, the separation and mass ratio ranges probed by the NaCo data is significantly different to that of other surveys. As discussed in Section 4.3.3.3, the separation range of the data presented here is 600–10000 au.

Oudmaijer & Parr (2010) give the following equation to estimate the mass ratio from the K–band magnitudes (assuming the system has little dust excess and both companions are on the Main Sequence):

$$q = 10^{-0.18\Delta K}, \tag{4.2}$$

where ΔK is the difference in absolute magnitudes. Using the difference between the limiting K magnitude of each observation and the magnitude of the primary as ΔK, the minimum observable mass ratio for each image can be determined. This varies between q_{min}=0.01–0.34, with an average of 0.13. The parameter space probed by this survey is presented graphically in Figure 4.10, which shows the minimum mass ratio as a function of minimum separation detectable in au.

The survey of Kraus *et al.* (2011) searched for binary companions to low–mass YSOs within 3–5000 au with $\Delta K \approx 6$ mag, corresponding to q_{min}=0.08. For a separation and mass ratio range comparable to that of our survey (600–5000 au and 0.13 respectively), the T Tauri multiplicity fraction is 11.4±0.1% and the companion fraction 12.2±0.1%. In the NaCo survey presented here, 4 binaries and one quadruple system are found between 600–5000 au, which correspond to MF=16±3% and CF=22±3%. Both the MF and CF of MYSOs determined from NaCo are higher than those of Kraus *et al.* (2011) within the same range, continuing the field star trend of multiplicity increasing with mass.

For class I embedded protostars, taking the data from the Connelley *et al.* (2008b) survey over 600–5000 au and q>0.12 (a similar range to that probed by my NaCo data), MF=17%±0.1% and CF=18.5%±0.1%. The multiplicity and companion fractions of MYSOs agree with results for class I embedded low–mass YSOs. This may point to primordial binary fractions being similar across the mass range, with dynamical interaction over the formation process and subsequent evolution resulting in the observed differences in multiplicity across the mass range for MS stars. However, it is worth pointing out that these surveys probe a larger sample than this NaCo pilot survey.

Turner *et al.* (2008) surveyed O stars in the I–band searching for wide companions. They present their discovered multiple systems in terms of separations in arcseconds and magnitude difference to the primary in the I–band. Applying the constraints of the NaCo data survey (separations 230 – 23000 au and q>0.12) to their findings results in MF=17%±0.1% and CF=23%±0.1%. These values are lower than the multiplicity and companion fractions of MYSOs from the NaCo data (MF=31%, CF=53%). This lends support to the idea that MS multiplicity fractions are lower than primordial fractions due to dynamical evolution.

In conclusion, the multiplicity fraction of MYSOs is larger than that of lower–mass Class II/III YSOs and than that of MS O stars over a similar range in separations and mass range. The multiplicity of embedded Class I YSOs (of a lower mass and at a potentially earlier evolutionary stage) is similar to the multiplicity fraction of MYSOs. These findings all lend support to the idea that multiplicity fractions increase with mass for objects of the same age and decrease with evolutionary stage for objects of the same mass due to dynamical interactions.

4.4.2 Masses and mass ratios

In principle, the K–band magnitude can be used as a proxy for the stellar mass of companions in a multiple system, assuming they are both on the MS. However, this applies to field stars unaffected by differential dust excess. When looking at tight MYSO binary systems, one could assume that the excess is the same for both objects. The NaCo data presented here covers separations of order 10^3 au, so it is very likely that the differential excess does play a role. Companions at an earlier evolutionary state than the primary target will appear more embedded. Additionally, strong accretion produces strong excess emission. Unfortunately, no multi–wavelength data is available to help quantify the embeddedness of the companions. High–resolution MIR data (1”) was taken with TIMMI2 by Mottram *et al.* (2007a) as part of the RMS survey. Many of the objects in the NaCo sample were also observed in MIR, and they appear to be point sources, with no strong excess component nearby.

Also, not all the K–band emission may come from the star itself, with some possibly arising from the disc, as in Class I/II low–mass YSOs. In spite of all these caveats, an analysis of the limits of mass ratios can provide insights on the composition of multiple young systems.

I estimate primary masses using the RMS bolometric luminosities and mass–luminosity relations for MYSOs presented by Davies *et al.* (2011), as described in Section 3.8.

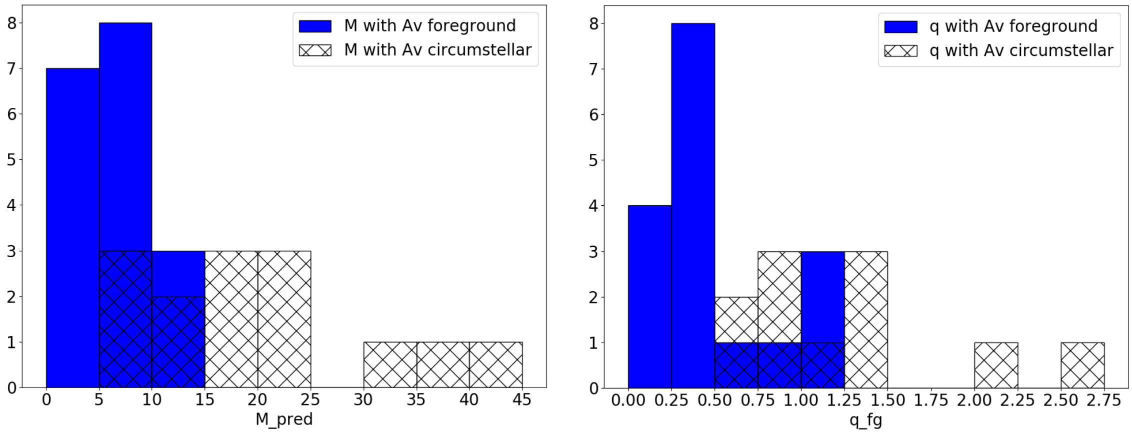

Figure 4.11: Histograms of companions masses (left) and mass ratios to the primary (right)

In order to calculate the mass of the companions, their measured K–band magnitude is first converted to absolute by adopting the RMS distance to the primary as the distance to the system. Next, a dust extinction needs to be applied. I assumed that the A_V to the binary is lower or equal to the extinction to the primary. For tight binaries, the extinction to the primary (I will refer to this as the circumstellar extinction for clarity from here) can be used, as the whole system may be embedded in the same dust cloud. In the case of wide binaries, the companion may not be shrouded by the same amount of dust as the primary, and as such the circumstellar extinction is likely to be inaccurate. The lower limit to the extinction is the foreground extinction at the given distance for the Galactic line of sight the system is located in.

Neckel *et al.* (1980) provide maps of foreground extinction for most of the Galaxy, and I adopt these as lower limits for the A_V. The circumstellar extinction of the primary can then be used as an upper limit. The circumstellar A_V is determined by comparing 2MASS $H - K$ photometry to the expected colours of a MS B0 star, as described in Section 2.4. The corrected absolute K–band magnitudes can then be used to determine the masses of the companions, by using the equation of Oudmaijer & Parr (2010) to estimate masses:

$$log(M/M_{\odot}) = -0.18K_{abs} + 0.64 \tag{4.3}$$

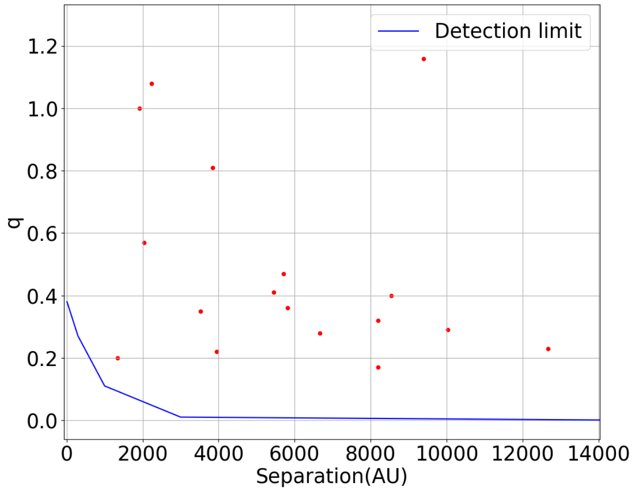

Figure 4.12: Mass ratios of detected companions as a function of physical separation, with the average detection limit (blue solid line), as given by converting the line from Figure 4.7 from arcsecond–magnitude space to au–mass ratio space.

As such, two limits to the mass of the companion can be determined: a lower limit by correcting the companion magnitudes with the foreground extinction and an upper limit by using the circumstellar extinction. The mass of the companion will be somewhere between these two values. A histogram of the resulting companion masses (determined from the absolute K–band magnitudes) and mass ratios, for both of the methods of estimating extinction is shown in Figure 4.11. The average mass of the companions is 6 $M_{\odot}$ (corresponding to a B2.5V star) when using foreground extinction and 29 $M_{\odot}$ with circumstellar extinction. The mass ratio averages are 0.5 for foreground extinction and 2.3 for circumstellar extinction. This points out to the inaccuracy of using the same extinction for the companion as for the primary star, as this results in companions more massive than the MYSOs for most systems. The disagreement is likely caused by the large separation of the binaries reported here. As explained above, wide secondary components may have lower amounts of extinction than the primaries, and so using the circumstellar extinction results in an overcorrection of the secondary magnitude. It is worth considering what effect large excesses may have on the secondary masses and mass ratios as determined here. Primary masses are determined from bolometric luminosities, rather than K band magnitudes, and as such are not affected by the excess. A large secondary K–band excess would result in a lower fraction than estimated here of the K–band magnitude being due to the companion itself, so the secondary masses, and the mass ratios would be lower than what I determined here. This analysis is however, beyond the scope of my data.

A large fraction of companions with a high mass ratio (>0.5) is found even when using the foreground extinction correction for the magnitudes. It is worth noting that the mass ratios obtained with this method are lower limits, so the real mass ratios are likely larger. The number of high mass companions is thus larger than one would expect if the companions were randomly drawn from the IMF, as predicted by the binary capture formation scenario.

Table 4.5: Binary and disc position angle measurements. * – disc position angle deduced from outflow or jet PA. ** – outflow seen as extended emission in 2MASS image

Object name	Binary_PA (°)	Disc_PA (°)	Reference
G221.9605-01.9926A	75	30*	Zhang *et al.* (2005)
G232.0766-02.2767B	178	175*	Navarete *et al.* (2015)
G268.3957-00.4842B	170	120*	Wheelwright *et al.* (2012)
G282.2988-00.7769B	126	80*	2MASS**
G290.3745+01.6615B	153	135*	Gredel (2006)
G301.8147+00.7808A_B	115	65*	2MASS**
G310.0135+00.3892B	41	45	Kraus *et al.* (2010)
G326.4755+00.6947B	179	125*	Navarete *et al.* (2015)

The mass ratios do not correlate with physical separations (Figure 4.12), even if the angular separations do correlate with magnitude difference (see Figure 4.7). The Pearson correlation factor for physical separations and mass ratios is –0.28, corresponding to a probability of false correlation of 28%. This points to the fact the observed correlation in angular separation and magnitude difference was likely induced by observational biases.

4.4.3 Semi–major axis and period distributions

As explained in Section 1.4.2, one of the main unsolved questions in binarity studies is finding the shape of the distribution of orbital periods. Several surveys (Connelley *et al.* 2008b for Class I protostars, Dhital *et al.* 2010 for subsolar mass M stars) have found it to follow a flat distribution in log space, which is refererred

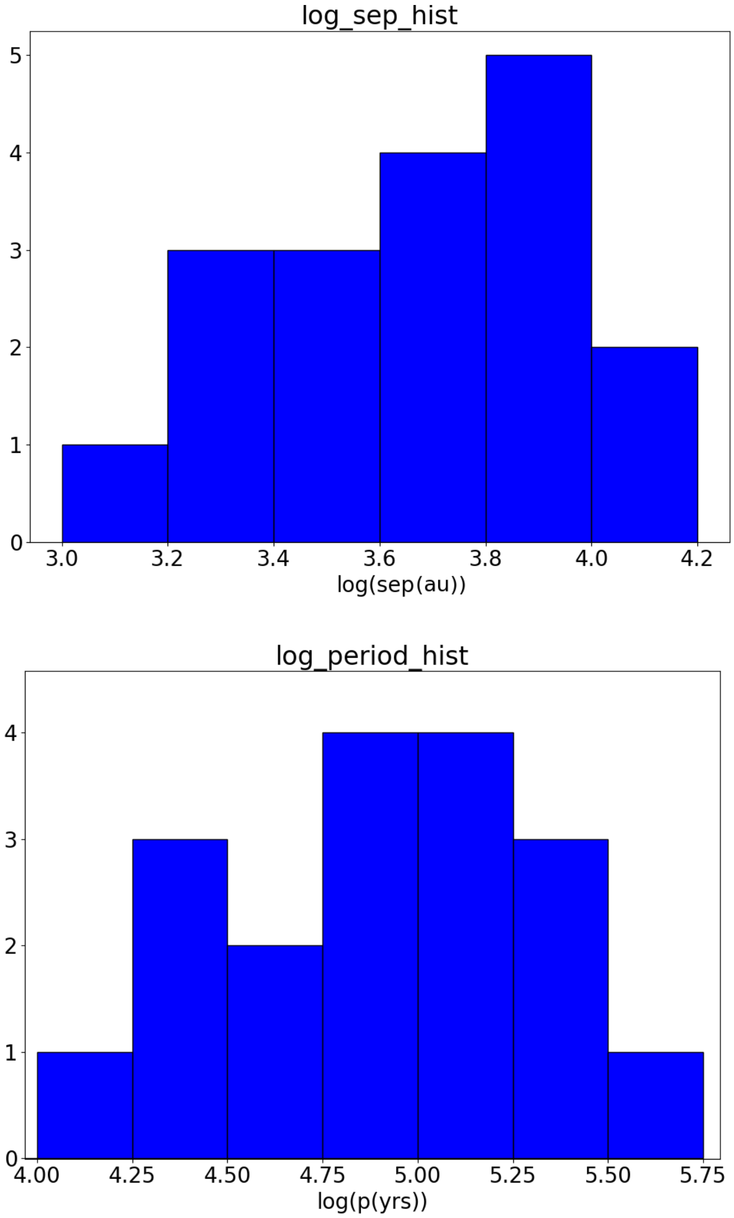

Figure 4.13: Histogram of logarithm of the physical separations of the detected bound companions (top) and of the calculated orbital periods, assuming the semi–major orbital axis is equal to the physical separation

to as Opik's law. Surveys in other mass and age ranges find disagreement with Opik's law (Raghavan *et al.* 2010 find solar mass stars on the MS are better described by a log–normal distribution). This is relevant as the shape of the period distribution can provide clues about the binary formation process. An Opik distribution suggests that the binary formation process is scale free, with no preferred binary system size. Dynamical evolution across the lifetime of a system will cause the observed distribution to be different from the primordial one. However, MYSOs and other objects at early evolutionary stages are likely to show a distribution closer to the primordial one than that of field stars.

According to Kepler's third law, orbital distributions are proportional to the semi–major axes of orbits in binary systems. The periods are given by:

$$P^2 = a^3 \frac{4\pi^2}{G(M_1 + M_2)}, \tag{4.4}$$

where P is the period, a the semi–major axis and M_1 and M_2 are the masses of the system components.

van Albada (1968) explains that most binary systems are highly eccentric, and so secondary companions spend most of their orbit close to the apastron. As such, the projected separation is a good estimate for the semi–major axis (to within 5%). The derived companion masses are deduced from the K–band magnitudes as explained above.

I plot histograms of the logarithm of the period distribution (in years) and the semi–major axis (in au) in Figure 4.13. Neither of these show a flat profile, with the semi–major axes histogram showing an increase towards larger values, and the period histogram appearing almost bell–shaped. It is unclear whether this a real effect or whether it is caused by the small number statistics of this sample or observational biases. Due to the large distance to the sources, wider binaries may be easier to detect. There is a decrease in the final bin, for periods larger than $10^{5.5}$ years, which may be a reflection of the rarity of very wide binary systems (of over 10,000 au separation) or due to the lower coverage at such large separations in this survey.

4.4.4 Alignment with discs

As mentioned in Section 4.1, one can test the different binary formation models by comparing the alignment of the accretion disc with that of the binary orbit. If the secondaries were formed as a result of the fragmentation of the accretion disc, the orbit of the companion should be located within the same plane as the accretion disc. The orbit of the companion is unlikely to have strayed significantly from the plane of the accretion disc in the short time from the formation of the companion to the MYSO phase. However, this is complicated by the unknown angle at which we are viewing the binary system. For edge–on systems (or at large viewing angles), an aligned disc–companion configuration will indeed result in the binary orbit and the accretion disc having the same position angle (PA). For angles at lower inclinations with respect to our line of sight, the disc and binary orbit may appear to be at different position angles even if they are within the same plane in reality. Wheelwright *et al.* (2010) surveyed the multiplicity of Herbig stars with spectro–astrometry. They used a model to predict the cumulative distribution function of the difference between the disc and binary PA when the orbits are coplanar and when the PAs are distributed randomly, comparing the observed disc–binary orbit PAs to these two different distributions. With this they showed that binary rotation axes and protostellar discs of Herbig stars are consistent with being aligned at a 2.2σ level, as predicted by the disc fragmentation binary formation theory.

Such an analysis is more complicated for MYSOs, first of all due to their lower relative numbers compared to Herbig stars – at least 100 measurements are required for a 3–σ precision, and 20 for 2σ. In addition, direct disc detections are rare. The other option for inferring the disc PA is modelling of disc tracers or other elements of the circumstellar environment. Finally, detections of binaries in MYSOs are also rare.

Nonetheless, I used the RMS database, 2MASS images and literature to investigate the presence of discs, outflows or jets in our targets and their position angles. If a jet, outflow or extended emission was detected, I assumed the disc PA would be oriented at 90° with respect to the PA of the outflowing gas. This is what most high–resolution observations of disc–outflow massive young systems find (eg. Gibb & Hoare 2007). I normalise angles to the (0,180)° range. Disc PA measurements are available for 8 of the detected companions. The data is shown in Table 4.5.

There is a weak correlation between the disc and the binary PA, with a Pearson correlation coefficient of 0.71, corresponding to a probability of false correlation of 0.1%. The plot is displayed in Figure 4.14.

I also compared the measured distribution of the difference between the disc and binary PA to the simulations of Wheelwright *et al.* (2010) in Figure 4.15. This data cannot distinguish between the two simulated distributions, with the

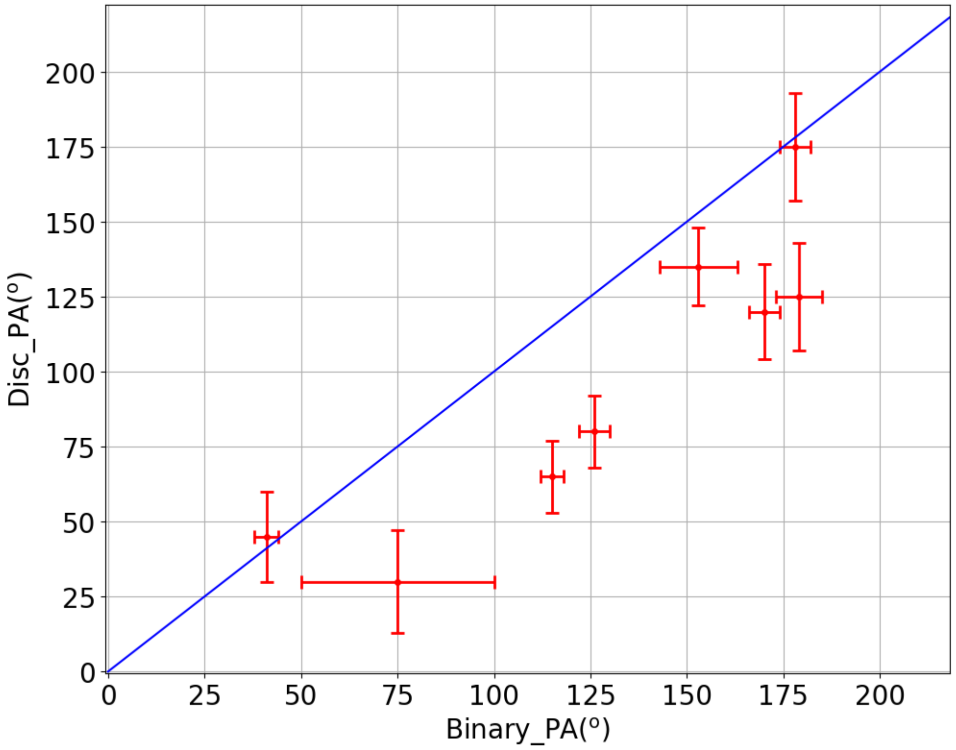

Figure 4.14: Position angle of the disc as a function of the position angle of the binary companion. The blue solid line is the 1–1 correlation, for equal disc and binary orientations.

distribution being located at equal distance from the coplanar and random distributions. The observed data are best fitted by the random distribution at low disc–binary PAs, and by the coplanar distribution at large disc–binary PAs. This is likely due to the smaller size of the NaCo data set compared to the sample of Wheelwright *et al.* (2010). Their sample contained 20 Herbig Ae/Be stars, whereas the NaCo sample only has 8 companions with PA measurements.

4.4.5 Are MYSOs with binaries special?

Following the approach of Ilee *et al.* (2013), I study the sample of MYSOs with binaries in order to determine whether their properties differ from single MYSOs. The average luminosity of binary MYSOs is 16,000 $L_\odot$, and the average distance is 3.1 kpc. This is similar to the average luminosities and distances of the whole

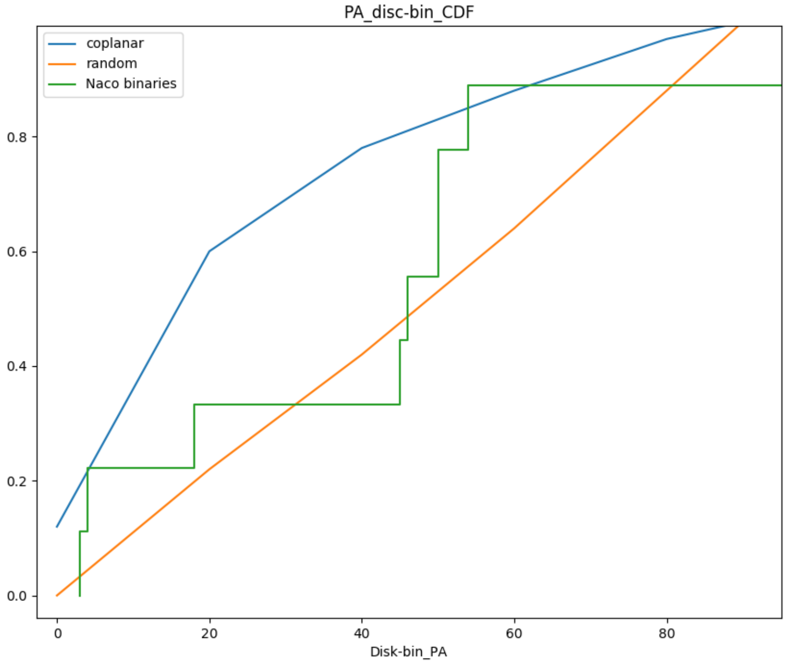

Figure 4.15: Comparison of the distribution of the disc–binary PA (green line) with the simulated distributions of Wheelwright *et al.* (2010) for coplanar (blue line) and random (orange line) orbits

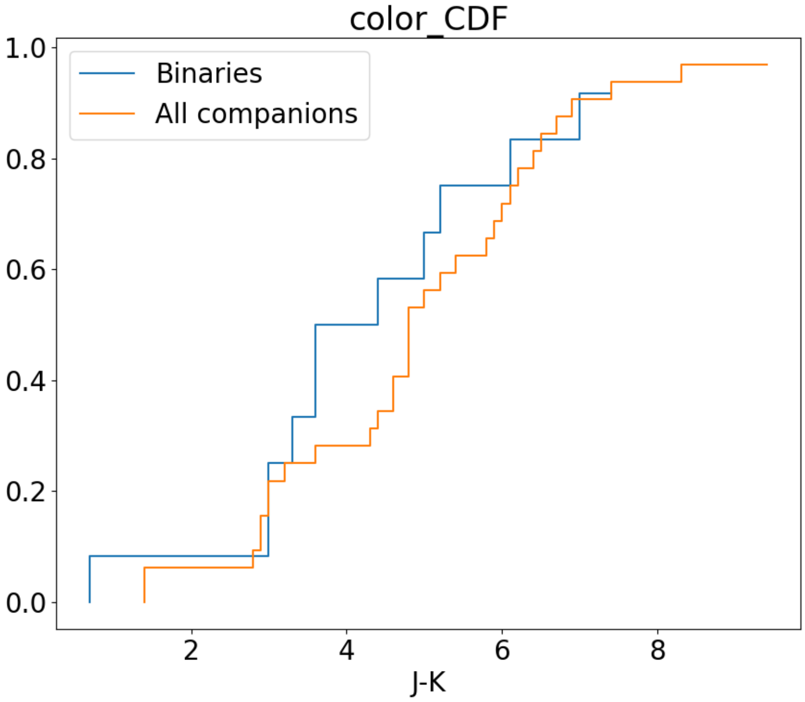

Figure 4.16: Comparison of the distribution of the J–K colour of MYSOs in our sample with (blue line) and without binaries (orange line).

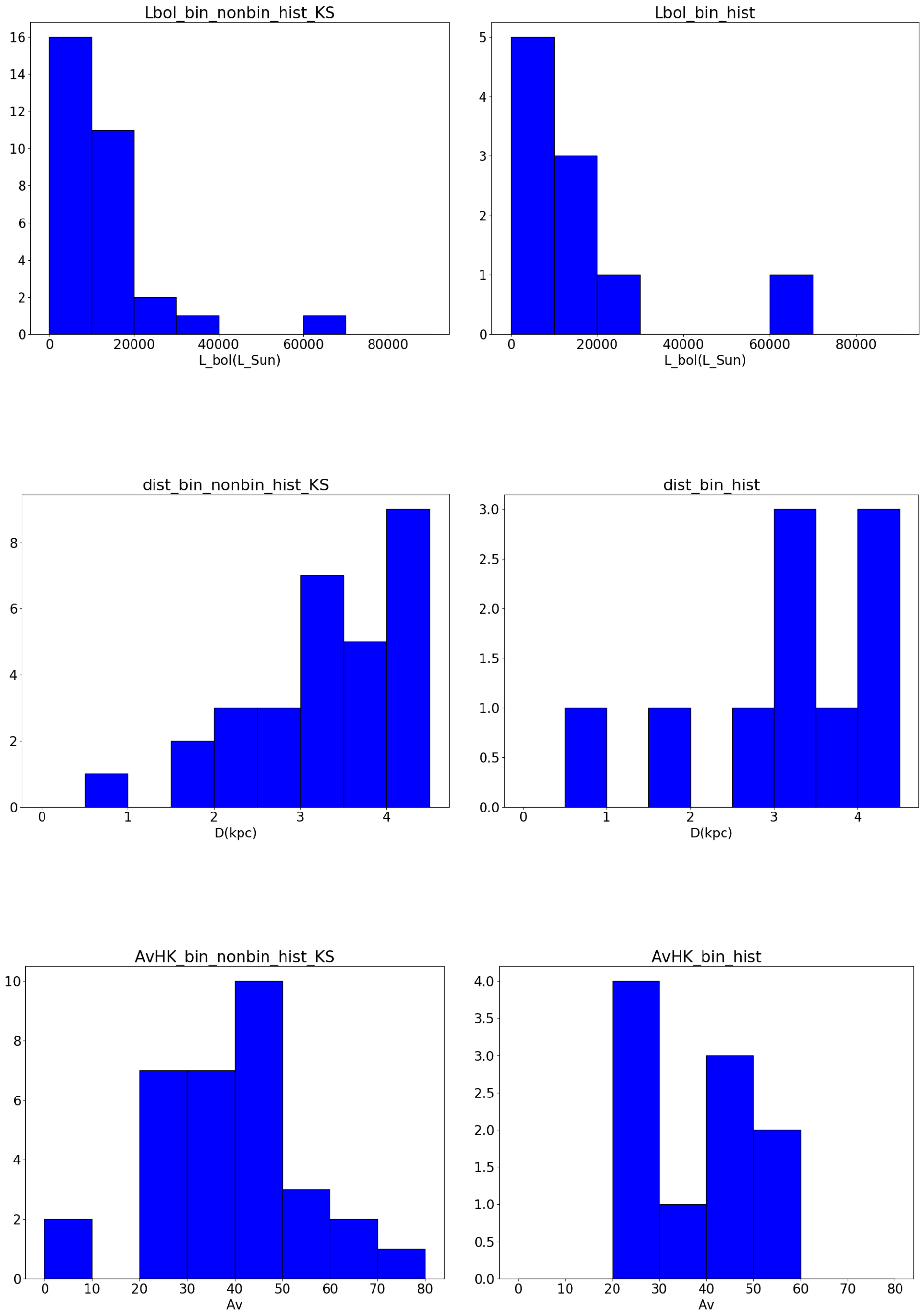

Figure 4.17: Top panels – Histogram of the bolometric luminosities of MYSOs without companions (left) and with companions (right). Middle – Histogram of the distances to MYSOs without companions (left) and with companions (right). Bottom – Histogram of the circumstellar extinctions (from $H - K$ photometry) to MYSOs without companions (left) and with companions (right)

NaCo sample, 15000 $L_\odot$ and 3.3 kpc respectively. The averages for all the RMS MYSOs are 11500 $L_\odot$ and 4.5 kpc. The difference in properties between the binaries and the whole RMS sample can be explained by the initial sample selection criteria of $L > 3500$ $L_\odot$ and $d < 5$ kpc. As such, the whole RMS database contains a large number of fainter and more distant MYSOs than this NaCo sample. Histograms of the luminosity and distance distributions of the MYSOs with binaries appear visually similar to the same distributions for the whole NaCo sample (see the top two panels of Figure 4.17). K–S tests were applied, and these confirmed this result. The luminosity distribution yielded a K–S statistic of 0.22, indicating that the probability of the binary sample to be drawn from the same distribution as the complete sample is 98%. The K–S test between the binary and the complete sample for the distance distribution resulted in a statistic of 0.16, which corresponds to a probability of 81% that the two distributions are drawn from the same initial sample. Therefore, based on the results from this data set, there is no difference between MYSOs with or without companions in terms of bolometric luminosities or distance. Again, this reinforces the idea that the environment MYSOs are found in is less likely to be a factor in their multiplicity properties.

I visually investigated the 2MASS images through spot checks, as well as other RMS multi–wavelength data to decide whether MYSOs are in a cluster or field stars. It appears that 50% of the MYSOs with bound companions and 55% of those with no companions are in a cluster, so there is no difference in clustering either. I also search for outflows or discs in the objects in the sample as in Section 4.4.5. 60% of MYSOs with companions and 40% of those with no companions have an outflow or disc. I conclude that there are no differences between the binary and single MYSOs in the NaCo sample in terms of clustering, outflow or disc detections.

I compared the embeddedness of the binary sample and of all the companions in the NaCo images through their $J - K$ colour. Cumulative distribution functions are shown in Figure 4.16, and K–S tests show that the probability of the two samples being drawn from the same distribution are larger than 60%. I also plot a histogram of A_Vs for the MYSOs with binaries (from $H - K$ photometry) and compare it to the same distribution for the whole sample (the bottom panel of Figure 4.17). Again they are very similar, and the K–S distribution agrees with this, with a statistic of 0.12, corresponding to a probability of 99% that the two distributions are drawn from the same sample.

Based on these observations, I conclude that the MYSOs sample with and without binaries are indistinguishable.

4.5 Conclusions

This chapter presents AO–assisted K–band observations of 32 MYSOs searching for new binary companions. The observations are complete to a contrast of ΔK=5 mag at 1–3" and ΔK=3 mag at 0.3". This corresponds to a physical separation range of 600 – 10,000 au, within the predictions of models and observations for multiplicity of MYSOs. Statistical methods based on background source density and separation are employed to determine the likelihood of the companions being bound rather than visual binaries. The main findings are as follows:

- The multiplicity fraction is 31±3% and the companion fraction 53±3%. These fractions are lower for MYSOs than the overall fractions for T Tauri or Main Sequence OB stars. However, for similar separation and mass ratio ranges, the multiplicity fraction of MYSOs is larger than that of T Tauri or OB stars. This lends support to theories suggesting multiplicity increases with mass and decreases with evolutionary stage.
- The average projected separation is 5700 au, indicating that this data surveys the widest MYSO binaries.
- Secondary masses and mass ratios to MYSOs are determined from K–band magnitudes. Mass ratios determined in this manner are generally>0.5. Such large mass ratios are inconsistent with randomly sampling the IMF, as the binary capture formation predicts.
- The period distribution was computed assuming that the semi–major axis is similar to the projected separation. Neither of these show a clear flat profile, as predicted by Opik's law. However, it is unclear whether this a real effect or whether it is caused by the small number statistics of this sample or observational biases.
- Due to the low number of sources with disc orientation measurements, this data set cannot differentiate between binary orbits being coplanar to discs or at random orientations.
- MYSOs with wide binaries do not show any different characteristics to the average MYSO in terms of luminosity, distance, clustering, outflow or disc presence.

Chapter 5

Conclusions

This thesis has employed near–infrared spectroscopy and imaging to study the evolution, environment and multiplicity properties of Massive Young Stellar Objects. These are pre–Main Sequence objects where accretion is still ongoing, but that have yet to ionise their circumstellar environment in order to produce an HII region. For more details on MYSOs see Section 1.4.2 or the review by Oudmaijer & de Wit (2014)

The MYSOs studied in this work have been drawn from the RMS catalogue (described in Section 1.4.2.1 and Lumsden *et al.* 2013), which was compiled in order to provide an unbiased sample of Galactic MYSOs. The RMS survey is complete to a level of 90% for objects above 10^4 $L_\odot$ and it contains 800 MYSOs and HII regions across the Galactic Plane.

The near–infrared is typically the shortest wavelength at which MYSOs can be studied, as UV and optical emission is absorbed by the dust cocoon in which these objects are embedded. Transition in the NIR wavelength range are particularly useful to study discs (CO bandhead, fluorescent FeII), winds (HI recombination lines) or shocks (H_2 and [FeII] lines).

In Chapter 2 I classified a Southern Hemisphere sample of MYSOs under the evolutionary sequence of Cooper (2013). 68 MYSOs were classified based on the presence of absence of certain spectral features. Results from other wavelengths were consistent with this being an evolutionary sequence, with early Type I and IIs being the most embedded in MIR colours, and more evolved Type III and IVs being bluer. This agrees with results from models which predict that at late stages, outflows and jets in MYSOs clear out a significant amount of the circumstellar dust. Measurements of P Cygni–type profiles (which trace outflowing motion) are seen at a maximum detection rate in late evolutionary types. In addition, inverse P Cygni profiles, indicative of infall (and so tracing strong accretion), were only found in Type II objects. By comparing with radio observations, I show that the strongest ionised jet activity is found in the early stages. The lowest jet detection rates were found in Type IV MYSOs, where, as predicted by models, the opening angle increases and jets become more like MS stellar winds. This is consistent with ionised jets being a by–product of the accretion process and entraining the material around the star, giving rise to shocks. Clump masses from the submillimetre ATLASGAL survey (Urquhart *et al.* 2014) showed that the earlier Type I MYSOs are located in more massive clumps and at earlier evolutionary stages than Type IV sources. Again, this agrees with model predictions that most of the clump material is processed onto the MYSO at the later stages. The work presented in Chapter 2, together with that of Cooper (2013) and of Ward et al., (in prep.), forms part of a larger project of NIR spectroscopic follow–up of RMS MYSOs and analysis of the properties of their evolution. Spectra of more than 400 RMS MYSOs will be analysed together in order to understand the interplay between accretion and outflows, how they shape evolution across the MYSO phase and the implications of all of this on different stellar populations.

Chapter 3 presented a cross–dispersed intermediate–resolution survey (R≈7000) of a sample of 36 MYSOs using the GNIRS instrument on the Gemini telescope. The MYSO G015.1288 was classified as an early A–type giant/supergiant with excess emission based on its HI absorption lines. This spectral classification is consistent with the swollen up MYSOs predicted by the Hosokawa *et al.* (2010) models. This is the first observational detection of such an MYSO. A Diffuse Interstellar Band (DIB) in MYSOs was found to be weaker than expected for the given extinctions. This discrepancy is likely because DIBs do not trace circumstellar extinction as well as they do foreground interstellar extinction, possibly due to the mechanisms that excite DIBs being less efficient in MYSOs, or the particles that give rise to DIBs being less efficiently formed or easier destroyed in the circumstellar region of MYSOs. The detection rates of P Cygni and inverse P Cygni profiles are lower than values reported for the lower mass counterparts of MYSOs, Herbig Ae/Be stars, which were also lower than values for T Tauri stars. This may be due to differences in the accretion mechanisms across the mass range. Observations of HAe/Be stars (Fairlamb *et al.* 2015) suggest that accretion changes from a process moderated by the stellar magnetic fields in TTaus and HAes to a different mechanism in HBes and MYSOs, possibly disc accretion, as predicted by simulations.

Velocity–resolved HI line ratios were analysed. These reveal a wide variety of

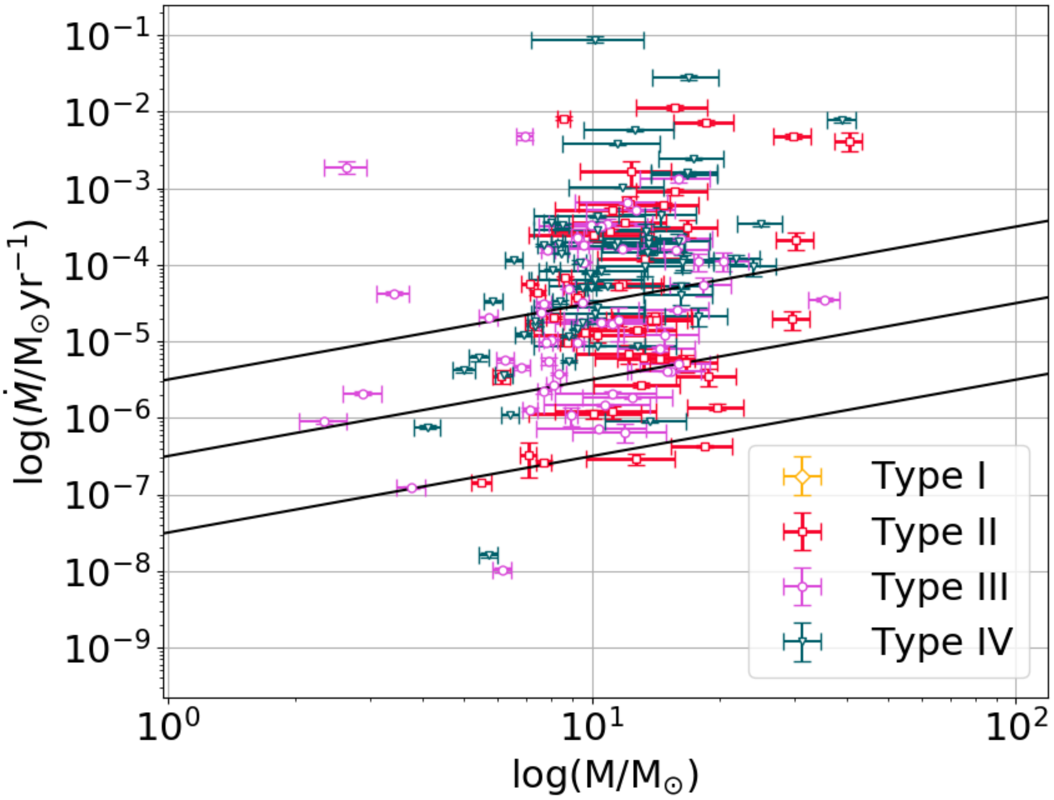

Figure 5.1: The accretion rate (deduced from the Brγ line flux) as a function of MYSO mass is presented here, colour coded for the C13 MYSO evolutionary types.

features, some similar to the previous results of Bunn *et al.* (1995) and Lumsden *et al.* (2012). The variety of observed Brγ/Br12 line ratio features may be a consequence different types of prestellar wind in MYSOs, or due to differences in the inclination of MYSOs with respect to the line of sight. Comparing these observed profiles with radiative line transfer modelling will help discern what gives rise to the observed variety of profile features, although higher resolution data may be needed.

Brγ luminosities and accretion rates from this line agree with values from lower–mass YSOs, pointing to a similar formation mechanism across the whole mass range, as predicted by monolithic collapse models. Here I combine the data from Chapter 2 and 3 with the data of Cooper (2013) in order to obtain the largest sample of MYSO accretion rates to date, with data from more than 200 MYSO.

This is shown in Figure 5.1, colour coded for the different MYSO evolutionary types of C13. Most accretion rates here range between $\dot{M}$=$10^{-7.5}$–$10^{-5.5}$ M_*, but a number of MYSOs do have accretion rates above $10^{-5.5}$ M_*. There is, however, no segregation of accretion rates with the C13 MYSO classes. Type IIs have an average $\dot{M}$=8.7×10^{-4} $M_\odot$, Type IIIs 2.2×10^{-4} $M_\odot$, Type IVs 9.8×10^{-3} $M_\odot$, and the whole sample average is 4.1×10^{-3} $M_\odot$. The reason for the large accretion rates and their lack of segregation with evolutionary classes may be that these objects are undergoing an accretion burst, or because of the presence of a non–wind, optically thin nebular Brγ component artificially increasing the line flux. Values of mass accretion rates deduced here are in agreement with theoretical predictions, for both quiescent (10^{-6}–10^{-3} $M_\odot$/yr, as assumed in the models of Davies *et al.* 2011 and Hosokawa *et al.* 2010) and outbursting (10^{-3}–10^{-1} $M_\odot$/yr as found in the simulations of Meyer *et al.* 2017) MYSOs. This result is consistent with the accretion process in MYSOs being scaled up from the mechanisms taking place in lower mass Herbig Ae/Be and T Tauri stars. This agrees with the results of Maud *et al.* (2015), who found that the outflow parameters in MYSOs scale with source luminosities in a similar manner to low–mass YSOs. All these results show that the way that massive star formation proceeds is likely a scaled–up version of the low–mass process. If this is the case, MYSO accretion discs should be scaled–up versions of low–mass discs. High–resolution observations of line tracers such as CO bandheads (as done by Ilee *et al.* 2013) or fluorescent FeII (Lumsden *et al.* 2012) can provide disc parameters. Doing a similar analysis on a large sample of MYSOs from the RMS will help setttle the question of whether the inner discs of high–mass protostars are scaled–up versions of the same regions in low–mass protostars.

Most of the pairs of line fluxes observed in both the Gemini and AAT samples correlate with one another, even when normalised by bolometric luminosity. Flux correlations include lines such as HeI and [FeII] that originate from completely different parts of the circumstellar environment. This wealth of correlations may be due to a scaling effect (as discussed by Mendigutía *et al.* 2015) and as such do not necessarily imply causality. More massive MYSOs are likely to have larger discs and stronger outflows, and so both the transitions probing discs and outflows are stronger.

Chapter 4 presented a pilot adaptive optics survey for MYSO binaries using K band imaging with the NaCo instrument at the VLT. 32 RMS MYSOs were studied, with companions detectable between 0.15–3” and to a magnitude difference of ΔK=5 mag from the primary. These angular separations are equivalent to average physical separations of 230–23,000 au, probing the widest binary systems. Statistical methods were employed in order to discern which of the companions were physical and which were chance alignments. Based on the background density of sources and the distance to the primary, 18 sources were determined to be likely physical companions. The number of companions detected corresponds to a multiplicity fraction of 31% and a companion fraction of 53%. These quantities do not vary significantly over distance, luminosity or extinction range. The multiplicity fraction of MYSOs is larger than that of low–mass Class II/III YSOs and Main Sequence O stars. Comparisons indicate that the frequency of wide companions is largest in the earliest, most embedded evolutionary phases. Also, multiplicity seems to be more frequent for the most massive stars, similar to the results from Main Sequence stars. Most of the lower limits to the mass ratios are larger than 0.5, more than expected by randomly sampling the field IMF, as is predicted by the capture binary formation theory. No difference is found between MYSOs with wide binaries and those without, or the full RMS sample in terms of bolometric luminosity, distance, clustering, outflow or disc presence.

The final step for the analysis of this multiplicity survey will be to constrain the selection effects. Work is currently being done using a Monte Carlo–based algorithm to constrain the observational biases of this survey and obtain corrected multiplicity and companion fractions. These multiplicity fractions can then be fed into future massive star formation simulations as initial conditions.

In conclusion, the key contribution of this thesis to the field has been to observe the largest samples to date of MYSOs and their potential companions with NIR methods. Results presented here show that MYSOs for in a similar fashion to low–mass YSOs, as predicted by monolithic collapse. On the other hand, MYSOs have many companions (at least on >hundreds of au scales), which probably influence their formation in ways that are not well understood by models or observations. Modelling of line profiles and combining high–resolution observations with full radiative transfer models will allow us to understand more about the circumstellar region of MYSOs, and the impact of binary companions on evolution.

5.1 Future work

5.1.1 Evolutionary trends in MYSOs

The data presented in this thesis, together with the previous results of Cooper (2013) form part of a larger RMS NIR spectroscopic survey follow up programme. By obtaining spectra of all the MYSOs found by the RMS survey, a better understanding of the inner 100s of au of these objects can be obtained. The structure of the circumstellar region of MYSOs can be compared with predictions from recent theoretical models such as Meyer *et al.* (2017) or Kuiper *et al.* (2011) in order to better understand the physics of accretion throughout this phase and the high–mass star formation process in general. For instance, the disc properties could be determined from full radiative transfer models of the fluorescent FeII line, following on from the work of Lumsden *et al.* (2012).

Comparisons of the data from Chapters 2, 3 and Cooper (2013) show that data at different spectral resolutions, obtained at different epochs and under different atmospheric conditions can be used concomitantly to draw significant conclusions about the evolution of MYSOs. Once spectra are obtained of all the MYSOs in the Galaxy above the completeness limit of the RMS survey of 10,000 $L_\odot$, the timescales of the different stages of MYSO evolution can be determined and compared with the predictions of the Hosokawa *et al.* (2010) or other models. Environmental effects can be studied in order to determine whether there are any differences in terms of MYSO evolutionary stages found between different Galactic star forming regions or with MYSOs in nearby Galaxies.

Our group has recently obtained X–Shooter data (PI Oudmaijer) for a sample of order 40 MYSOs. This data will be added to the already existing data in order to form a distance and luminosity complete sample. Comparing the fractions of P Cygni and inverse P Cygni profiles in the data will provide an estimate of the geometry of the accretion material. The prevalence of P Cygni–type features can be studied as a function of evolutionary stage, and combined with studies of velocity resolved ratios of HI recombination line profiles like in Section 3.9 in order to understand the geometry of the wind. Kinematic information from inverse P Cygni profiles will be used to determine the conditions of the infall.

5.1.2 Multi–wavelength studies of the circumstellar region

As shown in Chapter 2, NIR observations can be combined with information from other wavelength ranges in order to understand the interplay of emission components in MYSOs. Radio observations provide information about ionised jets, submillimetre observations give information about the clumps within which the MYSOs are located, and MIR observations provide clues about complex molecules in the circumstellar region. Several discs have already been detected around MYSOs with ALMA (Johnston *et al.* 2015), SMA (Ilee *et al.* 2016) and the VLT (Kraus *et al.* 2011). More direct disc measurements from multi–wavelength observations can be compared with predictions from simulations in order to distinguish between different star formation theories – monolithic collapse and competitive accretion offer different prescriptions as to the properties of discs as discussed in Section 1.3. All this data can be used to constrain the inclination of the disc–outflow system with regards to our line of sight and eliminate biases caused by varying inclination.

5.1.3 Multiplicity of MYSOs

Recent observations by Sana *et al.* (2012) have shown that multiplicity is ubiquitous for massive Main Sequence stars, with ≥90% of OB stars being in multiple systems. In addition, at least 70% of Main Sequence OB multiple systems are close enough for interactions to occur during their lifetimes. The large multiplicity fraction of OB stars has significant implications for stellar and cluster evolution models, which are mostly based on single stellar systems.

The data presented in Chapter 4 is part of a pilot survey of the multiplicity of MYSOs, surveying the widest binary separations (≈1000s of au). Recent simulations find many companions at closer separations (Meyer *et al.* 2017, Bonnell et al., in prep.). Kraus *et al.* (2017) have recently reported the discovery of a tight (170 au) binary MYSO system of 18 and 20 $M_\odot$ with VLTI–GRAVITY.

We are aiming to obtain VLTI–GRAVITY data for 10 MYSOs from the NaCo sample (PI de Wit), with baselines of 45 and 130 m, which at 2.2 μm will translate to separations of 1–160 au for the average MYSO distance of 2 kpc and to mass ratios of $q>0.1$. This data will be complementary to the current NaCo data set, probing the tightest binaries. With this sample size, a multiplicity fraction within 15% accuracy can be determined, which should help exclude either the

100% or 0% multiplicity fraction hypothesis.
In addition, H band adaptive optics imaging of companions detected at K would provide more useful information to complement the current data set. By combining H band data with the current NaCo data set, colour–colour magnitude plots can be constructed which will be used to eliminate any visual companions, or companions which are not MYSOs (based on the selection criteria of the RMS). Finally, IFU data from SINFONI can be used in order to obtain spectra of the already detected companions with NaCo. IFU data will provide clues on the circumstellar region of these wide companions, by comparing the detection rates of different disc and wind tracers in the system components. Accretion rates from Brγ will provide information about how the accretion proceeds in a multiple system. The companions will be classified under the evolutionary sequence detailed in Chapter 2. The results can be compared with recent simulations of multiple massive star formation.

5.2 Closing remarks

In conclusion, this thesis has presented follow–up RMS NIR spectroscopy and imaging surveys of MYSOs. Information about the evolution, circumstellar environment and multiplicity of MYSOs has been obtained through these observations. The evolutionary sequence of Cooper (2013) has been tested on higher resolution samples, and shown to be consistent with results from other wavelength ranges such as radio and submilimetre. The circumstellar region of MYSOs was probed with medium–resolution Gemini spectroscopy. These data have found the first observational evidence for the swollen up MYSOs predicted by the Hosokawa *et al.* (2010) models. A wide variety of protostellar winds was seen from ratios of HI recombination lines. Results from both the AAT and GNIRS samples find that the accretion and disc parameters of MYSOs are scaled–up versions of lower–mass HAe/Bes and TTaus. A pilot AO K band imaging survey has determined the multiplicity fraction of MYSOs and compared the multiplicity fractions with T Tauris and MS OB stars for wide companions from 100s to 10000s of au. The results pointed to multiplicity increasing with mass and decreasing with age.
Future studies of larger samples of MYSOs at higher resolution and using different multi–wavelength techniques can help explain the physics of the massive star–formation process even further. More sophisticated 3D full radiative transfer models including magnetic fields, turbulence and other important effects will

be useful and complement observations from the next generation of instruments from the ground and space (JWST, E–ELT, SKA).

Appendix A

AAT observing logs

Table A.1: AAT observing logs. RA and Dec are taken from the RMs catalogue. ZD is the zenith distance of the observations, where airmass=1/cos(ZD). Observing date, exposure time and position angles are also given. Source types as defined in the RMS catalogue are: YSO - Young Stellar Object; Y/O - Young/Old Star; ES - Evolved Star; HII - HII region; O - Other.

RMS name	RA	Dec	Date K	ZD K	Exp. K (s)	Date H	ZD H	Exp H (s)	PA (°)	RMS type
G010.8856+00.1221	18:04:04.40	-19:27:24.00	27/05/10		20				90	YSO
G012.5932-00.5708	18:15:10.26	-18:17:32.20	19/06/11	49	300				0	Y/O
G012.9090-00.2607	18:14:39.56	-17:52:02.30	07/06/06	49	200	20/07/07	44	400	0	YSO
G013.3310-00.0407	18:14:41.80	-17:23:27.70	21/05/08	46	200				0	YSO
G014.2166-00.6344	18:18:38.63	-16:53:36.80	21/05/08	51	200				0	YSO
G014.4335-00.6969	18:19:18.21	-16:43:56.10	06/06/06	53	300	08/06/06	57	300	90	YSO
G014.9958-00.6732	18:20:19.47	-16:13:29.80	06/06/06	57	100	08/06/06	40	300	90	YSO
G015.1288-00.6717	18:20:34.60	-16:06:28.20	07/06/06	43	200	08/06/06	47	300	58	YSO
G016.9261+00.2854	18:20:35.44	-14:04:13.90	07/06/06	56	200	22/07/07	66	200	0	YSO
G016.9270+00.9599	18:18:08.62	-13:45:07.00	07/06/06	54	200	20/07/07	61	400	0	YSO
G017.6380+00.1566	18:22:26.37	-13:30:12.00	07/06/06	61	150	25/07/07	60	300	135	YSO
G024.1260+00.3369	18:34:04.03	-07:40:31.60	19/06/11	57	300				0	ES
G025.4118+00.1052	18:37:16.99	-06:38:24.30	19/06/11	63	300				0	ES
G026.3050+00.1162	18:38:53.53	-05:50:30.50	20/05/08	41	200				0	O
G027.7571+00.0500	18:41:44.80	-04:34:52.90	27/05/10	31	30				0	YSO
G029.4332+00.1542	18:44:29.97	-03:02:35.60	21/05/08	57	20				0	ES
G029.8620-00.0444	18:45:59.55	-02:45:06.50	22/06/11	65	120	22/06/11	65	200	157	YSO
G231.7986-01.9682	07:19:35.92	-17:39:18.0	20/05/08	38	30	19/05/08	41	100	0	YSO

Table A.1: continued

RMS name	RA	Dec	Date K	ZD K	Exp. K (s)	Date H	ZD H	Exp H (s)	PA (°)	RMS type
G233.8306-00.1803	07:30:16.65	-18:35:49.1	20/05/08	37	30	19/05/08	45	100	0	YSO
G254.0548-00.0961	08:17:52.62	-35:52:47.60	09/06/06	40	150	08/06/06	37	300	60	YSO
G259.0453-01.5559	08:26:17.70	-40:48:40.50	27/05/10	47	30				0	YSO
G263.5846-03.9973	08:29:53.20	-45:55:09.5	20/05/08	30	300	19/05/08	38	400	0	YSO
G263.5994-00.5236	08:45:33.10	-43:49:47.60	07/06/06	43	150				0	YSO
G263.7434+00.1161	08:48:48.64	-43:32:29.0	07/06/06	45	200	08/06/06	41	300	0	YSO
G263.7759-00.4281	08:46:34.84	-43:54:29.8	09/06/06	45	150	08/06/06	37	300	135	YSO
G264.1444+02.0190	08:58:12.81	-42:37:37.70	09/06/06	35	150				90	YSO
G265.1438+01.4548	08:59:27.40	-43:45:03.7	09/06/06	38	150	22/06/11	53		90	YSO
G267.7336-01.1058	08:58:04.40	-47:23:05.60	20/05/08	32	200	19/05/08	44	400	21	YSO
G267.9094+01.7816	09:11:14.23	-45:35:10.6	09/06/06	38	150	08/06/06	49	200	95	YSO
G268.3957-00.4842	09:03:25.08	-47:28:27.60	09/06/06	47	150	21/05/08	18	300	145	YSO
G268.6162-00.7389	09:03:09.51	-47:48:27.3	07/06/06	46	150	08/06/06	46	200	0	HII
G269.1586-01.1383	09:03:31.76	-48:28:45.50	20/05/08	36	200	19/05/08	52	400	29	YSO
G274.0649-01.1460	09:24:42.54	-52:01:50.60	20/05/08	40	200				18	YSO
G282.2988-00.7769	10:10:00.38	-57:02:07.3	25/07/07	45	40	24/07/07	53	50	0	YSO
G282.8969-01.2727	10:11:31.70	-57:47:03.7	26/06/05	44	300	22/07/07	58	300	0	YSO
G283.9146-01.0485	10:18:49.96	-58:10:11.30	20/06/11	44	300				90	YSO
G284.2438-01.1302	10:20:35.17	-58:25:07.1	20/06/11	48	300	20/06/11	52	400	90	HII
G284.2637-00.3161	10:24:02.44	-57:44:35.7	09/06/06	52	200	24/07/07	56	200	90	O
G285.3472+00.0013	10:32:14.16	-58:02:12.7	09/06/06	49	200	08/06/06	41	200	90	HII

Table A.1: continued

RMS name	RA	Dec	Date K	ZD K	Exp. K (s)	Date H	ZD H	Exp H (s)	PA (°)	RMS type
G287.1921-01.4042	10:39:16.56	-60:10:24.1	07/06/06	44	200	08/06/06	45	200	45	Y/O
G287.3716+00.6444	10:48:04.63	-58:27:01.5	07/06/06	36	100	08/06/06	45	150	0	YSO
G293.5607-00.6703	11:30:07.10	-62:03:12.8	09/06/06	50	300	21/07/07	48	400	90	YSO
G293.8947-00.7825	11:32:32.82	-62:15:43.1	07/06/06	36	150	08/06/06	42	200	0	YSO
G294.6168-02.3440	11:34:32.85	-63:58:04.6	07/06/06	38	300	08/06/06	45	300	0	YSO
G295.5570-01.3787	11:45:04.73	-63:17:46.20	21/05/08	33	300				129	YSO
G296.2654-00.3901	11:53:10.93	-62:30:20.00				25/07/07	50	100	30	YSO
G297.4585-00.7636	12:02:43.47	-63:06:57.20	21/05/08	32	300	21/05/08	35	300	129	YSO
G298.1829-00.7860	12:09:01.27	-63:15:59.7	30/06/05	37	140	25/07/07	45	100	0	HII
G298.2620+00.7394	12:11:47.68	-61:46:18.8	21/05/08	36	300	22/05/08	32	400	19	YSO
G298.8591-00.4372	12:15:24.98	-63:01:20.60	21/05/08	33	300				0	HII
G300.3412-00.2190	12:28:35.74	-62:58:35.4	07/06/06	37	150	08/06/06	42	200	45	YSO
G301.1726+01.0034	12:36:31.98	-61:49:02.8	30/06/05	32	300	30/06/05	50	300	0	YSO
G301.8147+00.7808	12:41:53.86	-62:04:14.6	22/07/07	49	30	22/07/07	46	100	135	YSO
G302.4546-00.7401	12:47:08.62	-63:36:30.0	27/05/10	40	30	22/05/08	33	400	90	YSO
G302.6604-00.7908	12:48:59.36	-63:39:40.00	21/05/08	42	200	22/05/08	33	400	0	YSO
G304.7592-00.6299	13:07:47.42	-63:26:37.0	26/07/07	39	200	22/05/08	36	400	0	YSO
G305.2017+00.2072	13:11:10.45	-62:34:38.60	30/06/05	35	300		54	300	0	YSO
G305.4840+00.2248	13:13:35.99	-62:32:14.00	30/06/05	38	300				0	YSO
G306.1160+00.1386	13:19:08.79	-62:33:40.80	06/06/06	37	300	08/06/06	43	150	90	YSO
G308.0049-00.3868	13:36:04.91	-62:49:05.4	06/06/06	32	300	08/06/06	44	200	0	YSO

Table A.1: continued

RMS name	RA	Dec	Date K	ZD K	Exp. K (s)	Date H	ZD H	Exp H (s)	PA (°)	RMS type
G308.6480+00.6469	13:39:55.98	-61:40:58.90	20/06/11	40	300				35	YSO
G309.9206+00.4790	13:50:41.55	-61:35:06.40	22/07/07	45	100	22/07/07	50	300	159	YSO
G309.9796+00.5496	13:51:02.72	-61:30:14.1	07/06/06	32	200	08/06/06	37	400	45	YSO
G310.0135+00.3892	13:51:37.85	-61:39:07.5	06/06/06	31	20	08/06/06	44	50	0	YSO
G311.6380+00.3009	14:04:58.95	-61:19:16.70	19/05/08	31	300	22/05/08	33	400	357	YSO
G311.9799-00.9527	14:10:51.19	-62:25:16.40	06/06/06	37	300	08/06/06	45	200	90	YSO
G314.2964+00.1009	14:26:17.61	-60:39:40.9	06/06/06	30	90	08/06/06	41	150	0	Y/O
G315.4195-00.3140	14:36:03.48	-60:37:28.40	19/05/08	31	300				0	Y/O
G318.9480-00.1969	15:00:55.31	-58:58:52.60	20/06/11	39	300				10	YSO
G320.2046+00.8626	15:05:23.04	-57:26:49.2	22/05/08	45	300	22/05/08	30	400	21	YSO
G320.2437-00.5619	15:11:01.59	-58:39:37.1	20/07/07	37	200	25/07/07	32	300	0	YSO
G321.3824-00.2861	15:17:20.21	-57:50:00.3	27/05/10		20	22/07/07	48	300	90	YSO
G322.4679+00.6627	15:20:22.31	-56:27:06.00	21/05/08	26	200				0	Y/O
G323.4584-00.0787	15:29:19.36	-56:31:21.7	09/06/06	28	300	08/06/06	36	200	0	HII
G324.1594+00.2622	15:32:03.90	-55:50:35.50	07/06/06	25	200	22/07/07	52	300	65	YSO
G326.4755+00.6947	15:43:18.97	-54:07:35.60	30/06/05	40	300	08/06/06	39	300	0	YSO
G326.7249+00.6159	15:44:59.42	-54:02:17.4	06/06/06	27	300	22/07/07	57	200	90	YSO
G326.7796-00.2405	15:48:55.23	-54:40:37.60	26/07/07	29	300	22/06/11	31	300	45	YSO
G327.1192+00.5103	15:47:32.80	-53:52:39.3	19/06/11	23	300	22/05/08	27	400	0	YSO
G327.3941+00.1970	15:50:20.07	-53:57:07.1	19/06/11	24	300	22/06/11	23	300	90	YSO
G327.8097-00.6339	15:56:07.85	-54:19:51.30	30/06/05	43	200				0	YSO

Table A.1: continued

RMS name	RA	Dec	Date K	ZD K	Exp. K (s)	Date H	ZD H	Exp H (s)	PA (°)	RMS type
G327.9455-00.1149	15:54:34.65	-53:50:42.20	26/07/07	23	300				70	YSO
G328.3442-00.4629	15:58:09.62	-53:51:18.2	06/06/06	30	300	08/06/06	41	100	90	YSO
G328.3503-00.5586	15:58:36.82	-53:55:25.10	27/05/10	25	30				90	HII
G329.4925+00.8308	15:58:24.16	-52:07:33.90	19/05/08	21	300				0	Y/O
G330.9288-00.4070	16:10:44.92	-52:05:50.3	19/06/11	24	300	22/06/11	21	300	90	HII
G331.3546+01.0638	16:06:23.10	-50:43:27.2	22/06/11	35	200	22/06/11	28	300	90	HII
G331.7953-00.0979	16:13:28.03	-51:16:46.7	19/06/11	31	300	22/06/11	23	400	90	YSO
G332.8256-00.5498	16:20:11.14	-50:53:15.90	07/06/06	20	250	25/07/07	24	300	25	YSO
G332.9457+02.3855	16:08:12.00	-48:40:38.5	26/06/05	20	300	08/06/06	40	200	0	YSO
G332.9868-00.4871	16:20:37.81	-50:43:49.6	06/06/06	37	300	21/07/07	20	400	90	YSO
G333.1153+00.0950	16:18:38.14	-50:13:32.8	06/06/06	30	300	08/06/06	43	200	90	YSO
G333.4593+01.9795	16:12:09.06	-48:37:35.90	30/06/05	52	140				0	ES
G333.4747-00.2366	16:21:41.49	-50:12:32.1	06/06/06	48	300	21/07/07	30	400	90	YSO
G334.3272-00.2884	16:25:37.84	-49:38:13.6	26/07/07	36	150	25/07/07	28	100	0	ES
G337.8442-00.3748	16:40:26.69	-47:07:13.30	30/06/05	44	200	30/06/05	60	200	0	HII
G338.5459+02.1175	16:32:32.18	-44:55:30.6	06/06/06	38	90	08/06/06	47	300	90	YSO
G338.9196+00.5495	16:40:34.04	-45:42:07.9	30/06/05	52	300	30/06/05	65	300	0	YSO
G338.9341-00.0623	16:43:16.03	-46:05:40.5	07/06/06	18	200	25/07/07	31	300	135	YSO
G338.9377-00.4890	16:45:08.24	-46:22:18.5	26/07/07	41	300	25/07/07	40	300	78	ES
G339.3940-00.4084	16:46:25.30	-45:58:20.70	27/05/10	19	20				90	YSO
G339.5836-00.1265	16:45:58.48	-45:38:41.40	19/06/11	31	300				100	YSO

Table A.1: continued

RMS name	RA	Dec	Date K	ZD K	Exp. K (s)	Date H	ZD H	Exp H (s)	PA (°)	RMS type
G339.6221-00.1209	16:46:05.99	-45:36:43.9	26/07/07	55	300	22/06/11	38	300	135	YSO
G339.6816-01.2058	16:51:05.95	-46:15:52.40	30/06/05	38	200				0	YSO
G339.8838-01.2588	16:52:04.79	-46:08:36.30	19/06/11	38	300				300	YSO
G340.1537+00.5116	16:45:20.10	-44:47:49.8	06/06/06	53	300	22/06/11	29	200	90	YSO
G343.1261-00.0623	16:58:17.20	-42:52:07.10	22/06/11	47	300				320	YSO
G343.5024-00.0145	16:59:20.78	-42:32:37.5	07/06/06	28	200	25/07/07	45	150	20	HII
G344.4257+00.0451	17:02:09.35	-41:46:44.30	20/06/11	20	300	22/06/11	52	300	19	HII
G344.6608+00.3401	17:01:41.02	-41:24:48.1	07/06/06	40	150	25/07/07	55	400	135	YSO
G345.2619-00.4188	17:06:50.80	-41:23:46.4	07/06/06	37	150	21/07/07	41	300	138	YSO
G345.4938+01.4677	16:59:41.61	-40:03:43.30	19/06/11	45	300	20/06/11	54	400	131	YSO
G345.9561+00.6123	17:04:43.00	-40:13:13.4	07/06/06	33	150	25/07/07	57	200	20	YSO
G347.0775-00.3927	17:12:25.81	-39:55:19.9	07/06/06	41	150	22/07/07	52	200	110	YSO
G347.2667+00.0203	17:11:16.69	-39:31:31.2	07/06/06	47	150	22/07/07	59	200	45	HII
G348.7342-01.0359	17:20:07.93	-38:57:14.80	22/06/11	63	150	22/06/11	58	200	90	YSO

Appendix B

AAT data tables

Table B.1: AAT YSO parameters. Distances, bolometric luminosities are taken from the RMS database. Flux correction factors f$_o$/f$_c$ calculated as per the method described in Section 2.3. Circumstellar extinctions are determined from H-K near-infrared colours. Foreground extinctions from Neckel *et al.* (1980) and Green *et al.* (2015) (see Section 2.4).

RMS name	C13 Type	d (kpc)	L$_{bol}$ (10^3L$_\odot$)	m$_K$ (mag)	Δm$_K$ (mag)	m$_H$ (mag)	Δm$_H$ (mag)	m$_J$ (mag)	Δm$_J$ (mag)	f$_o$/f$_c$ H	Δf$_o$/f$_c$ H	f$_o$/f$_c$ K	Δf$_o$/f$_c$ K	Av$_c$ (mag)	ΔAv$_c$ (mag)	Av$_f$ (mag)	ΔAv$_f$ (mag)
G010.8856+00.1221	4	2.4	32.0	9.76	0.00	13.21	0.00	18.69	0.10			1.34	0.10	64.0	0.0	4.2	0.0
G012.9090-00.2607	2	2.4	32.0	13.61	0.00	15.40	0.00	15.40	0.00	0.08	0.00	0.02	0.01	32.7	0.0	2.9	0.1
G013.3310-00.0407	3	4.5	3.7	9.96	0.00	12.38	0.00					11.58	0.26	44.5	0.0	4.2	0.1
G014.2166-00.6344	4	1.1	0.3	9.57	0.00	11.74	0.00	14.66	0.00			0.92	0.02	39.9	0.0	0.8	0.1
G014.4335-00.6969	4	1.1	1.3	8.45	0.03	11.45	0.04			1.06	0.06	1.84	0.07	55.7	0.1	0.6	0.1
G014.9958-00.6732	3	2	13.0	7.25	0.02	9.76	0.04			3.41	0.12	1.04	0.02	46.3	0.1	1.0	0.0
G015.1288-00.6717	abs	2	12.0	8.89	0.03	10.99	0.00	12.81	0.00	0.94	0.01	1.49	0.05	38.5	0.1	0.7	0.0
G016.9261+00.2854	?	2.4	1.3	9.85	0.03	13.52	0.00			0.26	0.04	1.19	0.06	68.1	0.1	1.3	0.0
G016.9270+00.9599	4	2.1	7.6	9.40	0.02	12.87	0.00			0.51	0.03	1.64	0.05	64.6	0.1	1.4	0.1
G017.6380+00.1566	?	2.2	100.0	7.32	0.02	14.12	0.00	15.05	0.00	0.17	0.00	3.29	0.39	127.1	0.1	1.3	0.0
G027.7571+00.0500	4	5.4	13.0	9.57	0.00	13.09	0.00					0.88	0.02	65.5	0.0	3.8	0.0
G029.8620-00.0444	?	4.9	28.0	10.18	0.00	16.55	0.01			0.01	0.00	0.45	0.01	119.2	0.0	3.9	0.0
G231.7986-01.9682	4	3.2	5.6	6.44	0.02	7.76	0.05	9.23	0.02	0.23	0.01	0.86	0.02	24.0	0.1	1.6	0.0
G233.8306-00.1803	4	3.3	13.0	6.06	0.03	8.03	0.03			0.92	0.03	1.37	0.05	36.2	0.1	1.9	0.1
G254.0548-00.0961	3	2.8	1.9	9.57	0.08	12.07	0.15	13.71	0.12	0.37	0.06	3.10	0.33	46.1	0.5	2.0	0.1
G259.0453-01.5559	3	5.6	7.4	11.39	0.05	13.15	0.09	15.42	0.14			1.03	0.08	32.1	0.3	2.5	0.1
G263.5846-03.9973	3	11.7	5.9	10.36	0.03	12.15	0.05	14.43	0.08	0.39	0.02	0.54	0.02	32.8	0.2	1.5	0.1
G263.5994-00.5236	?	0.7	0.2	8.39	0.02	9.69	0.03	11.24	0.03			1.89	0.08	23.5	0.1	0.2	0.0
G263.7434+00.1161	?	0.7	1.2	9.01	0.03	12.25	0.08	15.40	0.13	0.11	0.01	0.96	0.05	60.1	0.2	0.2	0.0
G263.7759-00.4281	3	0.7	1.3	9.64	0.04	12.61	0.05	14.64	0.00	0.07	0.02	1.30	0.08	55.1	0.1	0.2	0.1
G264.1444+02.0190	4	0.7	0.8	9.66	0.03	12.77	0.06					1.00	0.06	57.6	0.2	0.7	0.1
G265.1438+01.4548	4	0.7	0.7	9.63	0.02	11.08	0.02	12.71	0.02	0.91	0.02	0.94	0.04	26.3	0.1	0.3	0.1
G267.7336-01.1058A	4	0.7	0.2	9.72	0.06	10.73	0.09	12.08	0.07	0.58	0.05	0.88	0.06	18.0	0.3	0.9	0.1
G267.9094+01.7816	?	0.7	0.2	9.23	0.03	10.53	0.05	12.39	0.05	2.41	0.13	0.35	0.03	23.7	0.2	0.2	0.0
G268.3957-00.4842	4	0.7	3.0	8.34	0.04	11.80	0.04	15.71	0.07	1.01	0.05	2.57	0.11	64.2	0.1	0.4	0.1

G269.1586-01.1383A	3	0.7	0.2	10.72	0.04	11.75	0.05	12.95	0.04	0.29	0.02	0.99	0.07	18.5	0.2	0.4	0.1
G274.0649-01.1460A	3	5.7	6.0	10.04	0.04	13.21	0.09	15.27	0.10			0.70	0.05	58.7	0.3	2.8	0.0
G282.2988-00.7769	4	3.7	4.0	6.97	0.02	8.36	0.04	10.22	0.03	0.49	0.02	1.02	0.04	25.4	0.1	1.7	0.1
G282.8969-01.2727	2	7	17.0	9.92	0.03	14.68	0.06			0.00	0.00	0.95	0.04	88.9	0.2	2.2	0.0
G283.9146-01.0485	1	4.9	6.0	12.45	0.07	14.23	0.08	15.52	0.09			1.05	0.14	32.7	0.2	2.3	0.0
G287.3716+00.6444	3	4.5	18.0	7.46	0.02	8.92	0.03	10.44	0.02	0.27	0.01	3.13	0.08	26.5	0.1	2.3	0.1
G293.5607-00.6703	3	3.4	4.0	9.55	0.00	12.17	0.13	14.91	0.16	0.36	0.05	1.27	0.06	48.5	0.4	3.2	0.0
G293.8947-00.7825	4	9.2	14.0	7.94	0.02	7.99	0.03	8.06	0.03	10.59	0.36	3.97	0.12	0.0	0.1	1.1	0.1
G294.6168-02.3440	3	1.6	0.6	9.94	0.03	11.84	0.06	14.22	0.05	0.48	0.03	1.79	0.05	34.9	0.2	1.2	0.0
G295.5570-01.3787	3	10	2.1	11.47	0.00	12.76	0.00	14.54	0.00			0.63	0.02	23.4	0.0	0.9	0.0
G298.2620+00.7394	2	4	15.0	11.78	0.00	15.51	0.01	17.20	0.01	0.52	0.19	0.59	0.04	69.5	0.0	1.3	0.1
G300.3412-00.2190	4	4.2	6.0	8.68	0.03	11.48	0.00	13.08	0.00	0.08	0.00	0.31	0.01	51.9	0.1	1.8	0.0
G301.1726+01.0034	3	4.3	21.0	7.92	0.03	10.17	0.04	12.00	0.00	0.45	0.02	1.02	0.04	41.5	0.1	1.9	0.0
G301.8147+00.7808	3	4.4	22.0	6.83	0.02	9.31	0.05	11.98	0.00	0.31	0.02	0.74	0.03	45.8	0.2	1.9	0.1
G302.4546-00.7401	3	11.5	16.0	11.73	0.00	13.80	0.00	16.17	0.01	0.78	0.05	0.54	0.03	38.0	0.0	4.1	0.1
G302.6604-00.7908	?	10.8	11.0	9.99	0.02	13.60	0.00	16.16	0.01	0.69	0.10	1.53	0.09	67.0	0.1	4.0	0.1
G304.7592-00.6299	3	11.2	4.1	10.04	0.03	12.53	0.00	15.02	0.01	6.98	2.96	0.56	0.03	45.9	0.1	4.0	0.1
G305.2017+00.2072A	2	4	30.0	10.34	0.00	12.03	0.00	14.04	0.00	0.55	0.02	0.52	0.01	30.9	0.0	2.3	0.0
G305.4840+00.2248	2	4	2.1	10.00	0.03	12.50	0.00	14.57	0.00			1.40	0.06	46.1	0.1	3.6	0.1
G306.1160+00.1386A	2	4	1.7	11.06	0.00	12.57	0.00	14.53	0.00	0.14	0.00	0.12	0.01	27.4	0.0	2.9	0.1
G306.1160+00.1386B	3	4	1.1	8.43	0.03	9.79	0.04	11.60	0.04	0.21	0.01	0.32	0.02	24.7	0.1	2.9	0.0
G308.0049-00.3868	4	7	8.3	9.46	0.03	12.07	0.00	14.23	0.00	0.67	0.01	0.13	0.01	48.3	0.1	2.8	0.1
G308.6480+00.6469A	2	4	0.5	10.62	0.03	13.55	0.10	14.69	0.02			0.61	0.05	54.1	0.3	1.2	0.1
G309.9206+00.4790B	2	5.4	11.0	11.40	0.00	12.20	0.06	14.46	0.00	2.00	0.33	1.22	0.14	14.1	0.2	1.4	0.0
G309.9796+00.5496	3	3.5	7.6	9.70	0.03	12.38	0.05	16.02	0.01	1.02	0.06	1.52	0.09	49.5	0.2	1.2	0.0
G310.0135+00.3892	4	3.2	67.0	4.87	0.02	7.57	0.02	12.35	0.00	0.79	0.02	0.16	0.01	50.0	0.1	2.0	0.1
G311.6380+00.3009A	3	7.3	1.8	11.43	0.00	13.53	0.00	16.78	0.02	0.94	0.11	1.07	0.05	38.6	0.0	2.3	0.1
G311.9799-00.9527	abs	3.2	2.9	10.65	0.00	11.78	0.00	11.91	0.00	0.10	0.00	0.11	0.00	20.4	0.0	1.8	0.1
G318.9480-00.1969A	1	2.4	14.0	11.72	0.00	15.06	0.01	18.47	0.08			1.00	0.05	62.1	0.0	2.3	0.1
G320.2046+00.8626B	3	2.8	0.5	9.69	0.03	12.56	0.00	14.63	0.00	1.16	0.15	4.06	0.21	53.2	0.1	3.6	0.0
G320.2437-00.5619	?	9.5	31.0	9.36	0.03	13.01	0.00	17.76	0.05	0.42	0.01	0.43	0.03	67.7	0.1	4.2	0.1

G321.3824-00.2861	1	9.4	26.0	9.34	0.03	13.38	0.00			0.35	0.05	0.56	0.05	75.2	0.1	4.2	0.1
G324.1594+00.2622	?	6.8	19.0	9.33	0.06	11.97	0.00	14.71	0.00	0.36	0.01	1.28	0.11	48.8	0.2	1.8	0.0
G326.4755+00.6947	?	1.8	4.1	9.25	0.03	12.39	0.07	15.58	0.01	0.73	0.05	10.28	0.89	58.2	0.2	3.1	0.1
G326.7249+00.6159	HII	1.8	1.6	7.63	0.03	9.47	0.04			0.16	0.01	17.75	0.79	33.8	0.1	3.1	0.0
G326.7796-00.2405	?	3.9	6.7	11.36	0.00	13.60	0.00	16.57	0.02	0.64	0.10	0.80	0.07	41.2	0.0	2.7	0.1
G327.1192+00.5103	2	4.9	37.0	11.92	0.00	14.62	0.07			0.24	0.02	0.98	0.06	50.0	0.2	3.4	0.0
G327.3941+00.1970	2	5.2	11.0	11.01	0.00	14.20	0.00			0.80	0.03	0.58	0.03	59.1	0.0	3.5	0.0
G327.8097-00.6339A	4	3	1.0	8.64	0.03	11.76	0.00	13.27	0.00			0.69	0.03	58.0	0.1	2.4	0.1
G327.8097-00.6339B	1	3	1.0	12.09	0.00	12.99	0.00	13.97	0.00			9.73	30.15	16.0	0.0	2.4	0.0
G327.9455-00.1149	2	3.1	4.3	10.01	0.04	12.91	0.00	16.09	0.01			1.10	0.08	53.7	0.1	2.4	0.1
G328.3442-00.4629	3	2.9	2.4	7.74	0.03	8.88	0.03	10.13	0.02	0.49	0.01	0.31	0.01	20.4	0.1	2.3	0.0
G331.7953-00.0979	4	14.5	190.0	9.80	0.03	14.55	0.01			0.55	0.02	0.81	0.05	88.6	0.1	5.0	0.0
G332.8256-00.5498A	HII	3.6	130.0	8.93	0.03	13.19	0.00	19.43	0.23	0.64	0.05	1.16	0.13	79.4	0.1	3.5	0.1
G332.9457+02.3855	2	2	0.9	9.68	0.03	10.82	0.03	12.26	0.03	0.85	0.03	0.21	0.01	20.5	0.1	3.2	0.0
G332.9868-00.4871	?	3.6	18.0	9.30	0.03	13.98	0.00			0.62	0.04	1.90	0.10	87.2	0.1	1.5	0.0
G333.1153+00.0950	4	3.6	1.5	7.70	0.02	9.77	0.03	12.77	0.00	1.16	0.04	3.45	0.08	37.9	0.1	2.6	0.1
G333.4747-00.2366	2	3.6	2.7	9.57	0.02	13.71	0.00	16.54	0.02	0.40	0.01	0.99	0.03	77.2	0.1	2.6	0.1
G338.5459+02.1175	3	0.5	0.1	7.18	0.02	8.60	0.03	10.18	0.03	8.74	0.27	1.72	0.04	25.9	0.1	0.8	0.0
G338.9196+00.5495	1	4.2	32.0	10.72	0.00	13.07	0.00	17.80	0.08	1.00	0.09	0.27	0.01	43.3	0.0	1.8	0.1
G338.9341-00.0623	3	3.3	1.8	10.91	0.00	13.04	0.00	15.67	0.01	0.17	0.00	0.60	0.03	39.2	0.0	2.7	0.1
G339.3940-00.4084	4	3	0.9	10.11	0.03	13.57	0.00	17.35	0.05			0.85	0.04	64.3	0.1	2.9	0.0
G339.5836-00.1265	?	2.8	1.8	9.13	0.02	11.33	0.00	13.60	0.00			0.43	0.04	40.5	0.1	2.6	0.1
G339.6221-00.1209	?	2.8	19.0	11.03	0.00	12.58	0.05	15.49	0.00	1.51	0.09	0.32	0.02	28.3	0.2	2.6	0.1
G339.6816-01.2058	3	2.4	6.5	8.54	0.03	10.41	0.03	13.04	0.00			0.67	0.02	34.4	0.1	3.5	0.0
G339.8838-01.2588	abs	2.7	64.0	12.03	0.03	13.21	0.04	13.79	0.04			0.20	0.06	21.4	0.1	3.6	0.1
G340.1537+00.5116	4	3.8	1.1	7.91	0.02	9.44	0.03	12.07	0.00	0.24	0.01	0.57	0.02	27.9	0.1	2.9	0.0
G343.1261-00.0623	?	2.8	19.0	13.97	0.08	15.58	0.08	17.96	0.10			0.47	0.14	29.4	0.2	2.0	0.0
G344.4257+00.0451B	?	4.7	6.4	9.60	0.05	11.60	0.07	14.32	0.00	7.93	0.69	4.03	0.29	36.7	0.2	2.3	0.0
G344.4257+00.0451C	3	4.7	8.4	11.63	0.00	14.65	0.01	18.01	0.05			0.89	0.31	56.0	0.0	2.6	0.0
G344.6608+00.3401	3	12.7	20.0	9.47	0.03	12.13	0.00	15.74	0.01	0.06	0.00	1.77	0.07	49.3	0.1	5.2	0.1
G345.2619-00.4188A	abs	2.7	1.2	8.63	0.03	10.52	0.04	13.85	0.00	0.41	0.02	0.60	0.03	34.7	0.1	3.8	0.0

G345.2619-00.4188B	abs	2.7	0.8	11.32	0.00	13.34	0.00	17.50	0.04	0.25	0.02	0.37	0.02	37.1	0.0	3.8	0.1
G345.4938+01.4677	3	2.4	150.0	9.27	0.00	12.71	0.18	15.81	0.22	1.86	0.33	1.38	0.07	64.0	0.5	3.2	0.0
G345.9561+00.6123	4	2.5	2.4	8.25	0.03	11.45	0.00	14.63	0.00	0.41	0.01	0.73	0.03	59.3	0.1	3.3	0.1
G347.0775-00.3927	4	1.7	3.0	8.53	0.03	12.00	0.00	14.17	0.00	0.16	0.00	1.28	0.04	64.4	0.1	1.4	0.1
G348.7342-01.0359	HII	2.83	5.6	10.26	0.05	11.70	0.05	12.80	0.06	0.75							

Table B.2: Spectral atlas of Brγ and accretion parameters. EWs are in Å, fluxes are uncorrected for extinction and in W/m^2 and luminosities are in L$_\odot$.

RMS name	UL	EW	ΔEW	F	ΔF	L	ΔL	L$_{acc}$	ΔL$_{acc}$	M$_*$	ΔM$_*$	R$_*$	ΔR$_*$	$\dot{M}$	Δ$\dot{M}$
G010.8856+00.1221	0.15	1.30	0.12	5.2E-18	2.8E-19	0.20	0.02	8.3E+2	8.7E+1	18	1.9	5.8	0.6	8.6E-6	7.5E-8
G012.9090-00.2607	0.32	2.25	0.53	2.2E-17	5.1E-18	0.00	0.00	2.2E+0	1.2E+0	18	10.0	5.8	3.2	2.3E-8	2.7E-8
G013.3310-00.0407	0.23	4.58	0.10	1.8E-18	7.8E-21	0.22	0.01	8.9E+2	2.5E+1	9.5	0.3	4.0	0.1	1.2E-5	2.1E-7
G014.2166-00.6344	0.26	9.13	0.15	6.3E-17	1.1E-19	0.02	0.00	1.1E+2	2.4E+0	4	0.1	2.6	0.1	2.4E-6	5.1E-8
G014.4335-00.6969	0.15	6.15	0.17	6.0E-17	2.6E-19	0.25	0.01	1.0E+3	4.4E+1	6.5	0.3	3.3	0.1	1.7E-5	1.4E-7
G014.9958-00.6732	0.19	26.73	0.16	1.4E-15	3.2E-19	3.73	0.07	1.2E+4	1.9E+2	14	0.2	5.0	0.1	1.3E-4	1.1E-6
G015.1288-00.6717	0.09	-2.96	0.06	-2.4E-17	1.6E-19					14	0.2	5.0	0.1		
G016.9261+00.2854	0.26	1.58	0.06	6.5E-18	1.4E-19	0.36	0.02	1.4E+3	7.7E+1	6.5	0.4	3.3	0.2	2.3E-5	6.8E-8
G016.9270+00.9599	0.15	32.89	0.64	1.5E-16	8.8E-20	5.71	0.21	1.7E+4	5.7E+2	12.5	0.4	4.7	0.2	2.1E-4	5.4E-7
G017.6380+00.1566	0.25				1.7E-18					30	0.4	7.3	0.2		
G027.7571+00.0500	0.27	3.11	0.06	2.3E-17	1.3E-19	3.40	0.09	1.1E+4	2.6E+2	14	0.3	5.0	0.1	1.2E-4	2.1E-7
G029.8620-00.0444	0.17	1.75	0.06	1.4E-17	2.4E-19	436.87	20.76	8.4E+5	3.6E+4	17	0.7	5.6	0.2	9.0E-3	1.0E-7
G231.7986-01.9682	0.06	3.52	0.03	4.7E-16	1.2E-18	0.20	0.01	8.5E+2	2.1E+1	10	0.2	4.2	0.1	1.2E-5	1.5E-6
G233.8306-00.1803	0.13	14.24	0.25	1.7E-15	2.1E-18	5.05	0.21	1.5E+4	5.7E+2	14	0.5	5.0	0.2	1.8E-4	9.9E-6
G254.0548-00.0961	0.21	3.54	0.24	7.3E-18	1.4E-19	0.11	0.01	4.9E+2	5.6E+1	7.5	0.9	3.6	0.4	7.6E-6	4.6E-7
G259.0453-01.5559	0.26	9.04	0.50	1.0E-17	6.4E-20	0.04	0.00	2.1E+2	1.8E+1	12.5	1.1	4.7	0.4	2.5E-6	5.0E-7
G263.5846-03.9973	0.07	7.82	0.21	4.4E-17	1.5E-19	0.45	0.02	1.7E+3	7.3E+1	11.5	0.5	4.3	0.2	2.1E-5	1.9E-6
G263.5994-00.5236	0.15				3.1E-19					3.7	0.5	2.3	0.2		
G263.7434+00.1161	0.15				4.8E-19					6.5	0.5	3.3	0.2		
G263.7759-00.4281	0.24	16.25	0.78	7.5E-17	2.2E-19	0.08	0.01	3.8E+2	2.7E+1	6.5	0.5	3.3	0.2	6.3E-6	9.5E-8
G264.1444+02.0190	0.28	9.44	0.45	5.5E-17	2.8E-19	0.06	0.00	3.0E+2	2.0E+1	5.5	0.4	2.8	0.2	5.0E-6	5.4E-8
G265.1438+01.4548	0.15	44.31	1.35	2.8E-16	2.0E-19	0.01	0.00	4.8E+1	2.2E+0	5.5	0.2	2.8	0.1	7.9E-7	1.5E-7
G267.7336-01.1058A	0.13	2.88	0.06	1.8E-17	1.2E-19	0.00	0.00	1.6E+0	1.0E-1	3.7	0.2	2.3	0.1	3.2E-8	2.0E-8
G267.9094+01.7816	0.33				1.8E-18					3.6	0.2	2.2	0.1		
G268.3957-00.4842	0.14	5.36	0.10	4.1E-17	1.4E-19	0.26	0.01	1.1E+3	4.4E+1	9	0.4	3.9	0.2	1.5E-5	5.0E-8
G269.1586-01.1383A	0.12	4.31	0.20	9.6E-18	1.0E-19	0.00	0.00	1.1E+0	7.8E-2	4	0.3	2.6	0.2	2.2E-8	1.5E-8
G274.0649-01.1460A	0.25	29.37	1.79	1.7E-16	3.6E-19	10.60	1.04	3.0E+4	2.6E+3	11.5	1.0	4.3	0.4	3.6E-4	4.6E-6

G282.2988-00.7769	0.11	7.59	0.21	5.2E-16	1.9E-18	0.42	0.02	1.6E+3	6.6E+1	9.5	0.4	4.0	0.2	2.2E-5	4.1E-6
G282.8969-01.2727	0.18	1.32	0.05	6.4E-18	1.4E-19	25.90	1.53	6.6E+4	3.5E+3	15	0.8	5.1	0.3	7.3E-4	2.5E-7
G283.9146-01.0485	0.38				4.5E-20					11.5	0.8	4.3	0.3		
G287.3716+00.6444	0.09	1.82	0.02	2.6E-17	1.2E-19	0.11	0.00	4.8E+2	1.1E+1	15.5	0.4	5.3	0.1	5.3E-6	5.1E-7
G293.5607-00.6703	0.18	6.71	0.27	3.4E-17	2.1E-19	0.42	0.02	1.6E+3	8.7E+1	9.5	0.5	4.0	0.2	2.2E-5	4.9E-7
G293.8947-00.7825	0.15	2.61	0.05	1.9E-17	1.4E-19	0.02	0.00	1.0E+2	3.4E+0	14	0.5	5.0	0.2	1.2E-6	2.5E-6
G294.6168-02.3440	0.15	3.10	0.17	7.8E-18	1.3E-19	0.01	0.00	3.7E+1	2.1E+0	5	0.3	2.6	0.1	6.2E-7	5.9E-8
G295.5570-01.3787	0.19	9.77	0.24	1.7E-17	4.2E-20	0.05	0.00	2.4E+2	7.7E+0	7.5	0.2	3.6	0.1	3.7E-6	6.6E-7
G298.2620+00.7394	0.27	4.49	0.29	6.3E-18	8.9E-20	0.56	0.05	2.1E+3	1.8E+2	15	1.3	5.1	0.4	2.3E-5	9.2E-8
G300.3412-00.2190	0.21	7.54	0.21	3.5E-16	1.3E-18	2.36	0.12	7.7E+3	3.4E+2	11.5	0.5	4.3	0.2	9.3E-5	1.2E-6
G301.1726+01.0034	0.11	4.19	0.13	1.2E-16	8.6E-19	0.83	0.04	3.0E+3	1.4E+2	15.5	0.7	5.3	0.2	3.3E-5	1.3E-6
G301.8147+00.7808	0.14	9.33	0.23	1.0E-15	2.6E-18	8.77	0.38	2.5E+4	9.7E+2	15.5	0.6	5.3	0.2	2.8E-4	5.9E-6
G302.4546-00.7401	0.23	7.70	0.43	1.2E-17	8.9E-20	0.22	0.02	9.1E+2	6.7E+1	15	1.1	5.1	0.4	1.0E-5	9.0E-7
G302.6604-00.7908	0.42				1.3E-19					12	1.1	4.5	0.4		
G304.7592-00.6299	0.21	17.62	0.76	1.3E-16	3.2E-19	5.61	0.41	1.7E+4	1.1E+3	9.5	0.6	4.0	0.3	2.3E-4	8.1E-6
G305.2017+00.2072A	0.19	1.83	0.06	1.1E-17	1.6E-19	0.01	0.00	5.6E+1	2.1E+0	18	0.7	5.8	0.2	5.9E-7	5.7E-8
G305.4840+00.2248	0.22	11.05	0.22	3.4E-17	6.1E-20	0.48	0.02	1.8E+3	7.4E+1	7.5	0.3	3.6	0.1	2.8E-5	6.1E-7
G306.1160+00.1386A	0.16	2.04	0.09	2.8E-17	5.6E-19	0.00	0.00	2.4E+1	1.4E+0	7	0.4	3.3	0.2	3.6E-7	7.7E-8
G306.1160+00.1386B	0.17	6.59	0.37	3.8E-16	3.2E-18	0.10	0.01	4.6E+2	3.6E+1	6	0.5	3.0	0.2	7.4E-6	2.9E-6
G308.0049-00.3868	0.31	23.43	1.35	1.3E-15	3.2E-18	6.60	0.59	1.9E+4	1.6E+3	12.5	1.0	4.7	0.4	2.4E-4	8.0E-6
G308.6480+00.6469A	0.32	0.43	0.07	1.7E-18	2.5E-19	0.03	0.00	1.4E+2	2.2E+1	4.5	0.7	2.3	0.4	2.2E-6	8.2E-8
G309.9206+00.4790B	0.54	9.83	1.08	9.5E-18	1.1E-19	0.01	0.00	3.2E+1	4.6E+0	12	1.7	4.5	0.7	3.9E-7	8.2E-7
G309.9796+00.5496	0.24	6.95	0.31	2.6E-17	1.7E-19	0.45	0.03	1.7E+3	1.1E+2	12.5	0.8	4.7	0.3	2.1E-5	5.1E-7
G310.0135+00.3892	0.35	3.68	0.11	1.1E-14	8.4E-17	18.00	0.84	4.8E+4	2.0E+3	25.5	1.1	6.9	0.3	4.2E-4	6.2E-6
G311.6380+00.3009A	0.20	12.52	0.50	1.3E-17	4.3E-20	0.20	0.01	8.4E+2	4.5E+1	7.5	0.4	3.6	0.2	1.3E-5	8.0E-7
G311.9799-00.9527	0.23				7.4E-19					9	0.4	3.9	0.2		
G318.9480-00.1969A	0.32				4.9E-20					14	0.4	5.0	0.2		
G320.2046+00.8626B	0.31	14.47	0.61	2.0E-17	6.0E-20	0.93	0.06	3.3E+3	2.0E+2	4.5	0.3	2.3	0.1	5.5E-5	8.5E-7
G320.2437-00.5619	0.30	2.41	0.13	4.3E-17	8.7E-19	12.74	1.01	3.5E+4	2.5E+3	18	1.3	5.8	0.4	3.7E-4	1.5E-6
G321.3824-00.2861	0.56				1.2E-18					17	1.3	5.6	0.4		
G324.1594+00.2622	0.58				3.8E-19					15.5	1.3	5.3	0.4		

G326.4755+00.6947	0.43				6.1E-20					9.5	1.3	4.0	0.4		
G326.7249+00.6159	0.10	34.69		2.0E-14	8.9E-18	172.25	8.13	3.7E+5	1.6E+4	7	0.3	3.3	0.1	5.6E-3	4.5E-4
G326.7796-00.2405	0.42				1.2E-19					11.5	0.3	4.3	0.1		
G327.1192+00.5103	0.39	2.18	0.13	1.6E-18	4.0E-20	0.04	0.00	1.9E+2	1.4E+1	20	1.5	6.0	0.5	1.8E-6	4.8E-8
G327.3941+00.1970	0.44	2.98	0.15	8.7E-18	1.4E-19	0.38	0.03	1.5E+3	9.7E+1	12	0.8	4.5	0.3	1.8E-5	1.6E-7
G327.8097-00.6339A	0.18	2.07	0.06	4.5E-17	5.3E-19	0.70	0.03	2.6E+3	1.1E+2	6	0.3	3.0	0.1	4.1E-5	2.7E-7
G327.8097-00.6339B	0.28				1.8E-19					6	0.3	3.0	0.1		
G327.9455-00.1149	0.23	5.05	0.27	2.0E-17	2.1E-19	0.31	0.03	1.2E+3	9.8E+1	9	0.7	3.9	0.3	1.7E-5	3.3E-7
G328.3442-00.4629	0.10	7.95	0.11	8.7E-16	1.5E-18	0.08	0.00	3.5E+2	1.0E+1	8.3	0.2	3.8	0.1	5.0E-6	1.1E-6
G331.7953-00.0979	0.30	7.64	0.37	4.9E-17	3.1E-19	691.53	54.61	1.3E+6	9.1E+4	40	2.8	8.7	0.6	9.0E-3	4.2E-6
G332.8256-00.5498A	0.34	30.77	3.11	3.0E-16	1.0E-18	132.21	20.13	2.9E+5	3.9E+4	33	4.5	7.7	1.1	2.2E-3	5.0E-6
G332.9457+02.3855	0.13	2.19	0.06	6.1E-17	6.6E-19	0.00	0.00	1.1E+1	4.6E-1	6	0.2	3.0	0.1	1.8E-7	5.7E-8
G332.9868-00.4871	0.38	2.29	0.10	9.8E-18	1.7E-19	17.30	1.16	4.6E+4	2.8E+3	15	0.9	5.1	0.3	5.1E-4	2.3E-7
G333.1153+00.0950	0.14	3.55	0.05	3.7E-17	1.3E-19	0.40	0.01	1.6E+3	3.9E+1	7	0.2	3.3	0.1	2.4E-5	7.4E-7
G333.4747-00.2366	0.27	0.96	0.02	6.2E-18	1.0E-19	1.79	0.07	6.0E+3	2.0E+2	8.3	0.3	3.8	0.1	8.7E-5	6.2E-8
G338.5459+02.1175	0.16	1.61	0.02	5.4E-17	3.6E-19	0.00	0.00	9.8E+0	2.4E-1	3	0.1	2.0	0.0	2.1E-7	2.2E-8
G338.9196+00.5495	0.26				3.3E-19					18	0.1	5.8	0.0		
G338.9341-00.0623	0.22	7.04	0.31	2.2E-17	1.4E-19	0.04	0.00	2.0E+2	1.2E+1	7.5	0.4	3.6	0.2	3.1E-6	2.0E-7
G339.3940-00.4084	0.48	0.56	0.04	2.6E-18	1.7E-19	0.10	0.01	4.5E+2	3.6E+1	6	0.5	3.0	0.2	7.3E-6	4.7E-8
G339.5836-00.1265	0.38				1.9E-18					7.5	0.5	3.6	0.2		
G339.6221-00.1209	0.31	1.42	0.08	7.4E-18	2.4E-19	0.00	0.00	1.0E+1	6.9E-1	15	1.0	5.1	0.3	1.1E-7	2.6E-8
G339.6816-01.2058	0.18	1.86	0.04	4.6E-17	4.8E-19	0.03	0.00	1.5E+2	5.3E+0	11.5	0.4	4.3	0.2	1.8E-6	1.1E-7
G339.8838-01.2588	1.00				9.1E-19					23	0.4	6.5	0.2		
G340.1537+00.5116	0.06	1.92	0.03	9.8E-17	6.2E-19	0.06	0.00	3.0E+2	8.1E+0	6	0.2	3.0	0.1	4.8E-6	4.6E-7
G343.1261-00.0623	1.67				6.3E-20					15	0.2	5.1	0.1		
G344.4257+00.0451B	0.13	9.81	0.48	1.5E-17	7.5E-20	0.29	0.03	1.2E+3	9.0E+1	11.5	0.9	4.3	0.3	1.4E-5	1.5E-6
G344.4257+00.0451C	0.27	12.06	3.91	1.3E-17	3.5E-19	0.50	0.24	1.9E+3	8.2E+2	12	5.2	4.5	1.9	2.3E-5	1.9E-6
G344.6608+00.3401	0.11	5.79	0.15	2.3E-17	1.1E-19	5.94	0.28	1.8E+4	7.4E+2	15	0.6	5.1	0.2	1.9E-4	3.1E-6
G345.2619-00.4188A	0.36	-49.42	12.99	-1.7E-16	9.0E-19					7	0.6	3.2	0.2		
G345.2619-00.4188B	0.25	-49.56	1.93	-1.7E-16	9.0E-19					5.8	0.6	2.8	0.2		
G345.4938+01.4677	0.22	1.78	0.03	4.5E-17	3.5E-19	1.75	0.09	5.9E+3	2.7E+2	35	1.6	8.0	0.4	4.3E-5	1.7E-7

G345.9561+00.6123	0.24	2.10	0.05	6.1E-17	6.2E-19	0.81	0.04	2.9E+3	1.2E+2	8.3	0.3	3.8	0.2	4.3E-5	2.4E-7
G347.0775-00.3927	0.18	0.46	0.01	6.0E-18	1.5E-19	0.12	0.00	5.1E+2	1.8E+1	9	0.3	3.9	0.1	7.1E-6	2.0E-8
G348.7342-01.0359	0.39	226.86	33.19	4.0E-16	2.6E-19	0.39	0.09	1.5E+3	3.0E+2	10	2.0	4.2	0.8	2.1E-5	1.7E-5

Table B.3: Spectral atlas of Br20 - Br15. Fluxes are uncorrected for extinction and in W/m^2

RMS name	ul_EW_H	F_Br20	ΔF_Br20	F_Br19	ΔF_Br19	F_Br18	ΔF_Br18	F_Br17	ΔF_Br17	F_Br16	ΔF_Br16
G010.8856+00.1221											
G012.9090-00.2607	0.88		2.2E-19		2.2E-19		2.2E-19		2.2E-19		2.3E-19
G013.3310-00.0407											
G014.2166-00.6344											
G014.4335-00.6969	0.50		5.3E-19		5.3E-19		5.3E-19		5.3E-19		5.3E-19
G014.9958-00.6732	0.19	1.4E-17	7.2E-20	1.6E-17	7.2E-20	2.5E-17	7.2E-20	2.2E-17	7.2E-20	3.3E-17	7.2E-20
G015.1288-00.6717	0.23	-1.6E-18	9.6E-20	-6.1E-18	9.6E-20	-3.2E-18	9.6E-20	-3.2E-18	9.6E-20	-3.4E-18	9.6E-20
G016.9261+00.2854	1.88		1.5E-18		1.5E-18		1.5E-18		1.5E-18		9.1E-19
G016.9270+00.9599	1.00		3.2E-19		3.2E-19		3.6E-19		3.6E-19		3.6E-19
G017.6380+00.1566	0.50	1.4E-18	6.1E-19	8.2E-19	6.1E-19	0.0E+00	6.1E-19	1.5E-18	6.1E-19	1.1E-18	3.0E-19
G027.7571+00.0500											
G029.8620-00.0444	0.58	3.4E-18	9.2E-19		9.2E-19		9.2E-19		6.1E-19		6.1E-19
G231.7986-01.9682	0.19	2.5E-16	3.5E-18	2.2E-16	3.5E-18	2.9E-16	3.5E-18	4.1E-16	4.5E-18	5.2E-16	4.5E-18
G233.8306-00.1803	0.18	2.4E-16	6.8E-19	2.2E-16	1.7E-18	3.4E-16	1.0E-18	3.6E-16	9.8E-19	4.1E-16	1.2E-18
G254.0548-00.0961	0.28	5.3E-18	3.1E-19	4.1E-18	3.1E-19	1.5E-17	3.1E-19	3.4E-18	3.1E-19	5.0E-18	3.1E-19
G259.0453-01.5559											
G263.5846-03.9973	0.25	4.3E-18	4.3E-19	2.1E-18	4.3E-19	5.0E-18	4.3E-19	7.5E-18	4.3E-19	6.1E-18	3.0E-19
G263.5994-00.5236											
G263.7434+00.1161	0.34		2.7E-19		2.7E-19		2.7E-19		3.6E-19		3.6E-19
G263.7759-00.4281	0.43	1.3E-17	1.1E-18	9.1E-18	1.1E-18	2.1E-17	1.1E-18	2.1E-17	1.1E-18	2.0E-17	1.4E-18
G264.1444+02.0190											
G265.1438+01.4548	0.17	1.5E-17	1.9E-19	1.4E-17	1.9E-19	1.8E-17	1.9E-19	2.4E-17	1.5E-19	3.0E-17	1.5E-19
G267.7336-01.1058A	0.14		2.9E-19		2.9E-19		2.9E-19		2.9E-19	8.8E-18	2.9E-19
G267.9094+01.7816	0.41		1.8E-19		1.8E-19		1.8E-19		2.2E-19		2.2E-19
G268.3957-00.4842	0.29		5.9E-20		6.4E-20	5.8E-19	9.2E-20	4.0E-19	4.3E-20	9.1E-19	7.3E-20
G269.1586-01.1383A	0.31		7.8E-19		7.8E-19		7.8E-19		5.2E-19		5.2E-19
G274.0649-01.1460A											
G282.2988-00.7769	0.18	3.3E-16	5.4E-18	2.7E-16	5.4E-18	4.3E-16	5.4E-18	4.8E-16	5.4E-18	6.8E-16	5.4E-18

G282.8969-01.2727	0.33		2.2E-17		2.2E-17		2.2E-17		1.3E-17		1.3E-17
G283.9146-01.0485											
G287.3716+00.6444	0.13		1.8E-18		1.8E-18		1.8E-18		1.8E-18		2.8E-18
G293.5607-00.6703	0.75		1.2E-18		1.2E-18		1.2E-18		1.0E-18		1.0E-18
G293.8947-00.7825	0.23	3.3E-18	1.7E-19	2.1E-18	1.7E-19	3.8E-18	1.7E-19	3.7E-18	1.7E-19	4.3E-18	1.7E-19
G294.6168-02.3440	0.32	6.2E-18	1.1E-19	4.3E-18	1.1E-19	8.1E-18	1.1E-19	1.1E-17	1.1E-19	7.0E-18	1.1E-19
G295.5570-01.3787											
G298.2620+00.7394	1.00		2.2E-20		6.3E-20		9.4E-20		3.2E-20		5.2E-20
G300.3412-00.2190	0.33	4.8E-17	7.7E-19	4.9E-17	7.7E-19	6.6E-17	7.7E-19	8.4E-17	9.7E-19	8.9E-17	9.7E-19
G301.1726+01.0034	0.22	2.7E-17	3.2E-19	1.8E-17	3.2E-19	4.3E-17	3.2E-19	4.3E-17	3.2E-19	4.4E-17	3.2E-19
G301.8147+00.7808	0.33	8.1E-17	1.9E-18	6.8E-17	1.9E-18	1.6E-16	1.9E-18	2.1E-16	1.9E-18	1.7E-16	3.1E-18
G302.4546-00.7401	0.29	4.2E-19	6.1E-20	2.9E-19	7.2E-20	5.1E-19	4.5E-20	1.4E-18	5.2E-20	8.1E-19	4.8E-20
G302.6604-00.7908	0.35		4.7E-20		4.3E-20		4.0E-20		4.3E-20		5.2E-18
G304.7592-00.6299	1.36		7.1E-18		1.7E-19		1.7E-19	7.5E-19	6.8E-20	7.0E-19	1.1E-19
G305.2017+00.2072A	0.31		5.5E-19		5.5E-19		5.5E-19		5.5E-19		3.2E-19
G305.4840+00.2248											
G306.1160+00.1386A	0.83		1.4E-18		1.4E-18		1.4E-18		1.4E-18		1.4E-18
G306.1160+00.1386B	0.22	9.8E-17	1.5E-18	9.8E-17	1.5E-18	1.2E-16	1.5E-18	1.8E-16	1.5E-18	1.9E-16	1.8E-18
G308.0049-00.3868	0.36	4.8E-18	1.5E-19	5.9E-18	1.5E-19	6.7E-18	1.5E-19	1.3E-17	1.5E-19	1.2E-17	1.5E-19
G308.6480+00.6469A											
G309.9206+00.4790B	3.75		4.4E-19		4.4E-19		4.4E-19		4.4E-19		4.4E-19
G309.9796+00.5496	0.47		2.0E-19		2.0E-19		2.0E-19		2.0E-19		2.0E-19
G310.0135+00.3892	0.38	6.8E-17	1.7E-18	4.2E-17	1.7E-18	9.2E-17	1.7E-18	9.3E-17	1.7E-18	9.9E-17	1.7E-18
G311.6380+00.3009A	0.35	1.5E-18	2.5E-20	1.2E-18	1.8E-20	1.4E-18	2.9E-20	1.5E-18	2.3E-20	2.2E-18	6.3E-20
G311.9799-00.9527	0.48	1.5E-18	2.5E-20	1.2E-18	1.8E-20	1.4E-18	2.9E-20	1.5E-18	2.3E-20	2.2E-18	6.3E-20
G318.9480-00.1969A											
G320.2046+00.8626B	0.22		8.1E-20		1.0E-19		4.9E-20	5.2E-19	4.0E-20	5.6E-19	7.7E-20
G320.2437-00.5619	0.56		3.2E-19		3.2E-19		3.2E-19		3.2E-19		3.2E-19
G321.3824-00.2861	3.00		1.6E-18		1.6E-18		1.6E-18		1.8E-18		1.8E-18
G324.1594+00.2622	0.33		2.4E-19		2.4E-19		2.4E-19		2.4E-19		2.4E-19
G326.4755+00.6947	0.56		3.5E-19		3.5E-19		3.5E-19		3.5E-19		3.5E-19

G326.7249+00.6159	0.26	1.5E-16	3.2E-18	1.4E-16	3.2E-18	2.2E-16	3.2E-18	2.3E-16	3.2E-18	2.9E-16	3.2E-18
G326.7796-00.2405	0.60		1.4E-19		1.4E-19		1.4E-19		1.4E-19		1.4E-19
G327.1192+00.5103	1.50		1.7E-20		3.1E-20		3.7E-20		3.4E-20		4.5E-20
G327.3941+00.1970	0.65		5.8E-20		5.8E-20		5.8E-20		5.0E-20		5.0E-20
G327.8097-00.6339A											
G327.8097-00.6339B											
G327.9455-00.1149											
G328.3442-00.4629	0.13	1.1E-16	2.0E-18	1.1E-16	2.0E-18	1.3E-16	2.0E-18	1.9E-16	2.0E-18	2.1E-16	2.0E-18
G331.7953-00.0979	0.88		1.5E-20		1.5E-20		1.5E-20		1.5E-20		1.5E-20
G332.8256-00.5498A	1.25		3.3E-19		3.3E-19		3.3E-19		1.9E-19		1.9E-19
G332.9457+02.3855	0.23		3.4E-19		3.4E-19		3.4E-19		3.4E-19		3.4E-19
G332.9868-00.4871	3.00		1.1E-19		1.1E-19		1.1E-19		1.1E-19		1.1E-19
G333.1153+00.0950	0.31	7.1E-18	4.9E-19	5.7E-18	4.9E-19	1.3E-17	4.9E-19	2.5E-17	4.9E-19	2.0E-17	4.9E-19
G333.4747-00.2366	1.15		2.4E-19		2.4E-19		2.4E-19		2.4E-19		2.3E-19
G338.5459+02.1175	0.19		1.8E-19		1.8E-19		1.8E-19		2.7E-19		2.7E-19
G338.9196+00.5495	1.67		2.4E-19		2.4E-19		2.4E-19		1.6E-19		1.6E-19
G338.9341-00.0623	0.48	2.9E-18	1.3E-19	3.8E-18	1.3E-19	4.3E-18	1.3E-19	7.6E-18	7.5E-20	1.2E-17	7.5E-20
G339.3940-00.4084											
G339.5836-00.1265											
G339.6221-00.1209	0.45		6.4E-20		6.4E-20		6.4E-20		6.4E-20		6.4E-20
G339.6816-01.2058											
G339.8838-01.2588											
G340.1537+00.5116	0.39		3.2E-18		3.2E-18		3.2E-18		3.8E-18	4.9E-17	3.8E-18
G343.1261-00.0623											
G344.4257+00.0451B	0.88		8.0E-20		8.0E-20		8.0E-20		8.0E-20		8.0E-20
G344.4257+00.0451C											
G344.6608+00.3401	0.37	1.4E-17	1.2E-18	1.5E-17	1.2E-18	1.7E-17	1.2E-18	1.3E-17	1.2E-18	2.5E-17	1.2E-18
G345.2619-00.4188A	0.71		1.2E-18		1.2E-18		1.2E-18		1.2E-18		1.2E-18
G345.2619-00.4188B	0.54		7.7E-19		7.7E-19		7.7E-19		7.7E-19		7.7E-19
G345.4938+01.4677	0.43	1.2E-18	4.0E-20	7.1E-19	4.0E-20	2.0E-18	4.0E-20	1.5E-18	4.0E-20	9.6E-19	4.0E-20
G345.9561+00.6123	0.31		5.6E-19		5.6E-19		5.6E-19		5.6E-19		5.6E-19

G347.0775-00.3927	0.39		1.0E-18		1.0E-18		1.0E-18		1.0E-18	1.3E-17	1.2E-18
G348.7342-01.0359	0.47	1.6E-17	2.0E-19	9.7E-18	2.0E-19	1.9E-17	2.0E-19	1.7E-17	2.0E-19	1.7E-17	2.0E-19

Table B.4: Spectral atlas of Br15 - Br10. Fluxes are uncorrected for extinction and in W/m^2

RMS name	F_Br15	ΔF_Br15	F_Br14	ΔF_Br14	F_Br13	ΔF_Br13	F_Br12	ΔF_Br12	F_Br11	ΔF_Br11	F_Br10	ΔF_Br10
G010.8856+00.1221												
G012.9090-00.2607		2.3E-19		2.3E-19		2.0E-19		2.4E-19		3.5E-19		4.0E-19
G013.3310-00.0407												
G014.2166-00.6344												
G014.4335-00.6969		5.3E-19	1.1E-17	7.3E-19	1.5E-17	7.3E-19	1.1E-17	7.3E-19	1.2E-17	7.3E-19	2.1E-17	9.2E-19
G014.9958-00.6732	3.9E-17	7.2E-20	4.1E-17	7.2E-20	4.9E-17	7.2E-20	6.6E-17	2.2E-19	8.3E-17	2.2E-19	8.7E-17	2.5E-19
G015.1288-00.6717	-6.4E-18	9.6E-20	-7.1E-17	1.6E-19	-9.5E-18	1.6E-19	-1.1E-17	1.6E-19	-1.1E-17	1.6E-19	-1.1E-17	6.3E-19
G016.9261+00.2854		9.1E-19		9.1E-19		8.0E-19		1.0E-18		8.6E-20		8.6E-20
G016.9270+00.9599		3.6E-19		3.6E-19		2.8E-19	8.7E-18	3.3E-19	8.9E-18	2.6E-19	1.7E-17	2.9E-19
G017.6380+00.1566		3.0E-19		6.8E-19		7.1E-19		2.4E-19		1.6E-19		3.2E-19
G027.7571+00.0500												
G029.8620-00.0444		4.7E-19	4.3E-18	4.7E-19	3.7E-18	5.9E-19	1.4E-17	5.9E-19	1.0E-17	9.1E-19	1.1E-17	5.3E-19
G231.7986-01.9682	4.8E-16	9.8E-18	7.6E-16	9.8E-18	9.3E-16	2.0E-17	1.2E-15	2.8E-17	1.6E-15	3.2E-17	1.9E-15	5.4E-17
G233.8306-00.1803	3.9E-16	1.2E-18	5.3E-16	1.8E-18	5.5E-16	2.0E-18	7.2E-16	2.5E-18	7.8E-16	1.7E-18	8.2E-16	1.0E-17
G254.0548-00.0961	5.7E-18	3.8E-19	1.5E-17	3.8E-19	1.7E-17	3.8E-19	2.5E-17	3.8E-19	1.8E-17	3.8E-19	2.6E-17	7.5E-19
G259.0453-01.5559												
G263.5846-03.9973	4.6E-18	3.0E-19	8.9E-18	3.0E-19	1.4E-17	2.8E-19	1.3E-17	2.5E-19	1.5E-17	2.3E-19	1.9E-17	2.3E-19
G263.5994-00.5236												
G263.7434+00.1161		1.3E-18		1.3E-18		1.8E-18		1.8E-18		3.1E-18		2.7E-18
G263.7759-00.4281	3.0E-17	1.4E-18	5.2E-17	1.4E-18	5.2E-17	1.4E-18	7.4E-17	2.6E-18	1.2E-16	2.6E-18	1.8E-16	5.5E-18
G264.1444+02.0190												
G265.1438+01.4548	4.4E-17	2.5E-19	4.6E-17	2.5E-19	6.0E-17	1.8E-19	9.1E-17	1.8E-19	1.0E-16	2.0E-19	1.3E-16	4.3E-19
G267.7336-01.1058A	2.4E-17	2.9E-19	2.1E-17	2.9E-19	4.2E-17	2.5E-19	1.8E-18	2.5E-19	2.0E-17	2.5E-19	5.1E-17	3.2E-19
G267.9094+01.7816		2.7E-19		2.7E-19		3.5E-19		2.4E-19		2.0E-19		2.4E-19
G268.3957-00.4842	5.9E-19	7.7E-20	2.0E-18	1.4E-19	1.0E-18	1.3E-19	1.9E-18	1.6E-19	3.9E-18	1.4E-19	5.7E-18	1.6E-19
G269.1586-01.1383A		5.2E-19		9.3E-19		9.3E-19	3.4E-18	5.2E-19	6.9E-18	4.7E-19	2.5E-17	2.0E-18
G274.0649-01.1460A												
G282.2988-00.7769	6.4E-16	5.4E-18	1.0E-15	1.5E-17	1.1E-15	1.5E-17	1.6E-15	2.3E-17	2.0E-15	4.1E-17	3.3E-15	8.6E-17

G282.8969-01.2727		1.3E-17		1.3E-17		1.7E-17		1.7E-17		1.7E-17		2.1E-17
G283.9146-01.0485												
G287.3716+00.6444	2.9E-16	2.8E-18	1.3E-16	2.8E-18	1.7E-16	2.8E-18	3.1E-16	2.8E-18	1.4E-16	2.8E-18	3.4E-16	3.4E-18
G293.5607-00.6703		1.0E-18		7.3E-19	1.8E-17	7.3E-19	2.5E-17	7.3E-19	3.2E-17	7.3E-19	4.0E-17	1.3E-18
G293.8947-00.7825	6.1E-18	1.7E-19	8.1E-18	3.5E-19	8.3E-18	3.5E-19	1.1E-17	7.0E-19	1.6E-17	3.5E-19	1.4E-17	9.5E-19
G294.6168-02.3440	8.3E-18	1.1E-19	8.4E-18	1.3E-19	1.3E-17	1.3E-19	9.5E-18	2.0E-19	1.6E-17	2.4E-19	1.6E-17	2.0E-19
G295.5570-01.3787												
G298.2620+00.7394		2.9E-20		5.4E-18		6.8E-20		4.1E-20		4.7E-20		4.9E-20
G300.3412-00.2190	1.1E-16	1.6E-18	1.3E-16	1.6E-18	1.5E-16	1.6E-18	1.8E-16	1.9E-18	2.0E-16	2.9E-18	2.5E-16	3.5E-18
G301.1726+01.0034	4.7E-17	3.2E-19	6.2E-17	3.2E-19	6.4E-17	5.6E-19	7.0E-17	8.0E-19	8.7E-17	1.3E-18	9.4E-17	8.0E-19
G301.8147+00.7808	1.8E-16	3.1E-18	2.6E-16	4.2E-18	2.8E-16	4.2E-18	4.1E-16	5.3E-18	5.2E-16	5.3E-18	6.1E-16	5.3E-18
G302.4546-00.7401	7.3E-19	3.9E-20	1.4E-18	9.1E-20	8.7E-19	5.6E-20	1.2E-18	3.7E-20	1.7E-18	4.4E-20	2.1E-18	4.0E-20
G302.6604-00.7908	3.9E-19	3.5E-20	8.1E-19	6.7E-20	6.2E-19	4.9E-20	4.0E-19	4.9E-20	1.2E-18	3.2E-20	1.2E-18	4.3E-20
G304.7592-00.6299	6.9E-19	1.4E-19	1.1E-18	1.5E-19	2.7E-18	1.6E-19	2.3E-18	7.4E-20	1.9E-18	1.4E-19	2.5E-18	1.4E-19
G305.2017+00.2072A		3.2E-19		3.2E-19		3.2E-19		3.2E-19		3.2E-19		3.2E-19
G305.4840+00.2248												
G306.1160+00.1386A		1.4E-18		1.4E-18		1.4E-18		9.2E-19		9.2E-19		3.2E-18
G306.1160+00.1386B	2.0E-16	1.8E-18	2.6E-16	1.8E-18	2.5E-16	2.9E-18	3.4E-16	2.9E-18	3.5E-16	2.9E-18	6.0E-16	3.1E-18
G308.0049-00.3868	1.4E-17	1.5E-19	2.1E-17	2.4E-19	2.3E-17	2.4E-19	3.2E-17	2.4E-19	3.7E-17	2.4E-19	4.8E-17	5.4E-19
G308.6480+00.6469A												
G309.9206+00.4790B		4.4E-19		4.4E-19		4.4E-19		4.4E-19		4.4E-19		4.4E-19
G309.9796+00.5496	1.4E-18	2.0E-19	2.8E-18	2.0E-19	1.9E-18	1.4E-19	3.9E-18	1.4E-19	4.8E-18	1.4E-19	1.0E-17	1.7E-19
G310.0135+00.3892	1.1E-16	3.3E-18	1.8E-16	3.3E-18	1.6E-16	6.2E-18	2.2E-16	1.4E-17	2.6E-16	1.4E-17	4.9E-16	1.4E-17
G311.6380+00.3009A	1.4E-18	3.7E-20	3.3E-18	5.2E-20	2.0E-18	3.7E-20	3.0E-18	3.1E-20	3.6E-18	5.3E-20	4.6E-18	4.6E-20
G311.9799-00.9527	1.4E-18	3.7E-20	3.3E-18	5.2E-20	2.0E-18	3.7E-20	3.0E-18	3.1E-20	3.6E-18	5.3E-20	4.6E-18	4.6E-20
G318.9480-00.1969A												
G320.2046+00.8626B	9.2E-19	6.8E-20	4.8E-19	3.6E-20	7.7E-19	8.3E-20	8.8E-19	5.2E-20	1.1E-18	9.3E-20	2.6E-18	7.5E-20
G320.2437-00.5619		3.2E-19		3.2E-19		3.2E-19		2.7E-19		2.7E-19		2.7E-19
G321.3824-00.2861		1.8E-18		1.8E-18		1.8E-18		9.8E-19		9.8E-19		9.8E-19
G324.1594+00.2622		2.4E-19		2.4E-19		2.4E-19		3.3E-19		3.3E-19		3.3E-19
G326.4755+00.6947		3.5E-19		3.5E-19		3.5E-19		2.7E-19		2.7E-19		2.7E-19

G326.7249+00.6159	3.3E-16	3.2E-18	5.0E-16	3.2E-18	6.4E-16	3.2E-18	8.6E-16	6.1E-18	1.2E-15	6.1E-18	1.8E-15	1.1E-17
G326.7796-00.2405		1.4E-19		1.4E-19		1.1E-19		1.1E-19		1.1E-19		8.0E-20
G327.1192+00.5103		3.5E-20		5.5E-20		4.3E-20		3.6E-20		4.6E-20		4.0E-20
G327.3941+00.1970		5.0E-20		5.0E-20		6.7E-20		6.7E-20		6.7E-20		6.7E-20
G327.8097-00.6339A												
G327.8097-00.6339B												
G327.9455-00.1149												
G328.3442-00.4629	2.2E-16	1.9E-18	2.9E-16	1.9E-18	3.0E-16	1.9E-18	3.6E-16	1.9E-18	3.8E-16	1.9E-18	4.0E-16	3.2E-18
G331.7953-00.0979		1.5E-20		2.5E-19		3.9E-20	1.3E-18	5.8E-20	1.2E-18	5.8E-20	3.5E-18	1.6E-19
G332.8256-00.5498A		1.9E-19	8.4E-18	1.9E-19	7.5E-18	1.9E-19	1.1E-17	4.1E-19	1.5E-17	4.1E-19	3.4E-17	5.2E-19
G332.9457+02.3855		3.4E-19		3.4E-19		3.4E-19		4.1E-19		4.1E-19		7.5E-19
G332.9868-00.4871		1.1E-19		1.1E-19		1.1E-19		1.1E-19		1.1E-19		1.1E-19
G333.1153+00.0950	1.8E-17	4.9E-19	2.1E-17	4.9E-19	2.2E-17	6.3E-19	3.2E-17	9.9E-19	4.2E-17	9.9E-19	4.1E-17	1.1E-18
G333.4747-00.2366		2.3E-19		2.3E-19		2.3E-19		2.5E-19		2.5E-19		3.5E-19
G338.5459+02.1175		2.7E-19	9.9E-18	1.0E-19	4.0E-18	1.0E-19	8.0E-18	1.0E-19	5.8E-18	1.7E-19	5.5E-18	1.7E-19
G338.9196+00.5495		1.6E-19		1.6E-19		2.5E-19		2.5E-19		2.5E-19		4.0E-19
G338.9341-00.0623	7.9E-18	7.5E-20	1.6E-17	1.0E-19	1.5E-17	1.0E-19	1.3E-17	8.8E-20	1.5E-17	8.8E-20	2.8E-17	1.3E-19
G339.3940-00.4084												
G339.5836-00.1265												
G339.6221-00.1209		6.4E-20		6.4E-20		6.4E-20		6.4E-20		6.4E-20		6.4E-20
G339.6816-01.2058												
G339.8838-01.2588												
G340.1537+00.5116		3.8E-18	8.4E-17	4.1E-18	7.9E-17	4.1E-18	1.0E-16	4.1E-18	1.5E-16	4.1E-18	7.0E-17	4.3E-18
G343.1261-00.0623												
G344.4257+00.0451B		8.0E-20		8.0E-20		8.0E-20		7.0E-20		7.0E-20		1.4E-19
G344.4257+00.0451C												
G344.6608+00.3401	4.0E-17	1.5E-18	5.6E-17	1.5E-18	7.5E-17	2.7E-18	6.8E-17	2.7E-18	1.2E-16	2.7E-18	1.9E-16	5.4E-18
G345.2619-00.4188A		1.2E-18		1.6E-18		1.6E-18		1.6E-18		1.6E-18		3.7E-18
G345.2619-00.4188B		7.7E-19		7.7E-19		7.7E-19		5.7E-19		5.7E-19		6.9E-19
G345.4938+01.4677	2.5E-19	5.6E-20	1.9E-18	5.6E-20	1.3E-18	5.6E-20	2.3E-18	5.6E-20	2.2E-18	5.6E-20	4.0E-18	7.4E-20
G345.9561+00.6123	7.5E-18	5.6E-19	1.1E-17	5.6E-19	2.2E-17	5.6E-19	1.3E-17	5.6E-19	1.6E-17	5.6E-19	2.5E-17	1.3E-18

G347.0775-00.3927		1.2E-18	2.0E-17	1.2E-18	3.0E-17	1.2E-18	2.5E-17	1.3E-18	1.7E-17	1.3E-18	4.6E-17	1.3E-18
G348.7342-01.0359	2.5E-17	2.1E-19	2.8E-17	2.1E-19	4.2E-17	2.1E-19	6.2E-17	1.0E-19	9.0E-17	1.0E-19	1.5E-16	4.0E-19

Table B.5: Spectral atlas of H band lines. Fluxes are uncorrected for extinction and in W/m^2. Numbers in the second row of the header correspond to central wavelengths of given lines, in μm.

RMS name	F_[FeII]	ΔF_[FeII]	F_flFeII	ΔF_flFeII	F_FeI	ΔF_FeI	F_HeI	ΔF_HeI	F_FeI	ΔF_FeI
					1.69		1.70		1.71	
G010.8856+00.1221										
G012.9090-00.2607		2.0E-19		2.4E-19		2.4E-19		2.4E-19		2.4E-19
G013.3310-00.0407										
G014.2166-00.6344										
G014.4335-00.6969	6.5E-18	7.3E-19	8.9E-18	7.3E-19	3.5E-18	7.3E-19		7.3E-19		7.3E-19
G014.9958-00.6732	1.8E-17	2.2E-19	3.5E-17	2.2E-19	1.5E-18	2.2E-19		2.2E-19		2.2E-19
G015.1288-00.6717		1.6E-19		1.6E-19		1.6E-19	-3.6E-18	1.6E-19		1.6E-19
G016.9261+00.2854		8.0E-19		8.6E-20		8.6E-20		8.0E-19		8.6E-20
G016.9270+00.9599	5.8E-18	3.3E-19	9.9E-18	2.6E-19		2.6E-19		2.6E-19		2.6E-19
G017.6380+00.1566	4.6E-18	2.4E-19		1.6E-19		1.6E-19		2.4E-19	4.2E-18	1.6E-19
G027.7571+00.0500										
G029.8620-00.0444		5.9E-19	7.2E-18	9.1E-19	9.5E-18	9.1E-19		5.9E-19		9.1E-19
G231.7986-01.9682		2.8E-17	1.6E-16	3.2E-17	4.2E-16	3.2E-17		3.2E-17	2.5E-16	3.2E-17
G233.8306-00.1803	1.8E-16	2.5E-18	1.1E-16	1.7E-18	4.0E-17	1.7E-18	7.1E-17	1.7E-18	1.9E-17	1.7E-18
G254.0548-00.0961	1.0E-16	3.8E-19	7.2E-18	3.8E-19	5.3E-18	3.8E-19		3.8E-19	3.2E-18	3.8E-19
G259.0453-01.5559										
G263.5846-03.9973	7.4E-18	2.5E-19	5.0E-18	2.3E-19	1.3E-18	2.3E-19		2.3E-19		2.3E-19
G263.5994-00.5236										
G263.7434+00.1161	6.5E-16	1.8E-18	2.7E-17	3.1E-18	1.4E-17	3.1E-18		1.8E-18	5.0E-17	3.1E-18
G263.7759-00.4281	6.5E-17	2.6E-18	5.6E-17	2.6E-18		2.6E-18		2.6E-18		2.6E-18
G264.1444+02.0190										
G265.1438+01.4548	6.7E-18	1.8E-19	9.9E-18	2.0E-19	1.6E-18	2.0E-19		2.0E-19		2.0E-19
G267.7336-01.1058A	4.3E-17	2.5E-19	3.5E-18	2.5E-19	1.8E-18	2.5E-19		2.5E-19		2.5E-19
G267.9094+01.7816		2.4E-19		2.0E-19	2.0E-18	2.0E-19		2.4E-19	-7.1E-18	2.0E-19
G268.3957-00.4842		1.7E-19	2.6E-18	1.7E-19		1.7E-19		1.7E-19	2.0E-18	1.7E-19
G269.1586-01.1383A	2.1E-17	5.2E-19	5.5E-18	4.7E-19	9.7E-18	4.7E-19		4.7E-19	5.0E-18	4.7E-19

G274.0649-01.1460A										
G282.2988-00.7769	1.6E-16	2.3E-17	1.0E-16	4.1E-17	1.1E-16	4.1E-17		4.1E-17	6.6E-17	4.1E-17
G282.8969-01.2727		1.7E-17		1.7E-17		1.7E-17		1.7E-17		1.7E-17
G283.9146-01.0485										
G287.3716+00.6444	7.9E-17	2.8E-18	8.7E-17	2.8E-18		2.8E-18		2.8E-18	7.8E-17	2.8E-18
G293.5607-00.6703	1.1E-17	7.3E-19	9.4E-18	7.3E-19	5.1E-18	7.3E-19		7.3E-19		7.3E-19
G293.8947-00.7825		7.0E-19	6.8E-18	7.0E-19	5.5E-18	7.0E-19		7.0E-19		7.0E-19
G294.6168-02.3440	6.4E-18	2.0E-19	8.2E-18	2.4E-19	3.1E-18	2.4E-19		2.4E-19	-2.2E-18	2.4E-19
G295.5570-01.3787										
G298.2620+00.7394		4.1E-20		4.8E-20		4.8E-20		4.8E-20		4.8E-20
G300.3412-00.2190	1.7E-17	1.9E-18	7.6E-17	2.9E-18		2.9E-18		2.9E-18		2.9E-18
G301.1726+01.0034	2.6E-17	8.0E-19	3.8E-17	8.0E-19	5.9E-18	8.0E-19		8.0E-19	1.3E-17	8.0E-19
G301.8147+00.7808	2.5E-16	5.3E-18	3.5E-16	5.3E-18		5.3E-18		5.3E-18		5.3E-18
G302.4546-00.7401	7.6E-19	3.7E-20	6.6E-19	4.4E-20	6.7E-19	4.4E-20	6.5E-19	4.4E-20		4.4E-20
G302.6604-00.7908	3.6E-19	5.0E-20		2.5E-20		2.5E-20	6.3E-19	5.0E-20		2.5E-20
G304.7592-00.6299		7.4E-20	1.1E-18	1.5E-19		1.5E-19		1.5E-19		1.5E-19
G305.2017+00.2072A	6.8E-17	3.2E-19		3.2E-19	3.2E-18	3.2E-19		3.2E-19	4.6E-18	3.2E-19
G305.4840+00.2248										
G306.1160+00.1386A		9.2E-19		9.2E-19		9.2E-19		9.2E-19		9.2E-19
G306.1160+00.1386B		2.9E-18	2.5E-17	2.9E-18		2.9E-18		2.9E-18		2.9E-18
G308.0049-00.3868	6.5E-18	2.4E-19	2.3E-17	2.4E-19		2.4E-19		2.4E-19		2.4E-19
G308.6480+00.6469A										
G309.9206+00.4790B	1.7E-17	4.4E-19		4.4E-19	1.6E-17	4.4E-19		4.4E-19	1.7E-17	4.4E-19
G309.9796+00.5496	5.7E-19	1.4E-19	2.2E-18	1.4E-19		1.4E-19		1.4E-19		1.4E-19
G310.0135+00.3892	7.3E-17	1.4E-17	1.2E-16	1.4E-17	1.4E-16	1.4E-17		1.4E-17	5.9E-17	1.4E-17
G311.6380+00.3009A	4.8E-19	3.1E-20	1.6E-18	3.4E-20		3.4E-20		3.4E-20		3.4E-20
G311.9799-00.9527	4.8E-19	3.1E-20	1.6E-18	3.4E-20		3.4E-20		3.1E-20		3.4E-20
G318.9480-00.1969A										
G320.2046+00.8626B	1.3E-18	4.2E-20	3.8E-18	9.3E-20	4.5E-19	9.3E-20	7.4E-19	9.3E-20		9.3E-20
G320.2437-00.5619		2.7E-19		2.7E-19	3.3E-18	2.7E-19		2.7E-19		2.7E-19
G321.3824-00.2861	2.1E-17	9.8E-19		9.8E-19		9.8E-19		9.8E-19	1.6E-17	9.8E-19

G324.1594+00.2622		3.3E-19		3.3E-19	4.0E-18	3.3E-19		3.3E-19		3.3E-19
G326.4755+00.6947	1.3E-17	2.7E-19	6.8E-18	2.7E-19		2.7E-19		2.7E-19	-3.1E-18	2.7E-19
G326.7249+00.6159	1.8E-16	6.1E-18	7.4E-17	6.1E-18		6.1E-18	3.7E-16	6.1E-18		6.1E-18
G326.7796-00.2405	3.5E-18	1.1E-19	9.1E-19	1.1E-19	6.9E-19	1.1E-19	-9.1E-19	1.1E-19		1.1E-19
G327.1192+00.5103	7.1E-19	3.6E-20		4.6E-20		4.6E-20		4.6E-20		4.6E-20
G327.3941+00.1970		6.7E-20		6.7E-20		6.7E-20		6.7E-20		6.7E-20
G327.8097-00.6339A										
G327.8097-00.6339B										
G327.9455-00.1149										
G328.3442-00.4629	4.3E-17	1.9E-18	2.9E-17	1.9E-18	1.6E-17	1.9E-18		1.9E-18	2.6E-17	1.9E-18
G331.7953-00.0979		5.8E-20	2.7E-18	5.8E-20		5.8E-20		5.8E-20		5.8E-20
G332.8256-00.5498A		4.1E-19	2.9E-18	4.1E-19		4.1E-19	5.6E-18	4.1E-19		4.1E-19
G332.9457+02.3855	2.1E-17	4.1E-19		4.1E-19		4.1E-19		4.1E-19		4.1E-19
G332.9868-00.4871		1.1E-19		1.1E-19		1.1E-19		1.1E-19		1.1E-19
G333.1153+00.0950		9.9E-19	1.4E-17	9.9E-19	1.9E-17	9.9E-19	1.9E-18	9.9E-19	1.2E-17	9.9E-19
G333.4747-00.2366		2.5E-19		2.5E-19		2.5E-19		2.5E-19		2.5E-19
G338.5459+02.1175	2.3E-18	1.7E-19	6.4E-18	1.7E-19	1.3E-18	1.7E-19		1.7E-19	5.4E-18	1.7E-19
G338.9196+00.5495		2.5E-19		2.5E-19		2.5E-19		2.5E-19		2.5E-19
G338.9341-00.0623	1.4E-17	8.8E-20	1.3E-17	8.8E-20		8.8E-20		8.8E-20		8.8E-20
G339.3940-00.4084										
G339.5836-00.1265										
G339.6221-00.1209	7.5E-18	6.4E-20	7.9E-19	6.4E-20	1.3E-18	6.4E-20		6.4E-20		6.4E-20
G339.6816-01.2058										
G339.8838-01.2588										
G340.1537+00.5116		4.1E-18	2.2E-16	4.1E-18	4.8E-17	4.1E-18		4.1E-18		4.1E-18
G343.1261-00.0623										
G344.4257+00.0451B	3.6E-18	7.0E-20	9.1E-19	7.0E-20		7.0E-20		7.0E-20		7.0E-20
G344.4257+00.0451C										
G344.6608+00.3401	1.0E-17	2.7E-18	2.4E-17	2.7E-18	2.5E-17	2.7E-18	1.0E-17	2.7E-18		2.7E-18
G345.2619-00.4188A		1.6E-18		1.6E-18		1.6E-18		1.6E-18		1.6E-18
G345.2619-00.4188B		5.7E-19		5.7E-19		5.7E-19		5.7E-19		5.7E-19

G345.4938+01.4677	8.1E-18	5.6E-20	1.7E-18	5.6E-20		5.6E-20		5.6E-20		5.6E-20
G345.9561+00.6123		5.6E-19	3.3E-18	5.6E-19	9.2E-18	5.6E-19		5.6E-19		5.6E-19
G347.0775-00.3927		1.3E-18		1.3E-18		1.3E-18		1.3E-18		1.3E-18
G348.7342-01.0359	7.6E-17	1.0E-19	5.2E-18	1.0E-19		1.0E-19	2.1E-17	1.0E-19	7.2E-18	1.0E-19

Table B.6: Spectral atlas of K band lines. Fluxes are uncorrected for extinction and in W/m^2. Numbers in the second row of the header correspond to central wavelengths of given lines, in μm.

RMS name	F_HeI	ΔF_HeI	F_H_2	ΔF_H_2	F_NaI	ΔF_NaI	F_H_2	ΔF_H_2	F_H_2	ΔF_H_2	F_CO	ΔF_CO
	2.06		2.12			2.22		2.24				
G010.8856+00.1221	-7.2E-18	7.5E-20		1.5E-19		1.8E-19		1.1E-19		1.2E-19		2.2E-19
G012.9090-00.2607		3.3E-20	8.7E-18	1.1E-19	5.3E-18	7.5E-20		6.7E-18		2.2E-19	3.9E-17	2.4E-19
G013.3310-00.0407		3.5E-20	3.4E-19	1.8E-20		1.9E-20		1.7E-20		1.9E-20	2.5E-18	1.6E-20
G014.2166-00.6344		8.4E-19		4.2E-19		3.5E-19		2.9E-19		3.3E-19		3.4E-19
G014.4335-00.6969		1.9E-19		2.8E-19		4.9E-19		2.9E-19		4.2E-19		6.5E-19
G014.9958-00.6732	1.4E-16	2.4E-19	1.1E-16	2.5E-19		3.1E-19		4.6E-19	1.6E-17	2.0E-19		9.3E-19
G015.1288-00.6717		1.5E-19	5.6E-18	1.2E-19		1.6E-19	2.4E-18	2.1E-19		1.6E-19		4.6E-19
G016.9261+00.2854		2.6E-19		2.0E-19		3.1E-19		1.6E-19		3.6E-19		6.9E-19
G016.9270+00.9599	1.9E-17	1.7E-19		3.1E-19		3.1E-19		2.6E-19		2.1E-19	6.2E-18	2.6E-19
G017.6380+00.1566		5.9E-19		1.6E-18		2.0E-18		8.7E-19		8.6E-19		3.1E-18
G027.7571+00.0500		2.8E-19		3.2E-19	9.3E-18	4.9E-19		4.0E-19		4.6E-19		4.2E-19
G029.8620-00.0444		3.5E-19		4.2E-19		4.5E-19		2.8E-19		2.5E-19		3.0E-19
G231.7986-01.9682	-1.1E-16	2.5E-18		1.4E-18		2.0E-18		2.4E-18		1.3E-18		4.4E-18
G233.8306-00.1803	7.2E-16	1.8E-18		2.2E-18		2.8E-18		3.5E-18		2.5E-18		5.5E-18
G254.0548-00.0961		1.2E-19	2.1E-17	9.9E-20		1.3E-19	6.4E-18	1.1E-19	3.6E-18	8.7E-20		1.5E-19
G259.0453-01.5559		1.1E-19	7.9E-18	5.6E-20		6.2E-20	3.3E-18	5.2E-20	1.3E-18	4.9E-20		6.4E-20
G263.5846-03.9973		2.1E-19	1.6E-17	9.4E-20		1.3E-19	7.4E-18	8.9E-20	2.4E-18	7.3E-20		1.4E-19
G263.5994-00.5236		4.9E-19		2.6E-19		3.0E-19		5.2E-19		3.0E-19		6.4E-19
G263.7434+00.1161		7.5E-19	1.3E-16	4.1E-19		4.8E-19	3.8E-17	8.8E-19	1.3E-17	5.4E-19		9.2E-19
G263.7759-00.4281		2.5E-19	2.1E-17	2.1E-19		2.6E-19	5.9E-18	2.1E-19	6.8E-18	2.6E-19		4.5E-19
G264.1444+02.0190		2.0E-19		2.9E-19		1.4E-19		2.9E-19		4.7E-19		4.4E-19
G265.1438+01.4548		1.8E-19		2.5E-19		3.3E-19		2.3E-19		2.7E-19		3.4E-19
G267.7336-01.1058A	-8.1E-18	1.9E-19		2.1E-19		1.5E-19		1.9E-19		1.4E-19		2.4E-19
G267.9094+01.7816		1.7E-18		1.5E-18		1.8E-18		1.6E-18		1.6E-18		6.7E-18
G268.3957-00.4842		1.7E-19		2.5E-19		1.7E-19		2.2E-19		2.5E-19		2.9E-19
G269.1586-01.1383A		1.0E-19	1.1E-17	8.3E-20		9.8E-20	5.6E-18	5.9E-20	3.0E-18	6.2E-20		1.2E-19

G274.0649-01.1460A	3.5E-17	2.7E-19	9.9E-18	2.3E-19	7.4E-18	2.1E-19	4.9E-18	1.2E-19	5.3E-18	2.8E-19		4.1E-19
G282.2988-00.7769	-1.4E-16	4.9E-18		3.8E-18	5.5E-17	2.0E-18		1.3E-18		1.1E-18		4.8E-18
G282.8969-01.2727		2.8E-19	1.5E-17	1.5E-19		2.3E-19	2.2E-18	1.2E-19		2.1E-19		2.6E-19
G283.9146-01.0485		7.0E-20	1.4E-18	3.6E-20		3.6E-20		4.7E-20		3.7E-20		5.3E-20
G287.3716+00.6444		4.0E-19	7.4E-17	1.3E-19		2.1E-19	1.8E-17	6.1E-20	9.5E-18	1.1E-19		2.5E-19
G293.5607-00.6703		3.1E-19	4.0E-18	2.6E-19		3.1E-19		2.5E-19		3.5E-19		2.2E-19
G293.8947-00.7825		2.7E-19		2.8E-19	2.5E-18	2.6E-19		2.3E-19		2.1E-19		3.4E-19
G294.6168-02.3440		1.5E-19	3.0E-18	7.6E-20		1.5E-19		1.1E-19		9.4E-20		1.5E-19
G295.5570-01.3787	1.2E-17	1.1E-19	2.2E-18	6.6E-20		5.9E-20	1.7E-18	6.6E-20	1.5E-18	6.1E-20		6.6E-20
G298.2620+00.7394		1.5E-19	1.3E-17	8.4E-20		8.7E-20	3.2E-18	9.9E-20	2.1E-18	1.1E-19		1.0E-19
G300.3412-00.2190	9.5E-17	1.5E-18		1.8E-18		1.1E-18		2.5E-18		1.1E-18		1.6E-18
G301.1726+01.0034		1.1E-18	5.9E-18	6.6E-19		7.9E-19		6.0E-19		8.8E-19		7.8E-19
G301.8147+00.7808		6.6E-18	7.7E-17	3.2E-18		3.5E-18	5.1E-17	2.1E-18		3.2E-18		3.1E-18
G302.4546-00.7401		1.0E-19	2.7E-17	7.5E-20		8.6E-20	8.4E-18	7.6E-20	4.0E-18	9.3E-20		1.3E-19
G302.6604-00.7908		3.2E-19		1.2E-19		1.9E-19		1.6E-19		1.8E-19		2.4E-19
G304.7592-00.6299	2.7E-17	1.8E-19	1.7E-17	1.9E-19		2.6E-19	7.1E-18	2.6E-19	6.8E-18	2.7E-19		3.6E-19
G305.2017+00.2072A		2.1E-19	4.2E-17	2.6E-19		2.4E-19	1.4E-17	2.0E-19	1.8E-18	1.7E-19	8.9E-17	5.1E-19
G305.4840+00.2248		2.0E-19	2.7E-18	1.6E-19		1.5E-19	2.6E-18	1.2E-19	2.1E-18	1.2E-19		1.6E-19
G306.1160+00.1386A		8.2E-19	1.7E-16	4.7E-19		8.3E-19	7.7E-17	6.0E-19	3.4E-17	4.4E-19		7.4E-19
G306.1160+00.1386B		2.0E-18	1.7E-16	1.5E-18		2.0E-19	2.7E-16	1.0E-18	5.7E-17	1.5E-18		1.8E-18
G308.0049-00.3868		4.1E-18		3.2E-18		4.0E-18		3.2E-18		3.0E-18		5.9E-18
G308.6480+00.6469A		1.4E-19	1.9E-18	1.2E-19		1.3E-19		1.6E-19		1.8E-19		2.6E-19
G309.9206+00.4790B		2.2E-19	4.1E-18	1.3E-19		1.8E-19		1.5E-19		1.6E-19		1.6E-19
G309.9796+00.5496		1.8E-19	3.2E-18	1.8E-19		2.9E-19		2.2E-19		2.2E-19		3.2E-19
G310.0135+00.3892		1.8E-16		1.0E-16	1.5E-15	1.4E-16		1.0E-16		1.3E-16		1.8E-16
G311.6380+00.3009A		4.8E-20	4.6E-18	4.2E-20		4.6E-20	1.6E-18	3.5E-20	1.5E-18	5.2E-20		7.0E-20
G311.9799-00.9527		1.0E-18	4.3E-17	1.6E-18		1.5E-18		1.3E-18		8.9E-19		4.3E-18
G318.9480-00.1969A		4.5E-20	3.5E-18	1.8E-20		3.6E-20	1.1E-18	2.8E-20	1.0E-18	3.5E-20		3.9E-20
G320.2046+00.8626B	7.6E-18	1.2E-19	4.9E-18	1.2E-19		9.3E-20	1.6E-18	8.6E-20	1.7E-18	6.4E-20		9.4E-20
G320.2437-00.5619		8.7E-19		1.1E-18		1.3E-18		8.9E-19		1.5E-18		1.8E-18
G321.3824-00.2861		3.6E-19	1.1E-17	5.4E-19		8.8E-19		8.6E-20		1.3E-18		6.1E-19

G324.1594+00.2622		3.0E-19		3.0E-19		3.4E-19		2.1E-19		3.5E-19		3.8E-19
G326.4755+00.6947		1.1E-19	2.0E-17	6.5E-20		9.2E-20	4.0E-18	7.7E-20	1.6E-18	8.5E-20		8.8E-20
G326.7249+00.6159	1.4E-14	1.3E-17	3.3E-16	2.7E-17		1.7E-17		9.9E-18		1.1E-17		1.1E-17
G326.7796-00.2405		1.4E-19	2.0E-17	8.8E-20		1.0E-19	4.8E-18	7.4E-20	2.4E-18	9.5E-20	3.9E-18	1.0E-19
G327.1192+00.5103		6.1E-20	9.3E-19	4.7E-20		5.7E-20		5.7E-20		6.0E-20		6.3E-20
G327.3941+00.1970		8.1E-20	9.0E-19	1.3E-19	2.9E-18	7.3E-20		1.5E-19		1.1E-19	2.3E-17	1.0E-19
G327.8097-00.6339A		9.2E-19		7.6E-19		7.5E-19		6.6E-19		8.0E-19		7.5E-19
G327.8097-00.6339B		2.4E-19	4.2E-18	1.7E-19		2.1E-19		2.3E-19		2.3E-19		2.1E-19
G327.9455-00.1149		1.7E-19	1.1E-17	1.3E-19		1.6E-19	5.3E-18	1.0E-19	2.2E-18	1.3E-19		2.3E-19
G328.3442-00.4629	1.4E-16	4.8E-18	2.5E-18	2.0E-18		3.6E-18		2.8E-18		2.5E-18		5.1E-18
G331.7953-00.0979		2.7E-19		4.3E-19		5.5E-19		4.5E-19		4.8E-19		6.6E-19
G332.8256-00.5498A	2.2E-16	2.5E-19		1.1E-18	1.7E-17	5.3E-19	1.6E-17	4.5E-19	3.6E-18	5.3E-19	9.0E-17	9.0E-19
G332.9457+02.3855		8.1E-19	5.1E-17	7.6E-19		1.0E-18		8.5E-19		7.5E-19	3.6E-16	1.0E-18
G332.9868-00.4871		3.0E-19		3.3E-19		4.8E-19		4.5E-19		2.5E-19	2.0E-17	4.5E-19
G333.1153+00.0950		3.2E-19		2.7E-19		2.1E-19		1.7E-19		1.4E-19		2.7E-19
G333.4747-00.2366		2.3E-19	3.3E-18	1.8E-19		2.2E-19		3.4E-19		2.9E-19		2.5E-19
G338.5459+02.1175		9.6E-19	2.8E-17	7.2E-19	5.0E-17	1.1E-18		1.1E-18		1.0E-18	2.2E-16	1.7E-18
G338.9196+00.5495		3.9E-19	1.9E-17	2.6E-19		3.7E-19		3.7E-19		2.9E-19		2.8E-19
G338.9341-00.0623		1.0E-19	1.6E-17	1.4E-19		8.2E-20	4.4E-18	1.3E-19	2.8E-18	1.2E-19		1.5E-19
G339.3940-00.4084		1.8E-19		2.5E-19		2.2E-19		2.4E-19		2.6E-19		3.5E-19
G339.5836-00.1265		1.5E-18		1.1E-18		9.3E-19		1.5E-18		9.2E-19		4.3E-19
G339.6221-00.1209		5.3E-19	3.9E-17	1.9E-19		2.5E-19	1.0E-17	1.8E-19	5.7E-18	2.4E-19		4.5E-19
G339.6816-01.2058		5.0E-19	6.9E-18	4.8E-19		8.1E-19		5.3E-19		6.5E-19		5.8E-19
G339.8838-01.2588		7.1E-19		7.7E-19		9.9E-19		8.4E-19		6.4E-19		1.1E-18
G340.1537+00.5116		8.2E-19		6.2E-19		1.0E-18	1.9E-17	4.8E-19		5.6E-19		1.1E-18
G343.1261-00.0623		8.8E-20		5.2E-20		7.8E-20		6.8E-20		8.4E-20		8.5E-20
G344.4257+00.0451B		8.6E-20	8.7E-18	4.3E-20		6.6E-20	2.9E-18	1.2E-19		1.1E-19		1.0E-19
G344.4257+00.0451C		2.8E-19	4.6E-18	1.2E-19		1.2E-19	1.4E-18	8.6E-20		9.3E-20		9.3E-20
G344.6608+00.3401		2.1E-19	9.4E-18	9.2E-20		1.1E-19	2.0E-18	8.2E-20	1.2E-18	9.4E-20		2.0E-19
G345.2619-00.4188A		9.0E-19		9.5E-19		7.8E-19		7.5E-19		7.0E-19		1.4E-18
G345.2619-00.4188B		9.0E-19		9.5E-19		7.8E-19		7.5E-19		7.0E-19		1.4E-18

G345.4938+01.4677	1.1E-17	1.5E-19	2.5E-17	3.4E-19		3.8E-19	8.4E-18	3.1E-19	6.3E-18	3.0E-19	3.4E-17	3.4E-19
G345.9561+00.6123		1.1E-18		8.9E-19		1.1E-18		1.4E-19		1.4E-19		1.8E-19
G347.0775-00.3927		4.4E-19		3.3E-19		4.3E-19		2.0E-19		3.9E-19		9.5E-19
G348.7342-01.0359	1.2E-16	2.1E-19	1.9E-17	3.5E-19		1.9E-19	7.6E-18	9.8E-20	2.9E-18	1.2E-19		2.5E-19

Table B.7: AAT Spectral atlas. FWHM and their uncertainties are in km/s, clump masses from ATLASGAL in $M_\odot$ and jet classifications from Purser *et al.* (2016). Jet(L) are jets with lobes; DW are disc-winds; Jet/DW represents an ambiguous classification between jet and disc-wind; U/K is no classification and N/D are non-detections. IPC signifies an inverse P Cygni profile detection.

RMS name	FWHM Brγ	ΔFWHM Brγ	FWHM Br11	ΔFWHM Br11	M_{cl}	PC Brγ	PC HeI 2.06	PC Br10	Purser *et al.* (2016) classification
G010.8856+00.1221					112.2				
G012.9090-00.2607	77.09	25.24			3176.9				U/K
G013.3310-00.0407	365.97	61.99			1116.9				
G014.2166-00.6344	224.68	49.09			11.4				UCHII
G014.4335-00.6969	151.46	40.11	160.22	52.86	117.5				Jet/DW
G014.9958-00.6732	139.02	38.16	283.09	77.64	6968.6		y		
G015.1288-00.6717	282.63	54.67			608.1	y			
G016.9261+00.2854	148.40	39.64			271.6	y			
G016.9270+00.9599	122.81	35.35	61.57	23.85	1318.3		y		
G017.6380+00.1566					756.8				
G027.7571+00.0500	219.41	48.54			1137.6		y		
G029.8620-00.0444	140.41	38.39	391.15	96.57	2857.6				Jet(L)
G231.7986-01.9682	190.87	45.35	207.40	63.23			y		
G233.8306-00.1803	124.92	35.74	166.38	54.31			y		
G254.0548-00.0961	196.38	46.00	164.52	53.88					
G259.0453-01.5559	94.85	29.60							
G263.5846-03.9973	244.48	51.09	203.10	62.35					
G263.5994-00.5236									
G263.7434+00.1161									Jet
G263.7759-00.4281	100.02	30.76	87.21	32.59					
G264.1444+02.0190	170.01	42.72							
G265.1438+01.4548	174.68	43.34	237.46	69.18					N/D
G267.7336-01.1058A			785.74	166.82			y		
G267.9094+01.7816									
G268.3957-00.4842	168.19	42.48	140.53	48.00				y	

G269.1586-01.1383A									
G274.0649-01.1460A	75.03	24.70					y		
G282.2988-00.7769	163.99	41.91	204.78	62.69	818.5		y		
G282.8969-01.2727	176.83	43.62			648.6	y			
G283.9146-01.0485					1318.3				
G287.3716+00.6444	158.25	41.10	788.67	167.36	591.6				
G293.5607-00.6703	154.49	40.56	219.16	65.61	413.0				Jet(L)
G293.8947-00.7825	159.55	41.29	108.08	39.06	2167.7				
G294.6168-02.3440	60.10	20.51	198.03	61.29					
G295.5570-01.3787	44.34	15.62			16651.2				
G298.2620+00.7394	533.50	76.75			683.9				DW
G300.3412-00.2190	61.52	20.92	35.85	14.25	539.5			y	N/D
G301.1726+01.0034	126.81	36.08	254.37	72.38	233.9				
G301.8147+00.7808	125.97	35.93	153.91	51.34	901.6				Jet
G302.4546-00.7401	121.53	35.11	179.89	57.37	1142.9	y			
G302.6604-00.7908	ul25		158.86	52.54	520.6				
G304.7592-00.6299	99.78	30.71			732.8		y		
G305.2017+00.2072A	55.29	19.06			6011.7				
G305.4840+00.2248	143.94	38.95			143.7				
G306.1160+00.1386A	180.38	44.07				y			
G306.1160+00.1386B	135.42	37.57	123.12	43.36	399.0	y		y	
G308.0049-00.3868	89.22	28.28	62.68	24.25	642.7				
G308.6480+00.6469A					939.7	y			
G309.9206+00.4790B	71.07	23.63			5000.3				Jet
G309.9796+00.5496	157.87	41.05	204.54	62.64	496.6				
G310.0135+00.3892	168.55	42.53	75.80	28.81	1119.4	y		y	
G311.6380+00.3009A	112.56	33.39	232.94	68.31	2365.9				
G311.9799-00.9527			232.94	68.31	263.0	y			Jet(L)
G318.9480-00.1969A					582.1				
G320.2046+00.8626B					841.4				Jet
G320.2437-00.5619	161.41	41.55			3556.3				

G321.3824-00.2861					7906.8				N/D
G324.1594+00.2622					1261.8				Jet(L)
G326.4755+00.6947					887.2				
G326.7249+00.6159	79.69	25.92			867.0				
G326.7796-00.2405					1074.0				
G327.1192+00.5103	104.78	31.79			2018.4				
G327.3941+00.1970	164.72	42.01			1995.3	IPC			
G327.8097-00.6339A	39.93	14.17							U/K
G327.8097-00.6339B					1435.5				Jet
G327.9455-00.1149	93.85	29.37			473.2				
G328.3442-00.4629	129.09	36.48	186.69	58.87	41.2	y			HCHII
G331.7953-00.0979	158.43	41.13			4731.5		y		
G332.8256-00.5498A	48.81	17.05			10000.0				
G332.9457+02.3855	125.13	35.78				IPC			
G332.9868-00.4871	113.23	33.52			4897.8				
G333.1153+00.0950	151.08	40.05	234.07	68.53	232.3				
G333.4747-00.2366	103.36	31.49			366.4	y			CHII
G338.5459+02.1175	175.22	43.41							
G338.9196+00.5495					12560.3				Jet/DW
G338.9341-00.0623	109.40	32.75	40.23	15.94	317.0				
G339.3940-00.4084					537.1				
G339.5836-00.1265					716.1				Jet(L)
G339.6221-00.1209	144.92	39.10			905.7	y			
G339.6816-01.2058	94.60	29.55			1081.4				
G339.8838-01.2588					2004.5				
G340.1537+00.5116	116.33	34.13	151.69	50.80	57.3				
G343.1261-00.0623					3184.2				
G344.4257+00.0451B	35.59	12.71							
G344.4257+00.0451C									
G344.6608+00.3401	123.44	35.47	161.84	53.24	4159.1				Jet(L)
G345.2619-00.4188A	1129.99	135.73			260.6				

G345.2619-00.4188B	1129.99	135.73					
G345.4938+01.4677	186.00	44.76	85.11	31.91	4456.6		Jet(L)
G345.9561+00.6123	133.19	37.19	190.67	59.73	205.9	y	
G347.0775-00.3927	35.01	12.52			75.5		Jet(L)
G348.7342-01.0359					8260.4		

Appendix C

Gemini spectral atlas

Table C.1: Spectral atlas of Brγ and accretion parameters. EWs are in Å, fluxes are uncorrected for extinction and in W/m^{2}Å and luminosities are in L$_\odot$.

Object	UL EW	EW	ΔEW	F	ΔF	L	ΔL	L$_{Acc}$	ΔL$_{Acc}$	M$_*$	R$_*$	$\dot{M}$	$\Delta\dot{M}$
G010.8411-02.5919	0.09	-0.6	0.2	5.4E-18	1.4E-18	0.15	0.04	650	180	15.9±0.8	6±0.3	7.9E-6	3.9E-7
G010.8856+00.1221	0.1	-1.8	0.2	1.1E-17	1.0E-18	0.59	0.16	2200	590	10.5±0.5	2.9±0.1	1.9E-5	9.7E-7
G012.9090-00.2607	0.11	-2.3	0.2	2.1E-17	1.7E-18	0.10	0.03	450	120	17.2±0.9	6.9±0.3	4.5E-3	2.2E-4
G014.9958-00.6732	0.07	-18.1	0.1	9.6E-16	6.2E-18	8.00	2.10	23000	6200	13.4±0.7	4.4±0.2	2.4E-4	1.2E-5
G015.1288-00.6717	0.05	-1.9	0.1	2.3E-17	1.0E-18	0.04	0.01	200	53	13.1±0.7	4.2±0.2	2.1E-6	1.0E-7
G017.6380+00.1566	0.01	-0.6	0	2.9E-17	1.3E-18	0.04	0.01	150	41	8.5±0.2	3.2±0.1	3.1E-5	8.4E-7
G018.3412+00.1566	0.06	-2.3	0.1	1.9E-17	8.0E-19	1.40	0.37	4800	1300	15.5±0.8	5.7±0.3	5.7E-5	2.9E-6
G023.3891+00.1851	0.08	-0.3	0.1	5.3E-18	2.3E-18	0.57	0.15	2100	580	15.9±0.8	6±0.3	2.6E-5	1.3E-6
G025.4118+00.1052A	0.18												
G026.2020+00.2262	0.07	-3.5	0.1	7.0E-17	2.3E-18	7.10	1.90	21000	5500	9.4±0.5	2.3±0.1	1.7E-4	8.3E-6
G026.3819+01.4057	0.05	-3.8	0.1	3.5E-17	8.5E-19	0.35	0.10	1400	370	14.4±0.7	5.1±0.3	1.6E-5	7.9E-7
G027.7571+00.0500	0.11	-2.4	0.2	1.9E-17	1.5E-18	10.00	2.70	29000	7700	13.4±0.7	4.4±0.2	3.0E-4	1.5E-5
G029.8620-00.0444	0.07	-1.9	0.1	1.3E-17	8.0E-19	0.73	0.20	2700	720	16.6±0.8	6.5±0.3	3.4E-5	1.7E-6
G030.1981-00.1691	0.06	-1.1	0.1	1.0E-17	8.6E-19	2.00	0.54	6700	1800	16.9±0.8	6.7±0.3	8.6E-5	4.3E-6
G033.3891+00.1989	0.07	-2.1	0.2	1.3E-16	9.9E-18	3.20	0.87	10000	2800	13.4±0.7	4.4±0.2	1.1E-4	5.5E-6
G033.5237+00.0198	0.07	-2.9	0.1	4.9E-17	2.0E-18	6.70	1.80	20000	5300	13.4±0.7	4.4±0.2	2.1E-4	1.1E-5
G034.0500-00.2977_A	0.08	-3.6	0.1	3.3E-17	1.3E-18	1.10	0.30	3900	1000	15.7±0.8	5.9±0.3	4.7E-5	2.4E-6
G034.0500-00.2977_B	0.08	-4.7	0.1	1.3E-16	4.0E-18	4.40	1.20	14000	3600	15.7±0.8	5.9±0.3	1.6E-4	8.2E-6
G034.7123-00.5946	0.06	-0.1	0.1	1.9E-18	1.4E-18	0.17	0.05	730	200	12.3±0.6	3.8±0.2	7.3E-6	3.6E-7
G056.4120-00.0277	0.05	-2.2	0.1	5.3E-17	2.3E-18	4.00	1.10	12000	3400	15.5±0.8	5.7±0.3	1.5E-4	7.5E-6
G073.6525+00.1944	0.14	-1.2	0.2	6.6E-18	1.3E-18	0.84	0.23	3000	820	23.7±1.2	12.3±0.6	5.1E-5	2.5E-6

G073.6952-00.9996	0.12	-2.5	0.2	5.7E-17	4.5E-18	18.00	4.90	48000	13000	14.4±0.7	5.1±0.3	5.5E-4	2.7E-5
G076.3829-00.6210	0.08	-15	0.1	2.8E-15	2.4E-17	4.80	1.30	15000	3900	18.4±0.9	7.7±0.4	2.0E-4	1.0E-5
G077.4622+01.7600	0.12	-0.4	0.2	3.9E-18	2.1E-18	0.02	0.01	100	27	9±0.4	2.2±0.1	7.9E-7	3.9E-8
G078.8867+00.7087	0.08	0.3	-0.1	-2.5E-17	-1.3E-17								
G094.3228-00.1671	0.11	-19.2	0.2	1.2E-16	1.2E-18	9.50	2.60	27000	7200	18.7±0.9	8±0.4	3.7E-4	1.9E-5
G094.6028-01.7966	0.08	-3.2	0.1	2.8E-16	1.2E-17	4.40	1.20	14000	3600	10.6±0.5	2.9±0.1	1.2E-4	6.0E-6
G102.3533+03.6360	0.06	-1.4	0.1	9.8E-17	6.7E-18	12.00	3.10	32000	8700	24.4±1.2	12.8±0.6	5.5E-4	2.8E-5
G106.7968+05.3121	0.05	-1.2	0.1	7.9E-17	5.4E-18	0.02	0.01	56	15	7.7±0.2	4.1±0.1	1.8E-4	4.7E-6
G110.1082+00.0473B_A	0.16												
G110.1082+00.0473B_B	0.04	-4	0.1	6.8E-17	1.8E-18	0.01	0.00	70	19	12.2±0.6	3.8±0.2	6.9E-7	3.5E-8
G111.2348-01.2385	0.35	-1.4	0.6	1.0E-17	4.3E-18	13.00	3.60	36000	9700	18.6±0.9	7.9±0.4	5.0E-4	2.5E-5
G111.5234+00.8004A	0.05	-2.4	0.1	8.3E-17	3.2E-18	0.72	0.19	2600	700	20.2±1	9.2±0.5	3.9E-5	1.9E-6
G111.5423+00.7776	0.19	-5.1	0.3	8.8E-17	5.8E-18	360.0	97.00	700000	190000	29.2±1.5	17.8±0.9	1.4E-2	6.9E-4
G120.1483+03.3745	0.05	-3.5	0.3	2.9E-16	2.3E-17	8.10	2.20	23000	6300	15.3±0.8	5.6±0.3	2.8E-4	1.4E-5
G151.6120-00.4575	0.09	-3.1	0.2	2.4E-16	1.2E-17	4.40	1.20	13000	3600	20.7±1	9.6±0.5	2.0E-4	1.0E-5
G213.7040-12.5971_A	0.03	-1.2	0.1	5.3E-18	2.7E-19	0.01	0.00	4	1	7.5±0.2	2.5±0.1	6.2E-4	1.7E-5
G213.7040-12.5971_B	0.01	-0.4	0.1	1.7E-18	8.4E-20	0.00	0.00	1	0	7.5±0.2	2.5±0.1	6.2E-4	1.7E-5
G233.8306-00.1803A	0.1	-17.4	0.2	2.4E-15	2.5E-17	42.00	11.00	100000	28000	13.4±0.7	4.4±0.2	1.1E-3	5.5E-5

Table C.2: Spectral atlas of Br12 and CO bandhead emission. EWs are in Å, fluxes are uncorrected for extinction and in W/m^{2}Å and luminosities are in L$_\odot$.

Object	EW CO	ΔEW	F	ΔF	L	Δ L	EW Br12	ΔEW	F	ΔF	L	ΔL
G010.8411-02.5919												
G010.8856+00.1221							-0.5	0.1	3.5E-19	3.3E-20	3.5E-1	1.3E-1
G012.9090-00.2607	-5.5	0.3	1.2E-16	5.2E-18	7.0E+2	6.0E+1						
G014.9958-00.6732							-12.5	0.1	1.6E-16	1.1E-18	1.1E+1	4.3E+0
G015.1288-00.6717							3	0.1	-2.4E-17	8.1E-19	1.5E-1	5.8E-2
G017.6380+00.1566												
G018.3412+00.1566							-1.7	0.1	1.1E-18	4.5E-20	5.3E+0	2.1E+0
G023.3891+00.1851							-2.2	0.9	5.6E-18	2.4E-18	1.6E-1	6.1E-2
G025.4118+00.1052A												
G026.2020+00.2262							-2.2	0.1	1.2E-17	3.8E-19	9.4E+0	4.1E+0
G026.3819+01.4057							-2.7	0.1	1.3E-17	3.2E-19	7.6E-1	3.0E-1
G027.7571+00.0500							-1.4	0.1	8.5E-19	6.7E-20	1.2E+1	4.6E+0
G029.8620-00.0444							-1.3	0.1	1.2E-18	7.5E-20	9.4E-1	4.3E-1
G030.1981-00.1691							-2.6	0.2	7.7E-18	6.4E-19	9.8E+0	3.8E+0
G033.3891+00.1989	-2.6	0.1	1.7E-16	9.4E-18	5.6E+0	2.7E-1	-3.1	0.2	4.1E-17	3.1E-18	8.0E+0	3.1E+0
G033.5237+00.0198							-1.9	0.1	3.7E-18	1.5E-19	7.2E+0	2.8E+0
G034.0500-00.2977_A							7.3	0.3	-1.2E-16	4.6E-18	3.6E+0	1.6E+0
G034.0500-00.2977_B							-2.1	0.1	3.4E-17	1.0E-18	5.2E+0	2.3E+0
G034.7123-00.5946	-1.1	0.7	1.6E-17	1.1E-17	2.8E+0	1.7E+0						
G056.4120-00.0277	-1.4	0.1	3.9E-17	1.5E-18	3.6E+0	1.4E-1	-1.3	0.1	1.4E-17	5.8E-19	6.2E+0	2.4E+0
G073.6525+00.1944	-5.3	0.8	3.6E-17	6.3E-18	5.1E+0	7.6E-1	-3.6	0.7	1.1E-17	2.2E-18	5.8E+0	2.2E+0

G073.6952-00.9996	-3.4	0.2	1.2E-16	7.1E-18	4.0E+1	4.9E+0	-0.5	0.1	2.7E-18	5.3E-19	1.1E+1	4.1E+0
G076.3829-00.6210	-4.7	0.5	9.5E-16	7.4E-18	2.0E+0	1.2E-1	-2.8	0.2	3.1E-16	2.2E-17	2.4E+0	9.5E-1
G077.4622+01.7600							-1.4	0.7	1.5E-17	7.7E-18	2.9E-1	1.1E-1
G078.8867+00.7087							-1.5	0.8	5.6E-18	3.0E-18	1.9E-2	1.0E-2
G094.3228-00.1671							-8.5	0.1	1.5E-17	1.5E-19	1.7E+1	6.8E+0
G094.6028-01.7966	-5.7	0.1	5.8E-16	2.3E-17	1.1E+1	3.3E-1	-1.2	0.1	4.4E-17	3.8E-18	2.2E+0	9.4E-1
G102.3533+03.6360							-0.4	0.1	6.7E-18	1.6E-18	6.9E+0	2.7E+0
G106.7968+05.3121	-3.4	-0.1	8.8E-16	3.3E-17	7.1E-2	2.7E-3						
G110.1082+00.0473B_A												
G110.1082+00.0473B_B							-0.2	0.1	2.7E-18	1.4E-18	2.0E-3	7.7E-4
G111.2348-01.2385												
G111.5234+00.8004A							-0.7	0.1	1.0E-17	1.5E-18	5.4E-1	2.1E-1
G111.5423+00.7776												
G120.1483+03.3745							-2.3	0.2	6.4E-17	5.1E-18	1.2E+1	4.6E+0
G151.6120-00.4575	-2.8	0.1	3.8E-16	1.4E-17	5.8E+0	1.5E-1	-1.3	0.1	4.4E-17	2.2E-18	3.8E+0	1.5E+0
G213.7040-12.5971_A							-0.8	0.1	1.4E-18	6.8E-20	3.8E-4	1.9E-5
G213.7040-12.5971_B							-0.7	0.1	1.2E-18	6.0E-20	3.4E-4	1.7E-5
G233.8306-00.1803A							-8.9	0.1	5.9E-16	6.1E-18	5.9E+1	2.3E+1

Table C.3: Spectral atlas of Br10-11. EWs are in Å, fluxes are uncorrected for extinction and in W/m^{2}Å and luminosities are in L$_\odot$.

Object	EW Br11	ΔEW	F	ΔF	L	ΔL	EW Br10	ΔEW	F	ΔF	L	ΔL
G010.8411-02.5919												
G010.8856+00.1221	-0.5	0.2	3.8E-19	1.5E-19	4.5E-1	1.8E-1	-0.1	0.1	1.5E-19	6.0E-20	6.6E-1	2.6E-1
G012.9090-00.2607												
G014.9958-00.6732	-13.7	5.3	1.8E-16	7.1E-17	1.3E+1	5.2E+0	-17.2	6.7	2.8E-16	1.1E-16	1.4E+1	5.6E+0
G015.1288-00.6717	2.7	1	1.8E-17	7.0E-18	1.5E-1	6.0E-2	3.4	1.3	2.4E-17	9.4E-18	2.4E-1	9.5E-2
G017.6380+00.1566												
G018.3412+00.1566	-2	0.8	1.5E-18	6.0E-19	7.9E+0	3.1E+0	-1.7	0.7	1.9E-18	7.3E-19	1.4E+1	5.5E+0
G023.3891+00.1851	-0.7	0.3	1.8E-18	7.0E-19	6.4E-2	2.5E-2	-0.7	0.3	2.4E-18	9.3E-19	9.2E-2	3.6E-2
G025.4118+00.1052A												
G026.2020+00.2262	-2.3	1	1.5E-17	6.4E-18	1.4E+1	6.1E+0	-2.6	1.2	1.9E-17	8.4E-18	2.0E+1	9.0E+0
G026.3819+01.4057	-3.1	1.2	1.6E-17	6.3E-18	1.0E+0	4.0E-1	-2.6	1	1.5E-17	5.7E-18	1.1E+0	4.3E-1
G027.7571+00.0500	-1.8	0.7	1.7E-18	6.5E-19	2.4E+1	9.3E+0	-1.8	0.7	2.8E-18	1.1E-18	3.8E+1	1.5E+1
G029.8620-00.0444	-1.6	0.7	1.8E-18	8.2E-19	1.4E+0	6.2E-1	-1.1	0.5	1.6E-18	7.3E-19	1.7E+0	7.8E-1
G030.1981-00.1691	-11.1	4.3	1.1E-17	4.3E-18	1.1E+1	4.4E+0	-7	2.7	9.7E-18	3.8E-18	1.4E+1	5.4E+0
G033.3891+00.1989	-2.5	1	3.8E-17	1.5E-17	8.6E+0	3.3E+0	-2.2	0.9	4.0E-17	1.5E-17	9.4E+0	3.7E+0
G033.5237+00.0198	-2.9	1.1	5.1E-18	2.0E-18	1.2E+1	4.5E+0	-2.8	1.1	6.6E-18	2.6E-18	2.2E+1	8.4E+0
G034.0500-00.2977_A	5.2	2.2	7.5E-17	3.2E-17	3.0E+0	1.3E+0	4.6	2	6.3E-17	2.7E-17	3.6E+0	1.5E+0
G034.0500-00.2977_B	-2.6	1.1	4.0E-17	1.7E-17	5.7E+0	2.5E+0	-5.6	2.4	8.7E-17	3.7E-17	1.4E+1	6.2E+0
G034.7123-00.5946												
G056.4120-00.0277	-1.4	0.5	1.6E-17	6.1E-18	7.0E+0	2.7E+0	-1.1	0.4	1.6E-17	6.3E-18	7.6E+0	3.0E+0
G073.6525+00.1944	-0.4	0.1	9.5E-19	3.7E-19	6.4E-1	2.5E-1	-0.4	0.2	1.2E-18	4.8E-19	9.6E-1	3.7E-1

G073.6952-00.9996	-0.9	0.4	6.1E-18	2.4E-18	2.5E+1	9.7E+0	-0.4	0.2	3.1E-18	1.2E-18	1.4E+1	5.3E+0
G076.3829-00.6210	-4.4	1.7	3.9E-16	1.5E-16	2.6E+0	1.0E+0	-4.2	1.6	4.2E-16	1.6E-16	4.0E+0	1.5E+0
G077.4622+01.7600	-1.6	0.6	9.9E-18	3.8E-18	3.5E-1	1.3E-1	-0.5	0.2	3.8E-18	1.5E-18	1.7E-1	6.5E-2
G078.8867+00.7087												
G094.3228-00.1671	-9.9	3.9	1.8E-17	7.0E-18	2.6E+1	1.0E+1	-12	4.7	2.7E-17	1.1E-17	4.0E+1	1.6E+1
G094.6028-01.7966	-1.7	0.7	3.7E-17	1.6E-17	2.8E+0	1.2E+0	-1.5	0.6	3.6E-17	1.5E-17	3.2E+0	1.3E+0
G102.3533+03.6360	-0.6	0.2	8.8E-18	3.4E-18	8.2E+0	3.2E+0	-0.8	0.3	1.5E-17	5.8E-18	9.5E+0	3.7E+0
G106.7968+05.3121												
G110.1082+00.0473B_A	-0.2	0.1	1.1E-18	5.4E-19	1.3E-3	5.1E-4	-0.3	0.1	3.8E-18	1.1E-18	4.6E-3	1.8E-3
G110.1082+00.0473B_B	-0.5	0.2	4.2E-18	1.6E-18	3.3E-3	1.3E-3	-0.8	0.3	7.0E-18	2.7E-18	7.1E-3	2.8E-3
G111.2348-01.2385												
G111.5234+00.8004A	-0.9	0.4	1.4E-17	5.4E-18	8.2E-1	3.2E-1	-1.3	0.5	2.2E-17	8.7E-18	1.1E+0	4.2E-1
G111.5423+00.7776												
G120.1483+03.3745	-2.9	1.1	7.8E-17	3.0E-17	1.7E+1	6.5E+0	-3.5	1.4	1.0E-16	4.0E-17	2.8E+1	1.1E+1
G151.6120-00.4575	-1.9	0.7	5.5E-17	2.1E-17	4.8E+0	1.9E+0	-1.7	0.7	5.2E-17	2.0E-17	3.8E+0	1.5E+0
G213.7040-12.5971_A	-0.9	0.3	1.9E-18	7.4E-19	5.4E-4	2.1E-4	-0.6	0.2	1.9E-18	7.2E-19	5.2E-4	2.0E-4
G213.7040-12.5971_B	-0.5	0.2	1.1E-18	4.1E-19	3.0E-4	1.2E-4	-0.6	0.2	1.3E-18	4.9E-19	3.6E-4	1.4E-4
G233.8306-00.1803A	-9.8	3.8	6.8E-16	2.7E-16	7.1E+1	2.8E+1	-12.6	4.9	9.9E-16	3.8E-16	1.2E+2	4.7E+1

Table C.4: Spectral atlas of NaI and H_2 2.24 μm. EWs are in Å, fluxes are uncorrected for extinction and in W/m^{2}Å and luminosities are in $L_\odot$.

Object	EW NaI	ΔEW	F	ΔF	L	ΔL	EW H_2	ΔEW	F	ΔF	L	ΔL
G010.8411-02.5919												
G010.8856+00.1221												
G012.9090-00.2607	-0.5	0.2	7.7E-18	2.1E-18	5.1E+1	1.4E+1						
G014.9958-00.6732							-0.2	0.1	1.4E-17	5.5E-18	1.8E-3	6.9E-4
G015.1288-00.6717												
G017.6380+00.1566												
G018.3412+00.1566												
G023.3891+00.1851												
G025.4118+00.1052A												
G026.2020+00.2262	-0.1	0.0	2.0E-18	5.5E-19	2.3E-1	6.3E-2						
G026.3819+01.4057												
G027.7571+00.0500	-0.7	0.2	6.5E-18	1.8E-18	3.6E+0	9.7E-1						
G029.8620-00.0444	-0.4	0.1	4.3E-18	1.2E-18	1.7E-1	4.6E-2						
G030.1981-00.1691												
G033.3891+00.1989	-0.4	0.1	2.7E-17	7.2E-18	5.9E-1	1.6E-1						
G033.5237+00.0198	-0.3	0.1	5.1E-18	1.4E-18	8.1E-1	2.2E-1						
G034.0500-00.2977_A	-0.1	0.0	2.5E-18	6.8E-19	3.9E-2	1.1E-2						
G034.0500-00.2977_B	-0.2	0.1	3.8E-18	1.0E-18	1.8E-1	4.9E-2						
G034.7123-00.5946	-0.5	0.1	4.6E-18	1.2E-18	7.5E-1	2.0E-1						
G056.4120-00.0277	-0.2	0.1	9.7E-18	2.6E-18	4.0E-1	1.1E-1						
G073.6525+00.1944	-0.2	0.1	2.7E-18	7.2E-19	1.3E-1	3.5E-2						

G073.6952-00.9996	-0.3	0.1	8.9E-18	2.4E-18	2.3E+0	6.2E-1						
G076.3829-00.6210	-0.7	0.2	1.6E-16	4.3E-17	2.4E-1	6.4E-2						
G077.4622+01.7600												
G078.8867+00.7087	-0.2	0.1	2.0E-17	5.2E-18	1.1E-2	3.0E-3						
G094.3228-00.1671							-0.3	0.1	2.2E-18	8.4E-19	1.3E-3	5.1E-4
G094.6028-01.7966	-0.6	0.2	5.5E-17	1.5E-17	9.4E-1	2.5E-1						
G102.3533+03.6360												
G106.7968+05.3121	-0.5	0.1	5.9E-17	1.6E-17	1.5E-2	4.0E-3						
G110.1082+00.0473B_A												
G110.1082+00.0473B_B	-0.2	0.1	8.4E-15	2.3E-15	6.5E-4	1.8E-4						
G111.2348-01.2385	-0.9	0.2	9.2E-18	2.5E-18	9.5E+0	2.6E+0						
G111.5234+00.8004A												
G111.5423+00.7776												
G120.1483+03.3745												
G151.6120-00.4575												
G213.7040-12.5971_A												
G213.7040-12.5971_B							-0.1	0.1	7.4E-19	2.9E-19	2.1E-5	8.1E-6
G233.8306-00.1803A												

Table C.5: Spectral atlas of HeI and OI. EWs are in Å, fluxes are uncorrected for extinction and in W/m^{2}Å and luminosities are in $L_\odot$.

Object	EW HeI	ΔEW	F	ΔF	L	ΔL	EW OI	ΔEW	F	ΔF	L	ΔL
G010.8411-02.5919												
G010.8856+00.1221												
G012.9090-00.2607												
G014.9958-00.6732							-15.5	4.2	1.1E-16	5.6E-18	2.6E+2	1.3E+1
G015.1288-00.6717	7.1	0.3	4.3E-18	1.9E-19	5.3E-4	1.4E-4						
G017.6380+00.1566												
G018.3412+00.1566												
G023.3891+00.1851												
G025.4118+00.1052A												
G026.2020+00.2262												
G026.3819+01.4057												
G027.7571+00.0500												
G029.8620-00.0444												
G030.1981-00.1691												
G033.3891+00.1989												
G033.5237+00.0198												
G034.0500-00.2977_A	1.7	0.1	7.8E-18	3.1E-19	4.0E-2	1.1E-2						
G034.0500-00.2977_B	-0.4	0.0	1.2E-18	3.6E-20	6.3E-3	1.7E-3	-3.9	1.0	5.2E-17	2.6E-18	1.7E+1	8.4E-1
G034.7123-00.5946												
G056.4120-00.0277	10.0	0.4	9.4E-18	4.1E-19	2.5E-2	6.8E-3						
G073.6525+00.1944												

G073.6952-00.9996												
G076.3829-00.6210												
G077.4622+01.7600												
G078.8867+00.7087												
G094.3228-00.1671												
G094.6028-01.7966	15.9	0.7	7.3E-17	3.1E-18	5.5E-2	1.5E-2	-1.4	0.4	2.0E-17	1.0E-18	3.8E+0	1.9E-1
G102.3533+03.6360												
G106.7968+05.3121												
G110.1082+00.0473B_A												
G110.1082+00.0473B_B	-4.9	0.1	4.0E-17	1.1E-18	2.3E-2	6.2E-3	-0.2	0.1	1.3E-18	6.5E-20	7.0E-3	3.5E-4
G111.2348-01.2385												
G111.5234+00.8004A							-2.6	0.7	3.4E-17	1.7E-18	1.5E+1	7.5E-1
G111.5423+00.7776												
G120.1483+03.3745							-1.7	0.5	1.1E-17	5.3E-19	3.1E+2	1.6E+1
G151.6120-00.4575	9.0	0.5	6.0E-17	3.0E-18	7.6E-2	2.1E-2						
G213.7040-12.5971_A												
G213.7040-12.5971_B												
G233.8306-00.1803A							-5.3	1.4	1.2E-17	6.0E-19	1.4E+3	6.8E+1

Table C.6: Spectral atlas of Paγ. EWs are in Å, fluxes are uncorrected for extinction and in W/m^{2}Å and luminosities are in L$_\odot$.

Object	EW Paγ	ΔEW	F	ΔF	L	ΔL
G010.8411-02.5919						
G010.8856+00.1221						
G012.9090-00.2607						
G014.9958-00.6732						
G015.1288-00.6717	-0.8	0.3	4.7E-19	1.8E-19	1.0E+0	3.9E-1
G017.6380+00.1566						
G018.3412+00.1566						
G023.3891+00.1851						
G025.4118+00.1052A						
G026.2020+00.2262						
G026.3819+01.4057						
G027.7571+00.0500						
G029.8620-00.0444						
G030.1981-00.1691						
G033.3891+00.1989						
G033.5237+00.0198						
G034.0500-00.2977_A	9.5	4.1	4.6E-17	2.0E-17	1.1E+0	4.7E-1
G034.0500-00.2977_B	4.2	1.8	1.3E-17	5.5E-18	2.3E+0	1.0E+0
G034.7123-00.5946						
G056.4120-00.0277	-7.6	3.0	8.4E-18	3.3E-18	6.3E-1	2.4E-1
G073.6525+00.1944						

G073.6952-00.9996						
G076.3829-00.6210	-12.4	4.8	5.5E-17	2.1E-17	2.0E+1	7.8E+0
G077.4622+01.7600						
G078.8867+00.7087						
G094.3228-00.1671						
G094.6028-01.7966	-14.1	6.0	7.1E-17	3.0E-17	3.8E+0	1.5E+0
G102.3533+03.6360						
G106.7968+05.3121						
G110.1082+00.0473B_A						
G110.1082+00.0473B_B	1.8	0.7	1.5E-17	5.7E-18	3.5E-1	1.4E-1
G111.2348-01.2385						
G111.5234+00.8004A	-8.4	3.3	2.8E-17	1.1E-17	1.0E+3	3.9E+2
G111.5423+00.7776						
G120.1483+03.3745	-24.2	9.4	4.0E-17	1.6E-17	1.1E+4	4.2E+3
G151.6120-00.4575	-9.3	3.6	6.8E-17	2.7E-17	1.7E+3	6.8E+2
G213.7040-12.5971_A						
G213.7040-12.5971_B						
G233.8306-00.1803A						

Appendix D

Gemini MYSO spectra

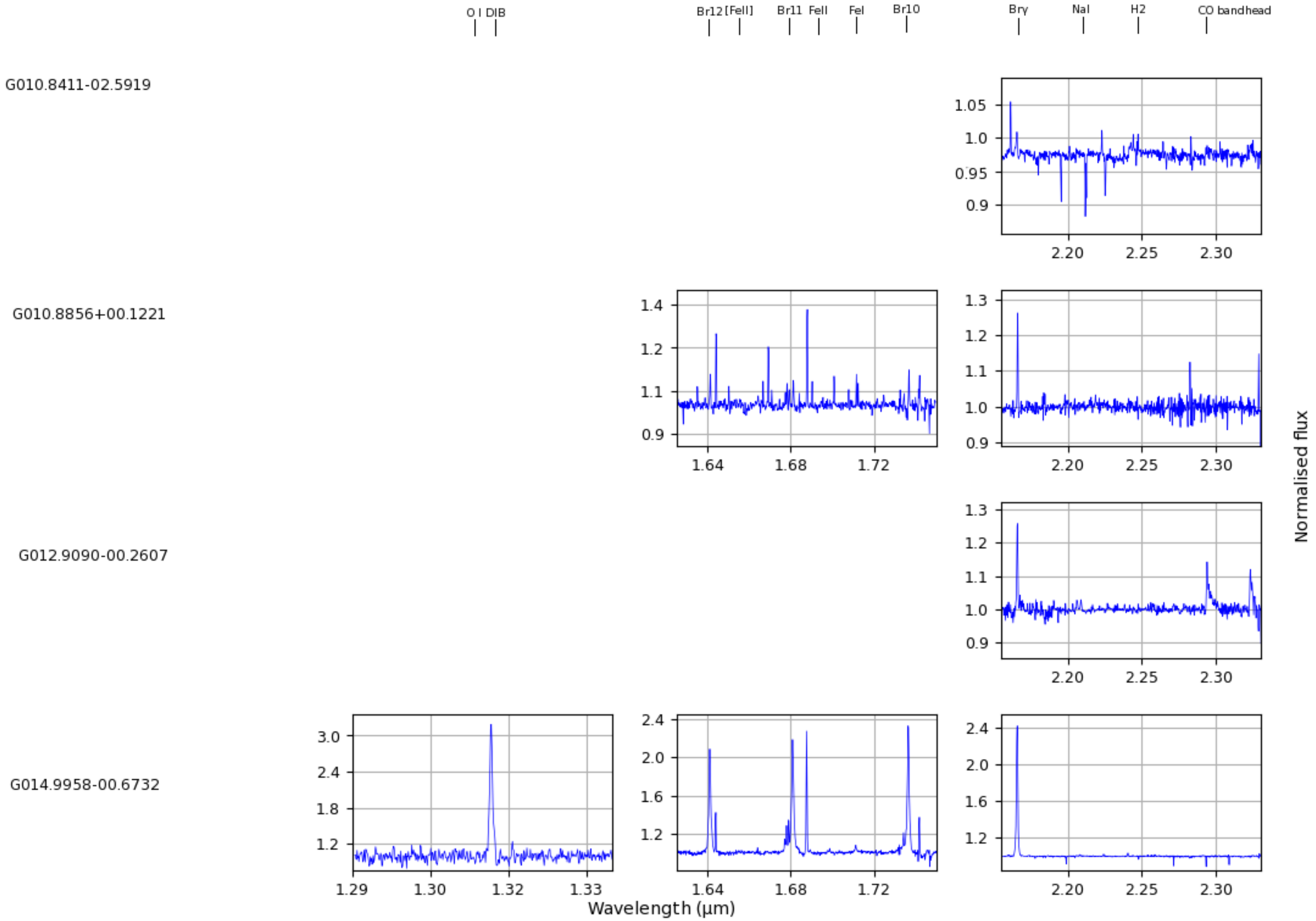

Figure D.1: Continuum normalised spectra, with left to right panels showing X, J, H and K bands

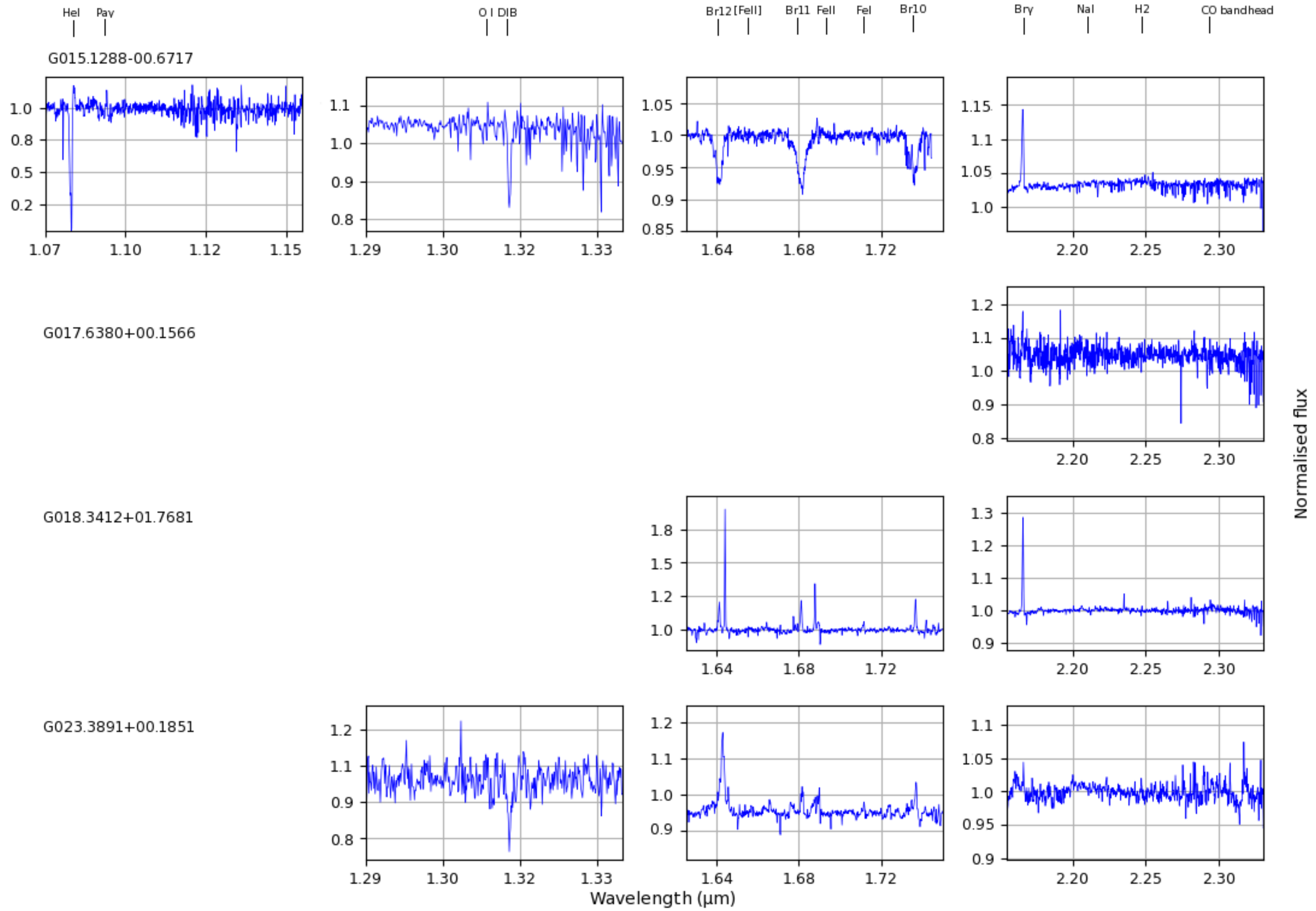

Figure D.2: Continuum normalised spectra, with left to right panels showing X, J, H and K bands

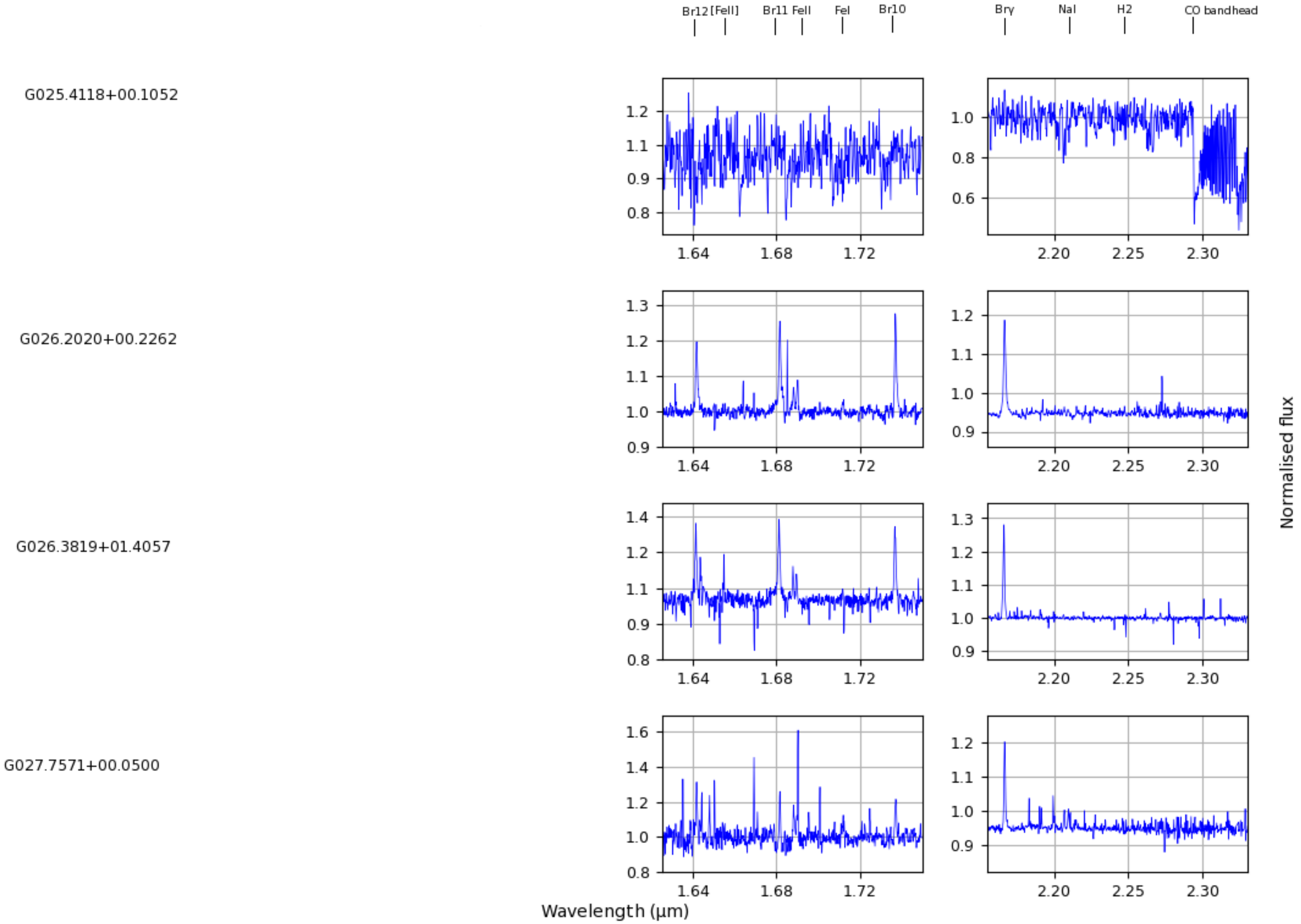

Figure D.3: Continuum normalised spectra, with left to right panels showing X, J, H and K bands

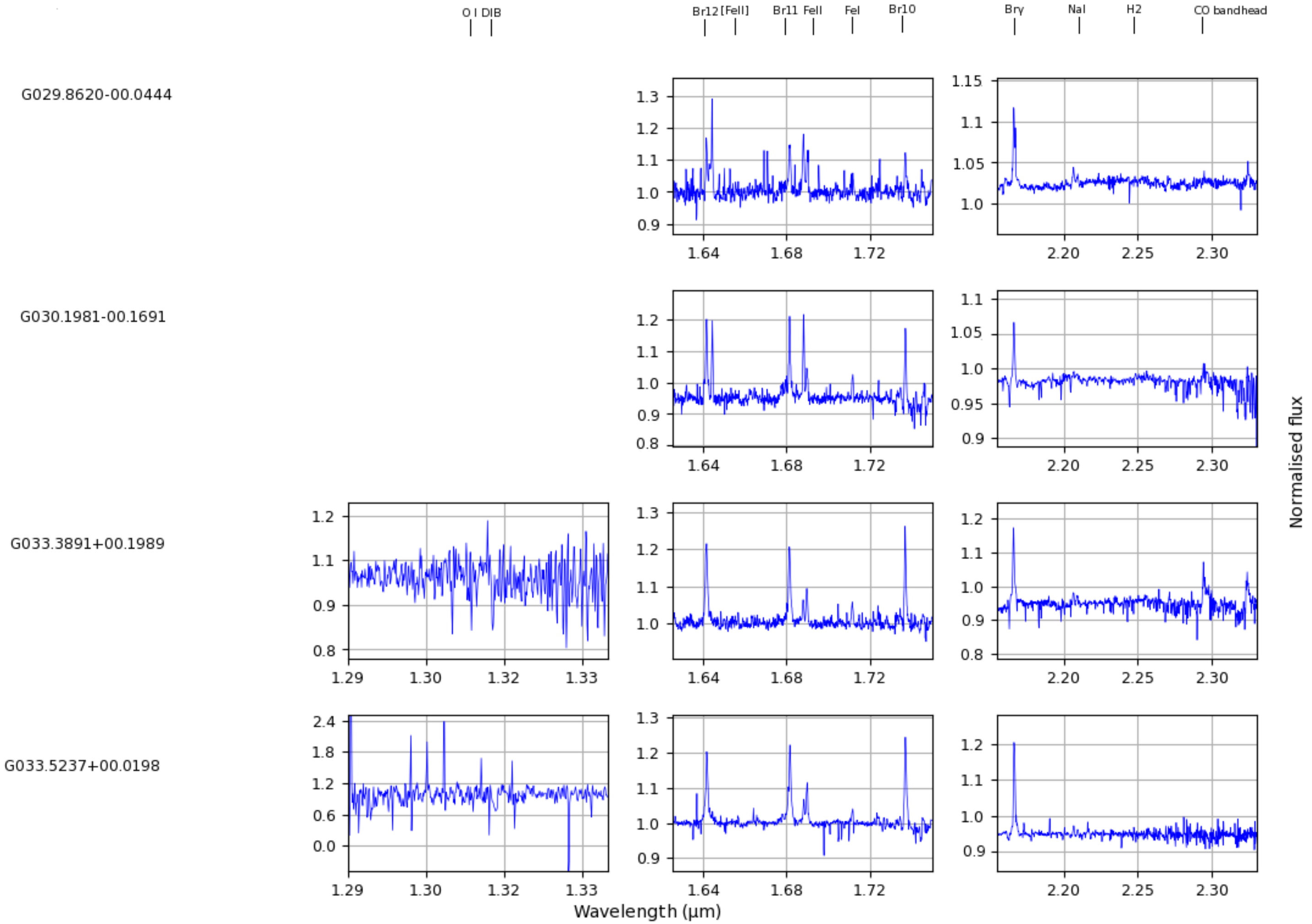

Figure D.4: Continuum normalised spectra, with left to right panels showing X, J, H and K bands

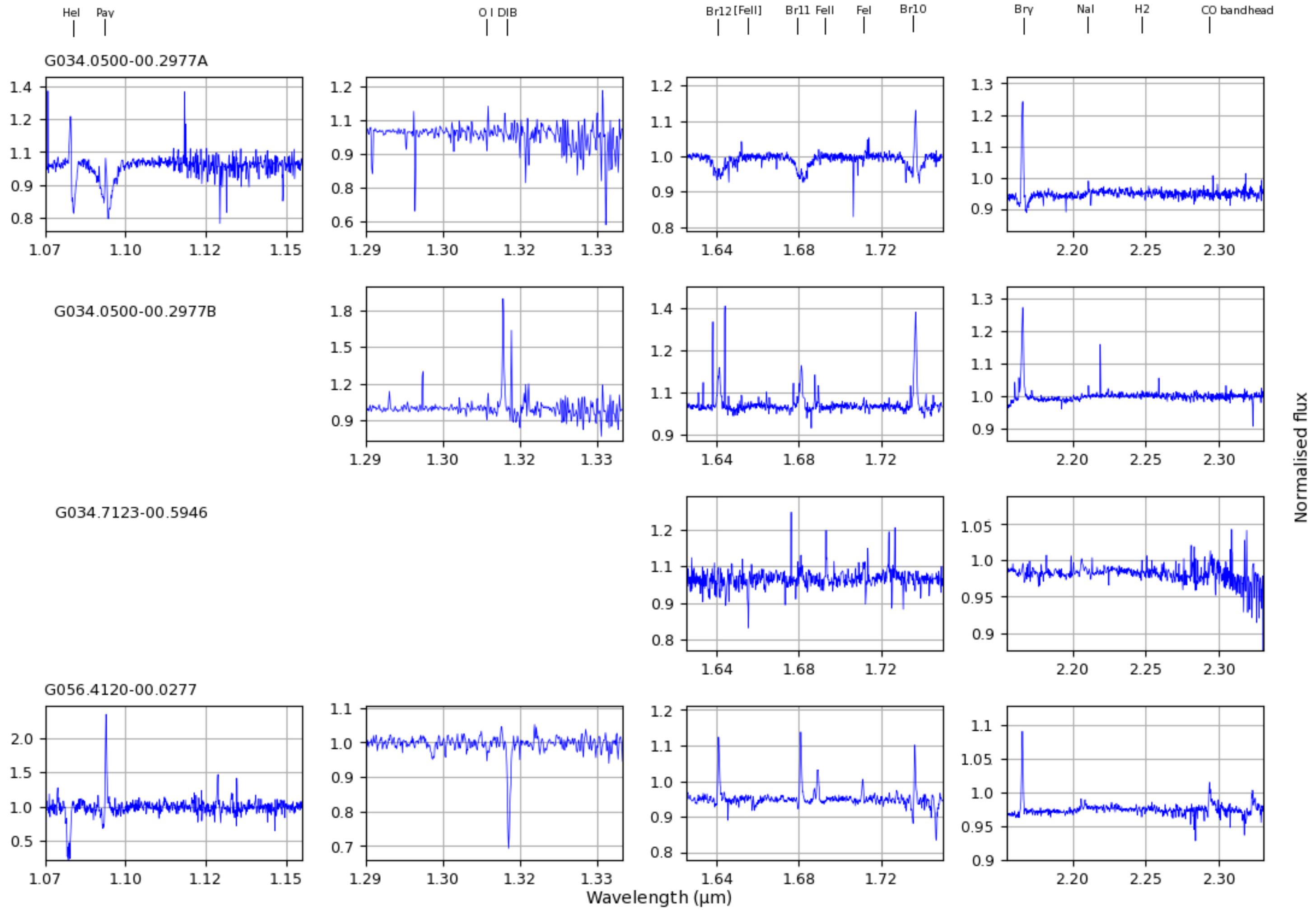

Figure D.5: Continuum normalised spectra, with left to right panels showing X, J, H and K bands

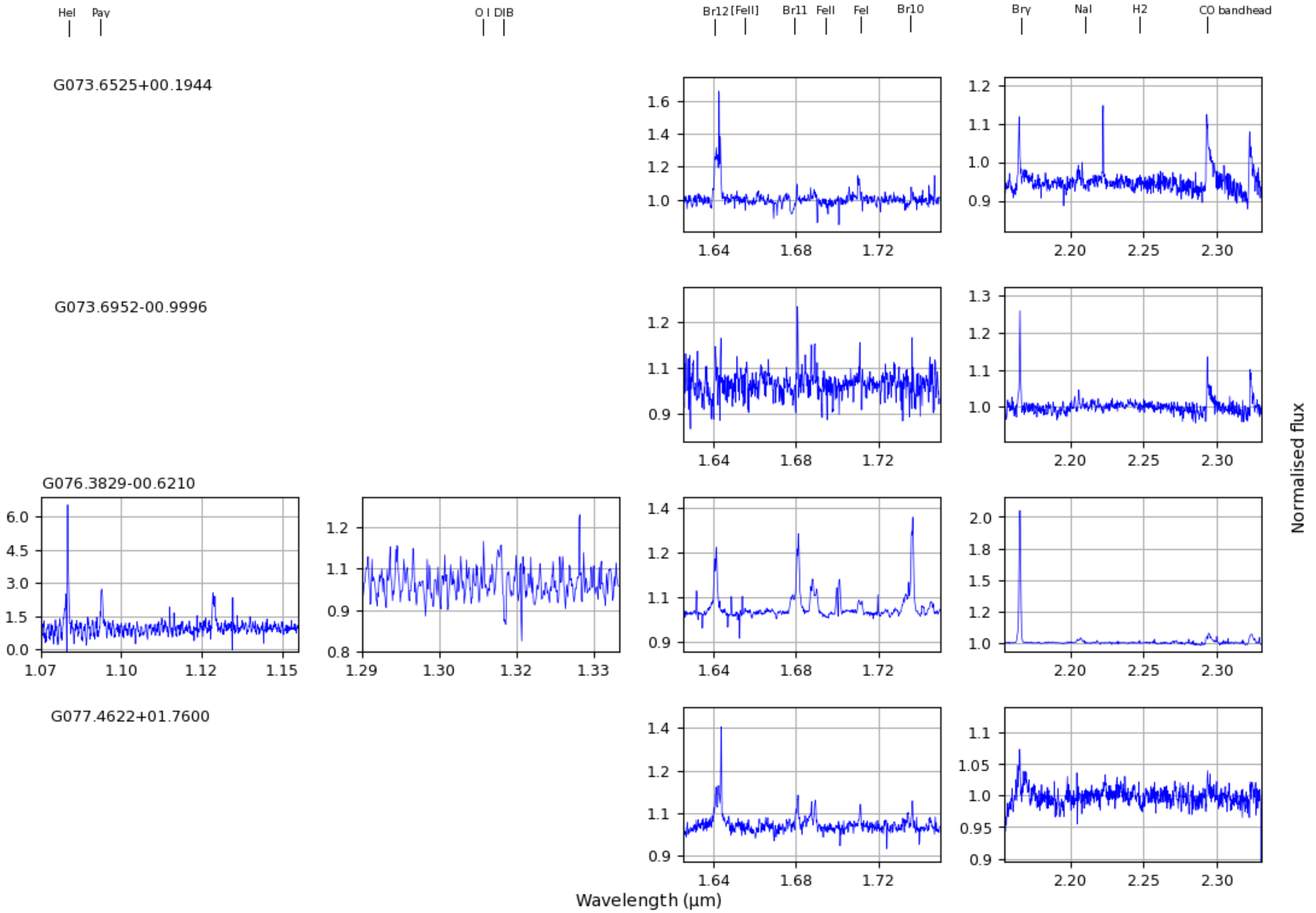

Figure D.6: Continuum normalised spectra, with left to right panels showing X,J,H and K bands

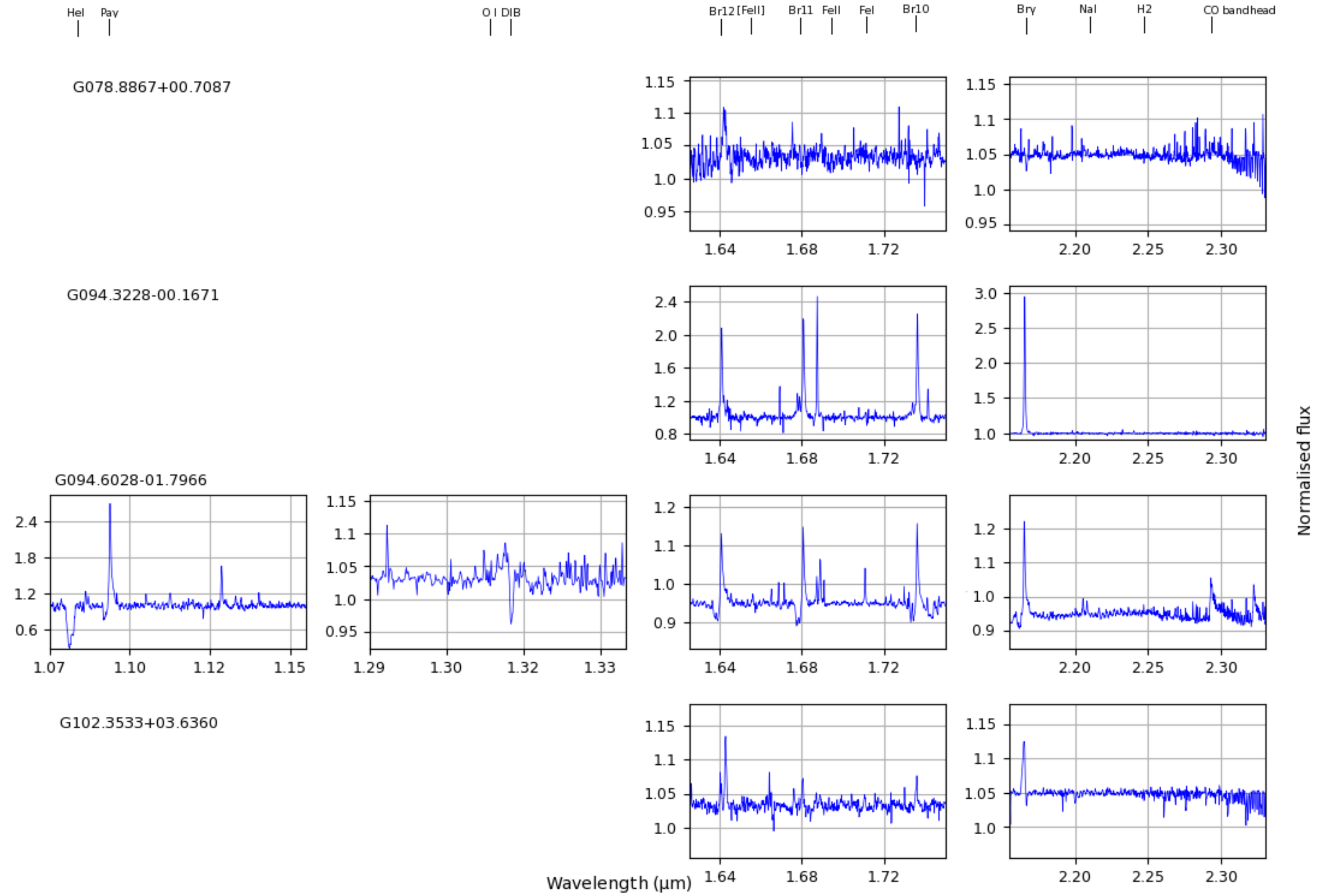

Figure D.7: Continuum normalised spectra, with left to right panels showing X, J, H and K bands

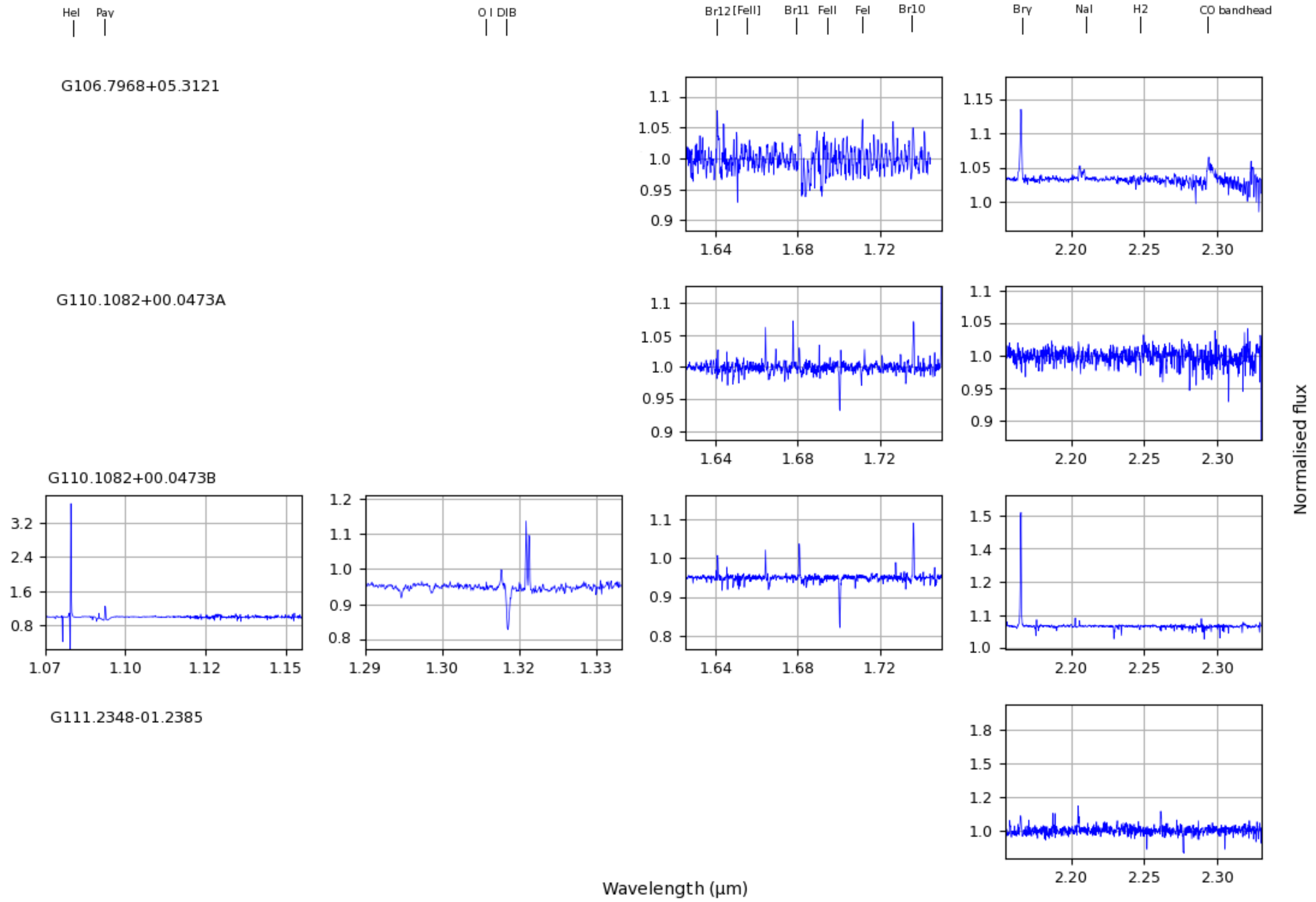

Figure D.8: Continuum normalised spectra, with left to right panels showing X,J,H and K bands

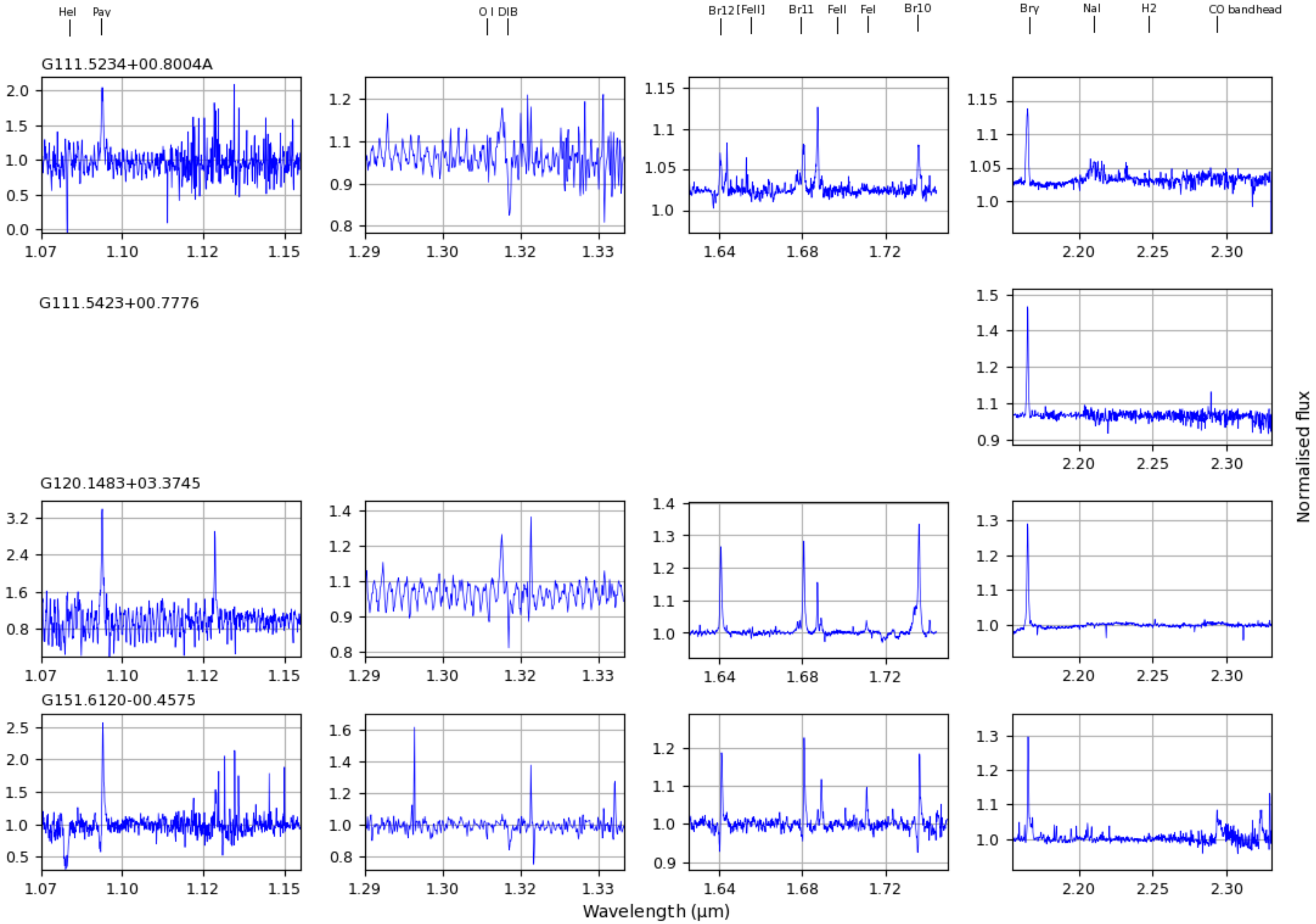

Figure D.9: Continuum normalised spectra, with left to right panels showing X, J, H and K bands

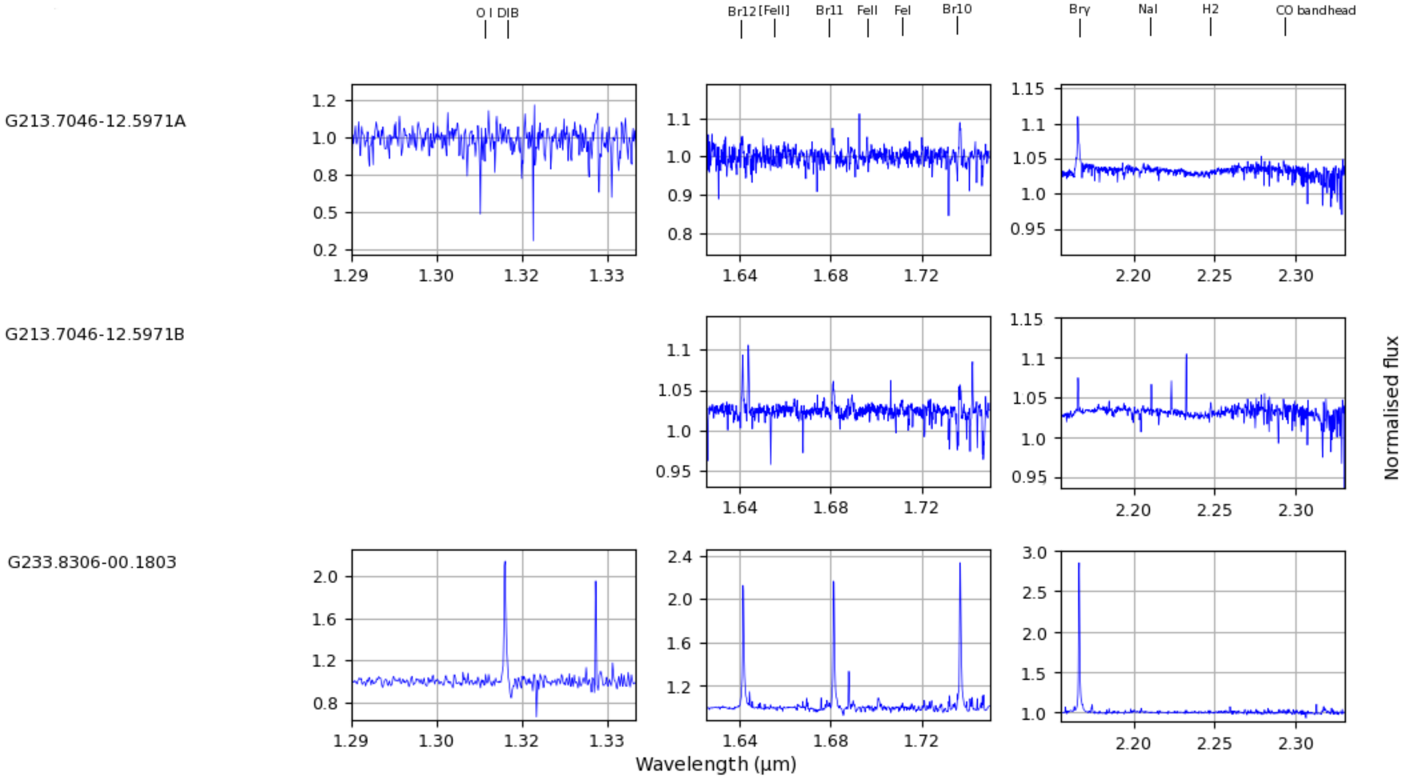

Figure D.10: Continuum normalised spectra, with left to right panels showing X, J, H and K bands

Appendix E

NaCo images

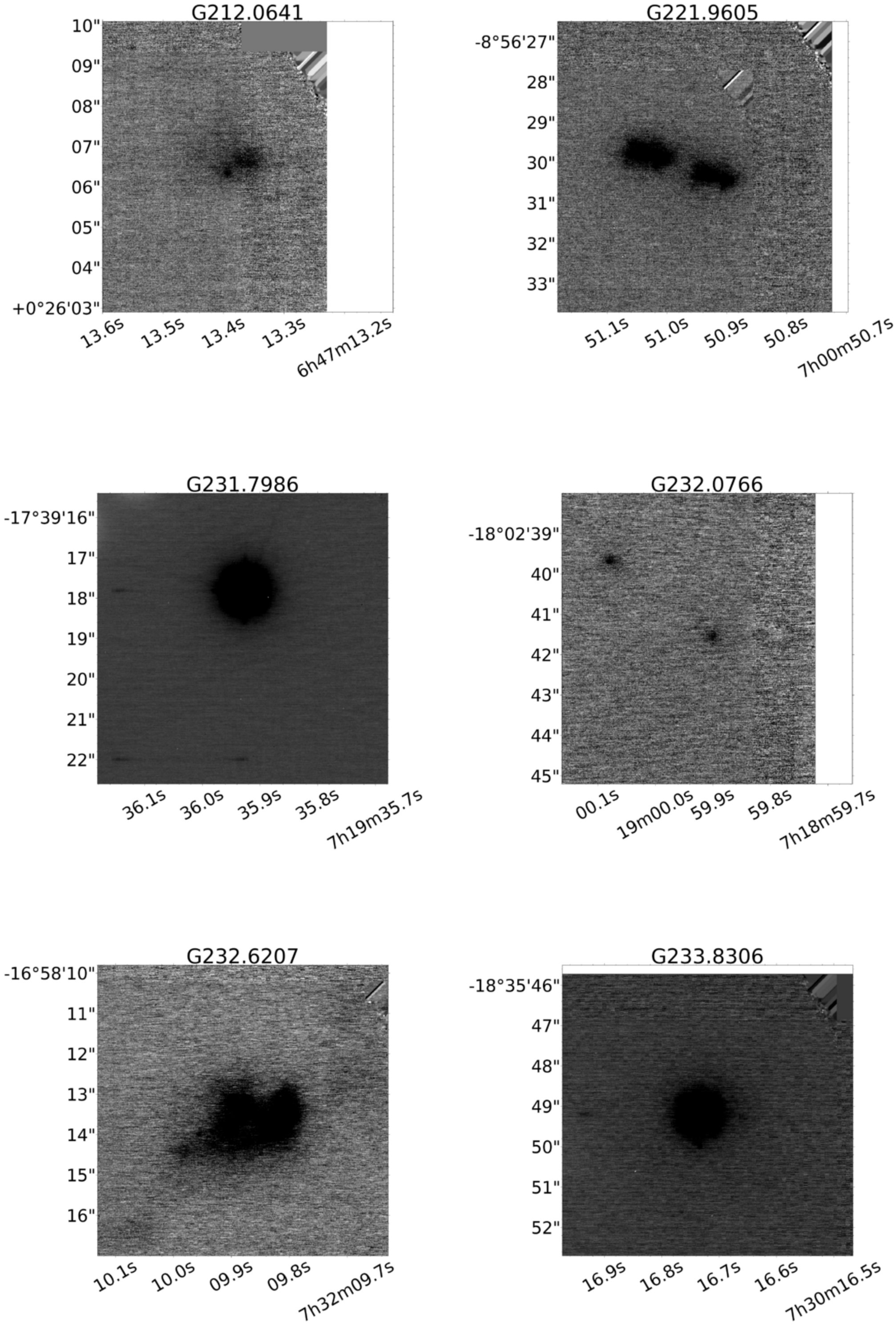

Figure E.1: 3 arcseconds reduced NaCo *K* band image. RA is on the x-axis and Declination on the y axis. North is up and East is right.

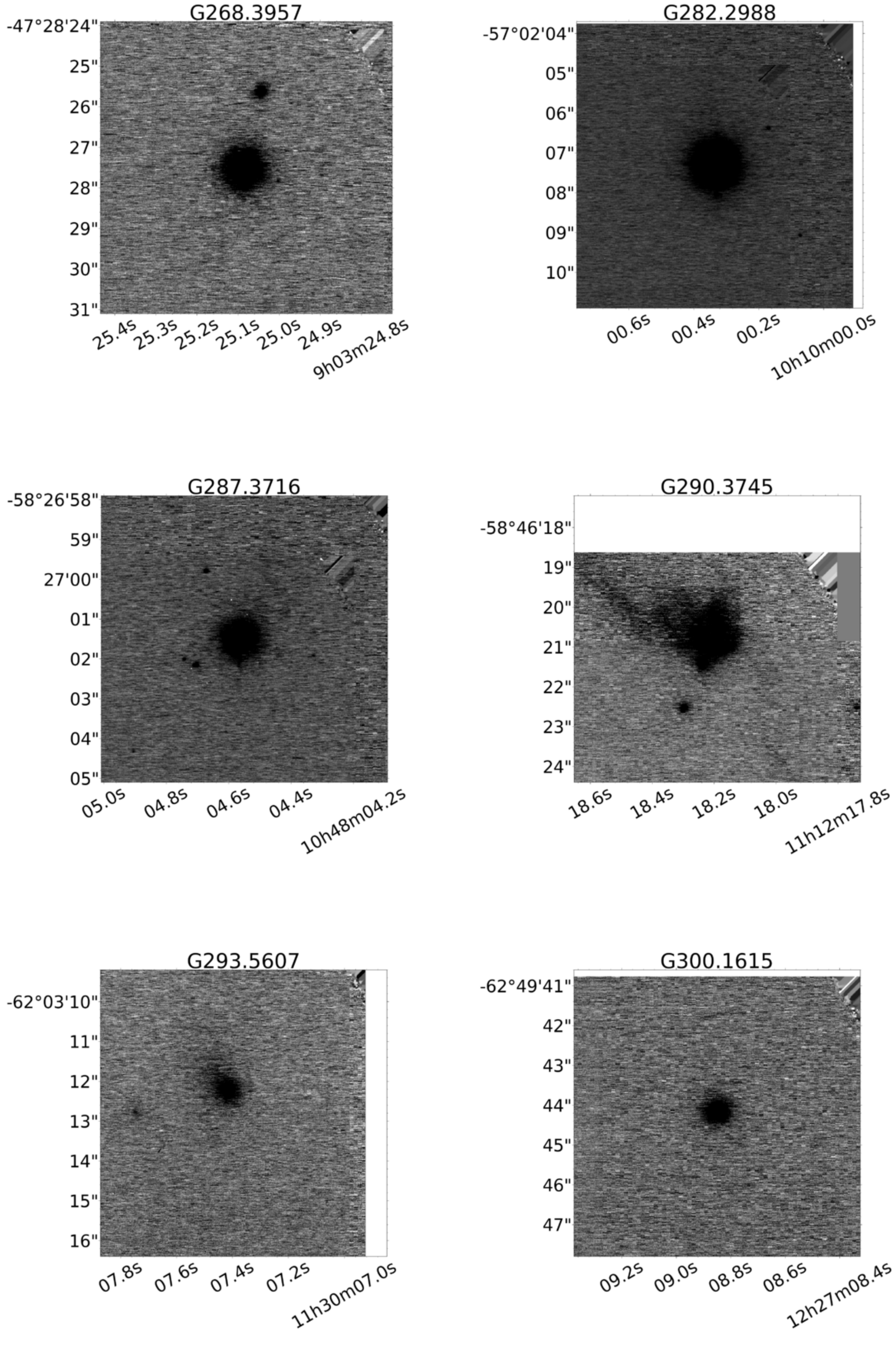

Figure E.2: 3 arcseconds reduced NaCo *K* band image. RA is on the x-axis and Declination on the y axis. North is up and East is right.

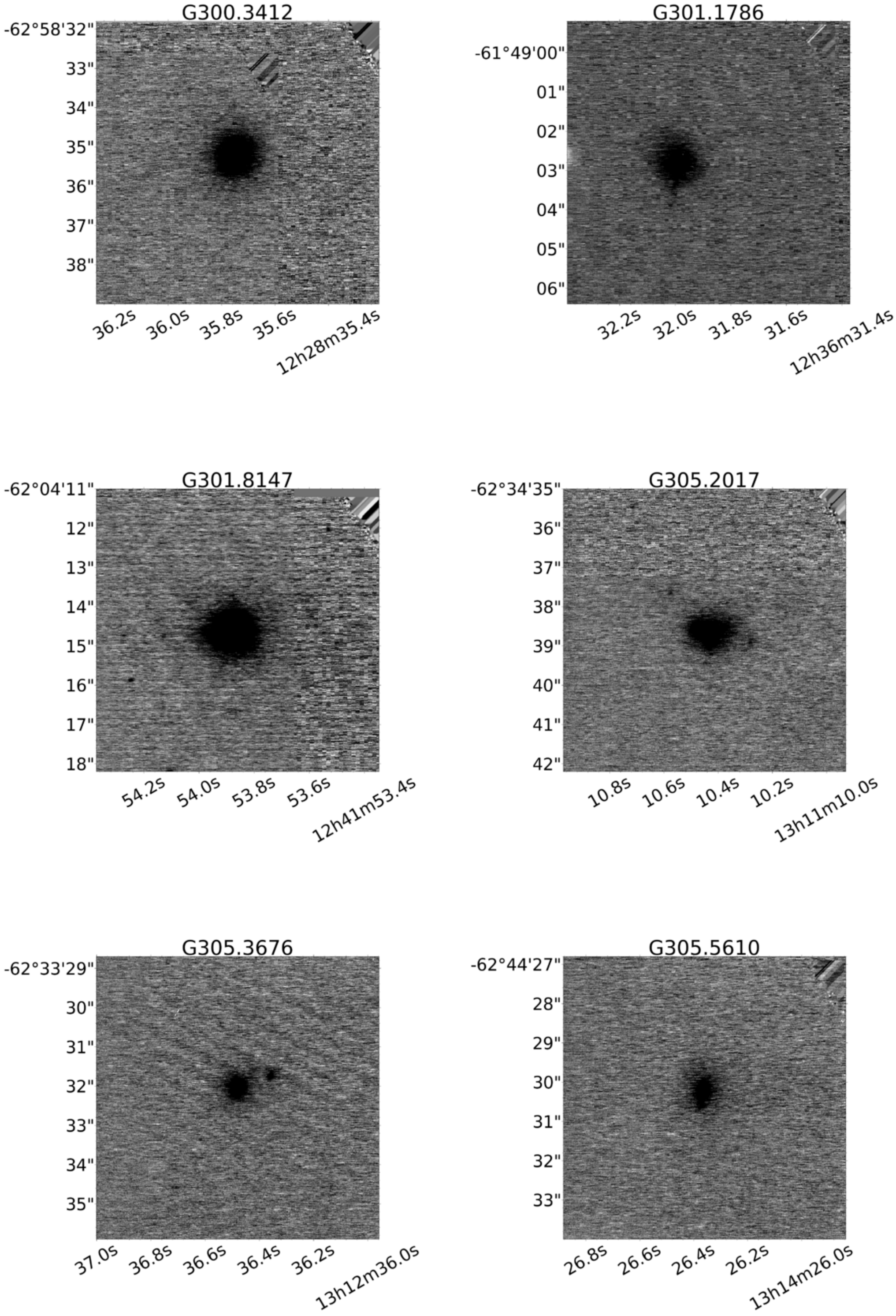

Figure E.3: 3 arcseconds reduced NaCo K band image. RA is on the x-axis and Declination on the y axis. North is up and East is right.

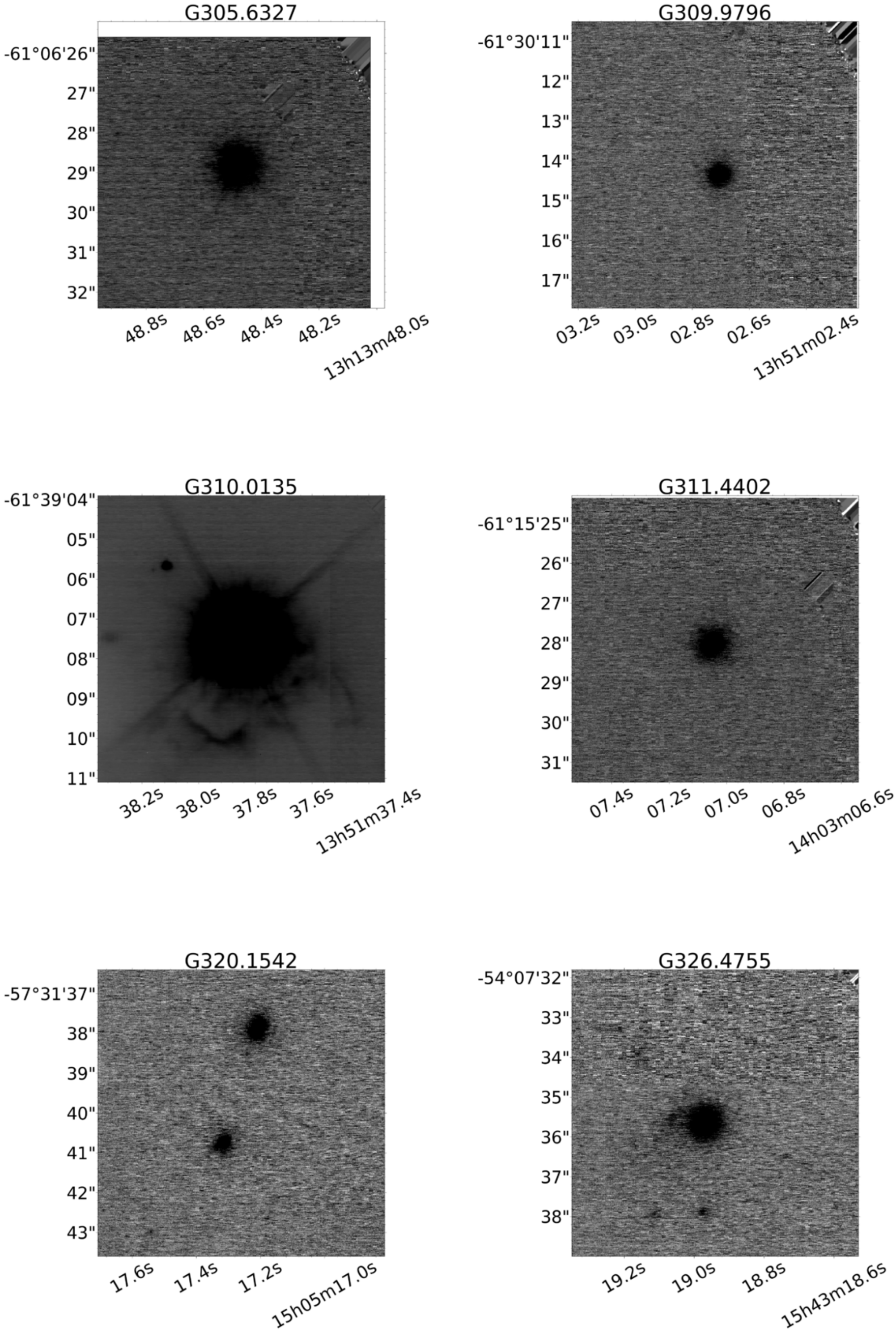

Figure E.4: 3 arcseconds reduced NaCo *K* band image. RA is on the x-axis and Declination on the y axis. North is up and East is right.

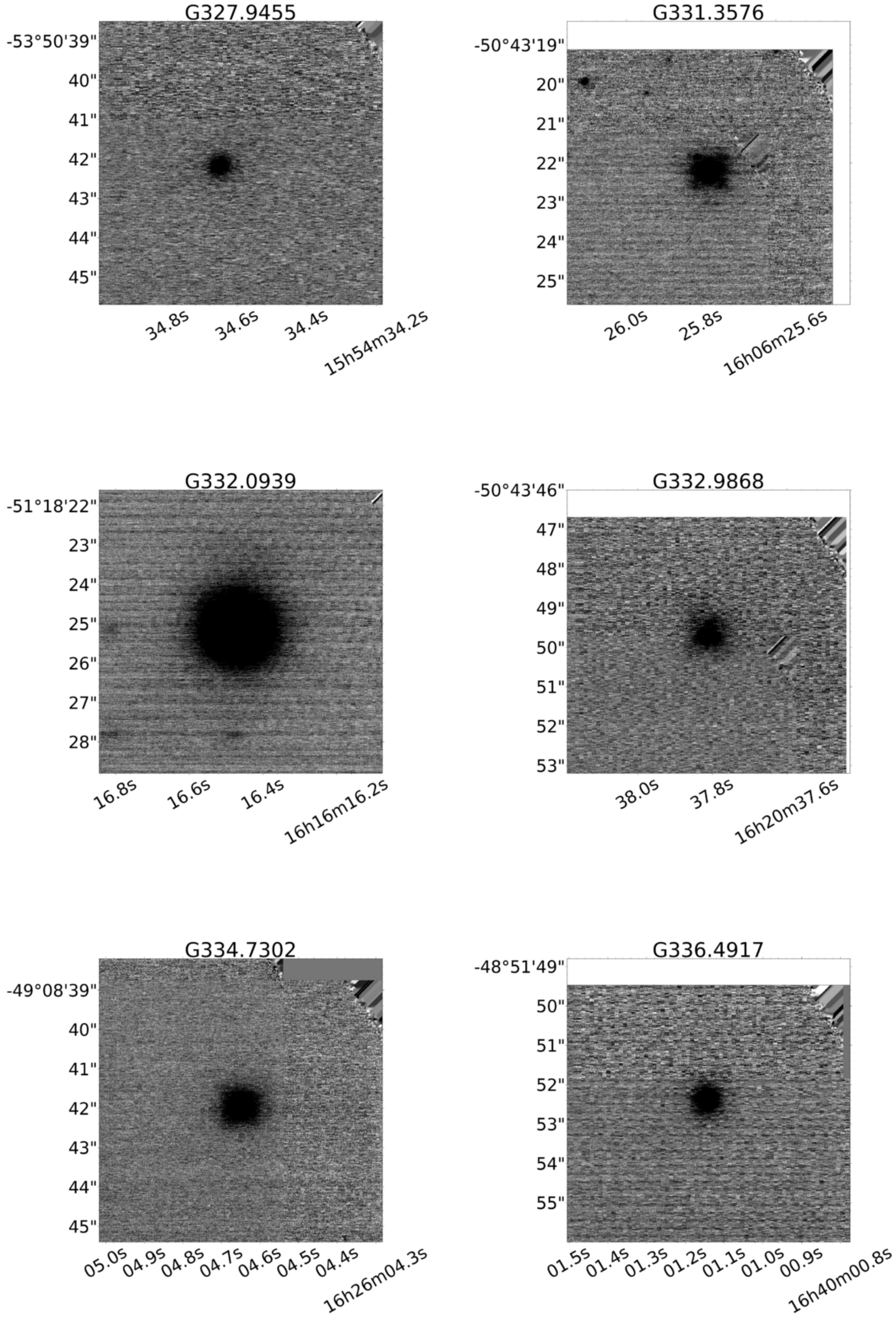

Figure E.5: 3 arcseconds reduced NaCo *K* band image. RA is on the x-axis and Declination on the y axis. North is up and East is right.

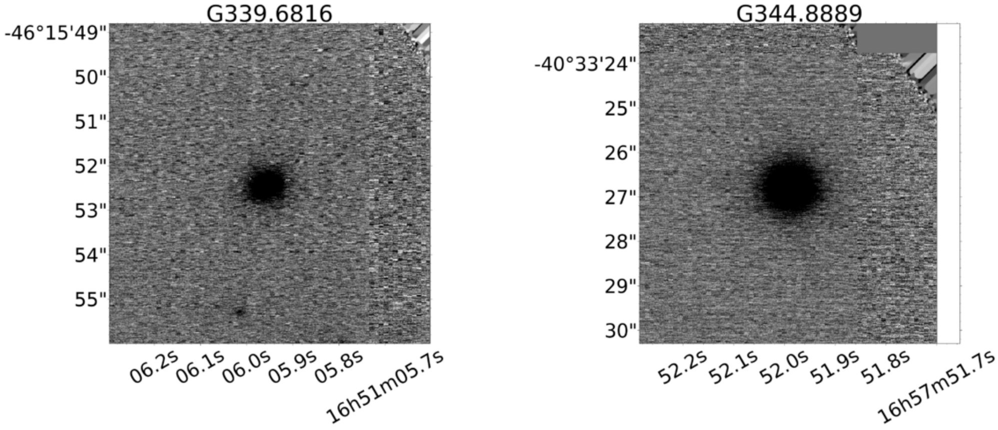

Figure E.6: 3 arcseconds reduced NaCo K band image. RA is on the x-axis and Declination on the y axis. North is up and East is right.

References

Ababakr, K.M., Oudmaijer, R.D. & Vink, J.S. (2017). A statistical spectropolarimetric study of Herbig Ae/Be stars. *Monthly Notices fo the Royal Astronomical Society*, **472**, 854–868. 8, 99

Alecian, E., Wade, G.A., Catala, C., Grunhut, J.H., Landstreet, J.D., Bagnulo, S., Böhm, T., Folsom, C.P., Marsden, S. & Waite, I. (2013). A high-resolution spectropolarimetric survey of Herbig Ae/Be stars - I. Observations and measurements. *Monthly Notices fo the Royal Astronomical Society*, **429**, 1001–1026. 8

André, P. (2017). Interstellar filaments and star formation. *Comptes Rendus Geoscience*, **349**, 187 – 197. 14

André, P., Men'shchikov, A., Bontemps, S., Könyves, V., Motte, F., Schneider, N., Didelon, P., Minier, V., Saraceno, P., Ward-Thompson, D., di Francesco, J., White, G., Molinari, S., Testi, L., Abergel, A., Griffin, M., Henning, T., Royer, P., Merín, B., Vavrek, R., Attard, M., Arzoumanian, D., Wilson, C.D., Ade, P., Aussel, H., Baluteau, J.P., Benedettini, M., Bernard, J.P., Blommaert, J.A.D.L., Cambrésy, L., Cox, P., di Giorgio, A., Hargrave, P., Hennemann, M., Huang, M., Kirk, J., Krause, O., Launhardt, R., Leeks, S., Le Pennec, J., Li, J.Z., Martin, P.G., Maury, A., Olofsson, G., Omont, A., Peretto, N., Pezzuto, S., Prusti, T., Roussel, H., Russeil, D., Sauvage, M., Sibthorpe, B., Sicilia-Aguilar, A., Spinoglio, L., Waelkens, C., Woodcraft, A. & Zavagno, A. (2010a). From filamentary clouds to prestellar cores to the stellar IMF: Initial highlights from the Herschel Gould Belt Survey. *Astronomy & Astrophysics*, **518**, L102. 9

André, P., Men'shchikov, A., Bontemps, S., Könyves, V., Motte, F., Schneider, N., Didelon, P., Minier, V., Saraceno, P., Ward-Thompson, D., di Francesco, J., White, G., Molinari, S., Testi, L., Abergel, A., Griffin, M., Henning, T., Royer, P., Merín, B., Vavrek, R., Attard, M., Arzoumanian, D., Wilson, C.D., Ade, P., Aussel, H., Baluteau, J.P., Benedettini, M., Bernard, J.P., Blommaert, J.A.D.L., Cambrésy, L., Cox, P., di Giorgio, A., Hargrave, P., Hennemann, M., Huang, M., Kirk, J., Krause, O., Launhardt, R., Leeks, S., Le Pennec, J., Li, J.Z., Martin, P.G., Maury, A., Olofsson, G., Omont, A., Peretto, N., Pezzuto, S., Prusti, T., Roussel, H., Russeil, D., Sauvage, M., Sibthorpe, B., Sicilia-Aguilar, A., Spinoglio, L., Waelkens, C., Woodcraft, A. & Zavagno, A. (2010b). From filamentary clouds to prestellar cores to the stellar IMF: Initial highlights from the Herschel Gould Belt Survey. *Astronomy & Astrophysics*, **518**, L102. 14

André, P., Di Francesco, J., Ward-Thompson, D., Inutsuka, S.I., Pudritz, R.E. & Pineda, J.E. (2014). From Filamentary Networks to Dense Cores in Molecular Clouds: Toward a New Paradigm for Star Formation. *Protostars and Planets VI*, 27–51. 14

Anglada, G. (1995). Centimeter Continuum Emission from Outflow Sources. In S. Lizano & J.M. Torrelles, eds., *Revista Mexicana de Astronomia y Astrofisica Conference Series*, vol. 1 of *Revista Mexicana de Astronomia y Astrofisica Conference Series*, 67. 149, 153

Appenzeller, I. & Mundt, R. (1989). T Tauri stars. *Astronomy & Astrophysics Review*, **1**, 291–334. 4

Arzoumanian, D., André, P., Didelon, P., Könyves, V., Schneider, N., Men'shchikov, A., Sousbie, T., Zavagno, A., Bontemps, S., di Francesco, J., Griffin, M., Hennemann, M., Hill, T., Kirk, J., Martin, P., Minier, V., Molinari, S., Motte, F., Peretto, N., Pezzuto, S., Spinoglio, L., Ward-Thompson, D., White, G. & Wilson, C.D. (2011). Characterizing interstellar filaments with Herschel in IC 5146. *Astronomy & Astrophysics*, **529**, L6. 14

Astropy Collaboration, Robitaille, T.P., Tollerud, E.J., Greenfield, P., Droettboom, M., Bray, E., Aldcroft, T., Davis, M., Ginsburg, A., Price-Whelan, A.M., Kerzendorf, W.E., Conley, A., Crighton, N., Barbary, K., Muna, D., Ferguson, H., Grollier, F., Parikh, M.M., Nair, P.H., Unther, H.M., Deil, C., Woillez, J., Conseil, S., Kramer, R., Turner, J.E.H., Singer, L., Fox, R., Weaver, B.A., Zabalza, V., Edwards, Z.I., Azalee Bostroem, K., Burke, D.J., Casey, A.R., Crawford, S.M., Dencheva, N., Ely, J., Jenness, T., Labrie, K., Lim, P.L., Pierfederici, F., Pontzen, A., Ptak, A., Refsdal, B., Servillat, M. & Streicher, O. (2013). Astropy: A community Python package for astronomy. *Astronomy and Astrophysics*, **558**, A33. 174

Audard, M., Ábrahám, P., Dunham, M.M., Green, J.D., Grosso, N., Hamaguchi, K., Kastner, J.H., Kóspál, Á., Lodato, G., Romanova, M.M., Skinner, S.L., Vorobyov, E.I. & Zhu, Z. (2014). Episodic Accretion in Young Stars. *Protostars and Planets VI*, 387–410. 30

Baines, D., Oudmaijer, R.D., Porter, J.M. & Pozzo, M. (2006). On the binarity of Herbig Ae/Be stars. *Monthly Notices fo the Royal Astronomical Society*, **367**, 737–753. 25, 163

Baker, J.G. & Menzel, D.H. (1938). Physical Processes in Gaseous Nebulae. III. The Balmer Decrement. *The Astrophysical Journal*, **88**, 52. 26

Baldwin, J.A., Ferland, G.J., Korista, K.T., Hamann, F. & LaCluyzé, A. (2004). The Origin of Fe II Emission in Active Galactic Nuclei. *The Astrophysical Journal*, **615**, 610–624. 29

Bate, M.R., Bonnell, I.A. & Bromm, V. (2002). The formation of close binary systems by dynamical interactions and orbital decay. *Monthly Notices fo the Royal Astronomical Society*, **336**, 705–713. 163

Beltrán, M.T. & de Wit, W.J. (2016). Accretion disks in luminous young stellar objects. *A&ARv*, **24**, 6. 78, 132

Bertin, E. & Arnouts, S. (1996). SExtractor: Software for source extraction. *Astronomy and Astrophysics*, **117**, 393–404. 171

Bertout, C., Basri, G. & Bouvier, J. (1988). Accretion disks around T Tauri stars. *The Astrophysical Journal*, **330**, 350–373. 6

Beuther, H., Schilke, P., Menten, K.M., Motte, F., Sridharan, T.K. & Wyrowski, F. (2002). High-Mass Protostellar Candidates. II. Density Structure from Dust Continuum and CS Emission. *The Astrophysical Journal*, **566**, 945–965. 16

Bik, A., Kaper, L. & Waters, L.B.F.M. (2006). VLT K-band spectroscopy of massive young stellar objects in (ultra-)compact HII regions. *Astronomy & Astrophysics*, **455**, 561–576. 28, 99

Blitz, L. (1993). Giant molecular clouds. In E.H. Levy & J.I. Lunine, eds., *Protostars and Planets III*, 125–161. 14

Blitz, L. & Shu, F.H. (1980). The origin and lifetime of giant molecular cloud complexes. *The Astrophysical Journal*, **238**, 148–157. 14

Blondel, P.F.C. & Djie, H.R.E.T.A. (2006). Modeling of PMS Ae/Fe stars using UV spectra. *A&A*, **456**, 1045–1068. 99

Blum, R.D., Barbosa, C.L., Damineli, A., Conti, P.S. & Ridgway, S. (2004). Accretion Signatures from Massive Young Stellar Objects. *The Astrophysical Journal*, **617**, 1167–1176. 28, 99

Bonnell, I.A. (2005). The Formation of Massive Binary Stars. *ArXiv Astrophysics e-prints*. 162

Bonnell, I.A. & Bate, M.R. (2006). Star formation through gravitational collapse and competitive accretion. *Monthly Notices of the Royal Astronomical Society*, **370**, 488–494. 2, 11, 12, 162

Bonnell, I.A., Bate, M.R. & Zinnecker, H. (1998). On the formation of massive stars. *Monthly Notices of the Royal Astronomical Society*, **298**, 93–102. 11

Borissova, J., Ramírez Alegría, S., Alonso, J., Lucas, P.W., Kurtev, R., Medina, N., Navarro, C., Kuhn, M., Gromadzki, M., Retamales, G., Fernandez, M.A., Agurto-Gangas, C., Chené, A.N., Minniti, D., Contreras Pena, C., Catelan, M., Decany, I., Thompson, M.A., Morales, E.F.E. & Amigo, P. (2016). Young Stellar Clusters Containing Massive Young Stellar Objects in the VVV Survey. *The Astronomical Journal*, **152**, 74. 32

Braithwaite, J. & Spruit, H.C. (2017). Magnetic fields in non-convective regions of stars. *Royal Society Open Science*, **4**, 160271. 8

Brand, J. & Blitz, L. (1993). The Velocity Field of the Outer Galaxy. *Astronomy & Astrophysics*, **275**, 67. 19, 29

Bunn, J.C., Hoare, M.G. & Drew, J.E. (1995). Observations of the IR recombination line emission from massive young stellar objects. *Monthly Notices of the Royal Astronomical Society*, **272**, 346–354. 16, 27, 35, 143, 146, 202

Burton, M.G., Lazendic, J.S., Yusef-Zadeh, F. & Wardle, M. (2004). The Eye of the Tornado - an isolated, high-mass young stellar object near the Galactic Centre. *Monthly Notices fo the Royal Astronomical Society*, **348**, 638–646. 149

Calvet, N. & Gullbring, E. (1998). The Structure and Emission of the Accretion Shock in T Tauri Stars. *The Astrophysical Journal*, **509**, 802–818. 6

Calvet, N., Muzerolle, J., Briceño, C., Hernández, J., Hartmann, L., Saucedo, J.L. & Gordon, K.D. (2004). The Mass Accretion Rates of Intermediate-Mass T Tauri Stars. *The Astronomical Journal*, **128**, 1294–1318. 7

Campbell, B., Persson, S.E. & Matthews, K. (1989). Identification of new young stellar objects associated with IRAS point sources. III - The northern Galactic plane. *The Astronomical Journal*, **98**, 643–658. 16

Caratti o Garatti, A., Stecklum, B., Linz, H., Garcia Lopez, R. & Sanna, A. (2015). A near-infrared spectroscopic survey of massive jets towards extended green objects. *Astronomy & Astrophysics*, **573**, A82. 25, 163

Caratti o Garatti, A., Stecklum, B., Garcia Lopez, R., Eislöffel, J., Ray, T.P., Sanna, A., Cesaroni, R., Walmsley, C.M., Oudmaijer, R.D., de Wit, W.J., Moscadelli, L., Greiner, J., Krabbe, A., Fischer, C., Klein, R. & Ibañez, J.M. (2017). Disk-mediated accretion burst in a high-mass young stellar object. *Nature Physics*, **13**, 276–279. 32, 58, 67

Carr, J.S. (1989). Near-infrared CO emission in young stellar objects. *The Astrophysical Journal*, **345**, 522–535. 30

Cauley, P.W. & Johns-Krull, C.M. (2015). Optical Mass Flow Diagnostics in Herbig Ae/Be Stars. *The Astrophysical Journal*, **810**, 5. 137, 138

Cesaroni, R. (2005). Hot molecular cores. In R. Cesaroni, M. Felli, E. Churchwell & M. Walmsley, eds., *Massive Star Birth: A Crossroads of Astrophysics*, vol. 227 of *IAU Symposium*, 59–69. 15

Cesaroni, R., Moscadelli, L., Neri, R., Sanna, A., Garatti, A.C.o., Eisloeffel, J., Stecklum, B., Ray, T. & Walmsley, C.M. (2018). Radio outburst from a massive (proto)star. When accretion turns into ejection. *ArXiv e-prints*. 32

Chandler, C.J., Carlstrom, J.E. & Scoville, N.Z. (1995). Infrared CO Emission from Young Stars: Accretion Disks and Neutral Winds. *The Astrophysical Journal*, **446**, 793. 28, 54

Chini, R., Hoffmeister, V.H., Nasseri, A., Stahl, O. & Zinnecker, H. (2012). A spectroscopic survey on the multiplicity of high-mass stars. *Monthly Notices fo the Royal Astronomical Society*, **424**, 1925–1929. 162

Churchwell, E., Povich, M.S., Allen, D., Taylor, M.G., Meade, M.R., Babler, B.L., Indebetouw, R., Watson, C., Whitney, B.A., Wolfire, M.G., Bania, T.M., Benjamin, R.A., Clemens, D.P., Cohen, M., Cyganowski, C.J., Jackson, J.M., Kobulnicky, H.A., Mathis, J.S., Mercer, E.P., Stolovy, S.R., Uzpen, B., Watson, D.F. & Wolff, M.J. (2006). The Bubbling Galactic Disk. *The Astrophysical Journal*, **649**, 759–778. 17

Churchwell, E., Watson, D.F., Povich, M.S., Taylor, M.G., Babler, B.L., Meade, M.R., Benjamin, R.A., Indebetouw, R. & Whitney, B.A. (2007). The Bubbling Galactic Disk. II. The Inner 20deg. *The Astrophysical Journal*, **670**, 428–441. 17

Churchwell, E., Babler, B.L., Meade, M.R., Whitney, B.A., Benjamin, R., Indebetouw, R., Cyganowski, C., Robitaille, T.P., Povich, M., Watson, C. & Bracker, S. (2009). The Spitzer GLIMPSE Surveys: A New View of the Milky Way. *Physics*, **121**, 213–230. 19

Close, L.M., Follette, K.B., Males, J.R., Puglisi, A., Xompero, M., Apai, D., Najita, J., Weinberger, A.J., Morzinski, K., Rodigas, T.J., Hinz, P., Bailey, V. & Briguglio, R. (2014). Discovery of Hα Emission from the Close Companion inside the Gap of Transitional Disk HD 142527. *apjl*, **781**, L30. 8

Connelley, M.S. & Greene, T.P. (2010). A Near-infrared Spectroscopic Survey of Class I Protostars. *The Astronomical Journal*, **140**, 1214–1240. 71, 75

Connelley, M.S. & Greene, T.P. (2014). Near-IR Spectroscopic Monitoring of Class I Protostars: Variability of Accretion and Wind Indicators. *The Astronomical Journal*, **147**, 125. 31

Connelley, M.S., Reipurth, B. & Tokunaga, A.T. (2008a). The Evolution of the Multiplicity of Embedded Protostars. I. Sample Properties and Binary Detections. *The Astronomical Journal*, **135**, 2496–2525. 25

Connelley, M.S., Reipurth, B. & Tokunaga, A.T. (2008b). The Evolution of the Multiplicity of Embedded Protostars. II. Binary Separation Distribution and Analysis. *The Astronomical Journal*, **135**, 2526–2536. 25, 186, 190

Contreras Peña, C., Lucas, P.W., Froebrich, D., Kumar, M.S.N., Goldstein, J., Drew, J.E., Adamson, A., Davis, C.J., Barentsen, G. & Wright, N.J. (2014). Extreme infrared variables from UKIDSS - I. A concentration in star-forming regions. *Monthly Notices fo the Royal Astronomical Society*, **439**, 1829–1854. 31

Cooper, H.D.B. (2013). *Observational Studies of Regions of Massive Star Formation*. Ph.D. thesis, University of Leeds, England. iii, iv, v, 16, 34, 35, 160, 200, 201, 202, 205, 207

Cooper, H.D.B., Lumsden, S.L., Oudmaijer, R.D., Hoare, M.G., Clarke, A.J., Urquhart, J.S., Mottram, J.C., Moore, T.J.T. & Davies, B. (2013). The RMS survey: near-IR spectroscopy of massive young stellar objects. *Monthly Notices of the Royal Astronomical Society*, **430**, 1125–1157. v, 16, 20, 28, 29, 30, 35

Correia, S., Zinnecker, H., Ratzka, T. & Sterzik, M.F. (2006). A VLT/NACO survey for triple and quadruple systems among visual pre-main sequence binaries. *Astronomy and Astrophysics*, **459**, 909–926. 175

COX, N.L.J., CAMI, J., KAPER, L., EHRENFREUND, P., FOING, B.H., OCHSENDORF, B.B., VAN HOOFF, S.H.M. & SALAMA, F. (2014). VLT/X-Shooter survey of near-infrared diffuse interstellar bands. *A&A*, **569**, A117. 123, 125

CROWTHER, P.A., CABALLERO-NIEVES, S.M., BOSTROEM, K.A., MAÍZ APELLÁNIZ, J., SCHNEIDER, F.R.N., WALBORN, N.R., ANGUS, C.R., BROTT, I., BONANOS, A., DE KOTER, A., DE MINK, S.E., EVANS, C.J., GRÄFENER, G., HERRERO, A., HOWARTH, I.D., LANGER, N., LENNON, D.J., PULS, J., SANA, H. & VINK, J.S. (2016). The R136 star cluster dissected with Hubble Space Telescope/STIS. I. Far-ultraviolet spectroscopic census and the origin of He II λ1640 in young star clusters. *Monthly Notices fo the Royal Astronomical Society*, **458**, 624–659. 2

CURRIE, M.J., BERRY, D.S., JENNESS, T., GIBB, A.G., BELL, G.S. & DRAPER, P.W. (2014). Starlink Software in 2013. In N. Manset & P. Forshay, eds., *Astronomical Data Analysis Software and Systems XXIII*, vol. 485 of *Astronomical Society of the Pacific Conference Series*, 391. 39

DAVIES, B., LUMSDEN, S.L., HOARE, M.G., OUDMAIJER, R.D. & DE WIT, W.J. (2010). The circumstellar disc, envelope and bipolar outflow of the massive young stellar object W33A. *Monthly Notices of the Royal Astronomical Society*, **402**, 1504–1515. 127

DAVIES, B., HOARE, M.G., LUMSDEN, S.L., HOSOKAWA, T., OUDMAIJER, R.D., URQUHART, J.S., MOTTRAM, J.C. & STEAD, J. (2011). The Red MSX Source survey: critical tests of accretion models for the formation of massive stars. *Monthly Notices of the Royal Astronomical Society*, **416**, 972–990. 78, 132, 149, 153, 187, 203

DAVIES, R. & KASPER, M. (2012). Adaptive Optics for Astronomy. *Astronomy & Astrophysics Review*, **50**, 305–351. 166

DHITAL, S., WEST, A.A., STASSUN, K.G. & BOCHANSKI, J.J. (2010). Sloan Low-mass Wide Pairs of Kinematically Equivalent Stars (SLoWPoKES): A Catalog of Very Wide, Low-mass Pairs. *The Astronomical Journal*, **139**, 2566–2586. 190

DODSON-ROBINSON, S.E. & SALYK, C. (2011). Transitional Disks as Signposts of Young, Multiplanet Systems. *The Astrophysical Journal*, **738**, 131. 7

Donehew, B. & Brittain, S. (2011). Measuring the Stellar Accretion Rates of Herbig Ae/Be Stars. *The Astronomical Journal*, **141**, 46. 8

Draine, B.T. & Lee, H.M. (1984). Optical properties of interstellar graphite and silicate grains. *The Astrophysical Journal*, **285**, 89–108. 45, 48

Drew, J.E., Bunn, J.C. & Hoare, M.G. (1993). Constraints on the Outflow in S:106IR from Hei 2.058-MICRON Absorption Line and HI Emission Line Profiles. *Monthly Notices of the Royal Astronomical Society*, **265**, 12. xii, 26, 27, 54, 57, 71, 80, 99, 116, 143

Duchêne, G. & Kraus, A. (2013). Stellar Multiplicity. *Astronomy & Astrophysics Review*, **51**, 269–310. 21, 22, 23

Duquennoy, A. & Mayor, M. (1991). Multiplicity among solar-type stars in the solar neighbourhood. II - Distribution of the orbital elements in an unbiased sample. *Astronomy & Astrophysics*, **248**, 485–524. 22

Egan, M.P., Shipman, R.F., Price, S.D., Carey, S.J., Clark, F.O. & Cohen, M. (1998). A Population of Cold Cores in the Galactic Plane. *The Astrophysical Journall*, **494**, L199–L202. 14

Egan, M.P., Price, S.D., Kraemer, K.E., Mizuno, D.R., Carey, S.J., Wright, C.O., Engelke, C.W., Cohen, M. & Gugliotti, M.G. (2003). VizieR Online Data Catalog: MSX6C Infrared Point Source Catalog. The Midcourse Space Experiment Point Source Catalog Version 2.3 (October 2003). *VizieR Online Data Catalog*, **5114**. 17

Fairlamb, J.R., Oudmaijer, R.D., Mendigutía, I., Ilee, J.D. & van den Ancker, M.E. (2015). A spectroscopic survey of Herbig Ae/Be stars with X-shooter - I. Stellar parameters and accretion rates. *Monthly Notices fo the Royal Astronomical Society*, **453**, 976–1001. 8, 132, 201

Fairlamb, J.R., Oudmaijer, R.D., Mendigutia, I., Ilee, J.D. & van den Ancker, M.E. (2017). A spectroscopic survey of Herbig Ae/Be stars with X-Shooter - II. Accretion diagnostic lines. *Monthly Notices fo the Royal Astronomical Society*, **464**, 4721–4735. 78

Feigelson, E.D. & Kriss, G.A. (1981). Discovery of three X-ray luminous pre-main-sequence stars. *apjl*, **248**, L35–L38. 5

GIBB, A.G. & HOARE, M.G. (2007). A high-frequency radio continuum study of massive young stellar objects. *Monthly Notices fo the Royal Astronomical Society*, **380**, 246–262. 193

GOODWIN, S.P., WHITWORTH, A.P. & WARD-THOMPSON, D. (2004). Simulating star formation in molecular cloud cores. I. The influence of low levels of turbulence on fragmentation and multiplicity. *Astronomy & Astrophysics*, **414**, 633–650. 24

GRADY, C.A., POLOMSKI, E.F., HENNING, T., STECKLUM, B., WOODGATE, B.E., TELESCO, C.M., PIÑA, R.K., GULL, T.R., BOGGESS, A., BOWERS, C.W., BRUHWEILER, F.C., CLAMPIN, M., DANKS, A.C., GREEN, R.F., HEAP, S.R., HUTCHINGS, J.B., JENKINS, E.B., JOSEPH, C., KAISER, M.E., KIMBLE, R.A., KRAEMER, S., LINDLER, D., LINSKY, J.L., MARAN, S.P., MOOS, H.W., PLAIT, P., ROESLER, F., TIMOTHY, J.G. & WEISTROP, D. (2001). The Disk and Environment of the Herbig Be Star HD 100546. *The Astronomical Journal*, **122**, 3396–3406. 7

GREDEL, R. (2006). HH135/HH136 - a luminous H_2 outflow towards a high-mass protostar. *Astronomy & Astrophysics*, **457**, 157–166. 190

GREEN, G.M., SCHLAFLY, E.F., FINKBEINER, D.P., RIX, H.W., MARTIN, N., BURGETT, W., DRAPER, P.W., FLEWELLING, H., HODAPP, K., KAISER, N., KUDRITZKI, R.P., MAGNIER, E., METCALFE, N., PRICE, P., TONRY, J. & WAINSCOAT, R. (2015). A Three-dimensional Map of Milky Way Dust. *The Astrophysical Journal*, **810**, 25. 49, 217

GULLBRING, E., CALVET, N., MUZEROLLE, J. & HARTMANN, L. (2000). The Structure and Emission of the Accretion Shock in T Tauri Stars. II. The Ultraviolet-Continuum Emission. *The Astrophysical Journal*, **544**, 927–932. 7

HAEMMERLÉ, L. & PETERS, T. (2016). Impact of initial models and variable accretion rates on the pre-main-sequence evolution of massive and intermediate-mass stars and the early evolution of H II regions. *Monthly Notices of the Royal Astronomical Society*, **458**, 3299–3313. 123, 159

HAMANO, S., KOBAYASHI, N., KONDO, S., IKEDA, Y., NAKANISHI, K., YASUI, C., MIZUMOTO, M., MATSUNAGA, N., FUKUE, K., MITO, H., YAMAMOTO, R., IZUMI, N., NAKAOKA, T., KAWANISHI, T., KITANO, A., OTSUBO, S., KINOSHITA, M., KOBAYASHI, H. & KAWAKITA, H. (2015).

Near-infrared Diffuse Interstellar Bands in 0.91-1.32 μm. *ApJ*, **800**, 137. 123, 125

Hanson, M.M., Kudritzki, R.P., Kenworthy, M.A., Puls, J. & Tokunaga, A.T. (2005). A Medium Resolution Near-Infrared Spectral Atlas of O and Early-B Stars. *The Astrophysical Journal*, **161**, 154–170. 121, 122, 126

Herbig, G.H. (1960). The Spectra of Be- and Ae-Type Stars Associated with Nebulosity. *apjs*, **4**, 337. 7

Hildebrand, R.H. (1983). The Determination of Cloud Masses and Dust Characteristics from Submillimetre Thermal Emission. *qjras*, **24**, 267. 88

Hinkle, K.H., Wallace, L. & Livingston, W. (1995). Kitt Peak Solar and Stellar Atlases. In A.J. Sauval, R. Blomme & N. Grevesse, eds., *Laboratory and Astronomical High Resolution Spectra*, vol. 81 of *Astronomical Society of the Pacific Conference Series*, 66. 104

Hoare, M.G. (2005). Ultra-Compact H II Regions. *apss*, **295**, 203–215. 21

Hoare, M.G. & Franco, J. (2007). Massive Star Formation. *ArXiv e-prints*. 11, 123

Hoare, M.G., Purcell, C.R., Churchwell, E.B., Diamond, P., Cotton, W.D., Chandler, C.J., Smethurst, S., Kurtz, S.E., Mundy, L.G., Dougherty, S.M., Fender, R.P., Fuller, G.A., Jackson, J.M., Garrington, S.T., Gledhill, T.R., Goldsmith, P.F., Lumsden, S.L., Martí, J., Moore, T.J.T., Muxlow, T.W.B., Oudmaijer, R.D., Pandian, J.D., Paredes, J.M., Shepherd, D.S., Spencer, R.E., Thompson, M.A., Umana, G., Urquhart, J.S. & Zijlstra, A.A. (2012). The Coordinated Radio and Infrared Survey for High-Mass Star Formation (The CORNISH Survey). I. Survey Design. *Physics*, **124**, 939–955. 19

Hoffleit, D. & Jaschek, C. (1991). *The Bright star catalogue*. 38

Hosokawa, T., Yorke, H.W. & Omukai, K. (2010). Evolution of Massive Protostars Via Disk Accretion. *The Astrophysical Journal*, **721**, 478–492. iii, 11, 37, 59, 78, 108, 123, 133, 159, 161, 201, 203, 205, 207

Hummer, D.G. & Storey, P.J. (1987). Recombination-line intensities for hydrogenic ions. I - Case B calculations for H I and He II. *Monthly Notices of the Royal Astronomical Society*, **224**, 801–820. 110

Ilee, J.D., Wheelwright, H.E., Oudmaijer, R.D., de Wit, W.J., Maud, L.T., Hoare, M.G., Lumsden, S.L., Moore, T.J.T., Urquhart, J.S. & Mottram, J.C. (2013). CO bandhead emission of massive young stellar objects: determining disc properties. *Monthly Notices of the Royal Astronomical Society*, **429**, 2960–2973. 28, 54, 99, 194, 203

Ilee, J.D., Fairlamb, J., Oudmaijer, R.D., Mendigutía, I., van den Ancker, M.E., Kraus, S. & Wheelwright, H.E. (2014). Investigating the inner discs of Herbig Ae/Be stars with CO bandhead and Brγ emission. *Monthly Notices fo the Royal Astronomical Society*, **445**, 3723–3736. 7, 77, 133, 134

Ilee, J.D., Cyganowski, C.J., Nazari, P., Hunter, T.R., Brogan, C.L., Forgan, D.H. & Zhang, Q. (2016). G11.92-0.61 MM1: a Keplerian disc around a massive young proto-O star. *Monthly Notices fo the Royal Astronomical Society*, **462**, 4386–4401. 16, 206

Ingleby, L., Calvet, N., Herczeg, G., Blaty, A., Walter, F., Ardila, D., Alexander, R., Edwards, S., Espaillat, C., Gregory, S.G., Hillenbrand, L. & Brown, A. (2013). Accretion Rates for T Tauri Stars Using Nearly Simultaneous Ultraviolet and Optical Spectra. *The Astrophysical Journal*, **767**, 112. 7

Isella, A. (2007). *Interferometric observations of pre-main sequence disks*. Ph.D. thesis, University of Milano, Italy. 6

Ishii, M., Nagata, T., Sato, S., Yao, Y., Jiang, Z. & Nakaya, H. (2001). K-Band Spectroscopy of Luminous Young Stellar Objects. *The Astronomical Journal*, **121**, 3191–3206. 30

Jackson, J.M., Finn, S.C., Chambers, E.T., Rathborne, J.M. & Simon, R. (2010). The “Nessie” Nebula: Cluster Formation in a Filamentary Infrared Dark Cloud. *apjl*, **719**, L185–L189. 14

Jeans, J.H. (1902). The Stability of a Spherical Nebula. *Royal Society of London Philosophical Transactions Series A*, **199**, 1–53. 3

Johns-Krull, C.M. (2007). The Magnetic Fields of Classical T Tauri Stars. *The Astrophysical Journal*, **664**, 975–985. 7

Johnston, K.G., Robitaille, T.P., Beuther, H., Linz, H., Boley, P., Kuiper, R., Keto, E., Hoare, M.G. & van Boekel, R. (2015). A Keplerian-like Disk around the Forming O-type Star AFGL 4176. *apjl*, **813**, L19. 16, 206

Joy, A.H. (1945). T Tauri Variable Stars. *The Astrophysical Journal*, **102**, 168. 5, 30

Kahn, F.D. (1974). Cocoons around early-type stars. *Astronomy & Astrophysics*, **37**, 149–162. 2, 9

Kendall, T.R., de Wit, W.J. & Yun, J.L. (2003). VLT/ISAAC H-band spectroscopy of embedded massive YSOs. *Astronomy and Astrohpysics*, **408**, 313–322. 121

Köhler, R., Petr-Gotzens, M.G., McCaughrean, M.J., Bouvier, J., Duchêne, G., Quirrenbach, A. & Zinnecker, H. (2006). Binary stars in the Orion Nebula Cluster. *Astronomy & Astrophysics*, **458**, 461–476. 25

Kolmogorov, A. (1941). The Local Structure of Turbulence in Incompressible Viscous Fluid for Very Large Reynolds' Numbers. *Akademiia Nauk SSSR Doklady*, **30**, 301–305. 13

Koornneef, J. (1983). Near-infrared photometry. II - Intrinsic colours and the absolute calibration from one to five micron. *Astonomy & Astrohpysics*, **128**, 84–93. 48, 108

Kratter, K.M. (2010). The Role of Disks in the Formation of Stellar Systems. In *American Astronomical Society Meeting Abstracts #215*, vol. 42 of *Bulletin of the American Astronomical Society*, 582. 24

Kratter, K.M. (2011). The Formation of Close Binaries. In L. Schmidtobreick, M.R. Schreiber & C. Tappert, eds., *Evolution of Compact Binaries*, vol. 447 of *Astronomical Society of the Pacific Conference Series*, 47. 163

Kraus, A.L., Ireland, M.J., Martinache, F. & Hillenbrand, L.A. (2011). Mapping the Shores of the Brown Dwarf Desert. II. Multiple Star Formation in Taurus-Auriga. *The Astrophysical Journal*, **731**, 8. 25, 185, 186, 206

Kraus, S., Hofmann, K.H., Menten, K.M., Schertl, D., Weigelt, G., Wyrowski, F., Meilland, A., Perraut, K., Petrov, R., Robbe-Dubois, S., Schilke, P. & Testi, L. (2010). A hot compact dust disk around a massive young stellar object. *Nature*, **466**, 339–342. 29, 190

Kraus, S., Kluska, J., Kreplin, A., Bate, M., Harries, T.J., Hofmann, K.H., Hone, E., Monnier, J.D., Weigelt, G., Anugu, A., de Wit, W.J. & Wittkowski, M. (2017). A High-mass Protobinary System with Spatially Resolved Circumstellar Accretion Disks and Circumbinary Disk. *apjl*, **835**, L5. 25, 206

Kron, R.G. (1980). Photometry of a complete sample of faint galaxies. *The Astrophysical Journal Series*, **43**, 305–325. 171

Krumholz, M.R., McKee, C.F. & Klein, R.I. (2005). The formation of stars by gravitational collapse rather than competitive accretion. *Nature*, **438**, 332–334. 12, 148

Krumholz, M.R., Klein, R.I., McKee, C.F., Offner, S.S.R. & Cunningham, A.J. (2009). The Formation of Massive Star Systems by Accretion. *Science*, **323**, 754–. 10, 24, 162, 165

Krumholz, M.R., Klein, R.I. & McKee, C.F. (2012). Radiation-hydrodynamic Simulations of the Formation of Orion-like Star Clusters. II. The Initial Mass Function from Winds, Turbulence, and Radiation. *The Astrophysical Journal*, **754**, 71. 162, 165

Kuiper, R. & Yorke, H.W. (2013). On the Simultaneous Evolution of Massive Protostars and Their Host Cores. *The Astrophysical Journal*, **772**, 61. 10

Kuiper, R., Klahr, H., Beuther, H. & Henning, T. (2011). Three-dimensional Simulation of Massive Star Formation in the Disk Accretion Scenario. *The Astrophysical Journal*, **732**, 20. 10, 32, 205

Kumar, M.S.N., Contreras Peña, C., Lucas, P.W. & Thompson, M.A. (2016). Highly Variable Young Massive Stars in ATLASGAL Clumps. *The Astrophysical Journal*, **833**, 24. 31

Kurtz, S. (2005). Hypercompact HII regions. In R. Cesaroni, M. Felli, E. Churchwell & M. Walmsley, eds., *Massive Star Birth: A Crossroads of Astrophysics*, vol. 227 of *IAU Symposium*, 111–119. xvi, 20, 21

Larson, R.B. (1981). Turbulence and star formation in molecular clouds. *Monthly Notices of the Royal Astronomical Society*, **194**, 809–826. 13

Larson, R.B. (2003). The physics of star formation. *Reports on Progress in Physics*, **66**, 1651–1697. 3

Lenzen, R., Hartung, M., Brandner, W., Finger, G., Hubin, N.N., Lacombe, F., Lagrange, A.M., Lehnert, M.D., Moorwood, A.F.M. & Mouillet, D. (2003). NAOS-CONICA first on sky results in a variety of observing modes. In M. Iye & A.F.M. Moorwood, eds., *Instrument Design and Performance for Optical/Infrared Ground-based Telescopes*, vol. 4841 of *SPIE*, 944–952. 165

Looney, L.W., Mundy, L.G. & Welch, W.J. (2000). Unveiling the Circumstellar Envelope and Disk: A Subarcsecond Survey of Circumstellar Structures. *The Astrophysical Journal*, **529**, 477–498. 25

Lucas, C. & Jim, J., B. (2017). V1647 Orionis: Optical Photometric and Spectroscopic Monitoring Through the 2003-2006 Outburst. *The Astronomical Journal*, **138**, 1137–1158. 31

Lucas, P.W., Hoare, M.G., Longmore, A., Schröder, A.C., Davis, C.J., Adamson, A., Bandyopadhyay, R.M., de Grijs, R., Smith, M., Gosling, A., Mitchison, S., Gáspár, A., Coe, M., Tamura, M., Parker, Q., Irwin, M., Hambly, N., Bryant, J., Collins, R.S., Cross, N., Evans, D.W., Gonzalez-Solares, E., Hodgkin, S., Lewis, J., Read, M., Riello, M., Sutorius, E.T.W., Lawrence, A., Drew, J.E., Dye, S. & Thompson, M.A. (2008a). The UKIDSS Galactic Plane Survey. *Monthly Notices of the Royal Astronomical Society*, **391**, 136–163. 19

Lucas, P.W., Hoare, M.G., Longmore, A., Schröder, A.C., Davis, C.J., Adamson, A., Bandyopadhyay, R.M., de Grijs, R., Smith, M., Gosling, A., Mitchison, S., Gáspár, A., Coe, M., Tamura, M., Parker, Q., Irwin, M., Hambly, N., Bryant, J., Collins, R.S., Cross, N., Evans, D.W., Gonzalez-Solares, E., Hodgkin, S., Lewis, J., Read, M., Riello, M., Sutorius, E.T.W., Lawrence, A., Drew, J.E., Dye, S. & Thompson, M.A. (2008b). The UKIDSS Galactic Plane Survey. *Monthly Notices of the Royal Astronomical Society*, **391**, 136–163. 107

Lumsden, S.L. & Puxley, P.J. (1996). Near-infrared spectroscopy of the ultracompact HII region G45.12+0.13. *Monthly Notices fo the Royal Astronomical Society*, **281**, 493–508. 50, 54, 149

Lumsden, S.L., Puxley, P.J. & Hoare, M.G. (2001). Near-infrared spectra of compact planetary nebulae. *Monthly Notices fo the Royal Astronomical Society*, **328**, 419–441. 54

Lumsden, S.L., Hoare, M.G., Oudmaijer, R.D. & Richards, D. (2002). The population of the Galactic plane as seen by MSX. *Monthly Notices of the Royal Astronomical Society*, **336**, 621–636. 17

Lumsden, S.L., Wheelwright, H.E., Hoare, M.G., Oudmaijer, R.D. & Drew, J.E. (2012). Tracers of discs and winds around intermediate- and high-mass young stellar objects. *Monthly Notices of the Royal Astronomical Society*, **424**, 1088–1104. 26, 27, 29, 54, 99, 143, 202, 203, 205

Lumsden, S.L., Hoare, M.G., Urquhart, J.S., Oudmaijer, R.D., Davies, B., Mottram, J.C., Cooper, H.D.B. & Moore, T.J.T. (2013). The Red MSX Source Survey: The Massive Young Stellar Population of Our Galaxy. *The Astrophysical Journals*, **208**, 11. 16, 17, 38, 99, 101, 164, 200

Maaskant, K.M., Honda, M., Waters, L.B.F.M., Tielens, A.G.G.M., Dominik, C., Min, M., Verhoeff, A., Meeus, G. & van den Ancker, M.E. (2013). Identifying gaps in flaring Herbig Ae/Be disks using spatially resolved mid-infrared imaging. Are all group I disks transitional? *Astronomy & Astrophysics*, **555**, A64. 7

Machida, M.N., Inutsuka, S.I. & Matsumoto, T. (2009). *Protostellar Jet and Outflow in the Collapsing Cloud Core*, 405–410. 5

Malbet, F., Benisty, M., de Wit, W.J., Kraus, S., Meilland, A., Millour, F., Tatulli, E., Berger, J.P., Chesneau, O., Hofmann, K.H., Isella, A., Natta, A., Petrov, R.G., Preibisch, T., Stee, P., Testi, L., Weigelt, G., Antonelli, P., Beckmann, U., Bresson, Y., Chelli, A., Dugué, M., Duvert, G., Gennari, S., Glück, L., Kern, P., Lagarde, S., Le Coarer, E., Lisi, F., Perraut, K., Puget, P., Rantakyrö, F., Robbe-Dubois, S., Roussel, A., Zins, G., Accardo, M., Acke, B., Agabi, K., Altariba, E., Arezki, B., Aristidi, E., Baffa, C., Behrend, J., Blöcker, T., Bonhomme, S., Busoni, S., Cassaing, F., Clausse, J.M., Colin, J., Connot, C., Delboulbé, A., Domiciano de Souza, A., Driebe, T., Feautrier, P., Ferruzzi, D., Forveille, T., Fossat, E., Foy, R., Fraix-Burnet, D., Gallardo, A., Giani, E., Gil, C., Glentzlin, A., Heiden, M., Heininger, M., Hernandez Utrera, O., Kamm, D., Kiekebusch, M., Le Contel, D., Le Contel, J.M., Lesourd, T., Lopez, B., Lopez, M., Magnard, Y., Marconi, A., Mars, G., Martinot-Lagarde, G., Mathias, P., Mège, P., Monin, J.L., Mouillet, D., Mourard, D., Nussbaum, E., Ohnaka, K., Pacheco, J., Perrier, C., Rabbia, Y., Rebattu, S., Reynaud, F., Richichi, A., Robini, A., Sacchettini, M., Schertl, D., Schöller, M., Solscheid, W., Spang, A., Stefanini, P., Tallon, M., Tallon-Bosc, I., Tasso, D., Vakili, F., von der Lühe, O., Valtier, J.C., Vannier, M. & Ventura, N. (2007). Disk and wind interaction in the young stellar object ¡ASTROBJ¿MWC 297¡/ASTROBJ¿ spatially resolved with AMBER/VLTI. *Astronomy & Astrophysics*, **464**, 43–53. 29

Mannings, V. & Sargent, A.I. (1997). A High-Resolution Study of Gas and Dust around Young Intermediate-Mass Stars: Evidence for Circumstellar Disks in Herbig Ae Systems. *The Astrophysical Journal*, **490**, 792–802. 7

Martin, P.G. & Whittet, D.C.B. (1990). Interstellar extinction and polarization in the infrared. *The Astrophysical Journal*, **357**, 113–124. 111

Massey, P., DeGioia-Eastwood, K. & Waterhouse, E. (2001). The Progenitor Masses of Wolf-Rayet Stars and Luminous Blue Variables Determined from Cluster Turnoffs. II. Results from 12 Galactic Clusters and OB Associations. *The Astronomical Journal*, **121**, 1050–1070. 21

Maud, L.T., Moore, T.J.T., Lumsden, S.L., Mottram, J.C., Urquhart, J.S. & Hoare, M.G. (2015). A distance-limited sample of massive molecular outflows. *Monthly Notices fo the Royal Astronomical Society*, **453**, 645–665. 203

McKee, C.F. & Ostriker, J.P. (1977). A theory of the interstellar medium - Three components regulated by supernova explosions in an inhomogeneous substrate. *The Astrophysical Journal*, **218**, 148–169. 13

McKee, C.F. & Tan, J.C. (2003). The Formation of Massive Stars from Turbulent Cores. *The Astrophysical Journal*, **585**, 850–871. 2, 9

MEEUS, G., WATERS, L.B.F.M., BOUWMAN, J., VAN DEN ANCKER, M.E., WAELKENS, C. & MALFAIT, K. (2001). ISO spectroscopy of circumstellar dust in 14 Herbig Ae/Be systems: Towards an understanding of dust processing. *Astronomy & Astrophysics*, **365**, 476–490. 7

MENDIGUTÍA, I., CALVET, N., MONTESINOS, B., MORA, A., MUZEROLLE, J., EIROA, C., OUDMAIJER, R.D. & MERÍN, B. (2011). Accretion rates and accretion tracers of Herbig Ae/Be stars. *Astronomy & Astrophysics*, **535**, A99. 8, 78, 84, 130, 132

MENDIGUTÍA, I., OUDMAIJER, R.D., RIGLIACO, E., FAIRLAMB, J.R., CALVET, N., MUZEROLLE, J., CUNNINGHAM, N. & LUMSDEN, S.L. (2015). On the origin of the correlations between the accretion luminosity and emission line luminosities in pre-main-sequence stars. *Monthly Notices fo the Royal Astronomical Society*, **452**, 2837–2844. 77, 135, 203

MEYER, D.M.A., KUIPER, R., KLEY, W., JOHNSTON, K.G. & VOROBYOV, E. (2017). Forming spectroscopic massive proto-binaries by disk fragmentation. *ArXiv e-prints*. 24, 32, 58, 67, 203, 205, 206

MEYER, M.R., EDWARDS, S., HINKLE, K.H. & STROM, S.E. (1998). Near-Infrared Classification Spectroscopy: H-Band Spectra of Fundamental MK Standards. *The Astrophysical Journal*, **508**, 397–409. 121, 126

MEYNET, G. & MAEDER, A. (2000). Stellar evolution with rotation. V. Changes in all the outputs of massive star models. *Astronomy & Astrophysics*, **361**, 101–120. 78

MINNITI, D., LUCAS, P.W., EMERSON, J.P., SAITO, R.K., HEMPEL, M., PIETRUKOWICZ, P., AHUMADA, A.V., ALONSO, M.V., ALONSO-GARCIA, J., ARIAS, J.I., BANDYOPADHYAY, R.M., BARBÁ, R.H., BARBUY, B., BEDIN, L.R., BICA, E., BORISSOVA, J., BRONFMAN, L., CARRARO, G., CATELAN, M., CLARIÁ, J.J., CROSS, N., DE GRIJS, R., DÉKÁNY, I., DREW, J.E., FARIÑA, C., FEINSTEIN, C., FERNÁNDEZ LAJÚS, E., GAMEN, R.C., GEISLER, D., GIEREN, W., GOLDMAN, B., GONZALEZ, O.A., GUNTHARDT, G., GUROVICH, S., HAMBLY, N.C., IRWIN, M.J., IVANOV, V.D., JORDÁN, A., KERINS, E., KINEMUCHI, K., KURTEV, R., LÓPEZ-CORREDOIRA, M., MACCARONE, T., MASETTI, N., MERLO, D., MESSINEO, M., MIRABEL, I.F., MONACO, L., MORELLI, L., PADILLA, N., Palma, T., Parisi, M.C., Pignata, G., Rejkuba, M., Roman-Lopes, A., Sale, S.E., Schreiber, M.R., Schröder, A.C., Smith, M., , L.S., Jr., Soto, M., Tamura, M., Tappert, C., Thompson, M.A., Toledo, I., Zoccali, M. & Pietrzynski, G. (2010). VISTA Variables in the Via Lactea (VVV): The public ESO near-IR variability survey of the Milky Way. *na*, **15**, 433–443. 19, 43, 171

Moeckel, N. & Bally, J. (2007). Capture-formed Binaries via Encounters with Massive Protostars. *The Astrophysical Journal*, **656**, 275–286. 162

Molinari, S., Brand, J., Cesaroni, R. & Palla, F. (1996). A search for precursors of ultracompact HII regions in a sample of luminous IRAS sources. I. Association with ammonia cores. *Astronomy & Astrophysics*, **308**, 573–587. 16

Molinari, S., Brand, J., Cesaroni, R., Palla, F. & Palumbo, G.G.C. (1998). A search for precursors of ultracompact H II regions in a sample of luminous IRAS sources. II. VLA observations. *Astronomy & Astrophysics*, **336**, 339–351. 16

Molinari, S., Pezzuto, S., Cesaroni, R., Brand, J., Faustini, F. & Testi, L. (2008). The evolution of the spectral energy distribution in massive young stellar objects. *Astronomy & Astrophysics*, **481**, 345–365. 88, 90, 92

Moore, T.J.T., Lumsden, S.L., Ridge, N.A. & Puxley, P.J. (2005). The near-infrared extinction law in regions of high A_V. *MNRAS*, **359**, 589–596. 115

Mottram, J.C., Hoare, M.G., Lumsden, S.L., Oudmaijer, R.D., Urquhart, J.S., Sheret, T.L., Clarke, A.J. & Allsopp, J. (2007a). The RMS survey: mid-infrared observations of candidate massive YSOs in the southern hemisphere. *Astronomy & Astrophysics*, **476**, 1019–1111. 19, 187

Mottram, J.C., Vink, J.S., Oudmaijer, R.D. & Patel, M. (2007b). On the difference between Herbig Ae and Herbig Be stars. *MNRAS*, **377**, 1363–1374. 99

Mottram, J.C., Hoare, M.G., Lumsden, S.L., Oudmaijer, R.D., Urquhart, J.S., Meade, M.R., Moore, T.J.T. & Stead, J.J. (2010). The RMS survey: far-infrared photometry of young massive stars. *Astronomy & Astrophysics*, **510**, A89. 20

Mottram, J.C., Hoare, M.G., Urquhart, J.S., Lumsden, S.L., Oudmaijer, R.D., Robitaille, T.P., Moore, T.J.T., Davies, B. & Stead, J. (2011a). The Red MSX Source survey: the bolometric fluxes and luminosity distributions of young massive stars. *Astronomy & Astrophysics*, **525**, A149. 20

Mottram, J.C., Hoare, M.G., Urquhart, J.S., Lumsden, S.L., Oudmaijer, R.D., Robitaille, T.P., Moore, T.J.T., Davies, B. & Stead, J. (2011b). The Red MSX Source survey: the bolometric fluxes and luminosity distributions of young massive stars. *Astronomy & Astrophysics*, **525**, A149. 102, 167

Muzerolle, J., Calvet, N. & Hartmann, L. (2001). Emission-Line Diagnostics of T Tauri Magnetospheric Accretion. II. Improved Model Tests and Insights into Accretion Physics. *The Astrophysical Journal*, **550**, 944–961. 7

Muzerolle, J., D'Alessio, P., Calvet, N. & Hartmann, L. (2004). Magnetospheres and Disk Accretion in Herbig Ae/Be Stars. *The Astrophysical Journal*, **617**, 406–417. 8

Natta, A., Testi, L., Muzerolle, J., Randich, S., Comerón, F. & Persi, P. (2004). Accretion in brown dwarfs: An infrared view. *Astronomy & Astrophysics*, **424**, 603–612. 7

Natta, A., Testi, L. & Randich, S. (2006). Accretion in the ρ-Ophiuchi pre-main sequence stars. *Astronomy and Astrophysics*, **452**, 245–252. 130

Navarete, F., Damineli, A., Barbosa, C.L. & Blum, R.D. (2015). A survey of extended H_2 emission from massive YSOs. *Monthly Notices fo the Royal Astronomical Society*, **450**, 4364–4398. 190

Neckel, T., Klare, G. & Sarcander, M. (1980). The spatial distribution of the interstellar extinction. **42**, 251–281. 49, 188, 217

Neugebauer, G., Habing, H.J., van Duinen, R., Aumann, H.H., Baud, B., Beichman, C.A., Beintema, D.A., Boggess, N., Clegg, P.E., de Jong, T., Emerson, J.P., Gautier, T.N., Gillett, F.C., Harris, S., Hauser, M.G., Houck, J.R., Jennings, R.E., Low, F.J., Marsden, P.L., Miley, G., Olnon, F.M., Pottasch, S.R., Raimond, E., Rowan-Robinson, M., Soifer, B.T., Walker, R.G., Wesselius, P.R.

& Young, E. (1984). The Infrared Astronomical Satellite (IRAS) mission. *apjl*, **278**, L1–L6. 16

Offner, S.S.R., Kratter, K.M., Matzner, C.D., Krumholz, M.R. & Klein, R.I. (2010). The Formation of Low-mass Binary Star Systems Via Turbulent Fragmentation. *The Astrophysical Journal*, **725**, 1485–1494. 24

Oliva, E. (1987). Forbidden lines in the near infrared (1-5 micron) - Their application to the study of SN's and SNR's. *memsai*, **58**, 215–221. 54

Oliva, E., Moorwood, A.F.M. & Danziger, I.J. (1989). Infrared spectroscopy of supernova remnants. *Astronomy & Astrophysics*, **214**, 307–320. 54

Oliveira, J.M., Van Loon, J.T., Stanimirovi, S. & Zijlstra, A.A. (2006). Massive young stellar objects in the large magellanic cloud: water masers and eso-vlt 34 m spectroscopy. *Monthly Notices of the Royal Astronomical Society*, **372**, 1509–1524. 30

Oliveira, J.M., van Loon, J.T., Sloan, G.C., Sewio, M., Kraemer, K.E., Wood, P.R., Indebetouw, R., Filipovi, M.D., Crawford, E.J., Wong, G.F., Hora, J.L., Meixner, M., Robitaille, T.P., Shiao, B. & Simon, J.D. (2013). Early-stage young stellar objects in the small magellanic cloud. *Monthly Notices of the Royal Astronomical Society*, **428**, 3001–3033. 30

Oudmaijer, R.D. & de Wit, W.J. (2014). Star Formation at milli-arcsecond resolution. In *EAS Publications Series*, vol. 69 of *EAS Publications Series*, 319–331. 16, 200

Oudmaijer, R.D. & Parr, A.M. (2010). The binary fraction and mass ratio of Be and B stars: a comparative Very Large Telescope/NACO study. *Monthly Notices of the Royal Astronomical Society*, **405**, 2439–2446. 165, 175, 186, 188

Oudmaijer, R.D., Busfield, G. & Drew, J.E. (1997). Diffuse interstellar bands in the spectra of massive young stellar objects. *MNRAS*, **291**, 797. 127

Padoan, P., Juvela, M., Goodman, A.A. & Nordlund, Å. (2001). The Turbulent Shock Origin of Proto-Stellar Cores. *The Astrophysical Journal*, **553**, 227–234. 14

PALMEIRIM, P., ANDRÉ, P., KIRK, J., WARD-THOMPSON, D., ARZOUMANIAN, D., KÖNYVES, V., DIDELON, P., SCHNEIDER, N., BENEDETTINI, M., BONTEMPS, S., DI FRANCESCO, J., ELIA, D., GRIFFIN, M., HENNEMANN, M., HILL, T., MARTIN, P.G., MEN'SHCHIKOV, A., MOLINARI, S., MOTTE, F., NGUYEN LUONG, Q., NUTTER, D., PERETTO, N., PEZZUTO, S., ROY, A., RYGL, K.L.J., SPINOGLIO, L. & WHITE, G.L. (2013). Herschel view of the Taurus B211/3 filament and striations: evidence of filamentary growth? *Astronomy & Astrophysics*, **550**, A38. 14

PARKER, R.J. & REGGIANI, M.M. (2013). The binary companion mass ratio distribution: an imprint of the star formation process? *Monthly Notices fo the Royal Astronomical Society*, **432**, 2378–2384. 23

PERAULT, M., OMONT, A., SIMON, G., SEGUIN, P., OJHA, D., BLOMMAERT, J., FELLI, M., GILMORE, G., GUGLIELMO, F., HABING, H., PRICE, S., ROBIN, A., DE BATZ, B., CESARSKY, C., ELBAZ, D., EPCHTEIN, N., FOUQUE, P., GUEST, S., LEVINE, D., POLLOCK, A., PRUSTI, T., SIEBENMORGEN, R., TESTI, L. & TIPHENE, D. (1996). First ISOCAM images of the Milky Way. *Astronomy & Astrophysics*, **315**, L165–L168. 14

PORTER, J.M., DREW, J.E. & LUMSDEN, S.L. (1998). Broad band infrared spectroscopy of massive young stellar objects. *Astronomy & Astrophysics*, **332**, 999–1016. 29, 48, 54, 108, 110, 111, 115

POWER, J., WADE, G.A., HANES, D.A., AURIER, M. & SILVESTER, J. (2007). Properties of a volume-limited sample of magnetic Ap/Bp stars. In I.I. Romanyuk, D.O. Kudryavtsev, O.M. Neizvestnaya & V.M. Shapoval, eds., *Physics of Magnetic Stars*, 89–97. 8

PRICE, S.D., EGAN, M.P., CAREY, S.J., MIZUNO, D.R. & KUCHAR, T.A. (2001). Midcourse Space Experiment Survey of the Galactic Plane. *The Astronomical Journal*, **121**, 2819–2842. 17

PURCELL, C.R., HOARE, M.G., COTTON, W.D., LUMSDEN, S.L., URQUHART, J.S., CHANDLER, C., CHURCHWELL, E.B., DIAMOND, P., DOUGHERTY, S.M., FENDER, R.P., FULLER, G., GARRINGTON, S.T., GLEDHILL, T.M., GOLDSMITH, P.F., HINDSON, L., JACKSON, J.M., KURTZ, S.E., MARTÍ, J., MOORE, T.J.T., MUNDY, L.G., MUXLOW, T.W.B., OUDMAIJER, R.D., PANDIAN, J.D., PAREDES, J.M., SHEPHERD, D.S., Smethurst, S., Spencer, R.E., Thompson, M.A., Umana, G. & Zijlstra, A.A. (2013). The Coordinated Radio and Infrared Survey for High-mass Star Formation. II. Source Catalog. *The Astrophysical Journals*, **205**, 1. 19

Purser, S.J.D., Lumsden, S.L., Hoare, M.G., Urquhart, J.S., Cunningham, N., Purcell, C.R., Brooks, K.J., Garay, G., Gúzman, A.E. & Voronkov, M.A. (2016). A search for ionized jets towards massive young stellar objects. *Monthly Notices fo the Royal Astronomical Society*, **460**, 1039–1053. xvi, 16, 86, 88, 149, 241

Raghavan, D., McAlister, H.A., Henry, T.J., Latham, D.W., Marcy, G.W., Mason, B.D., Gies, D.R., White, R.J. & ten Brummelaar, T.A. (2010). A Survey of Stellar Families: Multiplicity of Solar-type Stars. *apjs*, **190**, 1–42. 23, 164, 192

Rathborne, J.M., Jackson, J.M. & Simon, R. (2006). Infrared Dark Clouds: Precursors to Star Clusters. *The Astrophysical Journal*, **641**, 389–405. 15

Reipurth, B., Clarke, C.J., Boss, A.P., Goodwin, S.P., Rodríguez, L.F., Stassun, K.G., Tokovinin, A. & Zinnecker, H. (2014). Multiplicity in Early Stellar Evolution. *Protostars and Planets VI*, 267–290. 163

Robitaille, T.P. (2011). HYPERION: an open-source parallelized three-dimensional dust continuum radiative transfer code. *Astronomy and Astrophysics*, **536**, A79. 116

Robitaille, T.P., Whitney, B.A., Indebetouw, R. & Wood, K. (2007). Interpreting Spectral Energy Distributions from Young Stellar Objects. II. Fitting Observed SEDs Using a Large Grid of Precomputed Models. *The Astrohpysical Journal*, **169**, 328–352. 116

Robitaille, T.P., Meade, M.R., Babler, B.L., Whitney, B.A., Johnston, K.G., Indebetouw, R., Cohen, M., Povich, M.S., Sewilo, M., Benjamin, R.A. & Churchwell, E. (2008). Intrinsically Red Sources Observed by Spitzer in the Galactic Midplane. *The Astronomical Journal*, **136**, 2413–2440. 17

Rosen, A.L., Krumholz, M.R., McKee, C.F. & Klein, R.I. (2016). An unstable truth: how massive stars get their mass. *Monthly Notices fo the Royal Astronomical Society*, **463**, 2553–2573. 10, 24, 98

Rosero, V., Hofner, P., Claussen, M., Kurtz, S., Cesaroni, R., Araya, E.D., Carrasco-González, C., Rodríguez, L.F., Menten, K.M., Wyrowski, F., Loinard, L. & Ellingsen, S.P. (2016). Weak and Compact Radio Emission in Early High-mass Star-forming Regions. I. VLA Observations. *apjs*, **227**, 25. 149

Rousselot, P., Lidman, C., Cuby, J.G., Moreels, G. & Monnet, G. (2000). Night-sky spectral atlas of OH emission lines in the near-infrared. *Astronomy & Astrophysics*, **354**, 1134–1150. 39

Rousset, G., Lacombe, F., Puget, P., Hubin, N.N., Gendron, E., Fusco, T., Arsenault, R., Charton, J., Feautrier, P., Gigan, P., Kern, P.Y., Lagrange, A.M., Madec, P.Y., Mouillet, D., Rabaud, D., Rabou, P., Stadler, E. & Zins, G. (2003). NAOS, the first AO system of the VLT: on-sky performance. In P.L. Wizinowich & D. Bonaccini, eds., *Adaptive Optical System Technologies II*, vol. 4839 of *SPIE*, 140–149. 165

Salpeter, E.E. (1955). The Luminosity Function and Stellar Evolution. *The Astrophysical Journal*, **121**, 161. 2

Sana, H., de Mink, S.E., de Koter, A., Langer, N., Evans, C.J., Gieles, M., Gosset, E., Izzard, R.G., Le Bouquin, J.B. & Schneider, F.R.N. (2012). Binary Interaction Dominates the Evolution of Massive Stars. *Science*, **337**, 444. 23, 162, 186, 206

Schneider, N., Simon, R., Bontemps, S., Comerón, F. & Motte, F. (2007). A multiwavelength study of the S106 region. III. The S106 molecular cloud as part of the Cygnus X cloud complex. *Astronomy & Astrophysics*, **474**, 873–882. 21

Schuller, F., Menten, K.M., Contreras, Y., Wyrowski, F., Schilke, P., Bronfman, L., Henning, T., Walmsley, C.M., Beuther, H., Bontemps, S., Cesaroni, R., Deharveng, L., Garay, G., Herpin, F., Lefloch, B., Linz, H., Mardones, D., Minier, V., Molinari, S., Motte, F., Nyman, L.Å., Reveret, V., Risacher, C., Russeil, D., Schneider, N., Testi, L., Troost, T., Vasyunina, T., Wienen, M., Zavagno, A., Kovacs, A., Kreysa, E., Siringo, G. & Weiss, A. (2009). ATLASGAL - The APEX telescope large area survey of the galaxy at 870 μm. *Astronomy & Astrophysics*, **504**, 415–427. 88

Science Software Branch at STScI (2012). PyRAF: Python alternative for IRAF. Astrophysics Source Code Library. 43, 101

Shepherd, D.S. & Churchwell, E. (1996). Bipolar Molecular Outflows in Massive Star Formation Regions. *The Astrophysical Journal*, **472**, 225. 16

Shu, F., Najita, J., Ostriker, E., Wilkin, F., Ruden, S. & Lizano, S. (1994). Magnetocentrifugally driven flows from young stars and disks. 1: A generalized model. *The Astrophysical Journal*, **429**, 781–796. 6

Shu, F.H., Adams, F.C. & Lizano, S. (1987). Star formation in molecular clouds - Observation and theory. *Astronomy & Astrophysics Review*, **25**, 23–81. 1, 3, 98

Simon, M., Righini-Cohen, G., Cassar, L. & Fischer, J. (1981). Velocity resolved spectroscopy of the Brackett gamma line emission of CRL 490 and M17 IRS 1. *The Astrophysical Journal*, **251**, 552–556. 26, 57, 99, 101, 102

Simon, M., Felli, M., Cassar, L., Fischer, J. & Massi, M. (1983). Infrared line and radio continuum emission of circumstellar ionized regions. *The Astrophysical Journal*, **266**, 623–645. 26

Skrutskie, M.F., Cutri, R.M., Stiening, R., Weinberg, M.D., Schneider, S., Carpenter, J.M., Beichman, C., Capps, R., Chester, T., Elias, J., Huchra, J., Liebert, J., Lonsdale, C., Monet, D.G., Price, S., Seitzer, P., Jarrett, T., Kirkpatrick, J.D., Gizis, J.E., Howard, E., Evans, T., Fowler, J., Fullmer, L., Hurt, R., Light, R., Kopan, E.L., Marsh, K.A., McCallon, H.L., Tam, R., Van Dyk, S. & Wheelock, S. (2006). The Two Micron All Sky Survey (2MASS). *The Astronomical Journal*, **131**, 1163–1183. 19, 43, 171

Smette, A., Sana, H., Noll, S., Horst, H., Kausch, W., Kimeswenger, S., Barden, M., Szyszka, C., Jones, A.M., Gallenne, A., Vinther, J., Ballester, P. & Taylor, J. (2015). Molecfit: A general tool for telluric absorption correction. I. Method and application to ESO instruments. *Astronomy & Astrophysics*, **576**, A77. 41

SMITH, N. & BROOKS, K.J. (2008). *The Carina Nebula: A Laboratory for Feedback and Triggered Star Formation*, 138. 3

SMITH, N. & TOMBLESON, R. (2015). Luminous blue variables are antisocial: their isolation implies that they are kicked mass gainers in binary evolution. *Monthly Notices of the Royal Astronomical Society*, **447**, 598–617. 163

SRIDHARAN, T.K., BEUTHER, H., SCHILKE, P., MENTEN, K.M. & WYROWSKI, F. (2002). High-Mass Protostellar Candidates. I. The Sample and Initial Results. *The Astrophysical Journal*, **566**, 931–944. 16

STELZER, B. & NEUHÄUSER, R. (2001). X-ray emission from young stars in Taurus-Auriga-Perseus: Luminosity functions and the rotation - activity - age - relation. *Astronomy & Astrophysics*, **377**, 538–556. 5

STRAIZYS, V. & KURILIENE, G. (1981). Fundamental stellar parameters derived from the evolutionary tracks. *Astrophysics and space science*, **80**, 353–368. 121

SUGITANI, K., FUKUI, Y., MIZUNI, A. & OHASHI, N. (1989). Star formation in bright-rimmed globules - Evidence for radiation-driven implosion. *The Astrophysical Journal*, **342**, L87–L90. 1

THE, P.S., DE WINTER, D. & PEREZ, M.R. (1994). A new catalogue of members and candidate members of the Herbig Ae/Be (HAEBE) stellar group. *aaps*, **104**, 315–339. 7

TINNEY, C.G., RYDER, S.D., ELLIS, S.C., CHURILOV, V., DAWSON, J., SMITH, G.A., WALLER, L., WHITTARD, J.D., HAYNES, R., LANKSHEAR, A., BARTON, J.R., EVANS, C.J., SHORTRIDGE, K., FARRELL, T. & BAILEY, J. (2004). IRIS2: a working infrared multi-object spectrograph and camera. In A.F.M. Moorwood & M. Iye, eds., *Ground-based Instrumentation for Astronomy*, vol. 5492 of *Proceedings of SPIE*, 998–1009. 38

TOHLINE, J.E. (2002). The Origin of Binary Stars. *Astronomy & Astrophysics Review*, **40**, 349–385. 24

TURNER, N.H., TEN BRUMMELAAR, T.A., ROBERTS, L.C., MASON, B.D., HARTKOPF, W.I. & GIES, D.R. (2008). Adaptive Optics Photometry and Astrometry of Binary Stars. III. a Faint Companion Search of O-Star Systems. *The Astronomical Journal*, **136**, 554–565. 186

Urquhart, J.S., Busfield, A.L., Hoare, M.G., Lumsden, S.L., Clarke, A.J., Moore, T.J.T., Mottram, J.C. & Oudmaijer, R.D. (2007a). The RMS survey. Radio observations of candidate massive YSOs in the southern hemisphere. *Astronomy & Astrophysics*, **461**, 11–23. 19, 105

Urquhart, J.S., Busfield, A.L., Hoare, M.G., Lumsden, S.L., Oudmaijer, R.D., Moore, T.J.T., Gibb, A.G., Purcell, C.R., Burton, M.G. & Marechal, L.J.L. (2007b). The RMS survey. ^{13}CO observations of candidate massive YSOs in the southern Galactic plane. *Astronomy & Astrophysics*, **474**, 891–901. 19

Urquhart, J.S., Busfield, A.L., Hoare, M.G., Lumsden, S.L., Oudmaijer, R.D., Moore, T.J.T., Gibb, A.G., Purcell, C.R., Burton, M.G., Maréchal, L.J.L., Jiang, Z. & Wang, M. (2008a). The RMS survey. ^{13}CO observations of candidate massive YSOs in the northern Galactic plane. *Astronomy & Astrophysics*, **487**, 253–264. 19

Urquhart, J.S., Hoare, M.G., Lumsden, S.L., Oudmaijer, R.D. & Moore, T.J.T. (2008b). The RMS Survey: A Galaxy-wide Sample of Massive Young Stellar Objects. In H. Beuther, H. Linz & T. Henning, eds., *Massive Star Formation: Observations Confront Theory*, vol. 387 of *Astronomical Society of the Pacific Conference Series*, 381. 20

Urquhart, J.S., Hoare, M.G., Purcell, C.R., Lumsden, S.L., Oudmaijer, R.D., Moore, T.J.T., Busfield, A.L., Mottram, J.C. & Davies, B. (2009a). The RMS survey. 6 cm continuum VLA observations towards candidate massive YSOs in the northern hemisphere. *Astronomy & Astrophysics*, **501**, 539–551. 19

Urquhart, J.S., Hoare, M.G., Purcell, C.R., Lumsden, S.L., Oudmaijer, R.D., Moore, T.J.T., Busfield, A.L., Mottram, J.C. & Davies, B. (2009b). The RMS survey. 6 cm continuum VLA observations towards candidate massive YSOs in the northern hemisphere. *Astronomy & Astrophysics*, **501**, 539–551. 149

Urquhart, J.S., Moore, T.J.T., Hoare, M.G., Lumsden, S.L., Oudmaijer, R.D., Rathborne, J.M., Mottram, J.C., Davies, B. & Stead, J.J. (2011a). The Red MSX Source survey: distribution and properties of a sample of massive young stars. *Monthly Notices fo the Royal Astronomical Society*, **410**, 1237–1250. 90, 102, 167, 184

Urquhart, J.S., Morgan, L.K., Figura, C.C., Moore, T.J.T., Lumsden, S.L., Hoare, M.G., Oudmaijer, R.D., Mottram, J.C., Davies, B. & Dunham, M.K. (2011b). The Red MSX Source survey: ammonia and water maser analysis of massive star-forming regions. *Monthly Notices of the Royal Astronomical Society*, **418**, 1689–1706. 90, 102, 104

Urquhart, J.S., Moore, T.J.T., Csengeri, T., Wyrowski, F., Schuller, F., Hoare, M.G., Lumsden, S.L., Mottram, J.C., Thompson, M.A., Menten, K.M., Walmsley, C.M., Bronfman, L., Pfalzner, S., König, C. & Wienen, M. (2014). ATLASGAL - towards a complete sample of massive star forming clumps. *Monthly Notices fo the Royal Astronomical Society*, **443**, 1555–1586. 88, 90, 91, 201

van Albada, T.S. (1968). The evolution of small stellar systems and its implications for the formation of double stars. *bain*, **20**, 57. 192

Van Loon, J.T., Oliveira, J.M., Wood, P.R., Zijlstra, A.A., Sloan, G.C., Matsuura, M., Whitelock, P.A., Groenewegen, M.A.T., Blommaert, J.A.D.L., Cioni, M.R.L., Hony, S., Loup, C. & Waters, L.B.F.M. (2005). Eso-vlt and spitzer spectroscopy of iras 053286827: a massive young stellar object in the large magellanic cloud. *Monthly Notices of the Royal Astronomical Society: Letters*, **364**, L71–L75. 30

Varricatt, W.P., Thomas, H.S., Davis, C.J., Ramsay, S. & Currie, M.J. (2013). Star formation in the luminous YSO IRAS 18345-0641. *Astronomy & Astrophysics*, **554**, A9. 25, 163, 165

Vieira, S.L.A., Corradi, W.J.B., Alencar, S.H.P., Mendes, L.T.S., Torres, C.A.O., Quast, G.R., Guimarães, M.M. & da Silva, L. (2003). Investigation of 131 Herbig Ae/Be Candidate Stars. *The Astronomical Journal*, **126**, 2971–2987. 7

Vink, J.S., Drew, J.E., Harries, T.J. & Oudmaijer, R.D. (2002). Probing the circumstellar structure of Herbig Ae/Be stars. *Monthly Notices fo the Royal Astronomical Society*, **337**, 356–368. 7

Wall, J.V. & Jenkins, C.R. (2003). *Practical Statistics for Astronomers*. 134

Ward, J.L., Oliveira, J.M., van Loon, J.T. & Sewio, M. (2016). Integral field spectroscopy of massive young stellar objects in the n113 hii region in the large magellanic cloud. *Monthly Notices of the Royal Astronomical Society*, **455**, 2345–2362. 30

Ward, J.L., Oliveira, J.M., van Loon, J.T. & Sewio, M. (2017). K-band integral field spectroscopy and optical spectroscopy of massive young stellar objects in the small magellanic cloud. *Monthly Notices of the Royal Astronomical Society*, **464**, 1512–1552. 30

Wheelwright, H.E., Oudmaijer, R.D. & Goodwin, S.P. (2010). The mass ratio and formation mechanisms of Herbig Ae/Be star binary systems. *Monthly Notices of the Royal Astronomical Society*, **401**, 1199–1218. xiv, 163, 193, 194, 195

Wheelwright, H.E., Vink, J.S., Oudmaijer, R.D. & Drew, J.E. (2011). On the alignment between the circumstellar disks and orbital planes of Herbig Ae/Be binary systems. *Astronomy & Astrophysics*, **532**, A28. 25

Wheelwright, H.E., de Wit, W.J., Oudmaijer, R.D., Hoare, M.G., Lumsden, S.L., Fujiyoshi, T. & Close, J.L. (2012). Probing the envelopes of massive young stellar objects with diffraction limited mid-infrared imaging. *Astronomy & Astrophysics*, **540**, A89. 190

Whitney, B.A., Wood, K., Bjorkman, J.E. & Cohen, M. (2003a). Two-dimensional Radiative Transfer in Protostellar Envelopes. II. An Evolutionary Sequence. *The Astrophysical Journal*, **598**, 1079–1099. 64, 68

Whitney, B.A., Wood, K., Bjorkman, J.E. & Wolff, M.J. (2003b). Two-dimensional Radiative Transfer in Protostellar Envelopes. I. Effects of Geometry on Class I Sources. *The Astrophysical Journal*, **591**, 1049–1063. 64, 68

Williams, J.P., Blitz, L. & McKee, C.F. (2000). The Structure and Evolution of Molecular Clouds: from Clumps to Cores to the IMF. *Protostars and Planets IV*, 97. 13

Williams, S.J. (2015). What Massive Binaries are Telling Us. In S.M. Rucinski, G. Torres & M. Zejda, eds., *Living Together: Planets, Host Stars and Binaries*, vol. 496 of *Astronomical Society of the Pacific Conference Series*, 153. 162

Wolfire, M.G. & Cassinelli, J.P. (1987). Conditions for the formation of massive stars. *The Astrophysical Journal*, **319**, 850–867. 10

Wright, E.L., Eisenhardt, P.R.M., Mainzer, A.K., Ressler, M.E., Cutri, R.M., Jarrett, T., Kirkpatrick, J.D., Padgett, D., McMillan, R.S., Skrutskie, M., Stanford, S.A., Cohen, M., Walker, R.G., Mather, J.C., Leisawitz, D., Gautier, T.N., III, McLean, I., Benford, D., Lonsdale, C.J., Blain, A., Mendez, B., Irace, W.R., Duval, V., Liu, F., Royer, D., Heinrichsen, I., Howard, J., Shannon, M., Kendall, M., Walsh, A.L., Larsen, M., Cardon, J.G., Schick, S., Schwalm, M., Abid, M., Fabinsky, B., Naes, L. & Tsai, C.W. (2010). The Wide-field Infrared Survey Explorer (WISE): Mission Description and Initial On-orbit Performance. *The Astronomical Journal*, **140**, 1868–1881. 19

Yorke, H.W. & Sonnhalter, C. (2002). On the Formation of Massive Stars. *The Astrophysical Journal*, **569**, 846–862. 10

Zhang, Q., Hunter, T.R., Brand, J., Sridharan, T.K., Cesaroni, R., Molinari, S., Wang, J. & Kramer, M. (2005). Search for CO Outflows toward a Sample of 69 High-Mass Protostellar Candidates. II. Outflow Properties. *The Astrophysical Journal*, **625**, 864–882. 190

Zinnecker, H. & Yorke, H.W. (2007). Toward Understanding Massive Star Formation. *Astronomy & Astrophysics Review*, **45**, 481–563. 9, 13

Zorec, J., Arias, M.L., Cidale, L. & Ringuelet, A.E. (2007). Be star disc characteristics near the central object. *Astronomy & Astrophysics*, **470**, 239–247. 29